

# High-resolution VLBI Studies of the Blazars TXS 2013+370, OJ 287, and 3C 454.3

INAUGURAL-DISSERTATION

zur  
Erlangung des Doktorgrades  
der Mathematisch-Naturwissenschaftlichen Fakultät  
der Universität zu Köln



vorgelegt von

**Efthalia Traianou**  
aus Thessaloniki, Griechenland

Köln, 2020

Berichterstatter:

Prof. Dr. Andreas Eckart  
Prof. Dr. J. Anton Zensus

Tag der letzten mündlichen Prüfung: - [11.08.2020](#)

*To my Grandmother*

# ABSTRACT

Blazars are the most luminous sub-class of active galactic nuclei (AGN). Powered by an accreting supermassive black hole (SMBH), these systems are characterized by an axisymmetric pair of powerful relativistic jets that emanate from their central region and are closely aligned to the line of sight of the observer. Thanks to this geometrical coincidence, blazars constitute a unique case of astrophysical objects in which we can study the extreme physical conditions associated with the jet launching region and the strong magnetic fields in the vicinity of the central engine. To date, even though numerous observational and theoretical studies have been established for an improved understanding of the underlying jet physics, a number of questions are pending to be answered. The origin of the high-energy emission and the seed photon field, the true nature of the observed jet base, and the jet phenomenology are investigated in this thesis. For this purpose, we employ a state-of-the-art observational technique called very-long baseline interferometry (VLBI). Simultaneous radio observations at 86 GHz using the largest radio antennas in the world, as well as complementary observations of ground array elements with the space radio telescope *RadioAstron*, give us the unique opportunity to focus on three case studies: the blazars TXS 2013+370, OJ 287 and 3C 454.3.

In the blazar TXS 2013+370, quasi-simultaneous VLBI observations at 15, 43 and 86 GHz, along with space-VLBI data at 22 GHz, allowed us to investigate the jet base with an angular resolution of  $\geq 0.4$  pc. In combination with broad-band variability observations and  $\gamma$ -ray data, the high-resolution VLBI imaging revealed the ejection of new jet features, accompanied by flaring activity in radio/mm- bands and  $\gamma$  rays. The analysis of the transverse jet width profile constrained the mm-VLBI core to be located within  $\leq 2$  pc downstream of the jet apex, and also showed the existence of a transition from parabolic to conical jet expansion at a deprojected distance of  $\sim 54$  pc from the core. The estimation of the intrinsic jet parameters allowed us to determine the magnetic field strength in the 22 GHz VLBI core region to be  $B_{\text{SSA}} = 0.36 \pm 0.16$  G. Cross-correlation analysis of the broad-band variability revealed a strong correlation between the radio-mm and  $\gamma$ -ray data, with the 1 mm emission lagging  $\sim 49$  days behind the  $\gamma$  rays. Based on this, we infer that the high energy emission is produced at a distance of the order of  $\sim 1$  pc from the jet apex, suggesting that the seed photon field for the external Compton mechanism originates either in the dusty torus or in the broad-line region.

The study of the blazar OJ 287 was based on a unique data set, comprising 15, 43 and 86 GHz VLBI observations along with contemporaneous space-VLBI data at 22 GHz, which enabled us to reconstruct for the first time the fine structure of the innermost compact region with the record-resolution of  $10 \mu\text{s}$ . Total intensity and polarization images of the source revealed a complex structure, with the brightest core feature being located a  $\sim 10$  pc



downstream from the innermost jet component. The source modeling enabled us to perform a spectral decomposition analysis of the VLBI knots, which led us to the determination of the synchrotron turnover parameters. Additionally, through spectral index mapping we studied the spectral evolution along the radio jet. The results of the spectral fitting were used to obtain the magnetic field strength of the innermost jet features. We calculated the equipartition Doppler factor to be  $\geq \delta_{\text{eq}} = 2.9 \pm 0.26$ . A variation of the Doppler factor along the jet was also observed, and its origin is unclear. The most likely explanation is the presence of a strong jet bending towards the line of sight, a local change of the plasma speed, or a superposition of both. Polarization imaging and Faraday rotation analysis based on two independent methods helped us to probe the magnetic field topology on sub-parsec scales. A rotation measure analysis in the core region revealed a rotation between  $-440$  to  $-1100 \text{ rad/m}^2$  (obtained from a pixel-based analysis and single-dish flux density variability measurements). By combining the imaging and the rotation measure (RM) analysis, we report indications of the existence of a helical magnetic field in the OJ 287 core region, which is in agreement with similar polarization studies. Furthermore, during our observational interval, a prominent flaring event took place, which allowed us to study the observed brightness temperature evolution in the VLBI core region. We report a rising trend for the innermost VLBI feature during the flare evolution, rising from  $T_b = (33.6 \pm 0.8) \times 10^{11} \text{ K}$  up to  $5.5 \pm 0.9 \times 10^{12} \text{ K}$ . Using the computed  $\delta_{\text{eq}}$ , we estimated that the intrinsic brightness temperature is  $T_{\text{int}} \approx 10^{12} \text{ K}$  in the core region, which is significantly above from the equipartition limit of  $\sim 5 \times 10^{10} \text{ K}$ . This implies that the VLBI core in OJ 287 is particle-dominated.

Lastly, for the blazar 3C 454.3 we analyzed 24 epochs of VLBI data at 43 and 86 GHz. In this thesis, we present for the first time a five-year structural and kinematic study of the innermost jet region of this source, probed by the ultra-high resolution of  $50 \mu\text{as}$  ( $\geq 0.4 \text{ pc}$ ). The results of the analysis revealed that the flux density distribution along the jet is described by components that move with apparent speeds between  $6c$  to  $26c$ , as well as by stationary features. We trace the appearance of 7 new VLBI components during the observing interval of 2013-2017. The detected knots show unusual behavior in their velocity pattern, with a transition from fast motion to apparent stationarity and merging when they reach a radial distance of  $0.5 \text{ mas}$  from the core. The nature of this region was investigated by studying the spectral index variability and the linear polarization of an indicative epoch; however, the physical interpretation remains ambiguous, with possible scenarios involving local jet bending, standing shock or plasma instabilities. Also, indications of trailing jet components have been found, which are related to rarefaction in the near wake of the most prominent propagating disturbances. Lastly, we report that the newly detected features are ejected at different position angles, pointing to more complicated ejection scenarios related to accretion disk precession, jet nozzle precession, or jet instabilities.

# ZUSAMMENFASSUNG

Blazare bilden die leuchtstärkste Unterklasse der aktiven galaktischen Kerne (AGN). Sie werden von akkretierenden, supermassiven schwarzen Löchern (SMBH) angetrieben, und bilden zwei symmetrische, energiereiche, relativistische Jets aus, die eng an der Sichtlinie des Beobachters ausgerichtet sind. Dank dieser geometrischen Eigenschaft stellen Blazare einen besonderen Fall dar, bei denen wir die extremen physikalischen Bedingungen in der Region, in der die Jets produziert werden, und die starken Magnetfelder in der Umgebung des zentralen Antriebssystems untersuchen können. Obwohl viele beobachtende und theoretische Studien zum besseren Verständnis der Physik dieser Jets durchgeführt wurden, bleiben auch heute noch einige Fragen unbeantwortet. Der Ursprung der hochenergetischen Emission und des Ursprungs-Photonfeldes, die wahre Beschaffenheit der beobachteten Jetbasis, und die Jet-Phänomenologie werden in dieser Arbeit behandelt. Um dies zu erreichen, verwenden wir die moderne VLBI-Technik (Very Long Baseline Interferometry). Beobachtungen bei 86 GHz mit den größten Radioteleskopen der Welt, sowie Beobachtungen, bei denen Teleskope auf der Erde durch ein Weltraum-Radioteleskop (RadioAstron) ergänzt werden, erlauben einen Fokus auf drei Fallstudien: Die Blazare TXS 2013+370, OJ 287 und 3C 454.3.

Für den Blazar TXS 2013+370 wurden Beobachtungen bei 15, 43 und 86 GHz, sowie mit Weltraum-VLBI-Daten bei 22 GHz, durchgeführt, die eine Auflösung von  $\geq 0.4$  pc bei dieser Quelle haben. In Kombination mit Beobachtungen der Breitband-Variabilität und Daten bei  $\gamma$ -Wellenlängen zeigen die hochauflösenden VLBI-Bilder den Ausstoß neuer Jet-Komponenten, die mit einem Aufflackern im Radio/mm und  $\gamma$ -Bereich begleitet werden. Die Analyse des transversalen Jetprofils zeigt, dass sich der mm-VLBI-Kern  $\leq 2$  pc vom Scheitelpunkt des Jets entfernt befindet, und außerdem einen Übergang von parabolischer zu kegelförmiger Ausdehnung des Jets bei einem Abstand von  $\sim 54$  pc vom Kern. Die Abschätzung der Jet-Parameter ergab eine magnetische Flussdichte von  $B_{\text{SSA}} = 0.36 \pm 0.16$  G in der 22 GHz VLBI-Kernregion. Eine Kreuzkorrelationsanalyse der Breitband-Variabilität offenbart eine starke Korrelation zwischen den Radio-mm und  $\gamma$ -Daten, wobei die Emission bei 1 mm der  $\gamma$ -Emission  $\sim 49$  Tage nachläuft. Daraus leiten wir ab, dass die hochenergetische Strahlung in der Größenordnung von  $\sim 1$  pc Abstand vom Scheitelpunkt des Jets erzeugt wird. Dies weist darauf hin, dass das Ursprungs-Photonfeld für den externen Compton-Mechanismus im Staub-Torus oder in der Broad-Line-Region entsteht.

Für die Studie am Blazar OJ 287 ziehen wir einen einzigartigen Datensatz heran, der aus 15, 43 und 86 GHz VLBI-Daten und Weltraum-VLBI-Daten bei 22 GHz besteht. Dieser erlaubt es uns, die Feinstruktur des innersten, kompakten Bereichs der Quelle mit einer Rekord-Auflösung von  $10 \mu\text{as}$  zu untersuchen. Bilder in totaler Intensität und in Polarisation zeigen eine komplexe Struktur, wobei sich die hellste Komponente des Kerns  $\sim 10$  pc ablaufseitig

von der innersten Jet-Komponente befindet. Die Modellierung der Quelle erlaubte es uns, eine Analyse der spektralen Zerlegung der VLBI-Komponenten durchzuführen, durch die wir die Parameter des Synchrotron-Wendepunkts bestimmen konnten. Zusätzlich haben wir die spektrale Änderung entlang des Jets durch Kartierung des Spektralindex untersucht. Die Ergebnisse des Fits ergaben die magnetische Flussdichte der innersten Jet-Komponenten. Der Äquipartitions-Dopplerfaktor entlang des Jets wurde zu  $\leq \delta_{\text{eq}} = 4.13 \pm 0.26$  bestimmt, wobei eine Variation entlang des Jets festgestellt wurde, deren Ursprung unklar ist. Die wahrscheinlichste Erklärung ist eine starke Krümmung des Jets gegenüber der Sichtlinie, eine lokale Änderung der Plasmageschwindigkeit, oder eine Kombination aus beidem. Bildgebung in Polarisation und eine Analyse der Faraday-Rotation auf Basis zweier unterschiedlicher Methoden ermöglichten es uns, die Topologie des Magnetfeldes auf sub-pc Skalen zu untersuchen. Eine Analyse des Rotationsmasses (RM) in der Kernregion ergibt Werte zwischen -440 und -1100 rad/m<sup>2</sup> (aus einer pixel-basierten Analyse und Flussdichteveränderungen gemessen an Einzelteleskopen). Durch Kombination der Bildgebungs- und RM-Analyse offenbart sich ein spiralförmiges Magnetfeld in der Kernregion von OJ 287, was sich mit ähnlichen Studien zur Polarisation deckt. Außerdem gab es während der Zeit unserer Beobachtungen ein Aufflackern der Quelle, das uns eine Untersuchung der Entwicklung der beobachteten Helligkeitstemperatur möglich machte. Wir beobachteten einen steigenden Trend für die innerste VLBI-Komponente während der Entwicklung des Aufflackerns, von  $T_b = (33.6 \pm 0.8) \times 10^{11}$  K bis zu  $5.5 \pm 0.9 \times 10^{12}$  K. Mithilfe des berechneten  $\delta_{\text{eq}}$ , schätzen wir die intrinsische Helligkeitstemperatur auf  $T_{\text{int}} \approx 10^{12}$  K in der Kernregion, was signifikant höher ist als das Limit durch Äquipartition von  $\sim 5 \times 10^{10}$  K. Dies impliziert, dass der VLBI-Kern von OJ 287 Teilchenenergie dominiert ist.

Zu guter Letzt haben wir 24 Beobachtungsperioden von VLBI-Daten bei 43 und 86 GHz für den Blazar 3C 454.3 ausgewertet. In dieser Arbeit präsentieren wir zum ersten Mal eine strukturelle und kinematische Studie der innersten Jetregion dieser Quelle bei einer ultrahohen Auflösung von  $50 \mu\text{as}$  ( $\geq 0.4$  pc). Die Ergebnisse dieser Analyse zeigen, dass die Verteilung der Flussdichte entlang des Jets einerseits durch Komponenten beschrieben wird, deren scheinbare Geschwindigkeit zwischen  $6c$  und  $26c$  liegt, sowie andererseits durch stationäre Komponenten. Wir zeigen das Auftreten von 7 neuen VLBI-Komponenten im Beobachtungsintervall von 2013-2017 auf. Die detektierten Jetkomponenten zeigen ein ungewöhnliches Verhalten in ihrem Geschwindigkeitsmuster. Dabei wechseln sie von schneller Bewegung zu scheinbarer Stationarität und verschmelzen, wenn sie eine radiale Distanz von  $0.5$  mas vom Kern erreicht haben. Die Beschaffenheit dieser Region wurde durch die Variabilität des Spektralindex und der linearen Polarisation in einer bezeichnenden Epoche untersucht. Die physikalische Interpretation bleibt jedoch uneindeutig. Mögliche Szenarien sind lokale Krümmung des Jets, stehende Schocks oder Instabilitäten des Plasmas. Außerdem fanden wir Anzeichen nachfolgender Jetkomponenten, die in Beziehung zur Verdünnung des

Jets, in Verbindung mit den größten sich fortbewegenden Störungen, stehen. Die neu aufgetretenen Komponenten werden außerdem bei verschiedenen Positionswinkeln ausgestoßen, was auf komplexere Szenarien hinweist, bei denen die Präzession der Akkretionsscheibe oder der Jet-Düse, oder aber Instabilitäten im Jet eine Rolle spielen.

# Contents

<b>Abstract</b>	<b>iii</b>
<b>Zusammenfassung</b>	<b>v</b>
<b>1 The physical properties of blazars and their characteristics</b>	<b>1</b>
1.1 Active Galactic Nuclei . . . . .	1
1.1.1 Brief Historical Overview . . . . .	2
1.1.2 AGN Anatomy . . . . .	3
1.1.3 Unification Model and Classification . . . . .	7
1.2 The Blazar Phenomenon . . . . .	8
1.3 Relativistic Jets in AGN . . . . .	9
1.3.1 Radiation Mechanisms . . . . .	10
1.3.1.1 Synchrotron Radiation . . . . .	10
1.3.1.1.1 Synchrotron Self-Absorption . . . . .	13
1.3.1.2 Polarized Emission . . . . .	14
1.3.1.2.1 Linear Polarization . . . . .	14
1.3.1.2.2 Circular Polarization: . . . . .	16
1.3.1.2.3 Faraday Rotation: . . . . .	17
1.3.1.3 Inverse Compton Radiation . . . . .	17
1.3.1.4 Pion Decay . . . . .	19
1.3.1.5 Pair Annihilation . . . . .	19
1.4 Gamma-ray emission in Blazars . . . . .	20
1.4.1 Jet Formation, Acceleration and Collimation . . . . .	22
1.4.2 Shocks and Instabilities . . . . .	24
1.5 Brightness Temperature . . . . .	24
1.6 Special Relativity and Jets . . . . .	26
1.6.1 Relativistic Beaming . . . . .	27
1.6.2 Superluminal Motion . . . . .	29
<b>2 Observing Techniques and Instruments</b>	<b>32</b>
2.1 Fundamentals of Radio Interferometry . . . . .	32
2.1.1 Radio Telescope . . . . .	32
2.1.2 Interferometry and Aperture Synthesis . . . . .	34
2.1.2.1 Earth Rotation and Aperture Synthesis . . . . .	35

2.1.3	Very Long Baseline Interferometry . . . . .	38
2.1.4	VLBI Arrays . . . . .	39
2.1.4.1	Global Millimeter VLBI Array . . . . .	39
2.1.4.2	<i>RadioAstron</i> Satellite . . . . .	40
2.2	Calibration and Imaging of VLBI Data . . . . .	41
2.2.0.1	Fringe Fitting . . . . .	41
2.2.0.2	Amplitude Calibration . . . . .	42
2.2.0.3	Imaging . . . . .	44
2.2.0.4	Polarization Calibration . . . . .	44
2.3	<i>Fermi</i> Gamma Ray Space Telescope . . . . .	48
<b>3</b>	<b>Localizing the High-energy Emitting Region in the Blazar TXS 2013+370</b>	<b>49</b>
3.1	Introduction . . . . .	49
3.2	Observations and Data Reduction . . . . .	51
3.2.1	VLBI Observations . . . . .	51
3.2.1.1	VLBI Data Calibration . . . . .	52
3.2.2	<i>Fermi</i> -LAT Data Analysis . . . . .	52
3.2.3	Single-dish Observations . . . . .	53
3.3	Data Analysis and Results . . . . .	56
3.3.1	VLBI Imaging and Model-fitting . . . . .	56
3.3.2	Source Structure and Jet Kinematics . . . . .	57
3.3.3	Location of the Jet Apex . . . . .	59
3.3.4	Spectral Evolution and Turnover Frequency . . . . .	61
3.3.5	Multi-band Variability . . . . .	63
3.3.5.1	Discrete correlation function analysis . . . . .	63
3.3.5.2	Spearman's Rho Test . . . . .	64
3.4	Discussion . . . . .	66
3.4.1	Intrinsic Jet Parameters . . . . .	66
3.4.2	Location of the Gamma-ray Emission . . . . .	67
3.4.3	Transition from parabolic to conical expansion . . . . .	69
3.4.4	Magnetic Field Strength Estimation . . . . .	69
3.5	Conclusions . . . . .	70
<b>4</b>	<b>Revealing the Jet Fine Structure in the Blazar OJ 287</b>	<b>72</b>
4.1	Introduction . . . . .	72
4.2	Observations, Data Calibration, and Imaging . . . . .	74
4.2.1	Total Intensity Data Calibration . . . . .	74
4.2.2	Single-dish Observations . . . . .	75
4.2.3	Polarization Data Calibration . . . . .	77
4.2.4	Uncertainties in Polarization Quantities . . . . .	78
4.3	Data Analysis and Results . . . . .	80
4.3.1	Jet Morphology and Modeling . . . . .	80
4.3.2	Linear Polarization Morphology . . . . .	81
4.3.3	Spectral Index Analysis . . . . .	83
4.3.3.1	Synchrotron Spectra from VLBI Knots . . . . .	85
4.3.3.2	Pixel-based Spectral Decomposition . . . . .	85
4.4	Discussion . . . . .	88

4.4.1	Magnetic Fields and Doppler Factor . . . . .	88
4.4.2	Brightness Temperature Distribution . . . . .	90
4.4.3	Rotation Measure Analysis . . . . .	92
4.4.3.1	Magnetic Field Topology of the Core Region . . . . .	92
4.4.3.2	Rotation Measure from a Pixel-based Method . . . . .	93
4.4.3.3	Rotation Measure Between 10.45-235 GHz . . . . .	95
4.4.3.4	Plasma Electron Density . . . . .	95
4.4.4	The Nature of the Core Features of OJ 287 . . . . .	96
4.5	Conclusions . . . . .	96
<b>5</b>	<b>Probing the Peculiar Jet Kinematics in the Blazar 3C 454.3</b>	<b>98</b>
5.1	Introduction . . . . .	98
5.2	Observations and Data Reduction . . . . .	101
5.2.1	VLBI Observations . . . . .	101
5.2.1.1	VLBI Data Calibration and Imaging . . . . .	101
5.3	Data Analysis and Results . . . . .	101
5.3.1	Source Structure and Jet Kinematics . . . . .	101
5.4	Discussion . . . . .	107
5.4.1	Intrinsic Jet Parameters . . . . .	107
5.4.2	Comparison with Previous Studies . . . . .	109
5.4.3	The Nature of Region S . . . . .	110
5.4.4	Trailing Components? . . . . .	112
5.5	Conclusions . . . . .	114
<b>6</b>	<b>Concluding Remarks and Future Perspectives</b>	<b>115</b>
	<b>Appendix A</b>	<b>119</b>
A.1	Relevance of Interstellar scattering . . . . .	119
A.2	Image and model-fitting parameters of TXS 2013+370 . . . . .	120
	<b>Appendix B</b>	<b>125</b>
B.1	Image and model-fitting parameters of OJ 287 . . . . .	125
	<b>Appendix C</b>	<b>126</b>
C.1	Image and model-fitting parameters of 3C 454.3 . . . . .	126

# Chapter 1

## The physical properties of blazars and their characteristics

One of the most fascinating fields in astronomy is the study of the structure and evolution galaxies. Based on Hubble's Ultra Deep Field observations, it is estimated that the observable Universe contains  $\sim 200$  billion galaxies (Beckwith et al. 2006). The details of the formation and the evolution of those cosmic objects remains a matter of debate (Mo et al. 2010). Nevertheless, the development of technology and the improvement in the observational techniques across the electromagnetic spectrum has enabled the study and the classification of a range of extragalactic sources. Out of all galaxies, radio galaxies attract interest due to their high luminosity and prominent jet emission. In this thesis, we are going to study three objects that belong to the sub-category of powerful radio galaxies, which are called blazars.

### 1.1 Active Galactic Nuclei

A fundamental building block of the cosmic web is galaxies. A great variety of galaxies are situated across the Universe. Among them, there is a small-numbered group of  $\sim 15\%$  of all galaxies, which are called Active Galactic Nuclei (AGN). A galaxy is characterized as active when extremely energetic phenomena are taking place in its central region. The core of such an object is compact and brighter than the entire host galaxy, with a luminosity of  $L \approx 10^{48} \text{ erg s}^{-1}$ , emitted mostly from a small and compact central region of  $\leq 1 \text{ pc}^3$  (Krolik 1999). The luminosity that AGN produce is so enormous, that in many cases exceed the luminosity of a typical galaxy by four orders of magnitude, considering that the surface luminosity of a typical galaxy is  $L \approx 10^{44} \text{ erg s}^{-1}$  (Krolik 1998). A general feature of AGN is that are pan-chromatic emitters, which show characteristic emission patterns and extreme flux density variability within days, hours, and even minutes. Our current understanding of the driving mechanism behind these events is still far from being fully understood. Also, a significant aspect of deepening our knowledge in AGN behaviour, is that we have the opportunity to obtain indirect information about the host galaxy, or the evolution of the whole Universe. A characteristic example of such a case is the study of the causally connected relationship between the mass of the central engine and the velocity dispersion of the host galaxy stars. The study of the so-called  $M - \sigma$  relation (here  $M$  is the mass of the central engine and  $\sigma$  the central stellar velocity dispersion) is very important, as



it can reveal more details about the galaxy formation and SMBH-host galaxy evolution (e.g., [Ferrarese & Merritt 2000](#)). Also, it has been found indications that the terminal regions of the AGN jets, may have contributed significantly to the ionization of hydrogen in the late re-ionization epoch ([Bosch-Ramon 2018](#)). Moreover, the propagation of powerful relativistic jets that emanate from AGN, interact with the surrounding intergalactic medium, and in some cases can lead to the formation of large X-ray cavities ([Forman et al. 2005](#); [Randall et al. 2011](#); [Blanton et al. 2011](#)). Such cavities, can affect the evolution of the whole galaxy cluster through the suppression of the cooling flows that are created inside the cluster and which support the fast growth of central galaxies ([McNamara & Nulsen 2007](#)). Considering all the above it is easy to understand the importance of the observations and the detailed study of these objects. In the following sections, we are going to address some of the open questions about AGN and report the current status of related research.

### 1.1.1 Brief Historical Overview

Astronomy is the oldest of all natural sciences. Since the first humans looked up in the sky, they started wondering about the nature of the celestial objects and the possible connection with their lives. Only less than 100 years ago, independent astronomical observations by Harlow Shapley and Heber Curtis in 1920 lead to the 'Great Debate' ([Hoskin 1976](#)), a public discussion between them about the nature of "spiral nebulae" objects in the sky. The primary topics in this debate were the actual distance of those objects from the Earth and as an extension, the size of the Universe. The answer to this question came few years after by Edwin Hubble in 1925. Hubble determined the distances of NGC 6822, M 33, and M 31 ([Hubble 1929](#), and references therein) by observing periodic fluctuations of Cepheids, a type of star with a standard absolute magnitude. The calculated distance of those stars placed the location of their hosting "nebulae" to be well outside of our Galaxy. Extragalactic astronomy was born after that day, and a new window in astronomy and cosmology was opened. Several years before the event mentioned above, spectroscopic observations of nearby galaxies like NGC 1068 ([Fath 1909](#)), revealed the existence of emission lines in the nuclear spectrum, even though there was not yet a physical understanding of AGN objects. Carl Seyfert in 1943, suggested a new category of galaxies with bright central regions and spectra dominated by high-excitation emission lines ([Seyfert 1943](#)), by performing a systematic study of galaxies. This type of galaxy today, is named after him: *Seyfert Galaxies*.

The development of radio astronomy set the next milestone in AGN physics. Karl Jansky, in 1932, reported that faint radio emission was coming from the Milky Way, peaking in the direction of its center ([Jansky 1933](#)). Many astronomical studies followed, detecting strong radio emission from "radio-stars" with a counterpart in the optical regime, leading the astronomers to categorize these objects with the name "star-like", Quasi-Stellar Objects (QSOs) or quasars. A prominent quasar discovery was 3C 273. The optical spectrum of this radio source showed peculiar broad emission lines, which are untypical for a star. Additionally, the spectrum appeared to come from unknown excited atoms ([Hazard et al. 1963](#); [Schmidt 1963](#)). Later on, it turned out that these lines belonged to known atomic transitions, that are redshifted due to the Doppler effect. This fact implied that the source is not only extragalactic, but also that it moves away from Earth. By measuring the shifting of the lines, it was calculated that this galaxy is located at a distance of 2.4 Gly ( $z=0.158$ ). Note here that the Doppler redshift is expressed like  $\lambda = \lambda_0 (1 + z)$ , where  $\lambda$  is the observed wavelength,  $\lambda_0$  the emitted wavelength and  $z$  is the redshift of the source. Another salient

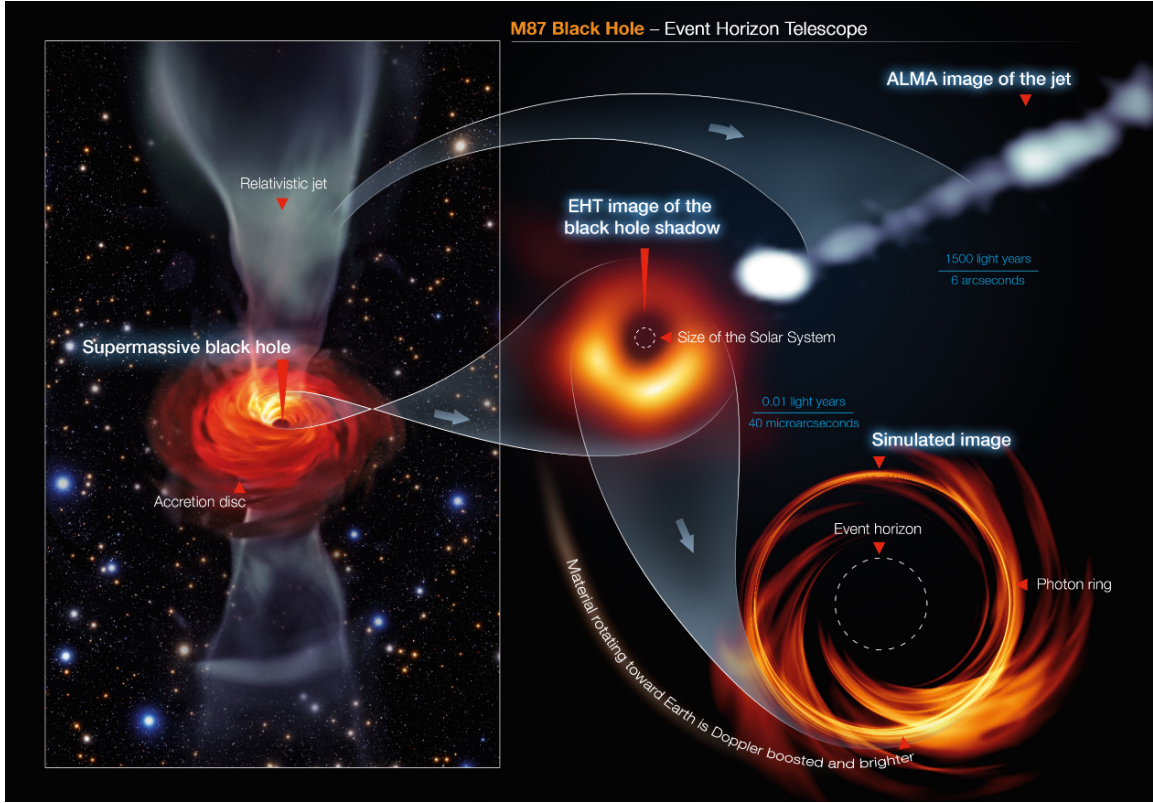


FIGURE 1.1: The first-time-ever image of the supermassive black hole at the center of the M 87 galaxy. Left: Simulation of the AGN that located in the heart of M 87. Matter is falling into the SMBH, forming an accretion disk. Perpendicular to each side of the accretion disk, two powerful jets of plasma are emanating from the central engine (Davelaar et al. 2018). Top right: High-resolution radio image of the M 87 jet, as seen by the ALMA array (Goddi et al. 2019). Bottom right: The bright ring around the compact center is formed as light bends in the strong gravitational field around a black hole with mass  $\sim 6.5 \times 10^9 M_{\odot}$  (Event Horizon Telescope Collaboration et al. 2019).

feature in some of these objects was the existence of a jet. The first detection of an AGN jet (M 87) was made by Curtis in 1918 (Curtis 1918), indicating that a violent mechanism is driving the launching of those objects. Moreover, the astonishing luminosities of these distant quasars were explained by Edwin Salpeter and Yakov Zeldovich in 1964 (Salpeter 1964; Zel'dovich 1964) as a result of a highly efficient astrophysical mechanism like the accretion of gas onto a supermassive black hole (SMBH).

Today, numerous ongoing studies are aiming to extend our understanding of AGN physics. The latest historical achievement in the field of AGN studies was obtained with the Event Horizon Telescope (EHT). The goal of this experiment was to capture for the first time the image of a black hole and its "shadow" by using an eight-element radio array, observing at 1 mm. In Figure 1.1 we can see the first image of the SMBH that is located at the center of the active galaxy M 87.

### 1.1.2 AGN Anatomy

The powerful cosmic engines called AGN are complex systems that can be decomposed into different parts. In the following, we will briefly describe the physical contribution of each

AGN component and its characteristics. A conceptual illustration of such a system can be seen in Fig. 1.2.

At the heart of an active galaxy is located the “central engine”. The central engine is a giant supermassive black hole, with a mass that usually exceeds  $10^6 M_\odot$ , reaching even  $10^{10} M_\odot$ . The physical process that allows a SMBH to gain such a large amount of mass is either via accretion of matter or via merging with other SMBH’s (Volonteri 2012, and references therein). The strong gravitational field around a SMBH plays the role of a “driving force” for the AGN system. As the surrounding matter falls into the central region, it encounters a characteristic spherical surface that is formed around the SMBH (assuming a Schwarzschild black hole), which is called the “event horizon”. The radius of the physical boundary where the escape velocity becomes greater than the speed of light is defined by the so-called Schwarzschild radius, which for a non-rotating Black Hole (BH) is  $R_s = 2GM/c^2$ , where  $G$  is the gravitational constant,  $M$  is the BH mass, and  $c$  is the speed of light. In General Relativity, the last stable orbit for a test particle around a black hole, called the Innermost Stable Orbit (ISCO) and usually set the inner edge of the accretion disk. Depending on the BH mass and spin, the ISCO radius can extend down to  $\sim 6R_s$ , for a non-spinning BH and to  $1.1 R_s$  for a BH with maximum spin.

Moving outer from the central object, we meet the accretion disk. Accretion disks around black holes are flows of gas that falls inwards to the black hole following tendex lines, the paths that matter follows when it falls into a black hole, due to the strong gravitational potential of the central object. The radiation of the accretion disk is thermal, as the gravitational and frictional forces compress the gas and raise its temperature. The observational signature of the accretion disk emission in an AGN Spectral Energy Distribution (SED) plot can be found mostly in the UV/optical wavelengths. A characteristic spectral feature known as “the blue bump” corresponds to this AGN part, whereas, a similar feature appears in the soft X-rays regime too, known as “the big blue bump”. The accretion disk radiation also plays a significant role in the production of GeV/TeV emission, as it contributes to the seed photons that are needed for the inverse Compton process to take place (see Section 1.3.1.3 and Section 1.4).

Accretion flows are mainly divided into two categories: hot and cold. Cold accretion plasma flows consists of temperature around  $T \sim 10^4$  K (Shakura & Sunyaev 1973) and dense plasma, are optically thick and usually, are relative to high mass accretion rates. Such kinds of flows produce geometrically thin and luminous accretion disks (Shakura & Sunyaev 1973). On the other hand, hot accretion plasma flows (close to virial temperature  $T \sim 10^{10}$  K, (Yuan & Narayan 2014)) are characterized by sub-Eddington’s accretion rate’s, are optically thin, and are described by accretion models such as the Advection-Dominated Accretion Flow (ADAF). The ADAF is a cooling mechanism where the heat transferring is channeled through the plasma’s bulk motion, instead of radiation. Such accretion disks are geometrically thick, and they resemble a sphere or corona of hot material that is characterized by non-thermal emission (Yuan & Narayan 2014). This specific type of accretion is particularly interesting as it is linked with the AGN jets. Furthermore, the strong magnetic fields expected in disks can play a crucial role in jet collimation.

Based on the observed hard X-ray AGN emission, many theoretical studies suggest that the X-rays originate from a hot gas corona ( $\sim 10^9$  K) above a cold accretion disc (Galeev et al. 1979; Haardt & Maraschi 1991; Poutanen & Svensson 1996). Reports in the literature indicate that this corona lies between 6 to  $20 R_s$  above the central engine (Fabian et al. 2009), and it is caused by thermal Comptonization (see Section 1.3.1.3) of the accretion

disk photons (Haardt et al. 1997, and references therein). It is believed that a substantial fraction of the gravitational accretion energy is dissipated directly into the corona, although the physical processes that heats the corona are still unknown.

In a spherical region around the accretion disk and the central engine, characteristic broad emission lines, correspond to a region known as Broad Line Region (BLR), are detected in the optical and UV band. The origin of these broadened lines is the high Keplerian-velocity clouds, exceeding the speed of  $10^3 \text{ km s}^{-1}$  and electron densities of  $n \simeq 10^{10} - 10^{11} \text{ cm}^{-3}$  (Netzer 2013). Theoretical models consider the formation of the BLR that it may arise from a gravitationally unstable outer disk or similar disk outflow mechanisms. The radius of BLR ( $R_{BLR}$ ) is related to the luminosity of the AGN continuum emission by the relation: the  $R_{BLR} \propto L^{1/2}$ . For estimating the  $R_{BLR}$  the technique of the *Reverberation Mapping* is widely used (Blandford & McKee 1982), by measuring the lag between the correlated variability of continuum source emission (usually the accretion disk or the SMBH) with the broad lines flux. Based on AGN observations as determined by the emissivity of  $H_\beta$  line, the BLR extends in a region of 0.01 - 1 pc (Peterson & Horne 2006). The knowledge of the  $R_{BLR}$  can lead us to estimate the mass of the central engine by the relation:  $M = f R_{BLR} V^2 / c$ , where  $f$  is a dimensionless factor, and  $V$  the BLR velocity. Nevertheless, significant uncertainties about the geometry, dynamics, and physics of BLR remain (Sulentic et al. 2003; Gaskell 2009).

Another building block of an AGN, is located at the outer edge of the BLR, extending from 1 to 10 pc radial distance downstream from the center (Netzer 2013), and is called *Molecular Torus* (MT). It is formed by gas from the host galaxy that falls into a region dominated by the gravitational potential of the central engine and due to angular momentum conservation forms an axisymmetric and toroidal structure around the SMBH. It is characterized by extreme column densities, exceeding the  $10^{25} \text{ cm}^{-2}$ . Because it extends over such a large region, we detect different emission signatures coming from different regions of the torus. For example, the inner parts of the torus interact with the nuclear radiation, resulting in the ionization of the existing material and the emission of the narrow Fe K $\alpha$  spectral line. The outer MT part is cold and optically thick, radiates primarily in infrared, and shows absorption lines. The orientation of the MT relates to our line of sight plays a crucial role in the categorization of AGN.

Gas clouds in the polar regions are ionized by radiation from the AGN and give rise to narrow UV/IR/optical permitted, semi-forbidden, and forbidden lines. This region named because of this characteristic *Narrow Line Region* (NLR). The full width at half maximum (FWHM) of the spectral lines indicates gas velocities of the order of 400-500 km/s, and the forbidden lines show gas densities of  $10^3 - 10^5 \text{ cm}^{-3}$  (Groves 2007). The NLR extends in a radial distance range from the center showing dimensions of 100 up to 300 pc. In Fig. 1.4 is shown the Spectral Energy Distribution (SED) of a typical, unobscured AGN galaxy, as well as the observed contribution of each part of it. The most prominent feature in all radio-loud AGN is the existence of highly relativistic and collimated plasma jets. In Section 1.3 we are going to discuss the physical jet procedures in more detail.

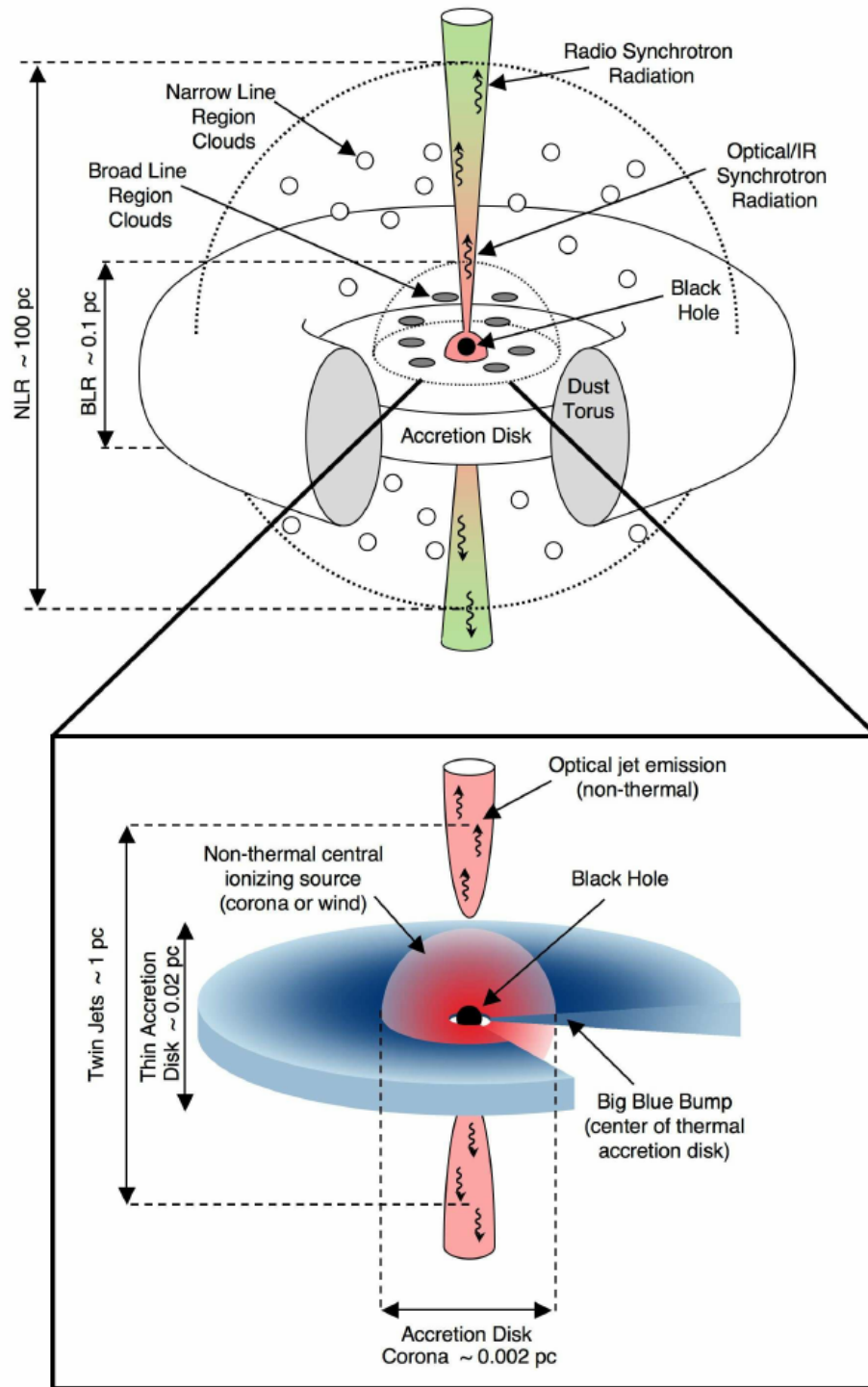


FIGURE 1.2: The main components of AGN, according to the unification model. Top: At the center of the system lies an accreting SMBH. The matter that falls into the central engine forms an accretion disk. Further outwards, a torus of dust can be found, regions of broad and narrow emission lines, as well as bipolar jets of plasma. Bottom: The inner structure of an AGN, on scales up to 1 pc. Image credits: [Unwin et al. \(2008\)](#).



### 1.1.3 Unification Model and Classification

Many years of systematic observations across the electromagnetic spectrum reveal that AGN shows a wide range of different properties between them. Several attempts have been performed to classify those objects, leading to the creation of a long list of AGN classes that is known as the AGN “zoo”. Among all these different criteria, however, the most widely accepted are based on the AGN radio and spectropolarimetric properties. For instance, all radio galaxies are classified into two main categories: the *radio-loud* and the *radio-quiet* (see Fig. 1.3).

The *radio loudness*  $R_L$  ratio between the radio luminosity of an AGN at 5 GHz over its optical luminosity at  $\lambda = 4400\text{\AA}$  ( $L_{5\text{GHz}} / L_{4400\text{\AA}}$ ) helps us to classify these objects based on jet radio emission. The radio-loud galaxies are characterized by  $R_L \geq 10$  whereas the radio-quiet by  $R_L \leq 10$ . In practice, the existence or the absence of the large scale radio jet in an AGN determines the radio loudness of the galaxy, as AGN jets are the primary emitters in the radio regime. Now, each AGN category is further divided into two sub-categories: *type 1* and *type 2* objects. The type 1 category includes Seyfert 1 galaxies and quasars. Some of the main characteristics of Seyfert 1 AGN are their orientation face-on to our line of sight, a spiral galaxy host, the narrow forbidden lines, and the strong, Doppler broad emission lines in their optical spectrum. The emission line broadening implies extremely high gas velocities, ranging from 500 up to 4000 km/s. On the other hand, quasars usually are found in elliptical galaxies. Broad emission lines also characterize them, and typically their redshift is quite large (the peak quasar population appears at  $z=2$  (Hewitt & Burbidge 1993)). Nevertheless, the most prominent feature of a quasar is the flux variability in several observing bands. As type 2 radio-quiet galaxies are considered the Seyfert 2. Seyfert 2 galaxies exhibit narrow permitted and forbidden lines, as well as broad lines. Most of the differences between Seyfert 1 and 2 galaxies are coming from their orientation (Antonucci & Miller 1985). Notably, spectropolarimetric studies in the Seyfert 2 galaxy NGC 1068 showed that the observed polarized light belongs to the nucleus of a Seyfert 1 galaxy. However, the continuum and broad Balmer line polarization seems to result via scattering by a dust cloud, the obscuring dust torus around the nucleus, orientated perpendicular to the nuclear symmetry axis in our line of sight. Besides this, there are four more intermediate sub-categories of Seyfert galaxies, the Seyfert 1.2, 1.5, 1.8 and 1.9, classified according to their  $H_\alpha/H_\beta$  lines intensity ratio (Osterbrock 1981).

Nevertheless, in some cases, the observed differences between AGN categories are caused exclusively by geometrical effects. Intrinsic physical parameters can alter an AGN appearance such as the gravitational interaction between neighboring AGN-galaxy pairs that cause temporary obscuration (Traianou et al. 2020 in prep.), tidal disruption events (TDE) or instabilities in the accretion flow (Śniegowska & Czerny 2019). All the alternatives mentioned above are known as the Changing Look phenomenon in AGN (CL AGN). Almost 90% of all known AGN belong to the radio-quiet classes (Urry & Padovani 1995). The other 10% of the known AGN are radio-loud objects that are divided into Radio Galaxies and Blazars. Fanaroff and Riley in 1974 proposed to categorize all the radio galaxies in two groups, the Class I and Class II. These categories are known today as Fanaroff-Riley 1 and 2 (FR I, FR II, Fanaroff & Riley 1974). The main characteristic of all FR type AGN is the existence of double and symmetrical relativistic jets, which can extend up to Mpc scales and end in large-scale structures that are known as radio lobes. The difference between the two classes is that FR I galaxies have radio luminosities  $\leq L^{25.2} \text{ W/Hz}$  and the brighter jet region are spotted close to the galaxy’s center. On the other hand, FR II galaxies are more luminous than the breaking point of  $L^{25.2} \text{ W/Hz}$  and have faint, but well-collimated jets

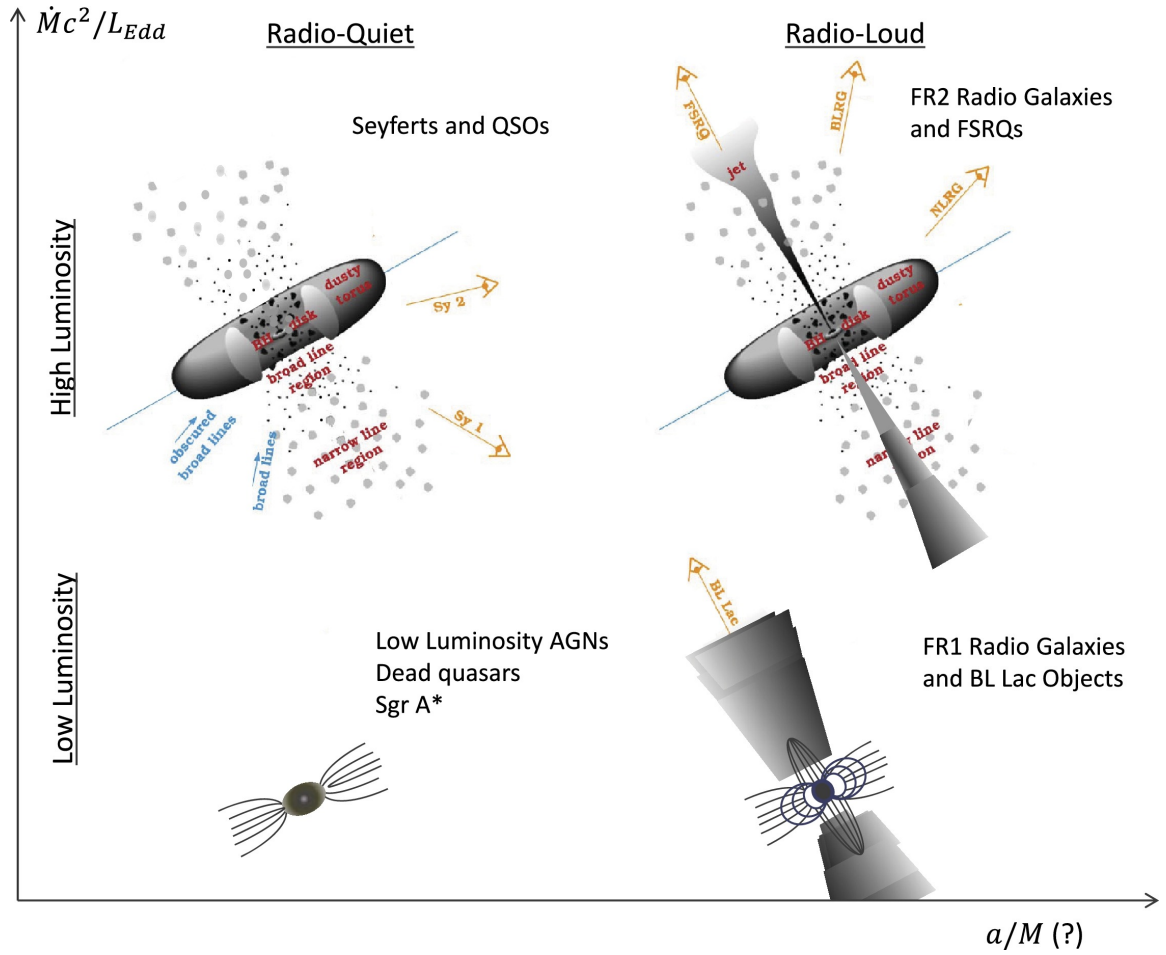


FIGURE 1.3: Classification of active galaxies based on their observed properties. AGN are subdivided into different classes depending on their radio loudness and/or the presence of optical lines in their spectra. This plot, implies a speculation about a link between mass accretion rate, SMBH rotation and AGN loudness ( $\alpha$  is the angular momentum of the SMBH and  $M$  its mass). Image credits: [Dermer & Giebels \(2016\)](#).

with bright "hot-spots" at the end of their radio lobes. The last category which we discuss here is the class of Blazars. For this, we will dedicate a separate section, because all the scientific targets in this thesis belong to this AGN category.

## 1.2 The Blazar Phenomenon

Blazars are the most extreme members of the AGN family. They comprise less than 5% of the entire AGN population, and they exhibit some of the most powerful phenomena in the Universe. By definition, blazars are jetted AGN, which are pointing towards our line of sight. Their general observational properties are the large amplitude variability of non-thermal continuum emission across all frequencies. The variability timescales can range from several years to a few hours, whereas high polarization degrees are detected from radio to optical regimes. Some blazars exhibit thermal emission features too, that originate from the accretion disk or the corona. The morphology of the spectral energy distribution (SED) of a blazar is dominated by a double-peaked structure, as shown in Fig. 1.4. The first spectral bump is produced in the jet, via synchrotron radiation by

relativistic electrons moving along the magnetic field lines (see Section 1.3.1.1). The nature of the second hump is related to the inverse Compton emission. Several theoretical models aim to reproduce this second SED component based on the jet particle population, with the two main categories being the hadronic and leptonic models. In hadronic models, the X-rays and  $\gamma$  rays emission considered as being produced by synchrotron radiation from photons within the jet, protons and via photo-pion-production (Boettcher 2012).

In reality, protons are quite massive to be accelerated to sufficient energies in order to produce this radiative output, without the presence of a very strong magnetic field. On the other hand, even though leptonic models can explain quite well the high energy emission through inverse-Compton scattering (IC) of low energy photons with ultra-relativistic electrons, for many blazars like AO 0235+164, leptonic models fail to reproduce the observed SED (Böttcher et al. 2013). To date, no definitive indication has been found to discern between these two scenarios, while some other models support that lepto-hadronic models are the most realistic (Rodrigues et al. 2019; Diltz & Böttcher 2016, and references therein). Ultimately, blazars are sub-divided into specific categories based on their emission characteristics. For instance, depending on which frequency the first peak appears, blazars can be sub-divided to low-energy peaked blazars (LBLs), when the first SED component peaks in radio to optical bands ( $< 10^5$  GHz), intermediate peaked blazars (IBLs) (between  $10^5$  GHz and  $10^6$  GHz) and high-energy peaked blazars (HBLs), when the first hump peaks in UV/X-rays (above  $10^6$  GHz) (Padovani & Giommi 1995; Sambruna et al. 1996; Ghisellini et al. 1997; Abdo et al. 2010).

Blazars are also classified based on their optical properties into the BL Lacertae objects (BL Lacs) and the Flat Spectrum Radio Quasars (FSRQs). FSRQs show broad and strong emission lines in their optical spectra, are characterized by high redshift, show extended and robust radio emission, and they are usually classified as LBL. On the contrary, BL Lacs exhibit almost featureless optical spectra (no evidence for any accretion disk spectrum), emit weakly in radio frequencies, have low redshifts and are hosted in giant elliptical galaxies. In both cases, relativistic effects amplify the jet luminosity and the amplitude of variability. We highlight the work of Fossati et al. (1998), who performed a statistical study of over 126 BL Lacs and FSRQs. Specifically, they divided and averaged the SEDs of the selected objects into radio luminosity bins. The scientific outcome of this project indicates that the peak frequencies of the Low Energy (LE) and High Energy (HE) components are correlated, with both LE and HE peaks shift to lower frequencies when the radio/total power increases (see the right panel in Fig. 1.4). This work is known as the *the blazar sequence*. Some other studies, however, suggest that the blazar sequence could be an apparent effect due to the selected sample (Padovani 2007). However, until today, many observations are in agreement with the blazar sequence model.

### 1.3 Relativistic Jets in AGN

Relativistic jets can be described as highly collimated plasma outflows that can be associated with many AGN. Even if jets are shining over a wide range of the electromagnetic spectrum, many issues remain open. Current research addresses the following topics:

- Which is the precise physical mechanism that leads to jet launching?
- Is the plasma composition changing along the jet?



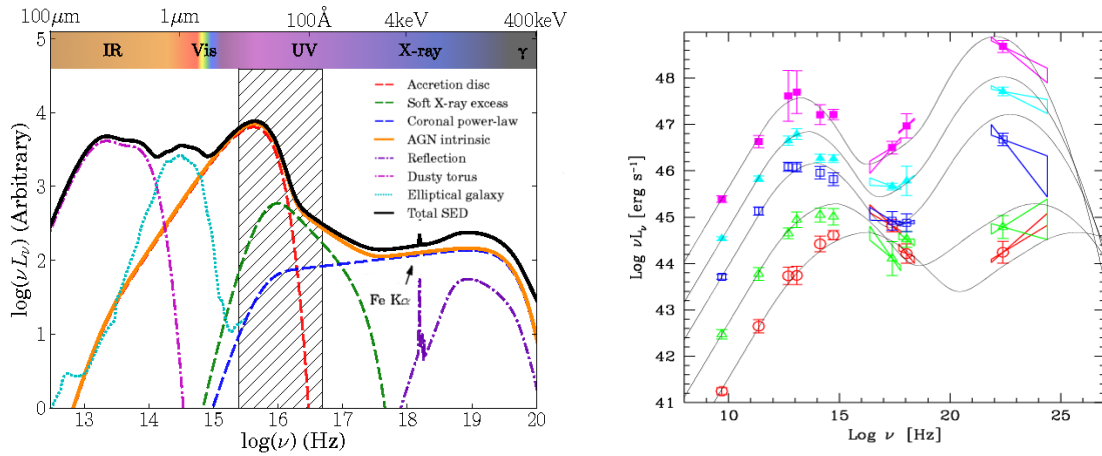


FIGURE 1.4: Left: A schematic representation of an AGN spectral energy density diagram. The contribution of each AGN physical component is displayed with a characteristic line shape and color. The hatched area displays the spectral range that is heavily obscured by absorption from the intergalactic medium. Figure credits: [Collinson et al. \(2017\)](#). Right: The so-called blazar sequence (see last paragraph of Sec. 1.2). Figure credits: [Donato et al. \(2001\)](#).

- Which is the main process that controls the energy dissipation?
- How do particles accelerate?
- Where is the exact location of the  $\gamma$ -ray-emitting regions?

In this section, we will try to briefly describe the basic knowledge that we already have about AGN jets and the most prominent phenomena that are taking place.

### 1.3.1 Radiation Mechanisms

The vast majority of the emission mechanisms that exhibit AGN jets have a non-thermal origin. This type of emission constitutes an indication of violent and energetic phenomena. In the next subsections, we are going to present the basic theoretical concept of those mechanisms, as well as their observational signature. For the full mathematical derivation of the presented equations, see [Pacholczyk \(1970\)](#), [Ghisellini \(2013\)](#) and references therein.

#### 1.3.1.1 Synchrotron Radiation

One of the most significant contributors to the jet emission in AGNs is *synchrotron radiation*. Synchrotron radiation production occurs when a relativistic charged particle accelerates, under the presence of magnetic field  $\mathbf{B}$ . The field forces the particle to follow a helical trajectory, along the direction of  $\mathbf{B}$ . The force that is applied on a single particle of charge  $q$ , with velocity  $\mathbf{v}$ , by a magnetic field  $\mathbf{B}$  is

$$\mathbf{F} = \frac{q(\mathbf{u} \times \mathbf{B})}{c}. \quad (1.1)$$

This is known as the *magnetic force* or Lorentz force  $\mathbf{F}$ . Note that  $\mathbf{F}$  as a cross product of  $\mathbf{u} \times \mathbf{B}$ , it acts perpendicular to both the velocity and the magnetic field. Therefore, the magnetic force work only to the velocity component, which is perpendicular to  $\mathbf{B}$ , forcing the particle to follow a circular trajectory. The strongest radiation is emitted at the characteristic frequency

$$\nu_g = \gamma^2 \frac{qB}{2\pi mc}, \quad (1.2)$$

with  $m$  being the mass,  $q$  the charge, and  $\gamma$  the Lorentz factor of the particle. Also,  $\nu_g \propto E^2 B_\perp$ , where  $E$  is the electron energy. For the non-relativistic case,  $\gamma \sim 1$ , the process is called *cyclotron radiation* and the characteristic frequency is defined as  $\nu_c = n_g/\gamma^2$ . In the relativistic case, the emitted radiation concentrates in a cone of semi-opening angle  $1/\gamma$ , with the cone's axis pointing in the direction of the velocity vector (see Fig. 1.5). In the observer's reference frame, this configuration translates into a recording of a series of widely spaced narrow pulses, coming from the direction of the cone. The emission frequency, in this case, is the Doppler-shifted gyro-frequency  $\nu'_g$ . The power  $P$  that is radiated by a single electron is proportional to the energy loss ( $dE/dt$ ) that is caused due to the acceleration under the presence of the magnetic field. By integrating the synchrotron emission over energy losses, the synchrotron power is given by

$$P = -\frac{dE}{dt} = 2\sigma_T \beta^2 \gamma^2 c U_B \sin^2 \psi, \quad (1.3)$$

where  $U_B = B^2/8\pi$  is the energy density of the magnetic field,  $\beta = u/c$  is the electron speed in units of  $c$ ,  $\sigma_T$  is the Thomson scattering cross-section and  $\psi = \arccos u_\parallel/u_\perp$  the electron pitch angle. By integrating over all possible pitch angles  $\sin \psi = 2/3$ , Eq. 1.3 becomes

$$P = \frac{4}{3} \sigma_T \beta^2 \gamma^2 c U_B. \quad (1.4)$$

Note here that for  $\gamma \gg 1 \rightarrow \beta^2 \sim 1$ . By assuming that synchrotron radiation is the only energy-loss mechanism for an electron, one can calculate its *cooling time*, which is the time the electron needs to radiate away all of its initial energy  $E = \gamma m_e c^2$  via synchrotron radiation. This characteristic quantity is given by

$$\tau_{\text{syn}} = \frac{E}{P} = \frac{3m_e c^2}{4\sigma_T c U_B \gamma \beta^2} \sim \frac{24.6}{B^2 \gamma} \text{ yr}. \quad (1.5)$$

For instance, an electron with  $\gamma \sim 1000$ , that is located close to SMBH with a typical magnetic field strength of  $B = 1000 \text{ G}$  the synchrotron cooling time is  $\tau_{\text{syn}} \sim 0.8 \text{ s}$ .

In practice, however, we are more interested in the emission from an ensemble of electrons, as this describes better the real synchrotron emission from AGN plasma outflows. For such a study, firstly, it is necessary to assume an isotropic distribution of possible pitch angles. Also, in order to describe the energy spectrum distribution of the electrons, we can safely assume a simple power-law distribution, as it has been observed as a result of particle acceleration in a shock, like Fermi acceleration. Thus, the *number density*,  $n$ , of electrons with energies between  $[E, E + dE]$  is given by

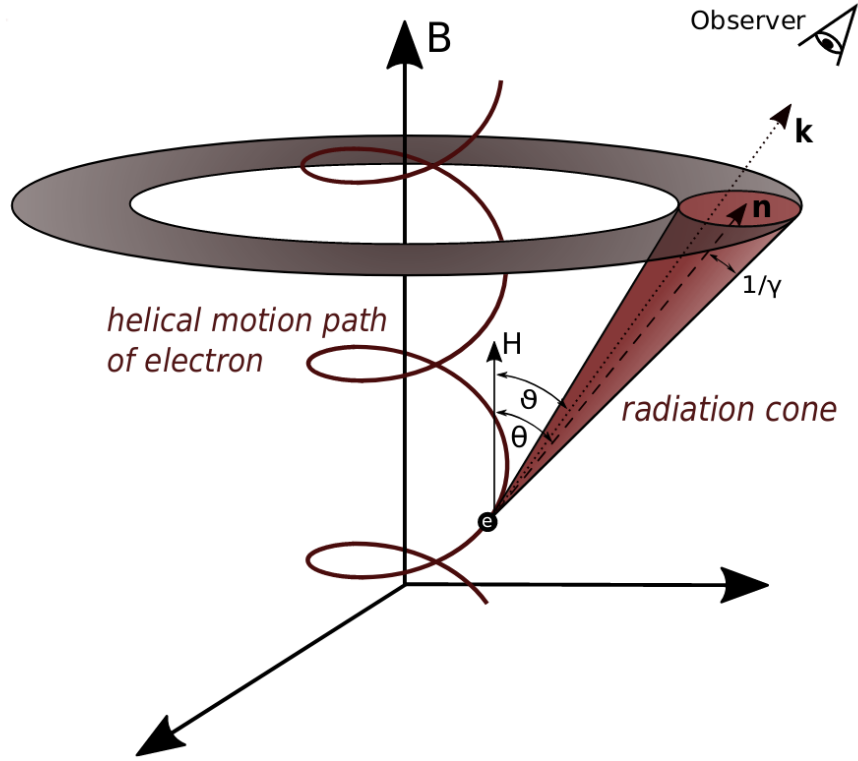


FIGURE 1.5: Geometrical configuration of the synchrotron radiation mechanism for a single electron. Credits: [Gokus \(2017\)](#).

$$n = N(E) dE = \int_{E_1}^{E_2} dE \propto CE^{-p}, \quad E_1 < E < E_2 \quad (1.6)$$

where  $C$  is an integration constant, the energies  $E_1$  and  $E_2$  are the lower and upper cut-off energies and  $p$  is the *electron spectral index*. Since the emission frequency is related to  $\gamma$ , Eq. 1.6 can be written as

$$n_\gamma = N(\gamma) = K\gamma^{-p}, \quad \gamma_1 < \gamma < \gamma_2 \quad (1.7)$$

where  $n_\gamma$  is the number density of electrons within a Lorentz factor range  $[\gamma, \gamma + d\gamma]$ ,  $\gamma_1$  and  $\gamma_2$  are the lower and upper cut-off, and  $K$  is a constant with the same units as  $n_\gamma$ .

For *optically thin* plasma (i.e., all the energy loss corresponds to the emission of photons), the synchrotron special emissivity is calculated by

$$j_\nu \sim \int n_\gamma P_\gamma d\gamma \propto KB^{\frac{(p+1)}{2}} \nu^{-\frac{(p-1)}{2}}, \quad (1.8)$$

and it measures the emitted power by the electrons population per volume, solid angle, and frequency. Equation 1.8 shows that the spectrum of optically thin synchrotron radiation from a power-law distribution of electrons is also a power-law, with  $\alpha = (p - 1) / 2$  to be the *synchrotron spectral index*.

As a final remark, the intensity of the synchrotron photons  $I(\nu) d\nu$  can also be expressed as the power-law

$$I(\nu) \propto \nu^\alpha. \quad (1.9)$$

**Synchrotron Self-Absorption** Our discussion concerning the synchrotron mechanism so far has been assumed optically thin emission. Nevertheless, as the intensity of radiating electrons increases, the emitted photons do not have sufficient energy to escape and the electrons absorb them. This process is called *synchrotron self-absorption* (SSA). When the emission from a source is optically thick, the SSA process dominates. The cross-section of the absorption is not the same for all frequencies. For low frequencies, the detected emission is coming from the outer synchrotron emitting layers, while deeper layers are visible at higher frequencies. The deepest layer that can be seen is the one where the mean free path for the emitted photon becomes comparable with the source size. However, the competition between synchrotron absorption and emission processes turns in favor of emission when the *optical depth* of the plasma becomes unity ( $\tau_{\text{SSA}} = 1$ ). The frequency at which this event takes place is called *turnover frequency*  $\nu_m$ , and it is unique for each source. Although a Maxwellian energy distribution does not describe the synchrotron electrons, they can be safely assumed to follow the Planck spectrum, with a slope  $\alpha_{\text{thick}} = 2.5$  (see Sec. 1.5), whereas the standard optically thin spectral index is  $-0.7$ . Based on this assumption, the optically thick emission can be compared with the thermal emission of a black body. This is enabling us to estimate a characteristic, energy-dependent effective temperature  $T_{\text{eff}}$  for ultra-relativistic electrons by

$$T_{\text{eff}} \sim \frac{E}{3k} = \frac{2\pi m_e c \nu}{qB} \frac{m_e c^2}{3k} \sim 1.18 \times 10^6 \left( \frac{\nu}{\text{Hz}} \right)^{1/2} \left( \frac{B}{\text{Gauss}} \right)^{-1/2}, \quad (1.10)$$

where  $k$  is the Boltzmann constant. The spectrum that we obtain from such emission can be seen in Fig. 1.6. As we will see later, the synchrotron turnover frequency, and the optically thin/thick spectral indices are crucial parameters, and can provide us with an estimation of the magnetic field strength, as well as the particle density of the emitting plasma (once we know the size of the emitting region) (Marscher 1983).

Lastly, it worth mentioning that in astrophysical sources, plasma outflows are inhomogeneous. The emission region can be imagined as a superposition of different layers, with each layer consists of different electron densities and magnetic fields. In this case, the observed SSA spectrum consists of a superposition of individual spectra, as can be seen in the right panel of Fig. 1.6. The turnover of the overall spectrum will also be a sum of all the turnover frequencies but mostly governed by the contribution from the layers with the highest electron density and the strongest magnetic field.

The optically-thin part is the same for all the layers, as at the highest frequencies, where all layers in the inhomogeneous source are transparent, and the majority of the observed flux density comes from the inner parts of the source. The spectral index at high frequencies is the same as the optically thin spectral index produced by each layer. The spectral index below the apparent turnover, therefore, is less than  $+2.5$ . Typical values of the spectral indices in the optically thick and thin regimes are  $\alpha_{\text{thick}} = 2.5$  and  $\alpha_{\text{thin}} = -0.7$ , respectively. The spectra that described by indices greater than zero are referred to as inverted, in the range 0.0 to 0.5, flat, and less than 0.5, steep.

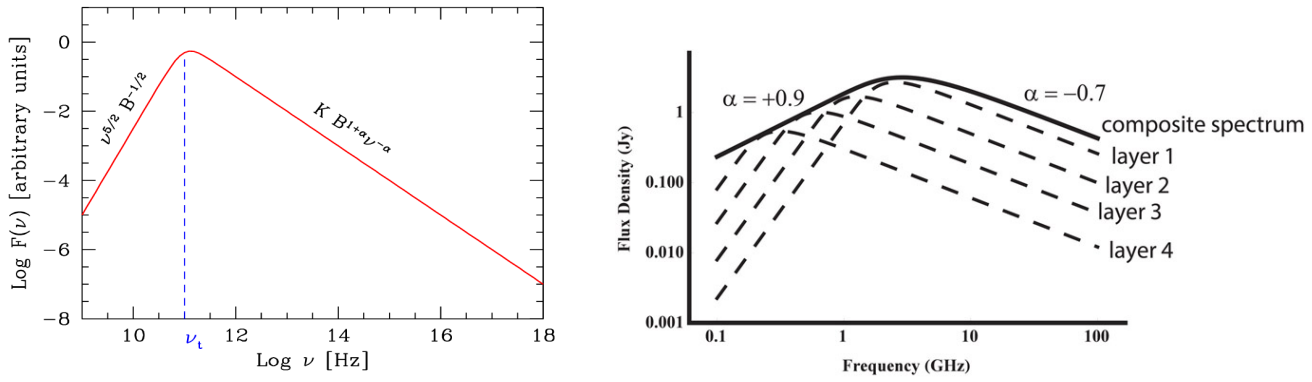


FIGURE 1.6: Left: Synchrotron spectrum of an ideal homogeneous and partially absorbed source. The dashed line shows the turnover frequency, where the plasma emission transits from optically thick state (self absorption) to optically thin. Right: Composite synchrotron spectrum of an inhomogeneous source. The optically thick spectral index can have any value between 0 and 2.5. Figures credits: [Ghisellini & Madau \(1996\)](#) and [Marr et al. \(2019\)](#) respectively.

### 1.3.1.2 Polarized Emission

Synchrotron emission emanating from blazars has a strong polarization signature. The fact that relativistic electrons gyrating around an ordered magnetic field is imprinted into the polarization of light, as light is polarized perpendicular to the magnetic field lines. The polarization consists of direct evidence for the existence of magnetic fields in the jets, and can help us to estimate the B-field's topology and strength.

**Linear Polarization** In the non-relativistic case, the synchrotron configuration that we described in Sec. 1.3.1.1 is known as *cyclotron*. The similarities between the two phenomena are many, with the most important difference being the electron speed. We are going to describe the polarization state of cyclotron radiation, and then we will mention what is happening when the electron's speed is approaching the speed of light. In the left panel of Fig. 1.7, a single non-relativistic electron will emit purely linearly polarized light along its orbital plane, with the electric vector oscillating perpendicular to the magnetic field, whereas parallel to the magnetic field we will see to emit purely circular polarized light. Nevertheless, in the relativistic case, because the radiation is beamed (see Sec. 1.3.1.1), the two components of the circular polarization are oriented into two opposite directions, with a result of canceling each other out. In this case, the *Linear Polarization* (LP) will not be affected.

For the case of an optically thin emission from an ensemble of electrons in a uniform magnetic field, the received synchrotron radiation will have a net LP, with the fractional polarization percentage to be

$$m = P/I = (p + 1) (p + 7/3) = (1 - \alpha) (5/3 - \alpha), \quad (1.11)$$

where P is the intensity of the polarized light, I the total intensity,  $p$  the power-law index and  $\alpha$  the spectral index [Pacholczyk \(1970\)](#). For a typical  $\alpha \sim -0.7$ , Eq. 1.11 results  $m = 72\%$ . Also, for a disordered B-field, we expect  $m_L$  to be less, since the perpendicular

polarization vectors cancel each other out. Hence, knowing the net polarization percentage can be a great indicator of how ordered a magnetic field is. On the other hand, optically thick emission can also be polarized, as  $m$  is independent by the observed frequency, and it can be calculated by

$$m = 3 / (6p + 13). \quad (1.12)$$

For typical values of  $\alpha$  for optically thick emission, the degree of polarization reaching the level of  $\sim 10\%$  (Pacholczyk 1970). A handful parameterization of the polarization properties introduced by Stokes (1851), is based on the electromagnetic wave components, as they are projected onto the plane of the sky. Specifically

$$E_x = \epsilon_1 \cos \omega t - \phi_1, E_y = \epsilon_2 \cos \omega t - \phi_2, \quad (1.13)$$

represent the wave components in x,y axes, whereas  $\epsilon_1, \epsilon_2$  are the amplitudes of each wave component,  $\omega$  is the frequency and  $\phi_1, \phi_2$  their corresponding phases (Rybicki & Lightman 1979). Therefore, the Stokes parameters are defined as

$$\begin{aligned} I &= \epsilon_1^2 + \epsilon_2^2, \\ Q &= \epsilon_1^2 - \epsilon_2^2, \\ U &= 2\epsilon_1\epsilon_2 \cos \phi_1 - \phi_2, \\ V &= 2\epsilon_1\epsilon_2 \sin \phi_1 - \phi_2. \end{aligned} \quad (1.14)$$

Stokes I, represents the total intensity. Stokes Q, measures the linear polarization oriented at  $0^\circ$  and  $90^\circ$  ( $\pm Q$  respectively), similar to Stokes U for  $\pm 45^\circ$ . Lastly, Stokes V provides the circular polarization, with the positive value to represent the right-handed circular polarization and the negative the left-handed. Based on Stokes parameters, we can estimate the corresponding fractional polarization percentages by

$$\begin{aligned} m_L &= (Q^2 + U^2)^{1/2} / I \\ m_c &= V / I \\ m &= (Q^2 + U^2 + V^2)^{1/2} / I \end{aligned} \quad (1.15)$$

where  $m_L, m_c$  and  $m$  are the degrees of linear, circular, and fractional polarization. Another very important polarization parameter is the *Electric Vector Position Angle* (EVPA). EVPA, or  $\chi$  is showing the oscillation's direction of the electric wave component and is perpendicular to the magnetic field and is computed by

$$\chi = \frac{1}{2} \arctan \left( \frac{U}{Q} \right). \quad (1.16)$$

Nevertheless, we should keep in mind that due to relativistic effects, the orientation of the magnetic field could be different from what we measure (Blandford & Königl 1979;

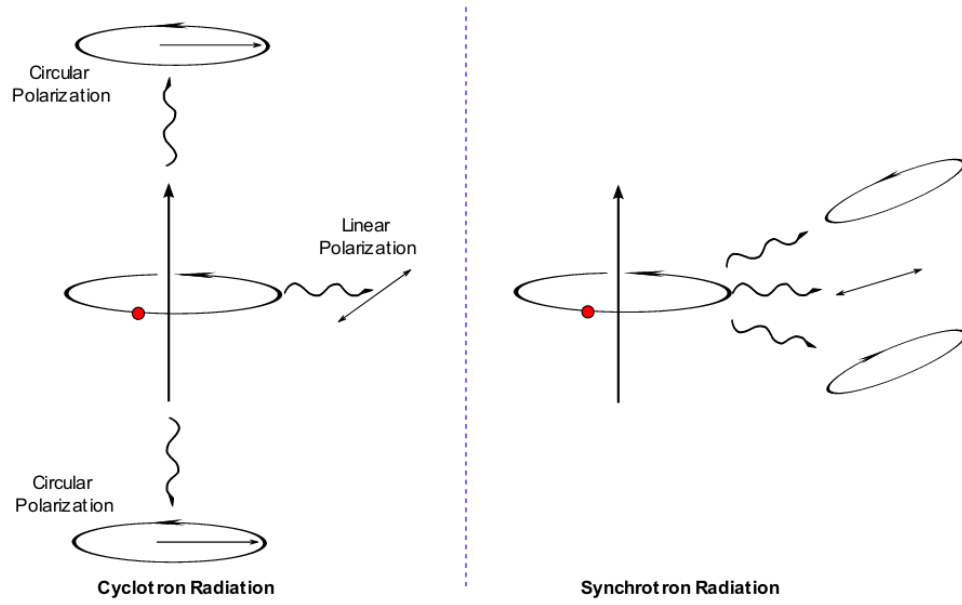


FIGURE 1.7: Left: Cyclotron configuration and observed polarization, as a dependence of the observer's line of sight. The axis of the electron orbit represents the direction of the magnetic field. Right: Synchrotron case. Here the electron moves with relativistic speed, with emission beamed into a narrow cone of opening angle  $2/\gamma$ . The circularly polarized components of the emitted light cancel each other, as a result, the observer sees mostly linearly or elliptically polarized light. Figure credits: Frank Rieger, Institute of Theoretical Astrophysics (ITA), University of Heidelberg.

[Lyutikov et al. 2005](#)). Hence, all the results that are presented in this thesis are inferred in the B-field direction that is observed in the laboratory's inertial frame.

**Circular Polarization:** Two fundamental mechanisms can produce circular polarization (CP):

- Direct emission from the magnetic field component, which is aligned with our point of view.
- Transition from linear polarization via Faraday conversion.

The second mechanism can be triggered either by the passing of linearly polarized emission through the magnetized plasma with a poloidal magnetic field component, or by conversion due to *internal Faraday rotation* (see Sec. 1.3.1.2). Even if it consists of a small fraction of the detected polarized light, its existence can give us a useful insight into the nature of jet's plasma. To begin with, CP emission from an astrophysical source indicates the presence of strong B-fields. For example, the detection of 1% polarized light requires an underlying homogeneous B-field with strength 0.01 G. Also, CP emission can probe the electrons - positrons population. Both  $e^-$  and  $e^+$  can emit CP, but with different signs. Therefore, if the ratio between  $e^-$  and  $e^+$  is one, no CP is expected. The CP emission from an ensemble of electrons depends on the observing frequency by  $m_C \propto \nu^{-1/2}$ . Although its elusive nature, CP has been detected in several blazars, often emanating from the VLBI

core (Wardle et al. 1998; Homan et al. 2009; Gabuzda 2015; Thum et al. 2017), as well as along the VLBI jet (Homan & Wardle 2003; Myserlis et al. 2018).

**Faraday Rotation:** Polarized emission, besides its production mechanisms, can interact and be affected by external fields and particles. When polarized light passes through a magnetized and sub-relativistic plasma (also known *Faraday screen*), it undergoes Faraday rotation (Fig. 1.8). Individually, the Right-hand Circular Polarized (RCP) component and the Left-hand Circular Polarized (LCP) component of the linearly polarized electromagnetic wave propagated with different speeds (Burn 1966). This phase asymmetry introduces an offset to polarization angle  $\chi$  of

$$\chi = \chi_o + \text{RM} \times \lambda^2 \quad (1.17)$$

where  $\lambda$  is the observed wavelength and  $\chi_o$  is the intrinsic electric vector position angle of the emission region. The Rotation Measure (RM), is defined by

$$\text{RM} = \frac{e^3}{8\pi^2\epsilon_0 m_e^2 c^3} \int \nu_e B_{\parallel} dl = 0.81 \int_{\text{source}}^{\text{observer}} \frac{\nu_e}{\text{cm}^3} \frac{\mathbf{B}}{\mu\text{G}} \cdot \frac{d\mathbf{l}}{\text{pc}} \quad (1.18)$$

where RM is measured in  $\text{rad}/\text{cm}^2$ ,  $\epsilon_0$  is the permittivity of the vacuum,  $\nu_e$  is the electron density,  $B_{\parallel}$  is the component of the magnetic field which is parallel to our line of sight, and  $dl$  is the path length through the de-polarizing plasma. In practice, for estimating the RM, it is necessary to observe the polarized source at multiple frequencies. The amount of rotation itself is proportional to  $\lambda^2$ , and the direction of the B-field determines the sign of the rotation. Faraday rotation can occur internally or externally to the emitting source. We note here that even though external Faraday rotation is proportional to the square of the wavelength, the internal process has been observed to deviate from the  $\lambda^2$  law (e.g., Wardle (2013) and references therein). For instance, an internal Faraday screen could be a jet region where plasma speed is lower and B-field different than the emitting region. In the case that a helical magnetic field dominates the emitting source, we are going to observe a gradient in RM along the jet, because of the different  $B_{\parallel}$  component of the magnetic field. Also, polarized radiation that is coming from more distant emitting regions to the observer can be depolarized, as the jet rotates differently from the closer regions (e.g., Reynolds et al. 2001). In the case of external Faraday rotation, the interstellar or intergalactic medium plays the role of a Faraday screen. The typical range of Faraday rotation for the case of quasars and BL Lacs is  $\sim 10^3$  to few thousands  $\text{rad}/\text{cm}^2$  in their core region, whereas  $\sim 10^2 \text{ rad}/\text{cm}^2$  from parts downstream in their jets (Homan (2005) and references therein). One of the highest RM detected until today is  $\text{RM} = 2 \times 10^7 \text{ rad}/\text{cm}^2$  in the gravitationally lensed quasar PKS 1830–211 (see e.g., Trippe et al. 2012; Martí-Vidal et al. 2015). A typical, strongly polarized blazar, like CTA 102, exhibits RM between 43 and 86 GHz of the order of  $6 \times 10^4 \text{ rad}/\text{cm}^2$  (Casadio et al. 2019).

### 1.3.1.3 Inverse Compton Radiation

Another important emission mechanism in AGN jets is *Inverse Compton scattering* (IC). In this process, low energy photons gain large amounts of energy via up-scattering from ultra-relativistic electrons (see Fig. 1.9). Eventually, the photons gain energy and the electrons



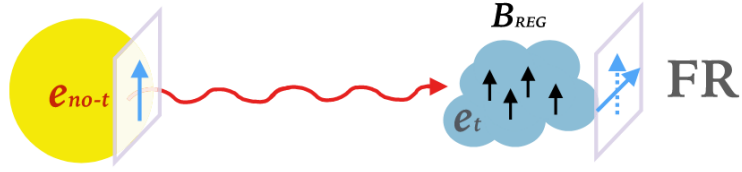


FIGURE 1.8: Sketch of the Faraday rotation (FR) configuration. The bright yellow area, labeled as  $e_{no-t}$ , designates the synchrotron emitting region, populated by non-thermal electrons. The red arrow indicates the polarized radiation, where the pale blue cloud represents a regular magnetized medium. This medium, usually is characterized by a magnetic field  $B_{REG}$ , which is populated mostly by thermal electrons ( $e_t$ ). The latter, act as a screen which alters the initial EVPA orientation of the incoming polarized radiation.

Credits: [Thompson et al. \(2012\)](#).

lose energy. In the case of standard Compton scattering, the energy balance is inverted, as the photons are more energetic. The energy loss rate for a single electron by IC scattering is estimated by

$$P_{IC} = - \left( \frac{dE}{dt} \right) = \frac{4}{3} \sigma_{TC} \beta^2 \gamma^2 U_{\text{rad}}, \quad (1.19)$$

where  $U_{\text{rad}}$  is the energy density of the photon field, in the electron's rest frame. We should note here the similarity of Eq. 1.19 with Eq. 1.4. Both at IC and synchrotron emission, the electrons are accelerated by the electric field that “see” in their inertial frame. In the case of IC, an electron is affected by the sum of all the E-fields of the incident waves. On the other hand, in the case of synchrotron radiation, a constant accelerating E-field is applied to the electron, as it is the cross product of the B-field and electron's velocity. The frequency of the scattered photons after the IC process is  $\nu \propto \gamma^2 \nu_0$ . For a typical Lorentz factor range  $\gamma \sim 100 - 1000$  as can be found in AGN jets, radio or optical radiation will be bumped up via the IC process into the UV and  $\gamma$ -rays regimes respectively. Hence, IC scattering provides an important means of  $\gamma$ -ray photons production in AGN. The radiation spectrum, produced by an ensemble of electrons over an energy spectrum of the incident photons of energy  $h\nu$  through IC scattering is  $dN \propto E^{-d} dE$  which results in an intensity spectrum of

$$I(\nu) \propto \nu^{\frac{(d-1)}{2}}, \quad (1.20)$$

where  $d$  is the power-law index ([Blumenthal & Gould 1970](#)). The required photon field for the IC process in jets depends critically on the location of the emitting region along the jet. For instance, if the process occurs close to the SMBH, the IC photon field could result from the accretion disk, supplying with optical/UV or even X-ray photons. For more distant emission regions, the BLR, the dusty torus, the jet sheath or even the Cosmic Microwave Background (CMB) can provide the essential photon field. When an external radiation source is involved in the IC process, the process is called *External Compton* scattering (EC). On the other hand, in AGN outflows, the seed photons for the IC scattering can be the synchrotron photons, up-scattered by the electron population that produced them. In this case, the process is known as *synchrotron Self-Compton* (SSC). The amount of energy that an electron transfers to a photon by IC, is significantly larger in comparison with the amount it loses via synchrotron radiation. Hence, if the number density of photons is large enough, the electrons can lose energy via IC faster than via the synchrotron emission

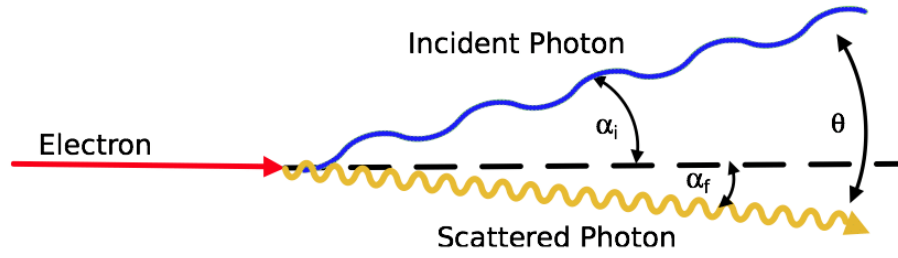


FIGURE 1.9: Cartoon illustration of the inverse Compton scattering process. Image credits: Ertley (2014).

process. Therefore, a significant cooling is introduced by IC scattering to the synchrotron electrons, which limits the temperature that a self-absorbed synchrotron source can reach to  $T = 10^{12}$  K (Kellermann & Pauliny-Toth 1969). This maximum synchrotron intensity is known as *inverse Compton limit*.

Knowing the background photon field, and the location of the primary emitting region, are key parameters in the understanding of AGN jets. Another significant aspect of IC scattering in AGN jets is its importance in the interpretation of the origin of the second SED component, as we discuss it in Sec. 1.3.1.3.

#### 1.3.1.4 Pion Decay

In extreme astrophysical environments, collisions between high energy protons can lead to electromagnetic cascades. The most common product of such an interaction are charged or *neutral pions* ( $\pi^\pm$  and  $\pi^0$  respectively)

$$p + p \rightarrow \pi^0 + X, \quad (1.21)$$

where  $X$  are secondary particles. However, neutral pions are unstable, with a short half-life time ( $\sim 8 \times 10^{-17}$  s). The product of a neutral pion's decay, is two  $\gamma$ -ray photons. Owing to those particles that are usually found moving with relativistic speeds, the energy range of the produced  $\gamma$ -ray photons is between GeV-PeV, in the observer's reference frame.

#### 1.3.1.5 Pair Annihilation

When a particle and anti-particle collide, they are annihilated, with the particle's energy transforms into electromagnetic radiation. For instance, the collision of an electron ( $e^-$ ) with a positron ( $e^+$ ) will produce two  $\gamma$ -ray photons with the same energy, but exactly the opposite direction. When the photons are emitted at rest, for both, their energy equals to 0.511 MeV. Nevertheless, the energy of the  $\gamma$ -rays that are produced by relativistically moving leptons (taking into account special relativity) will be

$$E = \frac{1}{2} m_e c^2 (1 \pm \beta). \quad (1.22)$$

Relativistic electrons and positrons which collide in the jet plasma will produce broad continuum emission in the MeV energy range (Boettcher & Schlickeiser 1995).

## 1.4 Gamma-ray emission in Blazars

In the previous paragraphs, we have briefly described the main radiation mechanisms that are taking place in blazars and explain the observed two-hump SED. However, the origin of  $\gamma$ -ray emission in blazars, the so-called “blazar zone”, it is far from fully understood. Because of the limited angular resolution that the current  $\gamma$ -ray detectors can achieve (e.g.,  $\sim 0.2^\circ$  at  $E \sim 10$  GeV), the direct pinpointing of the  $\gamma$ -ray production region is not possible.

Theoretical models suggest that the  $\gamma$ -ray emission should be located in low  $\gamma$ -ray opacity regions, in order to allow MeV/GeV  $\gamma$ -ray photons to escape (Dermer et al. 2012).

However, observational evidence indicates in several cases that the high-energy emission emanates close to the SMBH, in the vicinity to the accretion disk or the BLR (e.g., Blandford & Levinson 1995; Ghisellini et al. 1998; Ghisellini & Tavecchio 2008b, 2009; Finke 2013, and references therein). The combination of time-domain  $\gamma$ -ray observations, multi-frequency variability observations and radio interferometric data also showed that  $\gamma$ -rays could be located at a distance of sub-parsec to several parsecs downstream of the BLR (Aleksić et al. 2011, 2014; Agudo et al. 2012; León-Tavares et al. 2011; Fuhrmann et al. 2014). At such distances, the molecular dusty and clumpy torus can supply the IR photons for the EC mechanism and would help to produce  $\gamma$  photons.

Nonetheless, the interaction of moving features with the stationary features are often associated with  $\gamma$  ray flares, indicating that also shock-shock interaction can produce  $\gamma$  rays at distances larger than a few parsecs (e.g., Marscher 2013).

An alternative approach in localizing the high energy production region in AGN comes from determining the composition of the jet. For instance, in the framework of leptonic models, the broadband AGN emission is thought to be produced by leptons ( $e^-$  and  $e^+$ ) through synchrotron and inverse Compton (IC) processes. The photons which get scattered up to  $\gamma$ -ray energies can either be the same synchrotron photons radiated by the jet (Synchrotron-Self-Compton, Maraschi et al. 1992) or can originate in the jet surroundings (External Compton) (e.g., Ghisellini & Tavecchio 2008a; Dermer et al. 2009). With increasing distance from the black hole, possible reservoirs of these seed photons are the accretion disk (Dermer et al. 1992), the broad-line region (BLR, Dermer & Schlickeiser 1993; Sikora et al. 1994; Poutanen & Stern 2010; Dotson et al. 2012), or the dusty torus (Błażejowski et al. 2000; Kataoka et al. 1999). At larger distances, Cosmic Microwave Background (CMB) photons may play a role (Celotti & Ghisellini 2008). Alternatively, hadronic jet models can also explain  $\gamma$ -ray emission. If ultra-relativistic protons and leptons, compose the jet,  $\gamma$ -rays could be produced, through proton-synchrotron or photo-pion production (Mannheim & Biermann 1992; Aharonian 2000).

In summary, as can also be seen in Fig. 1.10, the possible emission locations start from a sub-parsec distance away from the central engine to further downstream of the jet. No clear consensus has been achieved on the location of the emission region(s), as the specific region and production mechanism for high energy photons appears to vary from event to event (see Agudo 2013, and references therein).

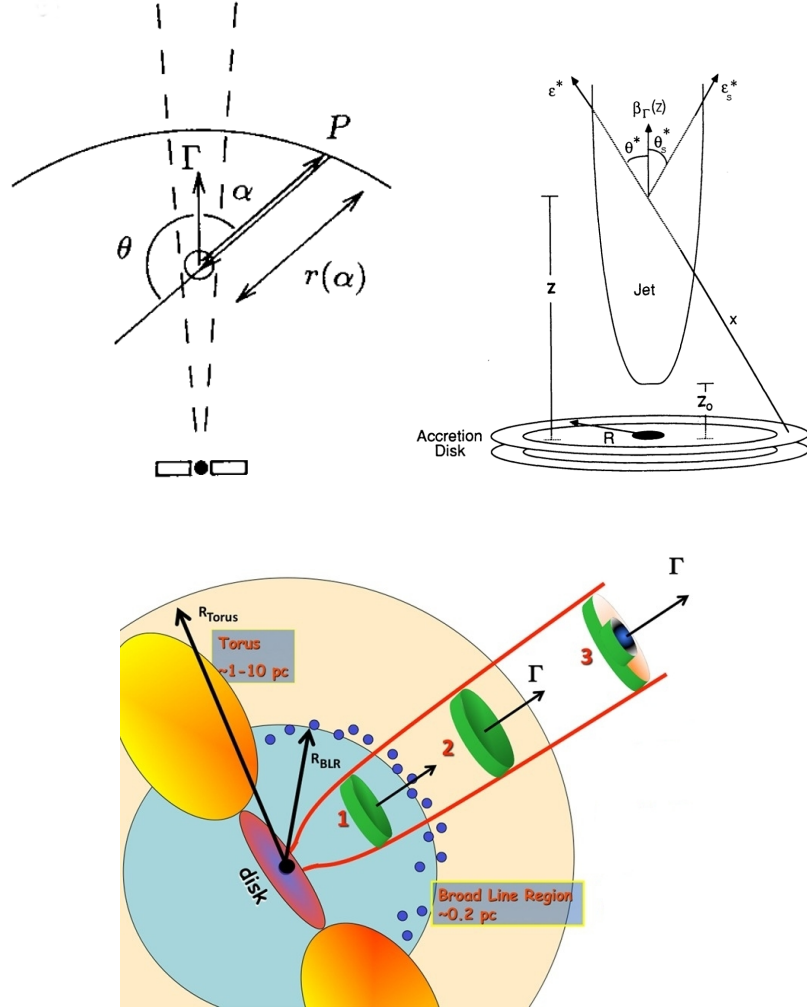


FIGURE 1.10: Artistic illustrations of possible  $\gamma$ -ray emission regions along an AGN jet. In all presented scenarios, high energy emission occurs when a blob travels relativistically, with bulk Lorentz factor  $\Gamma$ , away from the central engine and meets photons on its path from different sources. Left: A blob is propagating along the jet and receives radiation from the BLR illuminated by the blob itself. The distance  $r(\alpha)$  is the distance between a random point  $P$  on the BLR shell and the blob. Image credits: [Ghisellini & Madau \(1996\)](#). Right: The blob is located at a distance  $R\gamma$  from the accretion disc. In this scenario, the photons that are radiated from the surface of the disk will interact with the blob and will be upscattered via EC to  $\gamma$ -ray energies. Image credits: [Dermer & Schlickeiser \(1993\)](#). Lower panel: Three possible scenarios of  $\gamma$ -ray production. (1): via IC between relativistic electrons from the propagating knot and photons produced by the BLR. (2) via EC of using the infrared photons produced by the torus. (3) for distances larger than the radius of the BLR and the torus the main source of photons is the synchrotron radiation. Image credits: ([Ghisellini 2015](#)).

### 1.4.1 Jet Formation, Acceleration and Collimation

The physical mechanism that launches and powers relativistic jets remains an active area of research. It is widely accepted that some of the mechanisms that can produce jets are related to the accretion process and the strong potential wall of the central engine. This idea is supported by observational results such as that the speed of the jet reaches the escape velocity limit from the central engine [Livio \(1997\)](#), implying that the launching region is originating at the center of the disk.

Nevertheless, another parameter that can power relativistic jets is the black hole rotational energy. Numerical relativistic magnetohydrodynamic (RMHD) simulations of accreting, as well as spinning BHs, show that relativistic jets can be formed spontaneously under these conditions. [Penrose & Floyd \(1971\)](#) proposed a mechanism that can extract energy of a rotating BHs via angular momentum conservation. The basic idea of this model is that a particle with momentum  $p$  enters in the BH ergosphere and can split into a pair of particles, characterized by positive and negative mass-energy respectively. If the particle with the negative mass-energy passes the event horizon, the positive particle will carry away more energy than the initially possessed due to angular momentum conservation, resulting in an energy loss for the BH. However, the authors of the paper express their concerns about the validity of this model, because it is inefficient. This process is called the *Penrose process*. A modified version of this model is the *generalized Penrose process* ([Lasota et al. 2014](#)), where the authors suggest that magnetic field lines are frozen inside the accretion disk around the BH. The rotation of the BH leads to a frame-dragging effect (also known as *Lense-Thirring effect*) which twists the magnetic field lines into a helix, which transfer and accelerate plasma. Energy is thereby extracted from the spinning BH, forming a relativistic jet.

Some years later, [Blandford & Znajek \(1977\)](#) suggested a purely electromagnetic mechanism, today is known as *Blandford-Znajek* (BZ process). In this process, the rotating energy and the angular momentum of the BH can be extracted by the interaction with the strong magnetic field produced by the accretion disk. Under these conditions, charged particles that are located in the BH's magnetosphere are accelerated and radiate  $\gamma$ -ray photons. The  $\gamma$ -ray photons then are decaying, creating  $e^- - e^+$  pairs which are also accelerated by the existing electric field. The BH can behave as a conductor, with the voltage being induced between the poles and the equator, like a Faraday disk. The final result is that Poynting flux, bounded with the produced leptonic plasma streamed away from the BH, creating outflows. The power that produced from this process can be estimated by

$$P = \frac{4\pi}{\mu_o} B^2 R_S^2 c, \quad (1.23)$$

([Carroll & Ostlie 2006](#)), where  $P$  is the power generated by the Blandford-Znajek mechanism,  $B$  is the magnetic field of the accretion disk, and  $R_S$  is the Schwarzschild radius and  $\mu_o$  is the magnetic permeability in the vacuum. This power extraction eventually slows down the rotation of the BH. In this scenario, it is still under debate on how the Poynting flux is causally connected with the BZ mechanism ([Toma & Takahara 2014](#)).

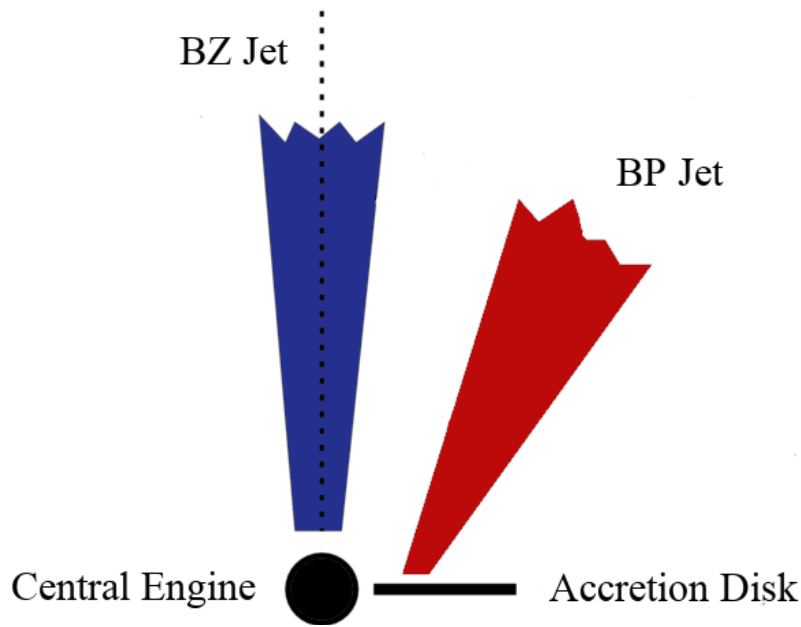


FIGURE 1.11: Conceptual illustration of BZ and BP jet launching mechanisms. The figure adapted from Hayashi et al. (2013).

Another widely known model is the *Blandford-Payne* (BP process) (Blandford & Payne 1982). This mechanism extracts energy and angular momentum through the accretion disk magnetic fields, not from the BH itself. More specifically, magnetic field lines of the disk are co-rotating with it, whereas thermal pressure gradients are lifting material of the disk (Pelletier & Pudritz 1992). If the field lines of the poloidal component of the magnetic field are inclined by  $\leq 60^\circ$  with the disk plane, they are not affecting the outflow, which can freely leave the disk and be accelerated outwards by the strong centrifugal force. Then, the toroidal component of the magnetic field takes action by collimating the outflow. The acceleration flow is achieved by the conversion of Poynting energy flux to kinetic energy flux. A considerable limitation of this scenario is that it requires high magnetic field strengths at the disk surface, which has not been detected yet. A schematic representation of both BZ and BP mechanisms is displayed in Fig. 1.11.

Nowadays, the current picture of AGN jets suggests the co-existence of more than one launching mechanism. The idea that the same source can produce jets of different speeds observations also support it (e.g., Meier 2003). The most popular scenario is that there is a fast, narrow, and leptonic jet launched by the BH, creating a relativistic *spine*. This spine is mostly Poynting-flux dominated and carries away from the center the energy of the magnetic fields. However, another part of the jet is launched by the accretion disk and envelops the spine-like jet as a *sheath*. This jet region is more substantial, broader and slower than the inner part. This part should be responsible for carrying mass and momentum along the jet (Sol et al. 1989; Bridle 1996; Marscher 2006). Figure 1.12 displays a jet simulation of an axisymmetric relativistic jet, which summarizes our current understanding of AGN jets.

After the jet is launched, it gets accelerated and creates a well-collimated continue outflow that extends up to kiloparsec scales. One way to accelerate a jet magnetically is through magnetocentrifugal acceleration from an accretion disk via the BP mechanism, where the acceleration steams from the conversion of Poynting flux to kinetic energy flux. However, observational pieces of evidence support that the jet collimation can take place close to

the launching region, up to a distance of  $\sim 10^3 R_s$  (Giovannini et al. 2018, and references therein). Jet collimation can be achieved alternatively via thermal confinement from the torus and the corona around the central region (Feretti et al. 1995). Specifically, Feretti et al. (1995) propose that the surrounding pressure gradient close to the jet base is collimating the outflow along its ejection axis. Additionally, MHD simulations by Komissarov et al. (2007) propose that sub-relativistic jets can *self-collimate* under the presence of a toroidal magnetic field configuration, through magnetic hoop stress produced by the field and jet current. Spruit et al. (1997) also mentions the idea that jet can be self-collimated. The authors suggest that if the jet plasma, which is driven by the toroidal magnetic field component, is turbulent, jets are collimated mostly by the poloidal component.

### 1.4.2 Shocks and Instabilities

Relativistic jets of AGN, even though extreme properties characterize them, often exhibit similarities with sub-relativistic jets (e.g., Konigl 1980). In fluid dynamics, plasma flows experiencing different types of instabilities. In such an environment, small plasma perturbations can rapidly grow, oscillate, and actively contribute to the energy dissipation of the outflow. In this paragraph, we are going to mention two of the most prominent instabilities in the AGN jet hydrodynamics. The current-driven kink instability ( $m=1$  mode), that is taking place close to the jet base due to magnetic pressure differences between the plasma flow and the surrounding field and the Kelvin Helmholtz instability (KHI) which happens due to pressure imbalance between the external medium and the jet or the different Lorentz factors ( $\Gamma$ ) between jet layers (Birkinshaw 1991; Begelman 1998; Appl et al. 2000; Narayan et al. 2011). One important result of the development of jet plasma instabilities is the formation of shocks. Both instabilities are dissipating their kinetic energy to form internal shocks waves, that propagate along the jet. The propagating shock's front increases locally the density of the plasma and accelerates the existing particles (Daly & Marscher 1988; Marscher 2006). The aforementioned procedure causes enhanced emission of non-thermal radiation which it is known as a *knot*, *blob* or *VLBI component*. Marscher & Gear (1985), based on a flaring event of the blazar 3C 273, introduced a model known as *shock-in-jet* model, which states that a shock that originates in the central region expands downstream of the jet and simultaneously shines in the radio and high energy regime. However, shocks can also originate from instabilities produced by the external medium, known as *recollimation* shocks. A recollimation shock can be formed by a pressure imbalance between the jet and the ambient medium in the launching region. When this pressure equilibrium is disturbed, a radial oscillating motion is taking place in the jet, resulting in the formation of multiple shock waves. Plasma thermal energy is converted into jet kinetic energy, leading to an increase of Lorentz factor in the shock region (Gómez et al. 1997; Komissarov & Falle 1997; Agudo et al. 2001; Aloy et al. 2003). Nevertheless, recollimation shocks could be initially standing at the observer's frame. Several AGN jets show such features in their structure (Fromm et al. 2013a), as well as a quasi-stationary feature that can be observed in the ending region of each jet, creating a bright bow shock, known as *hot-spot*.

## 1.5 Brightness Temperature

Radio emitting plasma is often optically thick at low frequencies, thus it can be considered that radiates as a black body in thermal equilibrium with its environment. In that case, one could define the equivalent temperature of the plasma by the specific intensity  $I_\nu$  by



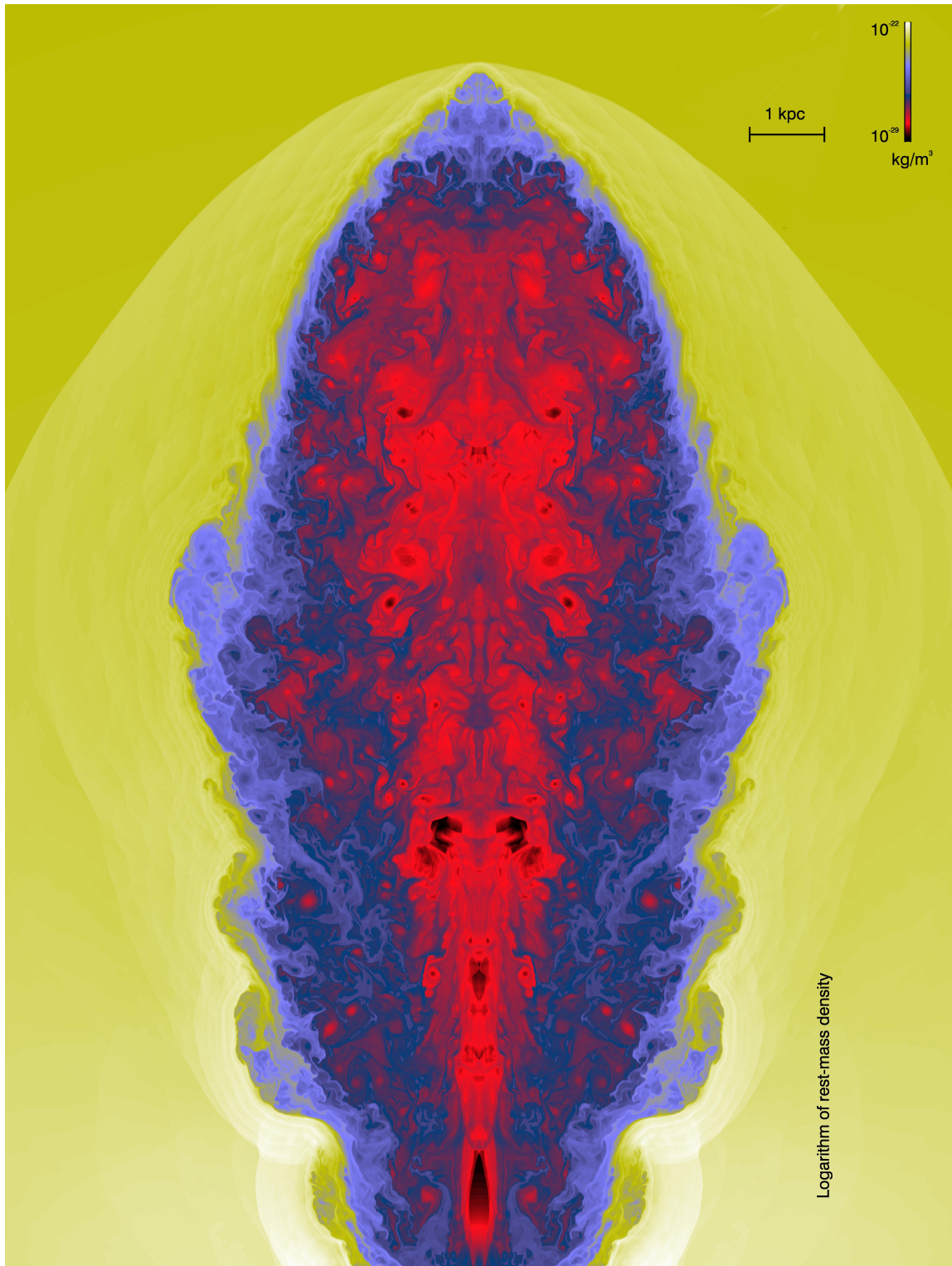


FIGURE 1.12: Simulation of an AGN jet propagation through external medium. At 1.5 kpc distance from the launching region a strong recollimation shock has been formed, which causes jet deceleration, leading to the development of KH instabilities (Perucho & Martí 2007).



$$I_\nu(T) = \frac{2k_B\nu^2}{c^2}T, \quad (1.24)$$

where  $T$  is the temperature, measured in K. This formula is an approximation of the Planck's law for the case that photons energy is much lower than the energy of the particle ( $h\nu \ll kT$ ) and it is known as the Rayleigh-Jeans approximation. However, the plasma becomes often optically thin at higher frequencies due to the non-thermal nature of the radiation. In that case, we cannot determine the plasma temperature. The only temperature equivalence to work with is by using the Rayleigh-Jeans limit, the so-called *brightness temperature*  $T_B$ , by

$$T_B = \frac{c^2}{2k_B\nu^2}I_\nu. \quad (1.25)$$

The  $T_B$  is not connected to the particle's kinetic energy but corresponds to the equivalent temperature that a black body in thermodynamic equilibrium should have in order to produce the same  $I_\nu$ . Brightness temperature estimation of a synchrotron emitting plasma plays an important role, because it can provide an estimation of the effective temperature  $T_e$  of the radiation at any frequency, because  $T_B$  cannot be less than the  $T_{\text{eff}}$ . At a given frequency  $\nu$ , the  $T_B$  of a synchrotron emitting ensemble of electrons will approach the  $T_e$  when the source stops to be transparent. By using Eq. 1.24 and setting  $T = T_B \sim T_e$  we obtain

$$I_\nu \propto \nu^{1/2}\nu^2B^{-1/2} = \nu^{5/2}B^{-1/2}. \quad (1.26)$$

Hence, because of  $S \propto I_\nu$

$$S(\nu) \propto \nu^{2.5}, \quad (1.27)$$

which tells us that the knowledge of  $T_B$  can lead us to an estimation of a flux density lower limit of a source for a given frequency.

## 1.6 Special Relativity and Jets

The Universe is an enormous laboratory where extreme physical phenomena are taking place. One of those phenomena is that matter can be accelerated and travel with speeds close to the speed of light. Under those circumstances, relativistic effects are playing a crucial role in what astronomers are observing, and can significantly alter the appearance of astronomical objects. Time dilation, length contraction, light aberration, relativistic beaming, and Doppler shifting are some of these effects. Astrophysical relativistic outflows in AGN are the ideal environment for such effects of taking place. In the next sections, we are going to describe those phenomena and their consequences to our measurements briefly.

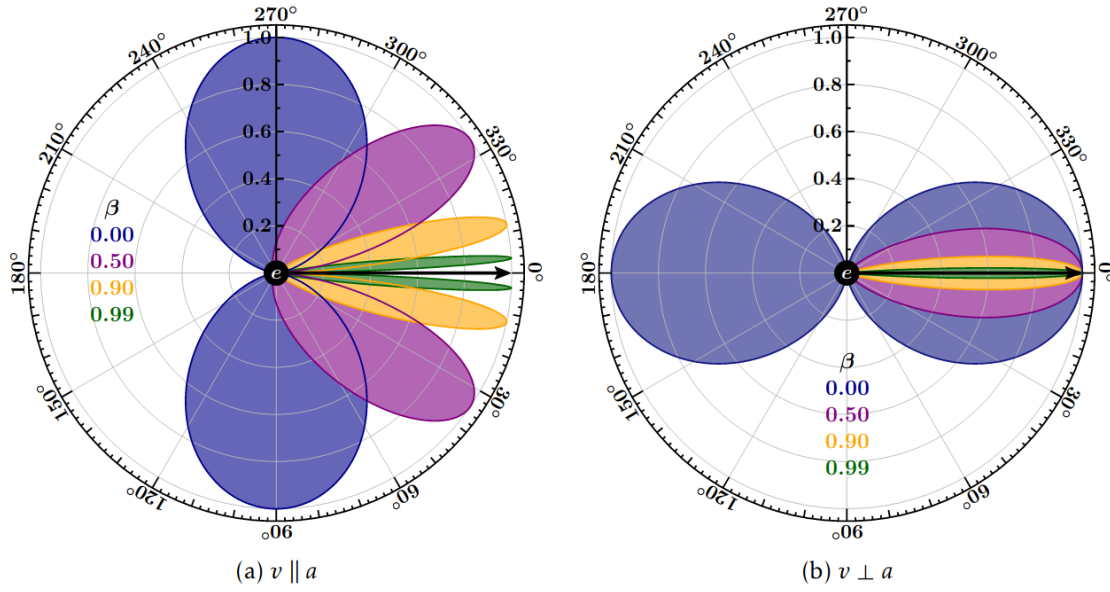


FIGURE 1.13: Schematic representation of the relativistic beaming effect in the electron's radiation for different speeds  $\beta$ . Right: The observed radiation shows beaming when the electron's velocity is along the line of sight. Left: The observed radiation beaming when the velocity is perpendicular to acceleration. Credits: [Gokus \(2017\)](#).

### 1.6.1 Relativistic Beaming

Let us imagine a source that radiates isotropically in its rest frame is moving with relativistic speed  $\beta$  towards our line of sight (where  $\beta$  is the source's speed, normalized by the light speed) (Fig. 1.13). By observing this source from our rest frame, we will realize that the emitting flux appears to be beamed to the direction in which the source is traveling within a cone with a semi-aperture angle

$$\theta_c = (1 - \beta^2)^{-1/2} = \frac{1}{\Gamma}, \quad (1.28)$$

where  $\Gamma$  is the bulk Lorentz factor of the source and  $\beta = v/c$ . This effect is known as *Relativistic* or *Doppler beaming*, and it is a combination of light aberration, time dilation, and frequency Doppler shifting.

One of the consequences of this effect is the enhancement of the measured flux density  $S$  in the traveling direction by a factor

$$S = S\delta^{3-\alpha}, \quad (1.29)$$

where  $\alpha$  is the spectral index of the optically thin emission region and  $\delta$  is the Doppler factor, which is defined by

$$\delta = \frac{1}{\Gamma(1 - \beta \cos \theta)}, \quad (1.30)$$

where  $\theta$  is the angle between our line of sight and source's velocity. Similar boosting is also observed in the  $T_B$ , as even if it is not a real temperature measurement, it is bounded with some theoretical upper limits. A characteristic  $T_B$  value is the *Inverse Compton limit* ( $T_B > 10^{12}$  K, [Kellermann & Pauliny-Toth \(1969\)](#)). For  $T_B$  above this limit, the luminosity produced by the Compton scattering is larger than the synchrotron luminosity. This can take place only since the photon energy reaches the electron energy. Above this point, the power drops, causing the cooling of the particles, also known as *Compton catastrophe*.

Another limit that is suggested by [Readhead \(1994\)](#) supports that if there is equipartition between the particle energy density and magnetic energy density, the peak brightness temperature should be  $T_B = 5 \times 10^{10}$  K. This limit is the so-called *Equipartition Brightness Temperature*  $T_{eq}$ . Nevertheless, VLBI observations have shown extremely high brightness temperatures in relativistic jets, reaching even  $T_B = 10^{16}$  K ([Ghisellini 2013](#)) in *Intraday Variable* sources (IDV). A given explanation for this behavior is to be the result of a possible Doppler boosting. Hence, the observed  $T_B$  should be divided by the Doppler factor of the flow in order to have an estimation of the intrinsic brightness temperature  $T'_B$

$$T'_B = T_B / \delta. \quad (1.31)$$

The high measured values of  $T_B$  are still a matter of debate, as in some extreme cases, effects such as interstellar scintillation and/or coherent radiation should also be taken into account ([Wagner & Witzel 1995](#)), to explain the apparent Doppler factors of the order of  $\delta > 100$ . Another critical observational result is the apparent amplification of small jet bendings due to plasma instabilities. Strong bendings in AGN jets are often observed in jets that are pointing close to our line of sight ([Singal 2016](#)).

It is commonly observed also in double-sided radio galaxies, that the jet that points closer to the Earth is more prominent than its axisymmetric pair. If the emitting plasma is moving relativistically, the radiation from the jet which is approaching us, is enhanced, while the one from the receding jet is dimmed. This is often referred to as *Doppler favoritism* and the Doppler factor for each flow is calculated as

$$\delta_\alpha = \frac{1}{\Gamma(1 - \beta \cos \theta)}, \quad \delta_r = \frac{1}{\Gamma(1 + \beta \cos \theta)}, \quad (1.32)$$

where  $\delta_\alpha$  corresponds to the approaching jet and  $\delta_r$  the receding flow, whereas their flux density ratio is defined as  $S_\alpha/S_r = (\delta_\alpha/\delta_r)^{3-\alpha}$ . In Fig. 1.14, we can see a characteristic example of this effect in the radio galaxy, Pictor A.



FIGURE 1.14: A composition of X-ray and radio images of the radio galaxy Pictor A. The right-hand jet it points closer to our line of sight with respect to the left-hand one. This case constitutes a nice example of the effect of Doppler favoritism. Image credits: X-ray: NASA ,CXC, Univiversity of Hertfordshire, M.Hardcastle et al., Radio: CSIRO ,ATNF, ATCA.

### 1.6.2 Superluminal Motion

A significant relativistic effect that is often observed in blazars is the detection of features that appear to travel along the jet with superluminal speeds. Martin Rees in 1996 (Rees 1966) predicted that apparent superluminal motion is possible in jets that are oriented close to our line of sight, due to the relativistic expansion of the plasma flow. Several observations followed, with the first one to be in the quasar 3C 279. In this case, the VLBI knots appeared to travel with an apparent speed of  $2c$  (Gubbay et al. 1969; Cohen et al. 1971; Whitney et al. 1971). This effect, in reality, is an illusion, which occurs when a radiating source (like a plasma blob) is moving with speed close to the speed of light towards us. The geometry of the phenomenon can be seen in Fig. 1.15, whereas an example of this effect, is displayed in Fig. 1.16. In order to fully understand the principles of the superluminal motion, let us imagine then that a blob is traveling along the jet, with speed  $u$  in time  $\Delta t$ . The time difference between two positions of the blob is computed by

$$\Delta t_{rec} = \Delta t (1 - \beta \cos \theta). \quad (1.33)$$

In the observer's inertial frame, the apparent distance that blob moved is

$$l_{\perp} = \nu \Delta t \sin \theta, \quad (1.34)$$

and, the blob's is moving with an apparent velocity  $\nu_{app}$  of

$$\nu_{app} = \frac{\nu \Delta t \sin \theta}{\Delta t (1 - \beta \cos \theta)} = \frac{\nu \sin \theta}{1 - \beta \cos \theta}. \quad (1.35)$$

By dividing both sides with  $c$ , we obtain

$$\frac{\nu_{\text{app}}}{c} = \beta_{\text{app}} = \frac{\beta \sin \theta}{1 - \beta \cos \theta}. \quad (1.36)$$

The smaller the value of  $\theta$ , the higher the  $\beta_{\text{app}}$  that we observe. It can be shown that the viewing angle for which the  $\beta_{\text{app}}$  becomes maximum is

$$\frac{d\beta_{\text{app}}}{d\theta} = \frac{(1 - \beta \cos \theta) \beta \cos \theta - \beta^2 \sin^2 \theta}{(1 - \beta \cos \theta)^2} = \frac{\beta \cos \theta - \beta^2}{(1 - \beta \cos \theta)^2}. \quad (1.37)$$

The derivative becomes zero when  $\cos \theta = \beta$ , hence

$$\beta_{\text{app}} = \frac{\beta \sin \theta}{1 - \beta \cos \theta} = \frac{\beta \sqrt{1 - \beta^2}}{1 - \beta^2} = \Gamma. \quad (1.38)$$

When  $\beta$  approaches unity and values of  $\Gamma$  are high,  $\beta_{\text{app}}$  can exceed the speed of light, and the Doppler factor increases too, as can be seen in the left panel of Fig. 1.15. Lastly, the apparent luminosity of the source is amplified by

$$L_{\text{app}} = \delta^4 L. \quad (1.39)$$

In summary, the tracing of the motion and the trajectory of superluminal knots it is an essential aspect in deepening our knowledge in jet physics. The measurement of the apparent speed of each jet feature helps us to draw valuable information about other essential jet parameters, such as the viewing angle of the jet, the existence of helical magnetic fields, the localization of high energy emission events, and more. The observed superluminal speed distribution ranges from 1 up to  $50c$ , peaking at the speed of  $10c$  for the most jets ([Lister et al. 2009](#)). In many cases, a wide range of component speeds is measured within a single jet. The relation between component speed and underlying plasma flow is complicated and not yet fully understood. To date, there are several monitoring projects such as the *MOJAVE* project at 15 GHz, or the BU project at 43 GHz, with one goal among others to be the study the component kinematics of AGN jets (e.g., [Jorstad et al. 2017](#)).

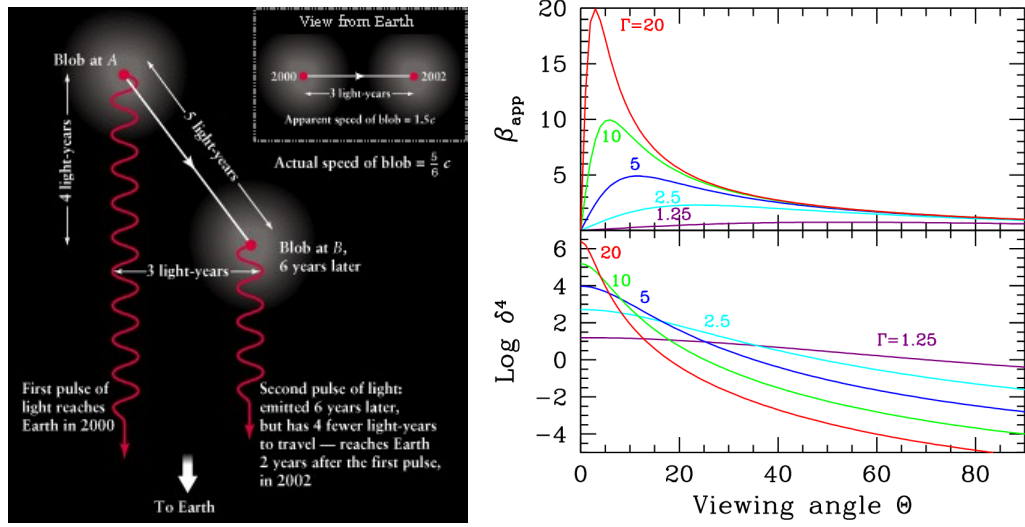


FIGURE 1.15: Left: A schematic representation of the geometrical configuration that causes the superluminal motion illusion. Image credits: Prof. Dr. Paul Eskridge. Right: The evolution of  $\beta_{app}$  (top panel) and Doppler factor (bottom panel) with  $\theta$  for different Lorentz factor values. Plot credits: Ghisellini (2013).

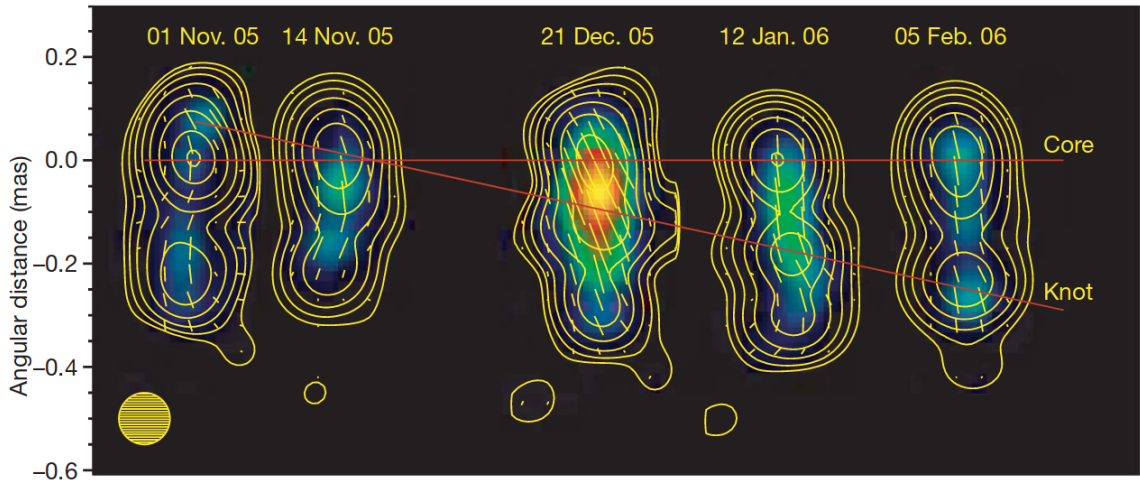


FIGURE 1.16: VLBI images of the morphological evolution of the blazar BL Lac, as was seen at 43 GHz during 2005-2006. In the first image, can be seen a new knot to appear. The observed proper motion of this feature is 1.2 mas/year, which corresponds to an apparent speed of  $5.0c$ . The slanted red line designates the position of the core feature, as well as of the new knot. It is worth to mention here that the new knot is lighting up the core feature, as it passes through it. Image credits: Marscher et al. (2008).

## Chapter 2

# Observing Techniques and Instruments

### 2.1 Fundamentals of Radio Interferometry

The development of radio astronomy is a relatively recent achievement in the history of observational astronomy: only after 1932, astronomers realized that the Universe is shining at radio waves. Thenceforth, the need to improve our ability to look deep into space and be able to distinguish fine structures of radio-emitting astrophysical objects led us to combine the existing knowledge about radio antennas and the wave nature of light. The advantage of observing in the radio regime is that such waves can penetrate our atmosphere, therefore observations from the ground are possible, also in day time unlike in the optical band. On the other hand, radio photons have extremely low energies, therefore radio telescopes need to be very sensitive to detect the faint astronomical signal. As discussed in the following, both the sensitivity and the angular resolution can be improved by increasing the telescope aperture. In the next paragraphs, we are going to briefly describe the basics of radio observations from the instrumentation up to the modern observing techniques.

#### 2.1.1 Radio Telescope

A radio telescope is an astronomical instrument that is designed to detect cosmic radio waves. The most common type is the parabolic reflector, which consists of 3 main components: the antenna, the receiver, and the backend. The radio wave-fronts impacting the telescope surface are reflected, due to the parabolic geometry of the dish, to the subreflector, and then are focused to the feed horn. The role of the feed horn is to select only the radiation of a specific frequency and polarization to be transmitted to the receiver. Two types of front-end devices can be present in a radio observatory: the bolometric and the heterodyne (mixer) receivers. The bolometric receiver performs total intensity measurements, whereas the mixer records the amplitude and the phase of the signal. As the incoming signal of the source is at a relatively high frequency, the *heterodyne principle* is used to reduce the losses in the signal processing. In this technique, the role of the heterodyne receiver is to mix the sky frequency with an artificial wave injected by the local oscillator (LOs). The frequency of the latter is comparable with that of the incoming radiation, but not identical. This new signal is again amplified and mixed to an intermediate frequency, known as IF. The

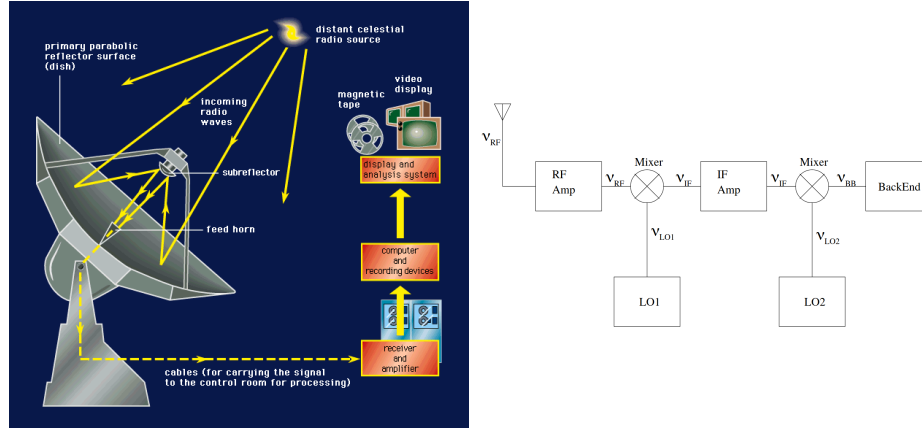


FIGURE 2.1: Radio data acquisition and processing in a radio station. Left: Schematic diagram of the radio signal collected by a parabolic antenna and processed in order to be ready for study. Right: Block diagram of a heterodyne receiver system. Image credits: Prof. J. Schombert personal web page: [www.http://abyss.uoregon.edu/~js/glossary/radio.telescope.html](http://abyss.uoregon.edu/~js/glossary/radio.telescope.html).

IF signal is fed into the backend for further processing. The signal contamination during this step can be reduced through the use of low noise solid state devices, called High Electron Mobility Transistors (HEMTs). The HEMTs are cooled down with liquid nitrogen or helium. Figure 2.1 illustrates what it is described above.

A radio telescope operates to measure the temperature distribution of the sky. The telescope sensitivity is, however, not uniform in all directions, but is defined by the so-called antenna *beam pattern*. This is the power received from a point source as a function of the angular distance from the antenna axis. The *main beam* or *main lobe* (see Fig. 2.2) describes the solid angle within which the telescope sensitivity is maximum. The beam pattern results as a consequence of Fraunhofer diffraction, which implies that, for a circular aperture of diameter  $D$ , the full width at half maximum (FWHM) of the main lobe  $\theta$ , i.e., the *angular resolution* of the telescope, is

$$\theta = a \frac{\lambda}{D} \quad (2.1)$$

where  $a$  is a factor close to unity and  $\lambda$  is the observed wavelength. Ultimately, the temperature distribution actually measured by the telescope, known as *antennas temperature*  $T_{\text{ant}}$ , results from the convolution of the sky brightness distribution and the beam pattern. For a given astronomical source with flux density  $S$ , the antenna temperature can be expressed as

$$T_{\text{ant}} = \frac{SA_{\text{eff}}}{2k_B} \quad (K) \quad (2.2)$$

where  $k_B$  is the Boltzmann's constant and  $A_{\text{eff}}$  is the effective area of the telescope, differing from the geometrical area  $A_g = \pi D^2/4$  by a factor  $\eta_A$  known as *antenna efficiency*, which depends on the elevation.



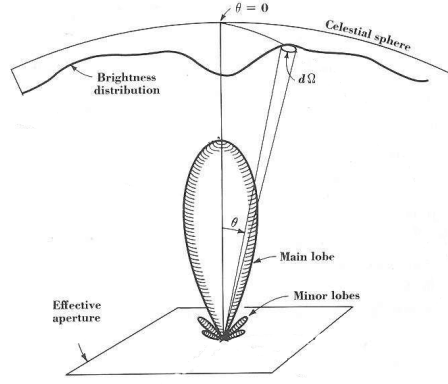


FIGURE 2.2: Illustration of the beam pattern, defining the antenna directional sensitivity.  
Image credits: [Kraus \(1966\)](#).

As in every scientific experiment, the output of the telescope measurement will of course include, in addition to the astronomical signal, different noise contributions, the sum of which is known as system temperature  $T_{\text{sys}}$ , and can be written as

$$T_{\text{sys}} = T_{\text{rec}} + T_{\text{loss}} + T_{\text{sky}} + T_{\text{spill}} \quad (\text{K}) \quad (2.3)$$

where  $T_{\text{rec}}$  is the noise of the receiver,  $T_{\text{loss}}$  comprises any additional loss during the signal transferring,  $T_{\text{spill}}$  is the random radiation from ground sources, and  $T_{\text{sky}}$  is the emission of the background sky brightness.

In general, the system temperature is large with respect to the antenna temperature. To increase the signal-to-noise ratio (SNR), one can either increase the integration time  $\Delta t$  or the bandwidth  $\Delta\nu$ , or both. This is expressed by the *radiometer equation*

$$\text{SNR} = \frac{T_{\text{ant}}}{T_{\text{sys}}} \sqrt{\Delta\nu \Delta t} \quad (2.4)$$

In addition, Eq. 2.2 shows that the antenna temperature is proportional to the telescope effective area, which implies that larger telescopes are more sensitive.

### 2.1.2 Interferometry and Aperture Synthesis

Radio interferometry is a powerful and elegant observing technique of modern astronomy. One of the most desirable features in radio observations is to achieve the highest possible angular resolution in order to resolve the fine structure of the astrophysical sources. As described in the previous paragraph (Eq. 2.1), one solution for maximizing the angular resolution is to build antennas with large diameter. However, even the largest antennas in the world today, such as the Green Bank radio telescope or Effelsberg, with  $\sim 100$  m antenna diameter, can only achieve a resolution of  $\sim 10$  arcsec, observing at 86 GHz. Building even larger antennas comes with significant engineering challenges. The solution for obtaining a higher angular resolution at a given wavelength came by extending the double-slit experiment by Thomas Young in 1801 and the interferometry principle, introduced by [Michelson & Morley \(1887\)](#), to develop a new technique, called *aperture synthesis*. Given an array of telescopes, aperture synthesis enables us to achieve the same angular resolution of a

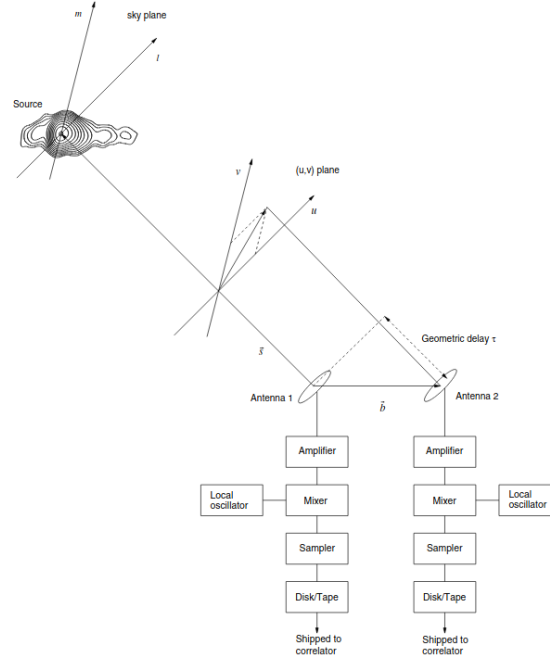


FIGURE 2.3: Illustration of a two-element radio interferometer and its block diagram. The interferometer observes the source, the direction of which is described by the vector  $\mathbf{s}$ . The  $u, v$  plane, as well as the direction cosine coordinate system ( $l, m$ ) are displayed. The radiation, after reaching each station, is post-processed in several steps. Image credits: [Middelberg & Bach \(2008\)](#).

telescope with diameter as large as the maximum separation between two elements of the array.

### 2.1.2.1 Earth Rotation and Aperture Synthesis

The most basic type of radio interferometer consists of two antennas, separated by a certain distance  $\mathbf{b}$  called *baseline*, which are receiving the same wavefront emitted by an astronomical source. The maximum baseline length of the interferometer plays here the role of the telescope diameter  $D$  from Eq. 2.1. For a better understanding of the interferometer configuration, let us consider that the antennas point towards a sky object, in a direction defined by the vector  $\mathbf{s}$  (see Fig. 2.3). The baseline vector is projected onto a plane perpendicular to  $\mathbf{s}$ , formed by unit vectors  $\mathbf{u}$  and  $\mathbf{v}$ . This plane is the so-called *uv plane* and describes the projected separation and orientation of the antennas in units of wavelengths.

In a two-element interferometer, the light-travel time of the signal from the source to each station is not the same. A *geometrical delay*  $\tau_g$  is introduced due to the difference in the radiation path length, and is expressed by

$$\tau_g = \frac{\mathbf{s} \cdot \mathbf{b}}{c}. \quad (2.5)$$

Then, the signals from the two stations are led to the correlator in the form of voltages  $V_1$  and  $V_2$

$$V_1 = V \cos [2\pi\nu (t - \tau_g)] \quad (2.6)$$

$$V_2 = V \cos [2\pi\nu t] \quad (2.7)$$

where  $V$  is the maximum amplitude,  $2\pi\nu(t - \tau_g)$  and  $2\pi\nu t$  are the phases of the waves.

The correlator is used to combine the two signals coherently, by multiplying and averaging them. This operation returns an even function  $F_{\text{even}}$  expressed as:

$$F_{\text{even}} = \langle V_1 V_2 \rangle = \frac{V^2}{2} \cos(2\pi\nu\tau_g). \quad (2.8)$$

This cosinusoidal correlation output is sensitive to the even part of the brightness distribution of the source. In order to fully reconstruct this distribution, a complementary sinusoidal function is produced by the correlator by adding a  $\pi/2$  phase rotation in one of the two signal and by repeating the multiplication and averaging operations. The sinusoidal correlation output is

$$F_{\text{odd}} = \frac{V^2}{2} \sin(2\pi\nu\tau_g). \quad (2.9)$$

At this point, the even and odd correlation outputs are combined into a complex function, known as *complex visibility function*  $V$ , and defined as

$$V = F_{\text{even}} - iF_{\text{odd}} = Ae^{i\Phi} \quad (2.10)$$

where  $A = \sqrt{F_{\text{even}}^2 + F_{\text{odd}}^2}$  is the visibility amplitude and  $\Phi = \tan^{-1}(F_{\text{odd}}/F_{\text{even}})$  is the visibility phase.

Based on the *van-Cittert Zernike theorem*, the spatial intensity distribution of the incoming signal,  $I_\nu$ , and the visibility function are Fourier pairs. For a given solid angle  $d\Omega$ , their relation is

$$V_\nu(\mathbf{b}) = \iint I_\nu(\mathbf{s}) e^{-2i\pi\nu(\mathbf{b}\cdot\mathbf{s}/c)} d\Omega \quad (2.11)$$

In literature, Eq. 2.11 is usually expressed in the reference system of the directional cosines  $(l, m, n)$  (see Fig. 2.3) measured with respect to the direction  $\mathbf{s}_0 = (0,0,1)$ , which is called *phase tracking center*. Hence, the visibility function transforms into

$$V_\nu(u, v) = \iint I_\nu(l, m) e^{-2i\pi(ul+vm)} dldm. \quad (2.12)$$

From this relation, one can recover the source brightness distribution from a number of visibility measurements as

---

<sup>1</sup>The complete form of the van Cittert-Zernike theorem is

$$V_\nu(u, v, w) \approx \iint I_\nu(l, m) e^{-2i\pi(ul+vm+wn)} \frac{dldm}{\sqrt{1-l^2-m^2}} \quad (2.13)$$

but as we are interested for only a small area in the celestial sphere  $n = \sqrt{1-l^2-m^2} \approx 1$ , and the  $w$ -term can be considered as  $w = 0$ .

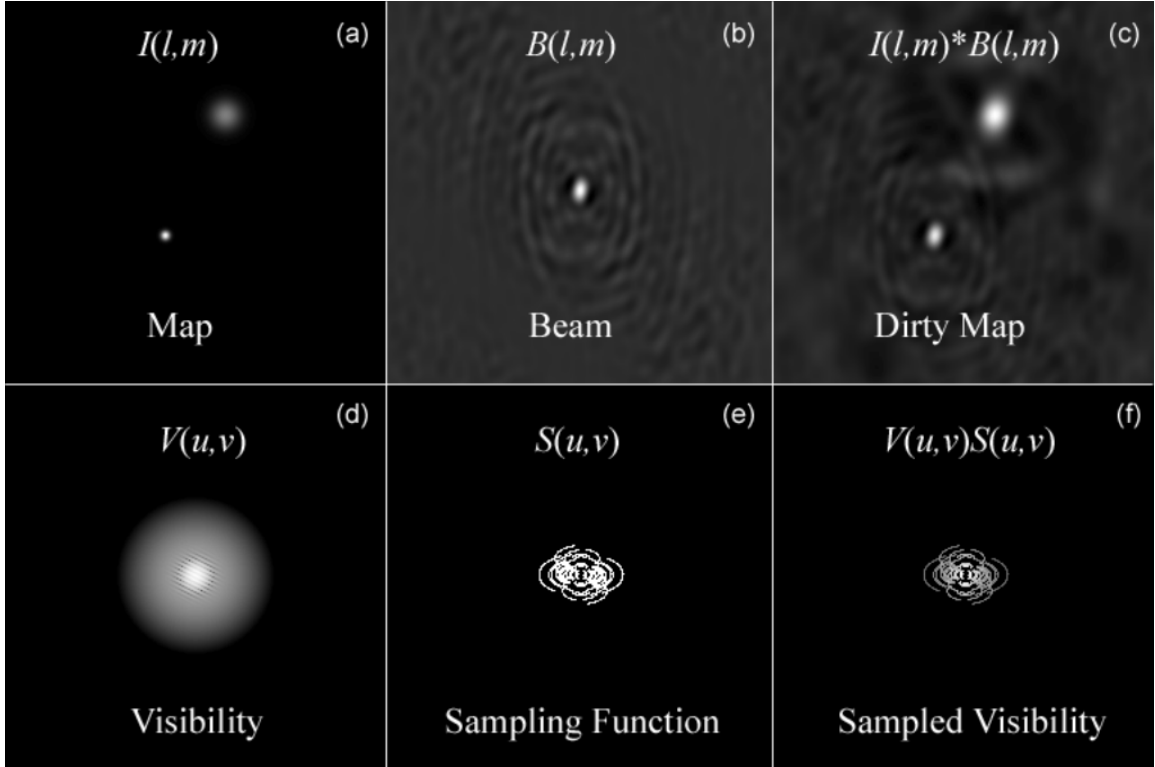


FIGURE 2.4: The connection between visibility and image domain. Image credits: lecture notes of Prof. Dale Gary, New Jersey Institute of Technology: <http://web.njit.edu/gary/728/Lecture6.html>.

$$I_{\nu}(l, m) = \iint V_{\nu}(u, v) e^{2i\pi(ul+vm)} du dv. \quad (2.14)$$

Lastly, since the response of the interferometer is by definition incomplete, a *sampling function*  $S(u, v)$  needs to be introduced in Eq. 2.14. The  $S(u, v)$  describes the points where  $V(u, v)$  is measured and is zero where there are no data. Ultimately, the *dirty image* of the source brightness distribution can be obtained as

$$I_{\nu}^D(l, m) = \iint S(u, v) V_{\nu}(u, v) e^{2i\pi(ul+vm)} du dv \quad (2.15)$$

where the dirty image is the convolution of the true brightness distribution  $I_{\nu}^D(l, m)$  with the Fourier transform of  $S(u, v)$ , expressed as

$$B(l, m) = \iint S(u, v) e^{2i\pi(ul+vm)/c} du dv. \quad (2.16)$$

The function  $B(l, m)$  is known as the *synthesised beam* of the interferometer or the *Point Spread Function (PSF)*. An illustration of the aforementioned quantities can be seen in Fig. 2.4.

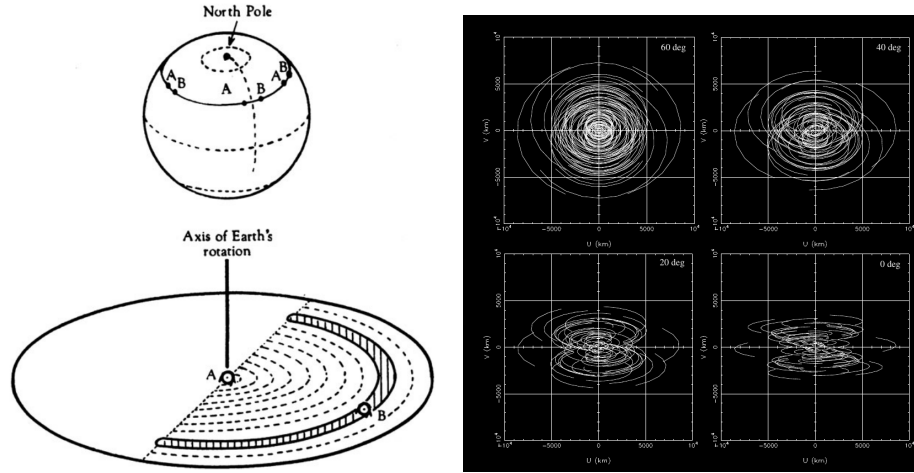


FIGURE 2.5: Conceptual illustrations of the Earth rotation aperture synthesis, and the resulting  $uv$ -coverage. Left: A two-element array which observes a source at the north celestial pole for a 12-hour time interval will obtain data over a full track  $uv$ -coverage (Ryle 1962). Right: Full-track VLBI observations of sources at different declination observed by the VLBA array (see Fig. 2.8).

An interferometer acts as a filter for spatial frequencies. The large  $uv$  spacings are sensitive to the fine structures of source, whereas the short  $uv$  spacings sample the large scale structures. Filling the  $uv$ -plane as much as possible is crucial for improving the image fidelity. The so-called *uv-coverage* is improved by the Earth rotation (Fig. 2.5) when performing observations over up to 12-hour (full track), or by increasing the number of stations forming the array.

The overall sensitivity of an interferometric array depends on the properties of each individual antennas, and on the number of elements forming the array (Walker 1995). Assuming an array formed by  $N$  identical antennas, the sensitivity is expressed as

$$\sigma = \frac{2k_B T_{\text{sys}}}{A_{\text{eff}} \sqrt{\Delta\nu \Delta t (N-1) N}}. \quad (2.17)$$

### 2.1.3 Very Long Baseline Interferometry

In 1967, driven by the motivation of resolving fine structures in quasars, the first very-long-baseline interferometric array looked at the radio sky (Moran 1998). This was made possible by the transition from the connected interferometric elements to the tape recording system in each station, which allowed the baseline length to be increased to intercontinental scales. In VLBI observations, each antenna stores the data independently from the other array elements, recording them on magnetic disks together with accurate clock tags provided by an atomic clock. Data are later sent to the correlator, which applies a complex model for delay compensation, as discussed in the previous section.

### 2.1.4 VLBI Arrays

VLBI is a widely used observational technique, that has allowed us to achieve breathtaking image sharpness, reaching angular scales down to the micro-arcseconds. The most recent and remarkable achievement is the first-time-ever imaging of the SMBH in M87 (see Chapter 1.1.1). Many of the largest antennas in the world are participating in VLBI experiments, forming Earth-size powerful arrays. Additionally, the development of space-VLBI has enabled the baseline length to be increased up to 350,000 km. In this paragraph, we briefly describe the instruments that were used for obtaining the data used in this thesis.

#### 2.1.4.1 Global Millimeter VLBI Array

The Global Millimeter VLBI Array (GMVA) is the largest interferometric array operating at 86 GHz. The array comprises up to 16 stations, which are either part of smaller arrays, or individual large-aperture antennas. GMVA consists of the following radio observatories: the Very Long Baseline Array (VLBA, eight out of the ten stations equipped with 86 GHz receivers), the Green Bank Telescope (GBT), Effelsberg, Pico-Veleta, Onsala, Metsaehovi, Yebes, and the Korean VLBI Network (KVN). All telescopes operate at their highest possible bandwidth. Currently, this results in a 2 Gbps data rate, except for the KVN telescopes, which operate a 1 Gbps mode. Occasionally, other radio telescopes or arrays such as *RadioAstron*, the Atacama Large Millimeter/submillimeter Array (ALMA), NOEMA (on Plateau de Bure) or the Event Horizon Telescope are participating to the observing sessions.

The typical angular resolution that can be achieved by the GMVA reaches  $\sim 50 \mu\text{as}$ . Such high resolution translates for the most nearby sources into a linear scale of a few tens of Schwarzschild radii. Also, due to a large number of array elements and the station locations all around the globe, GMVA provides a unique combination of excellent uv-coverage and high observing frequency, thanks to which high-quality, sharp VLBI images can be obtained (see Fig. 2.7). The GMVA supports total intensity and polarization observations, enabling us to probe the nuclear regions of active galaxies in the vicinity of the central engine.

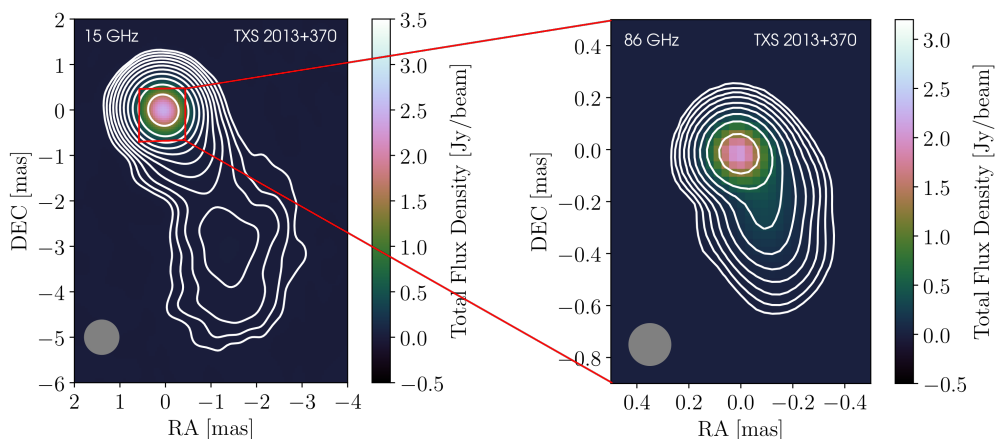


FIGURE 2.7: Stacked images of TXS 2013+370 at 15 GHz and 86 GHz. The image was convolved with a circular beam 0.75 mas, at 15 GHz, whereas the 86 GHz, the convolving beam is 0.08 mas. The high resolution GMVA observations allow us to zoom into the innermost regions of a jet.

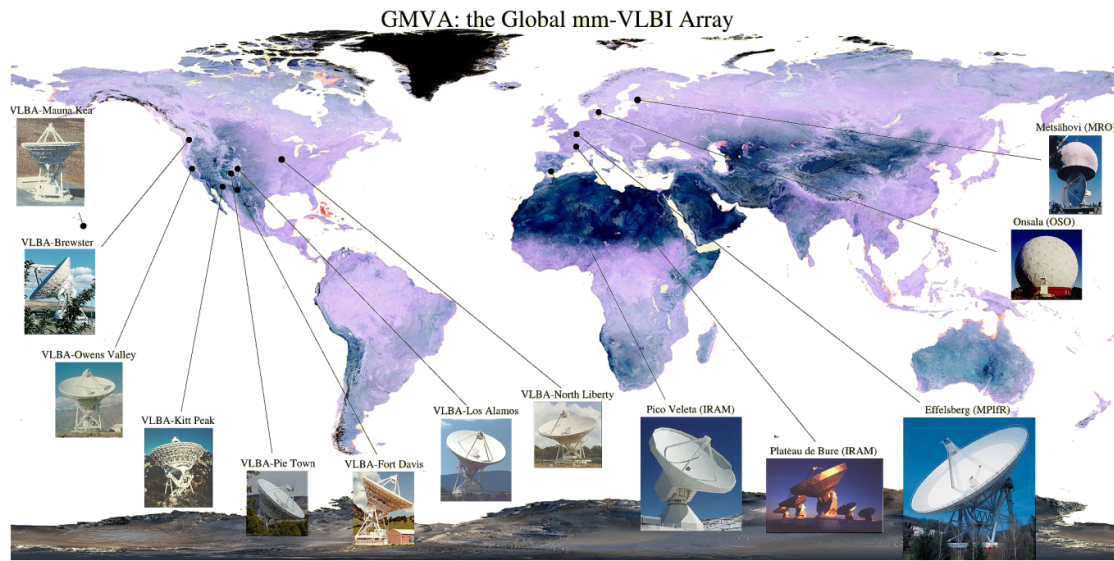


FIGURE 2.6: Radio telescopes forming the Global Millimeter VLBI Array (<http://www3.mpifr-bonn.mpg.de/div/vlbi/globalmm/>).

#### 2.1.4.2 *RadioAstron* Satellite

The *RadioAstron* space radio telescope (also known as Spektr-R) is a ten-meter antenna that was launched in July 2011 from the Baikonour Cosmodrome in Russia, in an elliptical orbit of ten days. The space antenna supports observations at 22, 5, 1.6 and 0.3 GHz, in dual polarization. The main goal of the mission is to use the space telescope to conduct space-VLBI observations in conjunction with Earth-based antenna arrays. The baseline length that *RadioAstron* provides in its apogee reaches the scale of 350,000 km. This remarkable baseline length corresponds to the angular resolution of 7, 35, 100, and 500  $\mu\text{as}$  respectively in the four radio bands. Therefore *RadioAstron* enables us to image the jet base in AGN with resolution comparable to that achieved with the GMVA, but at lower frequencies.

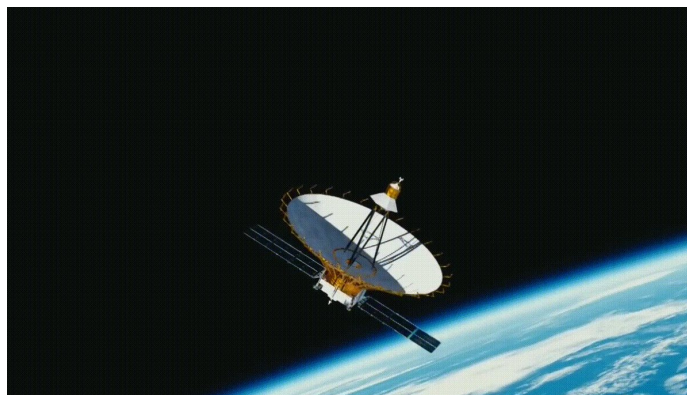


FIGURE 2.8: Artistic illustration of the 10-m space radio antenna *Radio Astron* Spektr-R. Credit: Lavochkin Association.



## 2.2 Calibration and Imaging of VLBI Data

After the data are exported from the correlator, a set of calibration steps needs to be performed before the science target can be studied. For an array formed by two elements,  $i$  and  $j$ , the observed visibilities  $V'_{i,j}(t, \nu)$  differ from the ideal visibilities  $V_{i,j}(t, \nu)$  due to some corrupting terms. Their relation is:

$$V'_{i,j}(t) = g_i(t) g_j^*(t) V_{i,j}(t) + \epsilon_{i,j}(t), \quad (2.18)$$

where  $g_i(t)$  is the *complex element gain* of each station and  $\epsilon_{i,j}(t)$  the baseline-based thermal noise. Since the complex gains are characterized by an amplitude and a phase, calibrating the data means to determine the amplitude and the phase of the gains, and finally apply the corrections. In the following paragraphs, we are going to briefly describe these calibration steps. For the projects that are presented in this work, the main software that was used to perform the *a-priory* calibration tasks was the National Radio Astronomy Observatorys (NRAO) Astronomical Image Processing System (AIPS, [Greisen 1990](#)). Due to the complex nature of the analysis, we developed a semi-automated pipeline based on scripts for performing most of the calibrating tasks, written in ParselTongue ([Kettenis et al. 2006](#)). ParselTongue is a Python interface for AIPS, which allows running AIPS tasks, access AIPS headers, visibilities, and manipulate AIPS tables through Python.

### 2.2.0.1 Fringe Fitting

After correlation, residuals systematic delay and phase offsets, as well as time depended drifts are still present. The procedure through which these residuals are determined is called *fringe fitting* (see [Cotton 1995](#), for an in-depth discussion). The time- and frequency-dependent relation between the phase  $\phi(t, \nu)$  and the delay is

$$\phi(t, \nu) = 2\pi\nu\tau_t \quad (2.19)$$

By differentiating the phase we obtain

$$\Delta\phi(t, \nu) = \phi_0 + \left( \frac{\partial\phi}{\partial\nu} \Delta\nu + \frac{\partial\phi}{\partial t} \Delta t \right) \quad (2.20)$$

where  $\phi_0$  is the constant phase offset at the reference time  $t_0$  and  $\nu$ . The terms

$$\tau = \frac{1}{2\pi} \frac{\partial\phi}{\partial\nu} \quad \dot{\tau} = \frac{1}{2\pi} \frac{\partial\phi}{\partial t} \quad (2.21)$$

are the so-called *delay residual* (or delay) and  $\partial\phi/\partial t$  is the *delay rate* (or rate) respectively. Once delays and rates are derived, the corrections are applied to the visibilities which, in the end, can be coherently integrated in time and frequency. The fringe fitting can be performed either in the delay-rate domain or in the time-frequency domain. In the former approach, the algorithm searches for the peak in the delay-rate space (see Fig. 2.9, left panel), i.e., for the delay and rate values which maximize the correlation coefficient. This is known



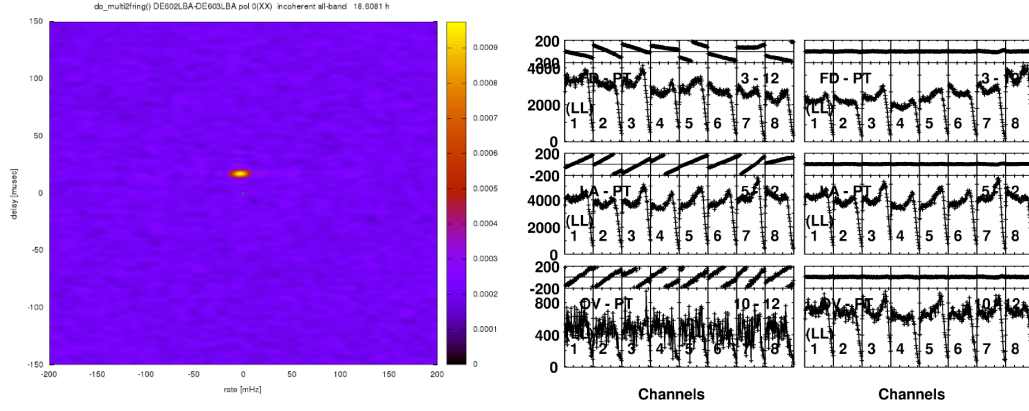


FIGURE 2.9: Left: Fringe search in the delay-rate domain. Right: Example of the appearance of the data before and after the fringe fitting, through which the phases become aligned. Image credits: [Wucknitz \(2010\)](#) and [Nair G. \(2019\)](#) respectively.

as *fringe search*. Once the peak is determined, data are averaged through the Fourier transform. In the time-frequency domain, instead, solutions are found by performing a linear fit to the phase variation as a function of time and frequency.

In practice, the phase calibration through the fringe fitting usually comprises two main steps: the *manual fringe fitting* and the *global fring fitting*. In AIPS, both of these steps are carried out with the task FRING. The manual fringe fitting determines residual delays in a single sideband (or IF) by considering a short time-range in which fringes are clearly detected on all baselines including a certain reference antenna. After the phases in each sideband are aligned, integration over the full bandwidth becomes possible. The manual fringe fitting may be run more than once if a single, good time-range cannot be found for all the baselines. After applying the solutions of this first fringe run, the global fringe fitting determines delays and rates by considering the entire data set. An example of the appearance of the data before and after the fringe fitting is shown in Fig. 2.9, right panel.

### 2.2.0.2 Amplitude Calibration

The visibility amplitudes delivered by the correlator are expressed in correlator units (Whitneys), therefore a conversion into astrophysical units (Janskys) is necessary. This conversion is performed in the amplitude calibration.

The antenna complex gains  $g_i(t)$  and  $g_j^*(t)$  from Eq. 2.18 can expressed as

$$g_i(t) = \alpha_i(t) e^{i\phi_i(t)} \quad \text{and} \quad g_j^*(t) = \alpha_j(t) e^{-i\phi_j(t)} \quad (2.22)$$

where  $\alpha_i(t)$ ,  $\alpha_j(t)$  are the signal amplitudes and  $\phi_i(t)$ ,  $\phi_j(t)$  are the phase correction terms for each antenna. Hence, Eq. 2.18 can be rewritten as

$$V'_{i,j}(t) = \alpha_i(t) \alpha_j(t) e^{i(\phi_i - \phi_j(t))} V_{i,j}(t) + \epsilon_{i,j}(t). \quad (2.23)$$

By defining  $A_{i,j} = \alpha_i(t) \alpha_j(t) V_{i,j}(t) + \epsilon_{i,j}(t)$  and  $\psi_{i,j} = (\phi_i - \phi_j(t))$ , Eq. 2.23 can be written in the compact form

$$V'_{i,j}(t) = B_{i,j} e^{i\psi_{i,j}} \quad (2.24)$$

where  $B_{i,j}$  is the visibility amplitude expressed as a correlation coefficient in arbitrary units. This quantity is converted to units of Janskys via the relation

$$S[Jy] = B_{i,j} b \frac{\sqrt{SEFD_i SEFD_j}}{2\Delta\nu\Delta t} \quad (2.25)$$

where  $b$  quantifies the losses due to the digital sampling.

The *System Equivalent Flux Density* (SEFD) corresponds to the flux density of a radio source that doubles the system temperature or, equivalently, the total noise power. Thus, for a source with flux density equal to the SEFD, the SNR would be unity. For each antenna, the SEFD can be expressed as

$$SEFD = \frac{2k_B T_{\text{sys}}}{A_{\text{eff}}} \quad (2.26)$$

In AIPS, the information on the  $T_{\text{sys}}$  and the elevation-dependent  $A_{\text{eff}}$  values of each station are stored in the TY and GC tables, and the conversion to astrophysical flux density units is performed through the task APCAL.

In mm-VLBI experiments, a very important factor that should be taken into consideration is the atmospheric opacity  $\tau$ , which attenuates the signal by a factor of  $e^{-\tau}$ . At short wavelengths, an opacity correction is applied during the amplitude calibration with the same task APCAL, by setting DOFIT=1.

The atmospheric opacity is expressed as

$$\tau = \int_0^\infty k_v(h) dh \quad (2.27)$$

where  $k$  is the absorption coefficient over the scale height,  $h$ , of the atmosphere above the observer<sup>2</sup>. The opacity is thus dependent on elevation.

The task APCAL performs the opacity correction by considering the measurements of  $T_{\text{sys}}$ ,  $T_{\text{rec}}$  and  $T_{\text{atm}}$ . The latter is the atmospheric temperature, derived using an atmospheric model (e.g. Pardo et al. (2001)) based on the weather data recorded at each station. The weather data can be stored in a WX table or read in AIPS from a text file. The opacity is then computed as

$$\tau = \log \left( 1 - \frac{T_{\text{sys}} - T_{\text{rec}}}{T_{\text{atm}}} \right). \quad (2.28)$$

A final step in the amplitude calibration is performed through the task BPASS, which applies the bandpass correction. This calibration is needed to compensate for the inhomogeneous response of the electronic system as a function of frequency, due to which the

<sup>2</sup>see e.g. <https://web.njit.edu/~gary/728/Lecture3.html>

signal is usually strongly attenuated at the edges of each sideband (IF). BPASS stores the information on the bandpass shape in a BP table, which needs to be applied before the frequency-averaging of the data.

A schematic overview of the main steps that should be followed to calibrate mm-VLBI data correctly is displayed in Fig. 2.10.

### 2.2.0.3 Imaging

The next step after the *a-priori* phase and amplitude calibration is to obtain the image of the source. In theory, this can be done by applying an inverse Fourier transform to the measured visibilities (Eq. 2.14). However, a direct *deconvolution* with the dirty beam (see Eq. 2.15 and 2.16) is often limited due to the sparsely sampled uv plane and the high sidelobe levels. The most widely used algorithms for imaging are the *Maximum Entropy Method* (MEM, Jaynes 1957; Wernecke & D’Addario 1977; Frieden & Wells 1978) and CLEAN (Högbom 1974). Here, we are going to focus on the CLEAN algorithm, implemented in the DIFMAP package (Shepherd et al. 1994), since it was the main algorithm used in this thesis.

The deconvolution in CLEAN is performed through a Fast Fourier Transform algorithm. The application of CLEAN is an iterative process: at each iteration, the algorithm finds the position of the peak flux density in the dirty image and it subtracts the dirty beam, which is the Fourier transform of the uv-plane. The peak is then modeled with a delta function. The user can define the number of iterations that are needed for recovering the source flux density. The image is finally restored with a *clean beam*, that is produced by fitting the central lobe of the dirty beam with a function, usually an elliptical Gaussian. In this process, the astronomer can guide the algorithm by setting CLEAN windows where residual flux density is present. Since the algorithm cannot distinguish by itself a strong sidelobe from real source structure, there is always the danger to erroneously model features that do not belong to the science target.

The quality of the image can be significantly improved through an iterative procedure which involve deconvolution as well as self-calibration cycles (see e.g. Cornwell & Fomalont 1999). Second order amplitude and phase corrections are usually still required at the end of the calibration process, and can be computed at this stage by considering a model of the source itself, built, as described, through CLEAN. Thus, by alternating CLEAN and self-calibration cycles, an increasingly better model of the source can be obtained. Self-calibration relies on the concept of *closure phases* and *closure amplitudes*, introduced by Jennison (1958): when considering 3 antennas, in the case of the phase, and 4 antennas in the case of the amplitude, the corruption terms associated to each individual antenna cancel out. The self-calibration algorithm determines the antenna gains through a least squares fit based on the closure quantities. In both cases, the larger the number of the antennas, the more the independent estimates of closure amplitudes and phases and, finally, the more accurate the result.

### 2.2.0.4 Polarization Calibration

Having established the fundamental polarization quantities in Section 1.3.1.2, we can proceed to connect the Stokes parameters Q and U with the correlator output. The correlator

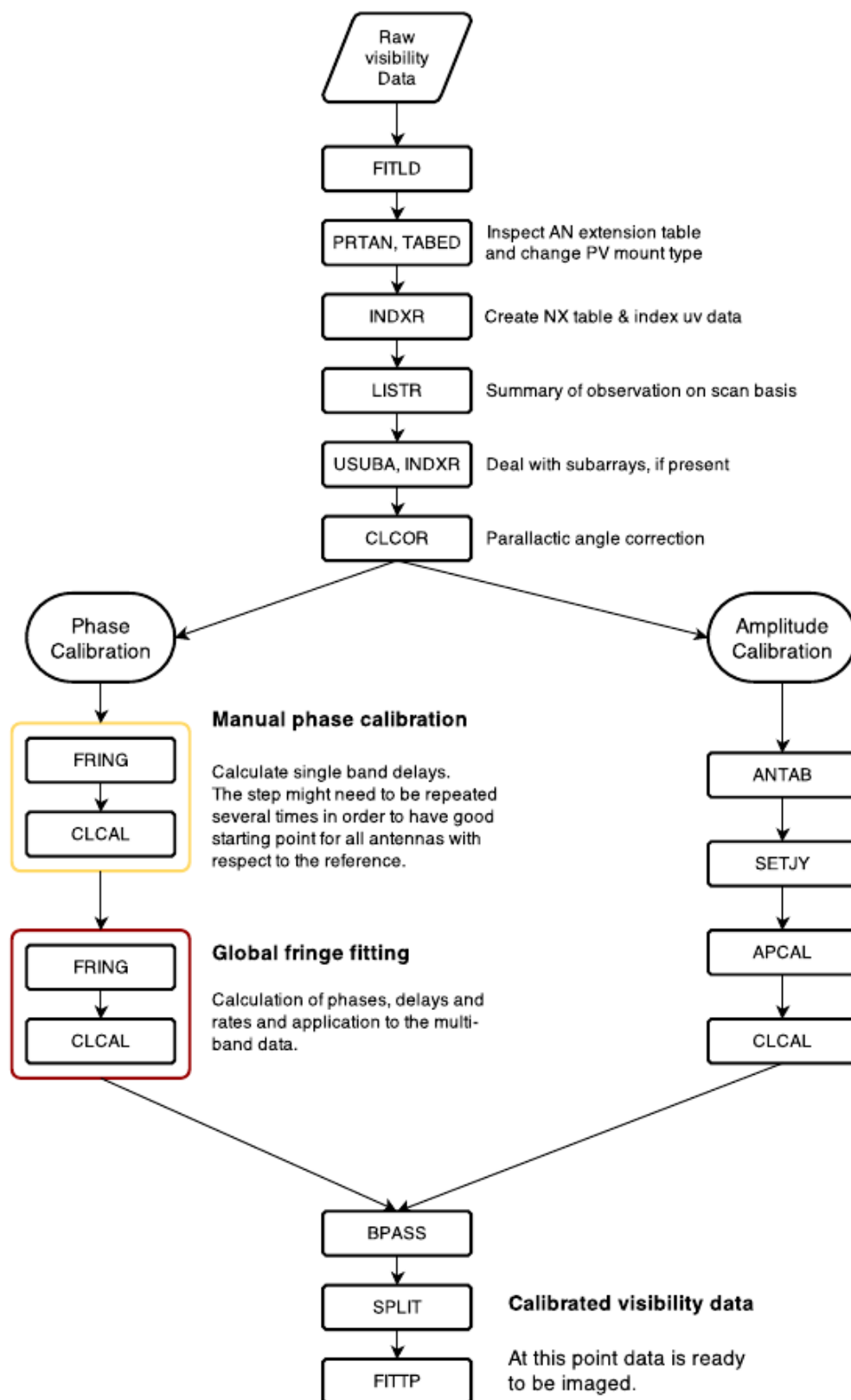


FIGURE 2.10: Flow diagram of mm-VLBI data calibration in AIPS. Image credits: [Karamanavis \(2015\)](#).

produces cross-correlations of the signals from the left and right circular polarization of each antenna. This results in the parallel (LL,RR) and the cross-hand (LR,RL) correlation coefficients. These coefficients are related to the Stokes parameters as follows (Roberts et al. 1994)

$$\langle LL^* (u, v) \rangle = I - V \quad (2.29)$$

$$\langle RR^* (u, v) \rangle = I + V \quad (2.30)$$

$$\langle RL^* (u, v) \rangle = Q + iU = P \quad (2.31)$$

$$\langle LR^* (u, v) \rangle = Q - iU = P^* \quad (2.32)$$

In practice, the incoming polarized light reaches the feed, as can be seen in Fig. 2.11. In the feed, there is a technical element, called *orthomode transducer* (OMT), which separates the right (RCP) and left circular polarization (LCP) component of the signal (see right panel of Fig. 2.11). However, technically this separation cannot be performed perfectly. That leads to the cross-over, with some percentage of the left polarized light to leak into the right and vice versa. This leakage can be expressed by a first-order approximation of the output voltage from the receiver as:

$$A_L = g_L \left( E_L e^{i\phi} + D_L E_R e^{-i\phi} \right) \quad (2.33)$$

$$A_R = g_R \left( E_R e^{-i\phi} + D_R E_L e^{i\phi} \right) \quad (2.34)$$

(Roberts et al. 1994), where  $L$ ,  $R$  stand for LCP and RCP respectively,  $V_L$ ,  $V_R$  are the corresponding complex visibilities for each polarization,  $E_L$ ,  $E_R$  are the complex electric fields,  $\phi$  is the parallactic angle, the  $g$  terms are the complex gain factors and  $D$  is the instrumental polarization leakage, known also as *D-terms* (Leppänen et al. 1994).

The D-terms magnitude ranges typically between  $\sim 1-10\%$  of the received radiation, hence, second or higher-order terms can be omitted. So, the correlator output for each baseline (comprised by antennas 1 and 2) can be expressed by the following set of equations

$$L_1 L_2^* = g_{L1} g_{L2}^* I e^{i(\phi_1 - \phi_2)} \quad (2.35)$$

$$R_1 R_2^* = g_{R1} g_{R2}^* I e^{-i(\phi_1 - \phi_2)} \quad (2.36)$$

$$L_1 R_2^* = g_{L1} g_{R2}^* \left[ P + I \left( D_{R2}^* e^{2i\phi_2} + D_{L1}^* e^{-2i\phi_1} \right) \right] \quad (2.37)$$

$$R_1 L_2^* = g_{R1} g_{L2}^* \left[ P + I \left( D_{L2}^* e^{2i\phi_2} + D_{R1}^* e^{2i\phi_1} \right) \right], \quad (2.38)$$

where  $I$  is the total intensity,  $P$  is the complex linear polarization of the radio source, and the superscript  $(*)$  stands for the complex conjugate. We refer the reader to (Leppänen et al. 1994; Thompson et al. 2017, and references therein) for a detailed discussion.

In practice, polarisation calibration requires high accuracy in the phase and amplitude calibration, which makes it very challenging.

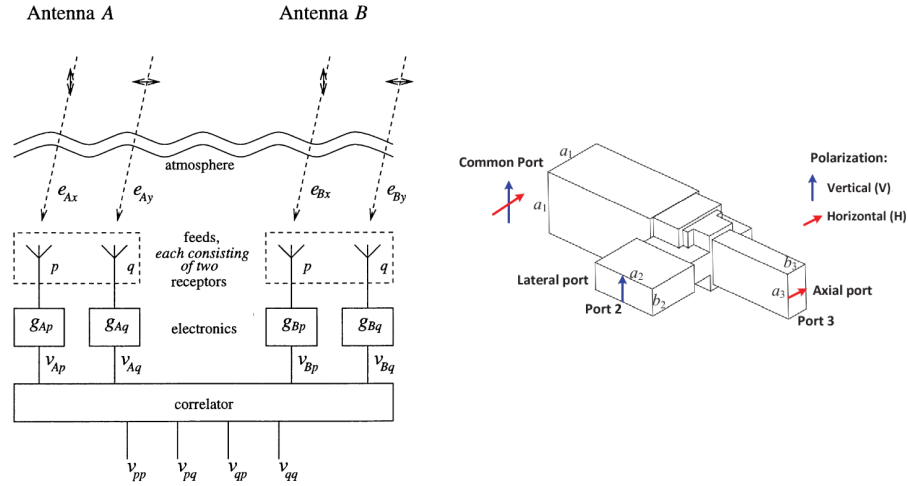


FIGURE 2.11: Conceptual illustrations of VLBI polarization set-up. Left: Block diagram of a two-element VLBI polarimetry configuration. Right: Drawing of an OMT. Credits: Hamaker et al. (1996) and Shang et al. (2016) respectively.

In this work, the polarization calibration is performed as a part of the main *a-priori* calibration in AIPS, following the procedure that is described in Cotton (1999) and <http://pc.astro.brandeis.edu/pdfs/evnmemo78.pdf>. In summary, the main calibration steps for mm-VLBI polarimetric data are

- CLCOR, by the setting `OPCODE = 'PANG'` applies parallactic angle corrections for each antenna. The feeds of the array elements that are equipped with altazimuth mount are rotating with respect to the sky during the observations. Because of this, a small angle offset is added to the main parallactic angle of the source.
- RLDLY, for removing the residual single-band delays and phase offsets in the cross-hand polarization signal.
- CALIB, for correcting the visibility amplitude and phase between the LL and RR channels.
- LPCAL (Leppanen et al. 1995), which is the most crucial step for performing the instrumental polarization correction. It is highly recommended at this stage to obtain the D-terms for more than one source that has been observed in the same session and apply in the end the mean D-term values to the data. With this approach, we minimize the estimation uncertainties. For a detailed description of this method, we refer the reader to Leppänen et al. (1994).
- SPLIT, by the setting `DOPOL ≥ 1` to apply the obtained D-terms to the data.

After the instrumental polarization calibration, the polarization imaging of the target sources is done similarly to the total intensity imaging. The last step is the correction of the EVPAs. To determine the linear polarization position angle, one needs external information concerning the absolute orientation of the EVPA, obtained for instance by considering single-dish observations at the same epoch and frequency. This calibration is applied to data via the task CLCOR.

## 2.3 *Fermi* Gamma Ray Space Telescope

The *Fermi* satellite is a pair-conversion detector sensitive to  $\gamma$ -rays. It was launched on June 11, 2008, on an orbit around Earth with an inclination of  $25.6^\circ$ , at an altitude of about 565 km (Atwood et al. 2009). The *Fermi* satellite carries two observing instruments, the Large Area Telescope (LAT) and the Gamma-ray Burst Monitor (GBM). The *Fermi* LAT is the main  $\gamma$ -ray detector with an observing window in the energy range of 20 MeV up to 300 GeV, a field of view of 2.4 steradians and an angular resolution of  $\sim 0.15^\circ$ . It consists of a silicon strip tracker that converts incoming radiation to  $e^- - e^+$  cascades. The goal of this conversion is to trace the  $\gamma$  photons direction, as the  $e^- - e^+$  pairs leave in the tracker approximately the same path as the parent  $\gamma$  rays. The energy of the incident high-energy radiation is estimated by using a cesium iodide calorimeter, which performs this task by measuring the energy of the cascade product particles. In order to recognize and eliminate the contribution of random cosmic-ray or back-scattering events, the tracker detector is covered externally by an anti-coincidence detector, which recognizes such events. The GBM, on the other hand, is a supportive instrument, which is composed of an array of sodium iodide and bismuth germanate crystal scintillators. This instrument aims to measure the energy spectrum of brief transient events like  $\gamma$ -ray bursts. The sensitivity of this detector ranges from 8 keV to 40 MeV, which corresponds to the soft and hard x-ray regime. Figure 2.12 displays the satellite configuration, as well as the location of the LAT and the GBM.

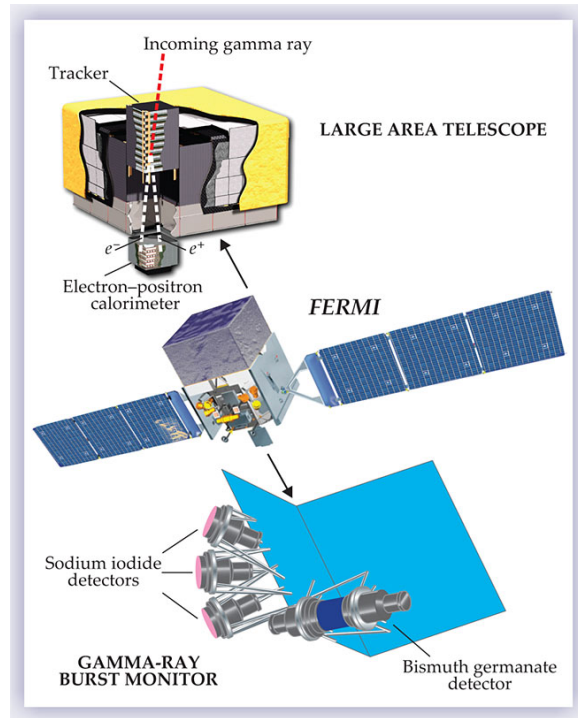


FIGURE 2.12: *Fermi* satellite sketch, with the LAT (top yellow area) and the GBM (bottom) instruments. Credits: Stecker (2010).

The high-energy activity of selected astrophysical objects is monitored, recorded and is made publicly available on the web page <https://fermi.gsfc.nasa.gov/ssc/data/access/lat/>.



## Chapter 3

# Localizing the High-energy Emitting Region in the Blazar TXS 2013+370

*The results discussed in this chapter is partially published in the journal *Astronomy & Astrophysics*, and is reproduced with the permission of the Editor-in-Chief. Credit: E. Traianou et al., 2020, *A&A*, 634, 112, reproduced with permission ©ESO.*

### 3.1 Introduction

The  $\gamma$ -ray loud object TXS 2013+370 is classified as blazar of uncertain type (Massaro et al. 2015), and is located in the Cygnus constellation. It lies at a redshift of  $z = 0.859$  (Shaw et al. 2013), and hosts a SMBH with a mass of  $4 \times 10^8 M_{\odot}$  (Ghisellini & Tavecchio 2015). The Cygnus region is one of the brightest regions of diffuse emission in our galaxy. A great variety of astronomical objects can be found in this small portion of the sky. Nine OB associations (clusters of hot blue-giant stars), over 14 pulsars (Matheson et al. 2013), many pulsar wind nebulae, dense molecular clouds, a superbubble (Ackermann et al. 2011; Uyaniker et al. 2001), more than 10 supernova remnants (Green 2014), and HII regions can be found within the Cygnus region (e.g., see Fig. 3.1). Additionally, as can also be seen in Fig. 3.2, TXS 2013+370 is located very close to the Galactic plane ( $b = 1.2^{\circ}$ ). This geometrical coincidence made the detection and identification of TXS 2013+370 challenging. Based on VLBI observations at 10 GHz, Geldzahler et al. (1984) postulated that, in addition to the super nova remnant G74.9+1.2, there exists a compact radio source in the Cygnus region. Many studies followed afterward, trying to shed more light on the nature of this object by searching for counterparts in different emission regimes, along with estimates of the angular broadening that is introduced by the intergalactic dust (e.g., Abeysekara et al. 2018; Bassani et al. 2014; Halpern et al. 2001; Spangler & Cordes 1998; Fey et al. 1989, and references therein).

Interferometric observations (at radio frequencies that are unaffected by the intervening dust) allow us to resolve the detailed source structure of TXS 2013+370. In this work, we present, for the first time, a VLBI case study of the source TXS 2013+370. We obtain a detailed description of the morphological evolution of the radio jet for over 10 years.



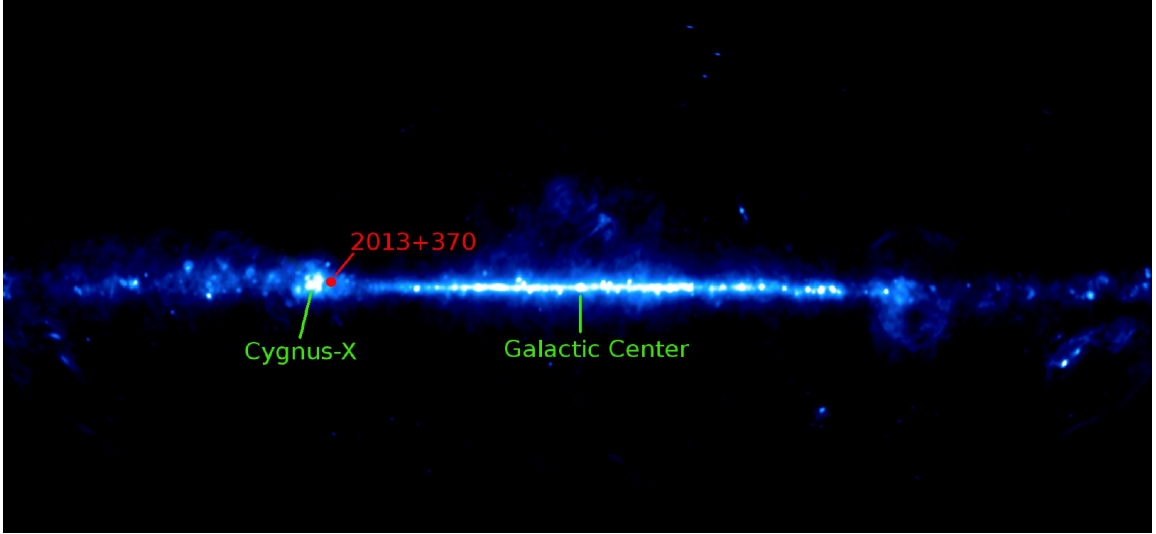


FIGURE 3.1: A panoramic, edge-on map of the Milky Way at 23 GHz, resulting from nine-year observations with the Wilkinson Microwave Anisotropy Probe (WMAP). In the map, the location of TXS 2013+370, as well as Cygnus X and the galactic center are designated. Credits: [Bennett et al. \(2013\)](#).

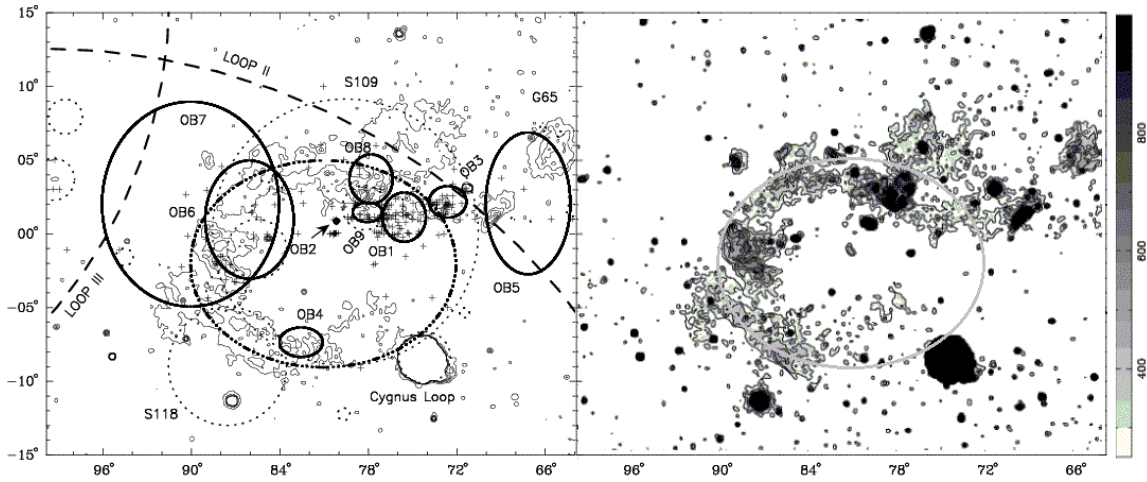


FIGURE 3.2: The two panels displaying the Cygnus region in Galactic coordinates, at 3/4 keV band. Left: The position of the OB associations in this sky frame. TXS 2013+370 is located in the region of the OB1 association. Thick dashed lines show the boundaries of the radio loops, plus signs represent the stars that can be found in this region ([Garmany & Stencel 1992](#); [Comeron et al. 1998](#)) and the dotted circles designate the most prominent H II regions. Right: The Cygnus superbubble at 1.5 keV. Contours start from 250 counts  $\text{s}^{-1} \text{arcmin}^{-2}$  and are plotted in steps of 100 counts  $\text{s}^{-1} \text{arcmin}^{-2}$ . Both plots Credits: [Uyaniker et al. \(2001\)](#).

Simultaneous flux density observations of the source from 4.8 to 43 GHz (obtained from the NRAO archives) allowed us to study the spectral evolution of the source and obtain the magnetic field strength along the jet. Ultimately, by combining the kinematic and geometrical data from the jet base with the results of correlated flux density variability in the cm- and mm- radio and in the  $\gamma$  ray bands, we were able to constrain the location of the  $\gamma$ -ray production region.

## 3.2 Observations and Data Reduction

### 3.2.1 VLBI Observations

The VLBI data set that we used for this work is comprised of observations at 15, 22, 43, and 86 GHz. In total, 23 images allowed us to study the jet kinematics of the blazar TXS 2013+370.

The 86 GHz observations obtained with the GMVA (see Sec. 2.1.4.1) and the 43 GHz observations with the Global VLBI array, with the four epochs to be observed in 2007–2009 and three epochs in 2009–2010, respectively.

For a single epoch, the *RadioAstron* space antenna (Kardashev et al. 2013), in combination with the VLBI ground array performed simultaneous observations at two frequencies, 22 GHz and 5 GHz, to facilitate a fringe search at the space-ground baselines. In this thesis we consider the 22 GHz data.

The space-VLBI data were correlated with a special *RadioAstron*-enabled version (Bruni et al. 2016) of DiFX software correlator running on a desktop computer. The fringe search performed with PIMA (Petrov et al. 2011) resulted in space-ground fringe detection at baselines up to 1.7 Earth diameters. The full description of the space-VLBI experiment will be given by K. Sokolovsky et. al. (in prep.). At 22 GHz, we re-imaged the source based on the data originally presented by Sokolovsky (2014) and Kardashev et al. (2015), who also show a 5 GHz image.

At 15 GHz we re-analyzed fifteen epochs of Very Long Baseline Array (VLBA, Napier 1994) observations that cover a period from 2002 to 2012 and are publicly available at the MOJAVE data archive<sup>1</sup> (see Lister et al. 2009a, 2011, 2018, and references therein).

A detailed overview of the individual VLBI observations are presented in Table 3.1.

---

<sup>1</sup><https://www.physics.purdue.edu/MOJAVE/sourcepages/2013+370.shtml>

TABLE 3.1: VLBI Observational Parameters. Columns from left to right: (1) Observing frequency, (2) Observing year, (3) Participating antennas, (4) Major axis of the convolving beam, (5) Minor axis of the convolving beam, (6) Position angle, (7) Image peak flux density, (8) Noise level, (9) Image total flux density. EB: Effelsberg, JB: Jodrell Bank, RO: Robledo, YS: Yebes, RA: *RadioAstron*, ON: Onsala, GB: Green Bank, NT: Noto, PV: Pico Veleta, PB: Plateau de Bure, MH: Metsahovi, VLBA: Very Long Baseline Array. <sup>a</sup> : Saint Croix did not participate in the observations. <sup>b</sup> : Ovro did not participate in the observations. <sup>c</sup> : Hancock and Saint Croix do not have 3 mm receivers.

Frequency (GHz)	Epoch (yyyy-mm-dd)	Array Elements	$b_{\text{maj}}$ (mas)	$b_{\text{min}}$ (mas)	PA (deg)	$S_{\text{peak}}$ (Jy)	rms (mJy/beam)	$S_{\text{total}}$ (Jy/beam)
15	2002.51	VLBA <sub>10</sub>	0.72	0.48	-16.3	4.26	0.23	5.07
15	2003.04	VLBA <sub>10</sub>	0.77	0.47	-4.89	2.82	0.08	3.69
15	2003.24	VLBA <sub>10</sub>	0.71	0.46	-11	2.97	0.38	3.92
15	2005.35	VLBA <sub>10</sub>	0.75	0.47	-3.62	2.1	0.39	2.66
15	2005.39	VLBA <sub>10</sub>	1.10	0.45	1.18	2.05	0.21	2.60
15	2005.44	VLBA <sub>10</sub>	0.99	0.37	-18.1	1.93	0.54	2.63
15	2005.99	VLBA <sub>10</sub>	1.00	0.37	-19.5	1.63	0.19	2.23
15	2006.00	VLBA <sub>8</sub> <sup>ab</sup>	1.22	0.41	0.45	1.75	0.35	2.14
15	2006.36	VLBA <sub>10</sub>	0.77	0.47	-11.2	1.945	0.19	1.35
15	2008.41	VLBA <sub>10</sub>	0.79	0.44	-19.7	2.93	0.38	3.52
15	2008.75	VLBA <sub>10</sub>	0.78	0.45	-14.9	2.56	0.49	3.07
15	2009.15	VLBA <sub>10</sub>	0.70	0.45	-16.9	3.36	0.41	4.3
15	2010.46	VLBA <sub>9</sub> <sup>b</sup>	0.78	0.43	-20.3	2.08	0.17	2.79
15	2011.53	VLBA <sub>10</sub>	0.77	0.44	-10.9	1.96	0.52	2.06
15	2012.48	VLBA <sub>9</sub> <sup>a</sup>	0.81	0.46	-24.1	3.37	0.25	4.23
22.2	2012.82	EB+JB+RO+YS+RA	0.25	0.08	-88.6	1.18	1.81	3.20
43	2007.81	VLBA <sub>9</sub> <sup>a</sup> +YS+EB+ON+GB	0.23	0.1	-23.5	2.75	0.56	3.46
43	2008.79	VLBA <sub>9</sub> <sup>a</sup> +YS+EB+ON+NT+GB	0.25	0.1	-15.9	2.17	0.06	3.77
43	2009.21	VLBA <sub>10</sub> +YS+EB+ON+GB	0.26	0.1	-14.6	4.43	0.33	6.76
43	2009.86	VLBA <sub>10</sub> +EB+ON+GB	0.22	0.1	-19.4	1.27	0.23	2.85
86	2009.35	VLBA <sub>8</sub> <sup>c</sup> +PV+EB+ON+PB+MH	0.15	0.05	-5.8	1.53	0.39	3.17
86	2009.77	VLBA <sub>8</sub> <sup>c</sup> +PV+EB+ON+PB	0.14	0.04	-2.56	1.71	0.83	3.43
86	2010.34	VLBA <sub>8</sub> <sup>c</sup> +PV+EB+ON+PB+MH	0.18	0.07	-8.72	1.91	0.36	3.08

### 3.2.1.1 VLBI Data Calibration

The data reduction was performed using the software package AIPS (see Sec. 2.2). The calibration of the GMVA data at 86 and 43 GHz was performed in the standard manner (see Sec. 2.2 and [Nair et al. 2019](#)): after an initial parallactic angle correction of the phases, we determined the inter-band phase and delay offsets between the intermediate frequencies using some high signal-to-noise ratio scans (manual phase calibration). After the phase alignment across the observing band, the global fringe fitting was performed, correcting for the residual delays and phases with respect to a chosen reference antenna. Finally, the visibility amplitudes were calibrated, taking into account corrections for atmospheric opacity computed using the measured system temperatures and gain-elevation curves of each telescope. The *RadioAstron* data were analyzed in a similar fashion as described in [Gómez et al. \(2016\)](#) and [Bruni et al. \(2017\)](#). The calibration of the 15 GHz data was carried out by the MOJAVE team, following the procedure described in [Lister et al. \(2009b\)](#).

### 3.2.2 *Fermi*-LAT Data Analysis

TXS 2013+370 has been a standard target of the *Fermi*-LAT All-Sky Survey, since the beginning of 2008. For this work, we used the publicly available data<sup>2</sup>, and we proceed with

<sup>2</sup><https://fermi.gsfc.nasa.gov/cgi-bin/ssc/LAT/QueryResults.cgi?id=L191104192203246D38FA36>

the analysis by considering as a starting sky model the *Fermi*-LAT third source catalog (3FGL) (Acerro et al. 2015). We set a Region of Interest (ROI) of  $10^\circ$  around the target position and we include in the model all the point sources from the 3FGL within  $15^\circ$  from the ROI center. Additionally, we took into account the corresponding model for the Galactic and isotropic diffuse emission (`gll_iem_v06.fits` and `iso_P8R2_SOURCE_V6_v06.txt`, respectively). Next, we performed a binned analysis in the energy range 0.1–300 GeV, with 10 bins per decade in energy and  $0.1^\circ$  binning in space. A likelihood analysis followed, over the full-time range of the data set (2008-08-04 15:43:36.000 UTC to 2017-03-04 15:43:36 UTC). The fitting of ROI with the initial  $\gamma$ -ray sky model was performed by allowing all the parameters of the target source to freely vary, along with the normalization of all sources within  $5^\circ$  of the ROI center. We checked for the possible detection of new sources by creating the map of Test Statistic (TS) of the region. For creating this, we insert a test source and check its significance, in comparison with the existing model. We point out that the TS is defined as  $2\log(L/L_0)$  where  $L$  is the likelihood of the model with a point source at the target position, and  $L_0$  is the likelihood without the source. A value of  $TS=25$  corresponds to a significance level of  $4.2\sigma$  (Mattox et al. 1996). Hence, we search for sources that  $TS>25$  peaks in the TS map, with a minimum separation of  $0.3^\circ$ . For the cases that a source was meeting these criteria, we add a new point to the model, assuming a power-law spectrum. After the fitting of the new ROI, we produce a new TS map. We continue this procedure until all sources with significant excesses were modeled out. Ultimately, we perform a localization analysis on the target source and all new sources with  $TS>25$  found in the ROI. For the variability analysis, we perform a likelihood fit in each time bin, using the average model as a starting point. We first attempt a fit leaving the full spectrum of the target source, which is described by a LogParabola, and is free to vary. If the statistics do not allow the fit to converge or results in a non-detection ( $TS<25$ ), we fix all parameters except the target source’s normalization. We consider the target source to be detected when  $TS>10$  in the corresponding bin and the signal-to-noise ratio in that bin is larger than two. For the cases that this was not the case, we report a 95% confidence upper limit. The resulted light curve is presented in the upper panel of Fig. 3.3.

### 3.2.3 Single-dish Observations

Single-dish radio data, contemporaneous to the VLBI observations, were provided by the 40-m telescope of the Owens Valley Radio Observatory (OVRO) at 15 GHz (Richards et al. 2011). The data at 235 GHz were obtained with the 8-element Submillimeter Array (SMA) (Gurwell et al. 2007) for the period 2008–2017.

As shown in Fig. 3.3, where the OVRO, SMA, and *Fermi* light curves are presented, the source was quite active during our monitoring period, and several flaring episodes occurred both at low and high energies. The investigation of possible correlated variability between the considered energy bands is presented in Sect. 3.3.5.

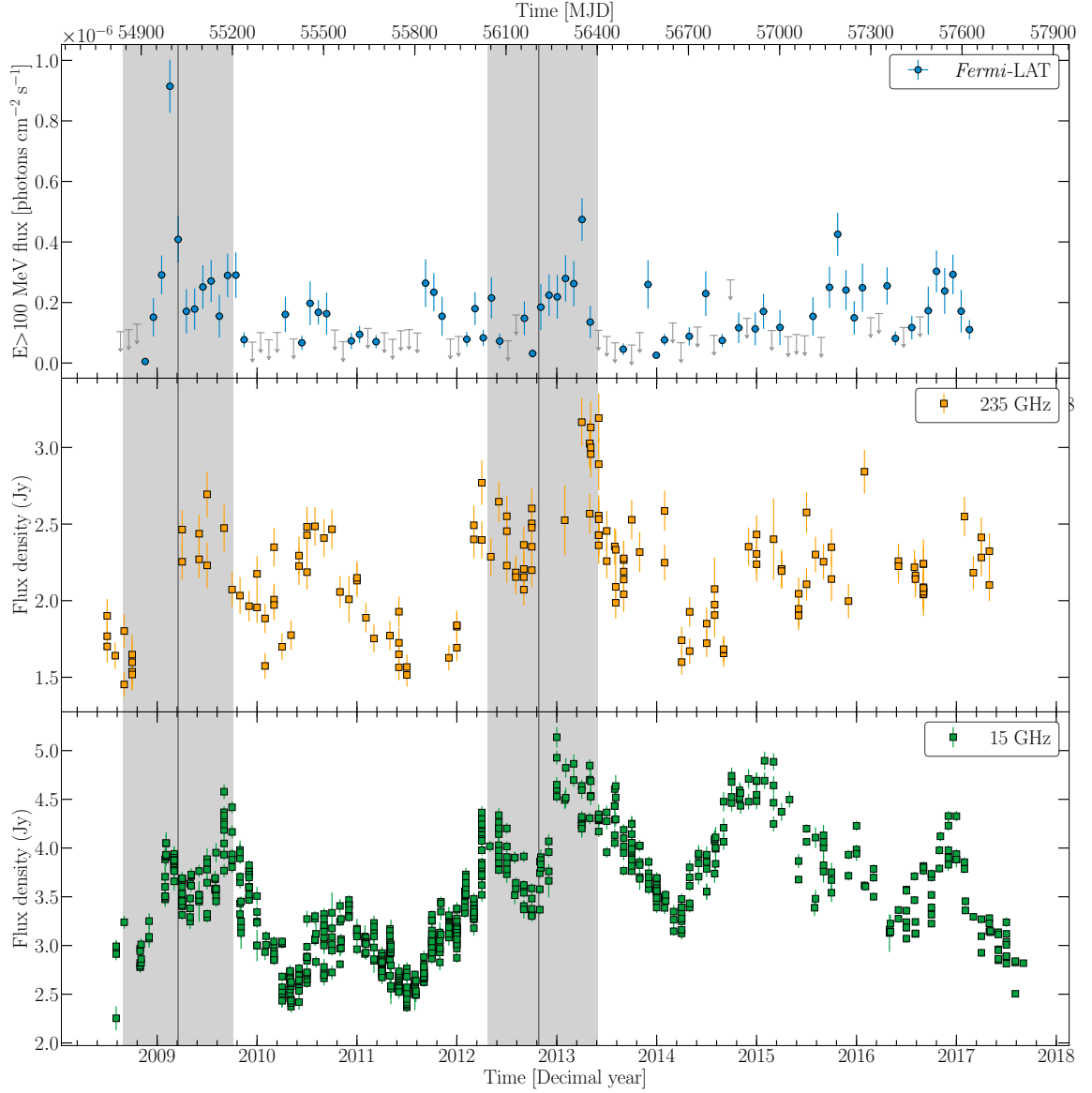


FIGURE 3.3: Light curves of the blazar TXS 2013+370 at different frequencies. From top to bottom: *Fermi*-LAT 0.1 – 300 GeV with 30 days binning, 235 GHz SMA and 15 GHz OVRO light curves, with flux plotted vs. time. The shadowed areas indicate the ejection time range of the new jet components N (see Fig. 3.6) and N1 (see Fig. 3.5) respectively. The vertical lines designate the estimated ejection time, whereas the width of the shadowed areas indicates the uncertainty of this estimation, based on the positional uncertainty of component A1. We adopt for N as ejection time the peak of the 43 GHz core flare, whereas for N1, we take the appearance time from the 22 GHz VLBI image. We set for N and N1 the same ejection time uncertainty as the most well-defined feature C2, owing to lack of data.

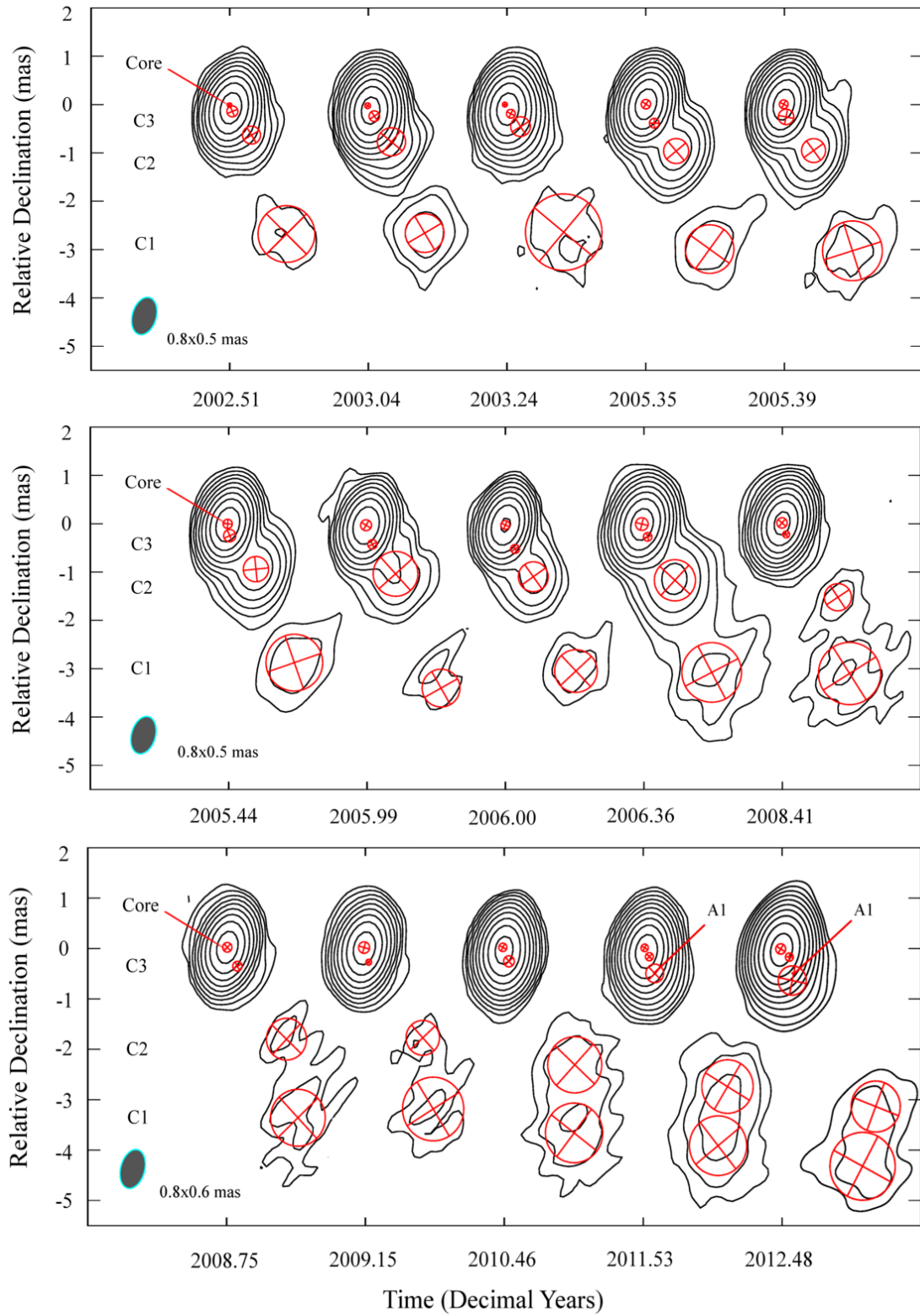


FIGURE 3.4: Modeled images of blazar TXS 2013+370 at 15 GHz. The 2 dimensional circular Gaussian component models the flux density distribution along the jet. The data were imaged under a uniform weighting. The contour levels are set to 0.25, 0.5, 1, 2, 4, 8, 16, 32, and 64% Jy/beam of each image peak flux density (see Table 3.1). All the images are convolved with a common beam of  $0.8 \times 0.5$  mas, oriented at a PA of  $-16^\circ$ . The time corresponding to each image is indicated in the x-axis.



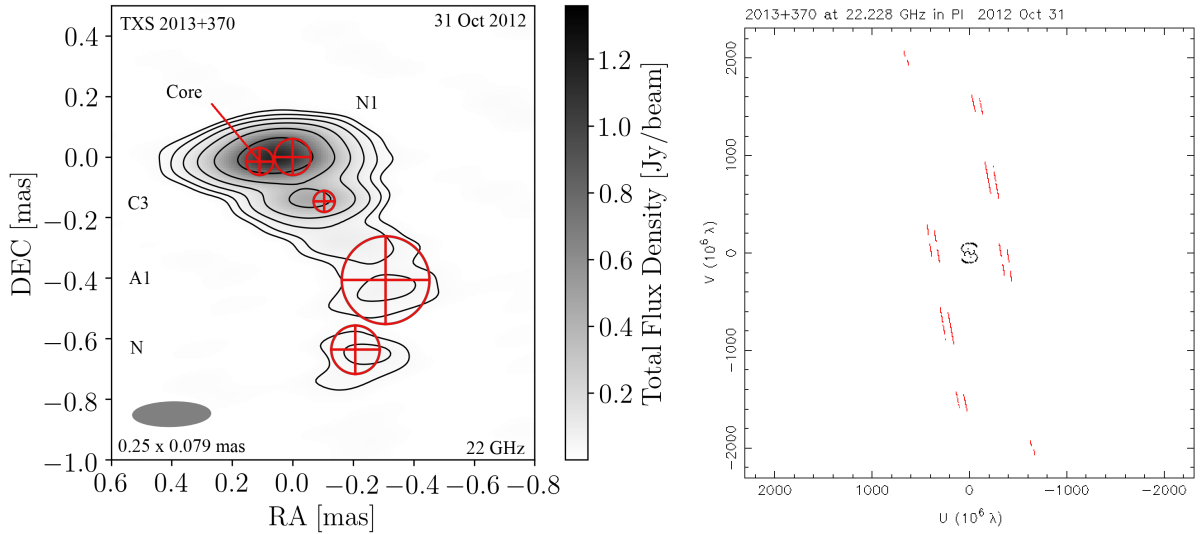


FIGURE 3.5: Left: 22 GHz model-fit and total intensity space-VLBI image of TXS 2013+370, obtained from a combined ground and space-VLBI array. The data were imaged under a uniform weighting. The convolved beam for the displayed image is set to  $0.25 \times 0.08$  mas and it is oriented at a position angle of  $-88.6^\circ$ . The contour levels are set to 2, 4, 8, 16, 32, and 64% of the peak flux density of 1.22 Jy/beam. Right: The uv-coverage of the space-ground baselines. The red data points correspond to ground-space baselines.

### 3.3 Data Analysis and Results

#### 3.3.1 VLBI Imaging and Model-fitting

Frequency and time-averaged data were imported to DIFMAP (Shepherd et al. 1994) for the imaging and Gaussian model-fitting. Before imaging, the visibilities were carefully inspected and spurious data points were flagged. Using the CLEAN algorithm (Högbom 1974) and SELFAL procedures, which are implemented in DIFMAP, we created the radio images of the source. While imaging the ground-based data at 15, 43, and 86 GHz was straightforward thanks to a large number of stations, the imaging of the *RadioAstron* 22 GHz data was more challenging due to the limited uv-coverage. Five stations (including the space telescope) provided useful data (Table 3.1). Robledo 70 m recorded only right-hand circular polarization while the space telescope recorded only left-hand circular polarization at 22 GHz (other telescopes recorded both polarizations), which resulted in no space-ground fringes to Robledo 70 m. The amplitude calibration of the Jodrell Bank Mark II telescope was corrupted for an unknown technical reason. A Gaussian source model derived from the near-in-time 43 GHz data was used to correct the amplitude of Mark II telescope data before producing the image with several iterations of CLEAN and SELFAL.

For all data sets, the jet brightness distribution was then parameterized by fitting two-dimensional Gaussian components to the fully calibrated visibility data by using the MODELFIT algorithm, which is implemented in DIFMAP. The uncertainty in the component positions was set to one-fifth of the beam size if the component's size was smaller than the equivalent circular beam  $b = (b_{\max} b_{\min})^{1/2}$ , otherwise, we assumed one-fifth of the component Full Width at Half Maximum (FWHM) as an estimate of the uncertainty. The uncertainty in the position angle, PA, was calculated based on the positional uncertainty  $\Delta X$  using the trigonometric formula  $\Delta PA = \arctan(\Delta X/r)$ , with  $r$  the radial separation in mas. For

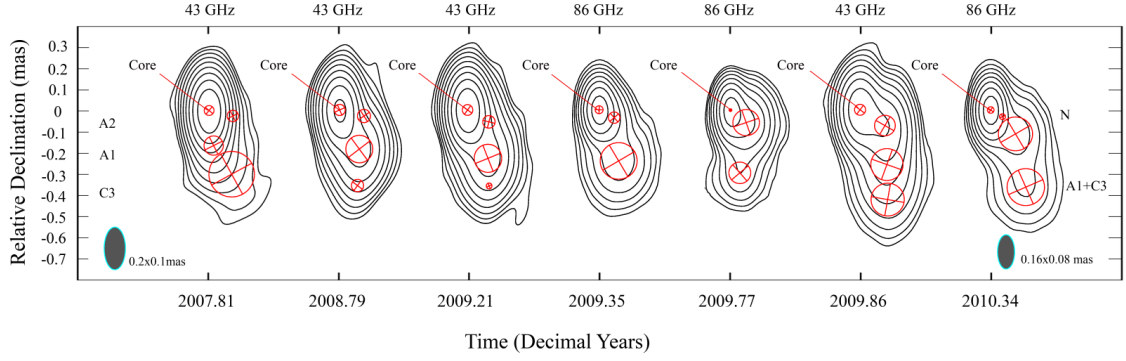


FIGURE 3.6: Model fit images of TXS 2013+370 at 86 and 43 GHz. The data were imaged under a uniform weighting scheme, with all the visibilities to be weighed equally and independently to their uv-distance. The common convolving beam of  $0.2 \times 0.1$  mas, oriented at a PA of  $0^\circ$  was used for the 43 GHz images, whereas the contour levels are set to 0.3, 0.6, 1.2, 2.4, 4.8, 9.6, 19.2, 38.4, and 76.8% of the peak flux density (see Table 3.1). At 86 GHz, images are restored with a beam of  $0.16 \times 0.08$  mas, oriented at a PA of  $0^\circ$ , and the contour levels are set to 0.5, 1, 2, 4, 8, 16, 32, and 64% of the peak flux density (see Table 3.1). The two beams are showed on the left and right respectively.

the component flux density and FWHM, we adopt an uncertainty of 10%, following [Lister et al. \(2009b, 2013\)](#) and [Karamanavis et al. \(2016\)](#) respectively. The resulting images are shown in Fig. 3.4, 3.5, 3.6, while the parameters of the Gaussian components are reported in Tables A.2, A.3, A.4, and A.5.

Since the source is located very close to the Galactic plane, where the column density of the interstellar medium is relatively high, there is the possibility that the images are affected by interstellar scattering. In order to verify the impact of scattering in TXS 2013+370, we investigated two possible observational effects that could be introduced by scattering: i) angular broadening and ii) fast flux density variations. By analyzing the dependence of the angular size with frequency and based on the variability properties inferred from Effelsberg monitoring at 5 GHz, we conclude that none of these effects play a dominant role at the frequencies considered in our study. The detailed analysis is presented in Appendix A.1.

### 3.3.2 Source Structure and Jet Kinematics

Our imaging at 15, 22, 43, and 86 GHz shows that TXS 2013+370 features a bright core and a bent jet extending to 5 mas at the lowest frequency. We determined the kinematics of the individual jet features using the parameters of the Gaussian components derived from the model fits of each data set. The component cross-identification between the observing epochs (and frequencies) was done by comparing their positions, flux densities, and sizes. The angular proper motion  $\mu$  of the components was computed through linear fits of their radial core separation as a function of time. The apparent speed  $\beta_{\text{app}}$  is related to  $\mu$  and the intrinsic speed  $\beta$  as ([Urry & Padovani 1995](#); [Rees 1966](#))

$$\beta_{\text{app}} = \frac{\beta \sin \theta}{1 - \beta \cos \theta} = \frac{\mu D_L}{c(1+z)}, \quad (3.1)$$

where  $\theta$  is the viewing angle of the jet,  $\mu$  is the proper motion in  $\text{rad s}^{-1}$ ,  $D_L$  is the luminosity distance in m,  $z$  the source redshift and  $c$  is the speed of light in  $\text{m s}^{-1}$ .



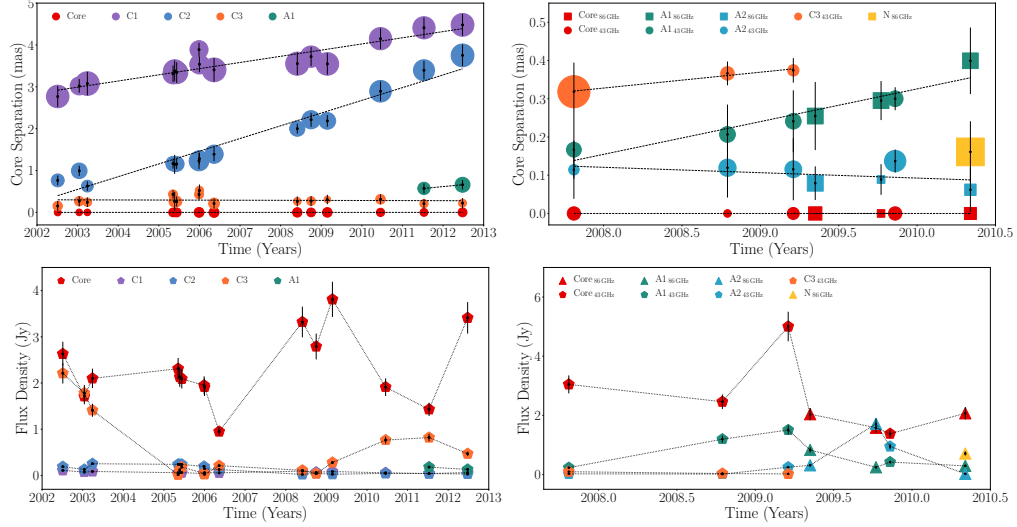


FIGURE 3.7: Time evolution of the core distance (top panels) and flux density (bottom panels) of model-fit components at 15 GHz (left panels) and at 43 and 86 GHz (right panels). In the top panels, the size of the data points is set to  $\sim 1/2$  of the Gaussian components size. Note here that the time range of 15 and 43-86 GHz data is different. The flux density of the core component showed a maximum in early 2009 at all frequencies. Based on the observational data, in this time range a new component emerges from the core. This new knot seems to "light up" component C3 on its passage, increasing the flux density of the latter.

**15 GHz:** Figure 3.4 presents the 15 GHz contour images with super-imposed circular Gaussian model-fit components, while the parameters of each component are listed in Table A.2.

At this frequency, the source is well modeled by four circular Gaussian components, a core component (labeled as Core) and three jet features (C3, C2, C1), numbered in order of decreasing distance from the core. During the observing interval 2002-2012, component C3 appears quasi-stationary (Lind & Blandford 1985), oscillating around an average distance of  $r \sim 0.2$  mas from the center (Fig. 3.7, top-left panel). Numerous studies have shown that when a moving shock passes through a stationary knot, the latter could be displaced in position for a short time and then return to its initial position (see Rani et al. 2015, and references therein). Component C3 seems to exhibit such behavior. The features C2 and C1 are, instead, moving components, separating from the core with apparent superluminal speed (see Table 3.2). From our kinematic analysis, we infer that C2 is the fastest component of the jet, moving with an apparent speed of  $\beta_{\text{app}} = 13.8 \pm 0.9$ . We note that a quadratic fit was performed by Lister et al. (2016) to describe the motion of C2. Their speed ( $\beta_{\text{app}} = 14.51 \pm 0.24$ ) is consistent with our result within the measurement uncertainty. Component C1 is the second fastest feature of the jet, moving at a speed of  $\beta_{\text{app}} = 7.0 \pm 0.8$ . We also note that a new component, labeled A1, becomes visible at 15 GHz in the last two VLBI epochs (after 2011.53), downstream of C3. See the last two images in Fig. 3.4, and the component separation as a function of time in Fig. 3.7 (top left panel). The observation of A1 in only two epochs limits the accuracy of its speed determination. Based on the 15 GHz data points, we obtain an apparent speed of  $\beta_{\text{app}} = 4.2 \pm 11.7$ , which is in agreement with the value derived for the same component at 43 and 86 GHz (see below).

**22 GHz:** Figure 3.5 shows the 22 GHz image of the inner jet region of TXS 2013+370, as observed by space-VLBI with *RadioAstron* (details in Sokolovsky 2014). The image

shows a core, which is elongated in the East-West direction and along the major axis of the elliptical observing beam. The jet appears to be propagating towards a South-West direction, with a slight curvature towards the southern direction beyond  $r = 0.4$  mas. The overall morphology of the VLBI structure is in good agreement with the 43 and 86 GHz images (Fig. 3.6). Two components can model the central region, the core and a new feature, labeled as N1 (the second grey area in Fig. 3.5). The appearance and the propagation of N1 probably is connected with the close-in-time increased activity seen in the radio and  $\gamma$ -ray bands (see Fig. 3.3). Further downstream, three additional Gaussian components represent the jet. Based on their core separation and flux density, we identify these features with the components C3 and A1 at 15 GHz, and with component N at 86 GHz (see below).

**43 & 86 GHz:** Figure 3.6 shows the model-fit images of the source at high radio frequencies. Only the most compact regions in the inner jet are visible. The source structure can be modeled by a compact core and three jet components, the innermost of which, A2, is not visible at lower frequencies. The core separation of each component as a function of time is shown in Fig. 3.7 (top-right panel), while the component parameters are reported in Tables A.4 and A.5. Component A2, located at  $r \sim 0.1$  mas from the core, appears to be quasi-stationary, showing some backward motion after 2009, probably due to the passage of a newly ejected feature, N, which becomes well separated from A2 in the final epoch at 86 GHz. The appearance of N followed a strong increase (by a factor of  $\sim 2$ ) of the core flux density, observed in March 2009 at 43 GHz (Fig. 3.7, bottom-right panel). At around this time, a prominent  $\gamma$ -ray flare was also observed by *Fermi*-LAT (see Fig. 3.3). Further downstream, component A1, which is resolved at 15 GHz only after 2011, moves with an apparent speed  $\beta_{\text{app}} = 4.0 \pm 0.7$ . The motion of the outermost component, C3, is not well constrained at 86 GHz, since in the region occupied by C3 the jet becomes faint and partially resolved, and after 2009 there is a possible blending between C3 and A1. However, the 43 GHz data show a well defined C3 component in the first three epochs, from which we infer a proper motion  $\mu = (0.07 \pm 0.02)$  mas/yr, which corresponds to an apparent speed of  $\beta_{\text{app}} = 3.3 \pm 1.1$ . This result is comparable to the speed of the nearest upstream component A1. As discussed above, C3 appears quasi-stationary in the long 15 GHz monitoring, therefore the small displacement observed at 43 GHz in the short time is likely associated with flowing plasma crossing C3 at that time.

In summary, the source TXS 2013+370 shows a bent jet, curving from an east-western to a southern orientation. The VLBI core is much more variable in flux density than the jet components. These move at apparent superluminal speeds of  $\sim (3-14)c$ , indicating highly relativistic motion of the jet plasma. Near the core, stationary components, as well as newly ejected features, are observed. The ejection times for several jet components could be estimated and are reported in Table 3.2. A discussion of possible reasons for the wide range of apparent speeds and on the implications for the jet intrinsic parameters (e.g., Lorentz factor and viewing angle) is reported in Sect. 3.4.1.

### 3.3.3 Location of the Jet Apex

In this section, we aim to constrain the location of the jet apex with respect to the VLBI core. Such an estimate can be obtained through an analysis of the frequency-dependent shift of the VLBI core position, caused, in the simplest scenario, by synchrotron opacity and self-absorption. In the case of TXS 2013+370, however, this approach cannot be used directly, since a formal 2-D cross-correlation using close-in-time pairs of images at 15 GHz, 43 GHz, and 86 GHz, yielded no measurable shifts. As we will discuss in Sec. 3.4 based on

TABLE 3.2: Kinematic parameters of all identified components at 15, 43, and 86 GHz. Columns from left to right: (1) Component ID, (2) Observing frequency, (3) Proper motion, (4) Apparent speed (5) Ejection time

Knot	Freq. (GHz)	$\mu$ (mas/year)	$\beta_{\text{app}}$ ( $c$ )	$t_{\text{ej}}$ (year)
A1	15	$0.09 \pm 0.20$	$4.2 \pm 11.7$	$2005.27 \pm 1.20$
C3	15	-	-	quasi-stationary
C2	15	$0.30 \pm 0.02$	$13.9 \pm 0.9$	$2001.08 \pm 0.55$
C1	15	$0.15 \pm 0.02$	$7.0 \pm 0.8$	$1982.72 \pm 0.49$
A2	43/86	-	-	quasi-stationary
A1	43/86	$0.09 \pm 0.01$	$4.2 \pm 0.5$	$2006.14 \pm 0.22$
C3	43/86	$0.07 \pm 0.02$	$3.3 \pm 1.1$	1997–2003

the variability time lags, the core shift is indeed much smaller than our resolution limits in the considered frequency regime.

In order to obtain an estimate of the jet apex location with respect to the VLBI core, we then follow a geometrical approach based on the investigation of the transverse jet expansion profile. At each frequency, we convolved all images with the average equivalent circular beam (0.08 mas at 86 GHz, 0.16 mas at 43 GHz, and 0.75 mas at 15 GHz) and created stacked images. We have not considered the 22 GHz *RadioAstron* data since there is only one epoch available. We then measured the jet width as a function of core separation in stacked images. This was done by slicing the jet pixel-by-pixel in the direction perpendicular to the jet axis, and by fitting single Gaussian profiles to the transverse intensity distribution to infer the jet width. For the error of the jet width, we used one-tenth of the convolved FWHM.

The expansion profile is presented in Fig. 3.8, top panel. Distances along the x-axis are relative to the position of the VLBI core, which we assume as being fixed, due to the negligible core-shift. The de-convolved FWHM values inferred for the inner jet region based on the 86 and 43 GHz data smoothly connect to those inferred at 15 GHz for the outer regions. By fitting a power-law of the form  $d = ar^b$  to the 15 GHz data at distances between  $\sim 0.4$  and  $\sim 3$  mas from the core, we infer that the jet has a conical shape ( $d \propto r^{(1.02 \pm 0.01)}$ ). However, this power law does not describe well the higher frequency data, as in the inner jet we observe a flattening of the expansion profile. By fitting a power law of the same form to the 43 GHz and 86 GHz data, we obtain  $d \propto r^{(0.49 \pm 0.04)}$ , i.e., the jet has a parabolic shape in the proximity of the black hole. This is expected based on theoretical models for jet formation (e.g., Meier et al. 2001, and references therein), which predict the jet to be actively collimating and accelerating at its onset. While we have not considered in the fit the 15 GHz data relative to the inner jet, the lower resolution data points also lie on the same profile. The fact that the jet is collimating on the scales probed by mm-VLBI is also evident by examining the evolution of the apparent opening angle with distance (Fig. 3.8, bottom panel). The angle decreases in the inner  $\sim 0.5$  mas, and then reaches a roughly constant value of  $\sim 23^\circ$  on the scales probed at 15 GHz, until the recollimation region at a distance of  $\sim 4$  mas. As observed in other more nearby jets like M 87 (Asada & Nakamura 2012) or Cygnus A (Boccardi et al. 2016), for which higher spatial resolution is achieved, a single parabolic profile describes the expansion of the jet from its onset up to the parsec scales. Therefore, we take the inferred expansion law to back-extrapolate the location of the jet apex, which should have an approximately zero width, with respect to the 86 GHz core. Such a method has been applied in literature before (Agudo et al. 2011; Karamanavis

et al. 2016), considering the core size as a reference and then assuming a conical expansion between the black hole and the core. Similarly, we can compute the distance  $R$  it takes for the jet to reach the width of the core, assuming the inferred parabolic expansion rate. Based on the analysis of the stacked image at 86 GHz, the jet width at the location of the emission peak is  $d_c \leq (0.04 \pm 0.01)$  mas, from which we infer that the jet apex is located at a distance of  $R \leq ((0.019 \pm 0.009)/\sin \theta)$  mas, or  $((0.146 \pm 0.07)/\sin \theta)$  pc upstream, where  $\theta$  is the viewing angle of the jet.

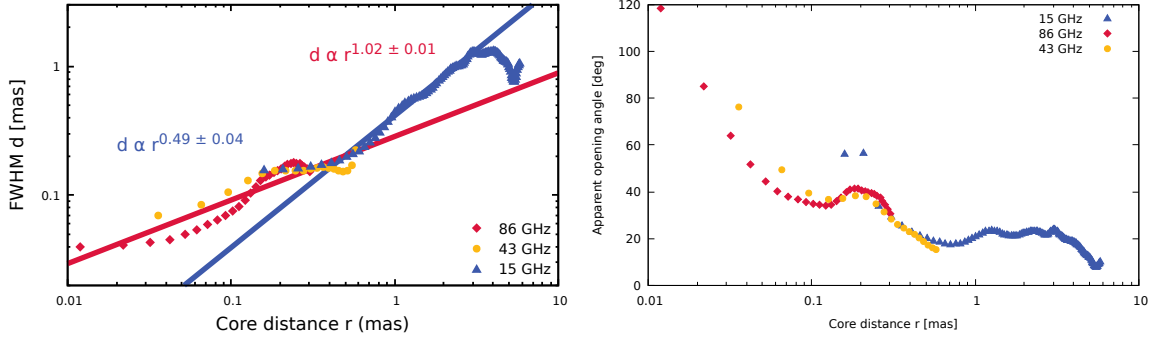


FIGURE 3.8: Left: Transverse expansion profile of the jet in TXS 2013+370, based on 86 GHz, 43 GHz, and 15 GHz data. Uncertainties are set equal to one-tenth of the convolved FWHM, but are not displayed in the plot for clarity. The jet follows a parabolic-shaped flow in the innermost regions, which is changing in a conical on larger scales. The transition occurs at a projected distance of  $\sim 0.5$  mas from the central engine. Right: Apparent opening angle as a function of distance from the core.

### 3.3.4 Spectral Evolution and Turnover Frequency

An important parameter which defines a jet (or specific regions of the jet), is the knowledge of the turnover frequency, the frequency which the relativistic plasma outflow becomes optically thin to radio waves. As we discuss in Section 1.3.1.1, the radio spectrum of blazars can be modeled by a power-law of the form  $S \propto \nu^\alpha$ , where  $S$  is the observed flux density and  $\alpha$  the spectral index. For this analysis we adopt a model of the jet emission as described in Blandford & Königl (1979). The fundamental assumptions of this model are i) that the magnetic field energy and the kinetic energy of the jet are in equipartition, ii) that a standard spectral index best describes the optically-thin part of the outflow. By setting these constraints, we can compute the turnover frequency and the expected flux density by fitting a spectral model of the form (Türler et al. 2000)

$$S_\nu = S_m \left( \frac{\nu}{\nu_m} \right)^{\alpha_t} \frac{1 - \exp[-\tau_m(\nu/\nu_m)^{\alpha-\alpha_t}]}{1 - \exp(-\tau_m)} \quad [\text{Jy}], \quad (3.2)$$

where  $S_\nu$  is the observed flux density in Jy,  $\nu_m$  is the turnover frequency in GHz,  $S_m$  is the turnover flux density in Jy,  $\tau_m \sim 3/2 \left[ (1 - (8\alpha/3\alpha_t))^{1/2} - 1 \right]$  is the optical depth at  $\nu_m$ ,  $\alpha_t$  is the spectral index of the optically thick part of the emission, and  $\alpha$  is the optically-thin spectral index.

Publicly available flux density observations of the source from the NRAO archive from 4.8 to 43 GHz allowed us to study the spectral evolution of the jet. Evidence of a self-absorbed synchrotron spectrum (SSA) featuring a spectral break at the turnover frequency and flux density was visible in all frequencies. The observations were conducted by the

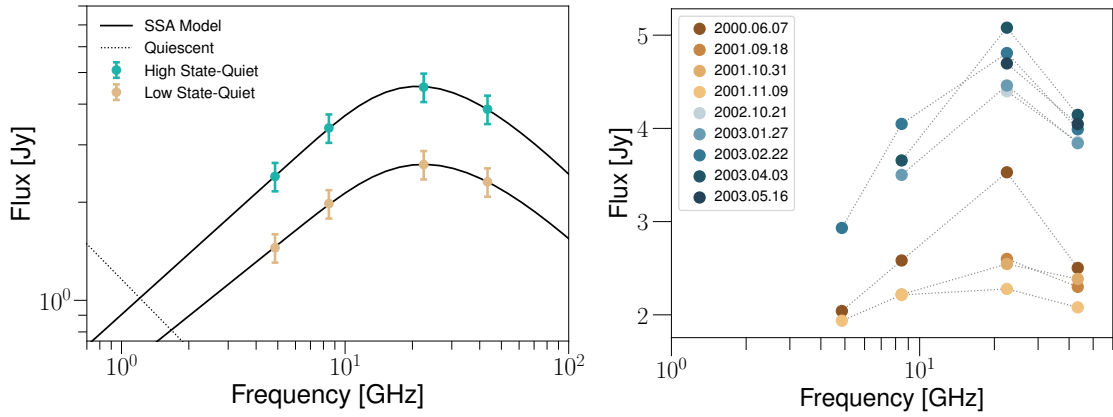


FIGURE 3.9: Data set and results of the SSA spectral fitting. Left: The dotted line represents the quiescent spectrum, whereas the data points are after of its subtraction. Right: The simultaneous snapshot-measurements of TXS 2013+370 with the VLA Array. In this plot is presented the flux density level versus frequency during the period 2000-2003. We set the errors of flux density 10% of the measured value, but are not displayed in the plot for illustration purposes.

Karl G. Jansky Very Large Array (VLA), Socorro, New Mexico during the period 2000-2003. The averaged data are presented in Fig. 3.9. In order to calculate the turnover frequency, we separated the data that corresponded to a high flux density level (from 4 to 5 Jy) from the rest (from 2 to 3.5 Jy), and we calculated the average flux density among them. We fit the data using the model of Eq. (3.2), which was applied in both cases. During a flare, the obtained spectrum comprises by the superposition of a steady state (quiescent) spectrum of the jet and the spectrum of the disturbance which is traveling down the jet, and is responsible for the flare. In order to estimate and subtract the quiescent spectrum of the TXS 2013+370 emission, we used low-frequency archival data from the NRAO archive. The source observed from the VLA at 1.4 GHz, and found to exhibit a flux density of  $S = 1.25 \pm 0.12$  Jy during the period 1998-2000. We identified the quiet state with the minimum flux density for the light-curve, and we fit the value with a power-law  $S_q = b\nu^\alpha$ , where  $\alpha$  is the optically thin spectral index, fixed to the canonical value -0.7. The fitting process result that  $b = 1.6 \pm 0.16$ , whereas the flux density  $S_q$ , considered to be a representative value for the quiescent flux density. The uncertainties of the remaining flaring spectrum were calculated by error propagation, taking into account a 15% error due to  $(u, v)$ -coverage difference (Fromm et al. 2013b).

During the fitting process we allowed both spectral indices,  $\alpha_t$  and  $\alpha$  to vary. Thus, the spectral turnover for the non flaring state occurs at  $\nu_m = (21 \pm 4)$  GHz with the flux density of  $S_m = (2.6 \pm 0.9)$  Jy, the optically thin spectral index  $\alpha = -0.71 \pm 0.14$  whereas the optically thick  $\alpha_t = 0.55 \pm 0.10$ . The same parameters during the flaring state were  $\nu_m = (20 \pm 3)$  Jy,  $S_m = (4.5 \pm 0.7)$  GHz,  $\alpha = -0.75 \pm 0.15$  and  $\alpha_t = 0.61 \pm 0.11$ . Figure 3.9 shows the result of the spectral fitting graphically.

The obtained optically thin spectrum at  $\alpha \sim -0.7$  in both cases is in agreement with the typical observed value in AGN (Verschuur & Kellermann 1988). A uniform slab-shaped magnetized cloud with a power-law energy distribution of synchrotron-emitting electrons will have  $\alpha_t = 5/2$  and  $\alpha$  directly related to the slope of the electron energy spectrum (Pacholczyk 1970). The optically thick spectral index at  $\sim 0.5$  is an indication that the flaring component is inhomogeneous, and the flux density increase is caused by the ejection

of more than one component (Aloy et al. 2003). Luckily, the aforementioned flaring event, based on our kinematic analysis, coincides with the appearance of knot C2. This special occasion provides us the opportunity to study the evolution of the flare. The turnover point that corresponds to the whole jet spectrum or a specific region is time depended. The observational signature of a propagating shock during time has been extensively studied in the past years (Türler 2011; Daly & Marscher 1988; Marscher & Gear 1985; van der Laan 1966). One of the most widely accepted theoretical models that describe the spectral changes of a propagating shock front in a relativistic jet introduces is the "shock-in-jet" model. Figure 3.10 illustrates the basic concept of this scenario. When a shock is traveling downstream of the jet, the electrons that were crossing the shock front are accelerated, emitting synchrotron radiation at the backside of the shock front. The emission spectrum is changing through time, as different emission-loss mechanisms are taking place. In the beginning, the energy loss occurs via inverse Compton process. At this stage, we observe that the peak emission frequency decreases, while the peak flux density rises. At the moment that the photon energy density becomes equal to the magnetic energy density, the bulk energy decreases due to synchrotron process. Observationally, this translates to the shifting of the spectral peak from high to lower frequency, whereas the flux density remains at the same level. Ultimately, a shock at the last stage of its evolution, is expanding adiabatically and this mechanism dominates the energy losses. At this stage, both the turnover frequency and flux density decrease with time. The slope of the optically thin branch of the spectrum appears to be steeper at the first two than the last phase. The evolution stage of the shock wave is imprinted in the frequency that the peak of flare flux density appears.

Here, in the case of the flare mentioned above of TXS 2013+370, we witnessed that during the flare, the shift of the turnover frequency was almost negligible ( $\Delta\nu_m = 0.7$  GHz). This behavior doesn't fit in the discussed model. A possible explanation for this phenomenon is the relativistic nature of the emitted photons. Observed flux density is proportional to the emitted flux, boosted by a factor  $S_{\text{obs}} = \delta^{2-\alpha}$ . Changes that alter the Doppler factor are achromatic, thus can cause an achromatic flare. A component that moves along a bend jet cools down, but following a curved trajectory can be passed from a position with a small viewing angle with respect to the line of sight, which will increase the Doppler boosting and the observed flux density. However, this is the case only when the spectral index is constant over all frequencies considered. When there is a spectral feature like a turnover, the frequency could increase too with the Doppler factor, which implies an underlined chromatic effect.

### 3.3.5 Multi-band Variability

#### 3.3.5.1 Discrete correlation function analysis

The combination of the  $\gamma$ -ray activity of TXS 2013+370 together with contemporaneous radio flux variability observations provide us with the unique opportunity to search for any correlated activity between them. One suitable statistical method that can deal with unevenly sampled data is the Discrete Cross-Correlation Function (DCCF), suggested by Edelson & Krolik (1988). The basis of the DCCF is the cross-correlation function (CCF), which is a standard method of estimating the degree to which two evenly sampled data series  $x_t$  and  $y_t$  are correlated, as well as any possible time lag. The CCF is defined by



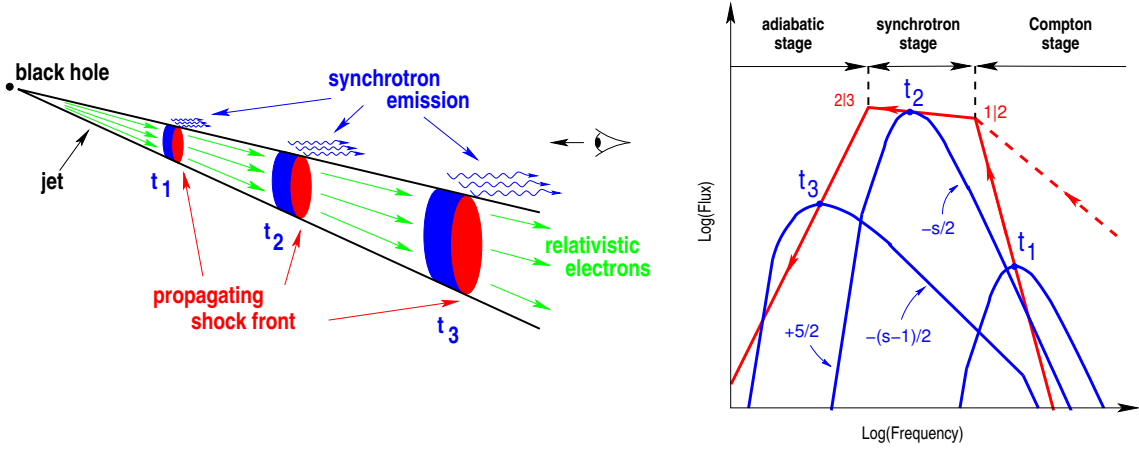


FIGURE 3.10: The three-stage spectral evolution model for a shock which is propagating in a relativistic outflow. Credits: [Türler \(2011\)](#).

$$CCF_l = \sum_{N=1}^{t=1} = \frac{(x_t - \bar{x})(y_{t+1} - \bar{y})}{N\sigma_{x,l}\sigma_{y,m}} \quad (3.3)$$

where  $l = [0, \pm 1, \pm 2 \dots (N-1)]$  the possible time lag,  $\sigma_{x,l}\sigma_{y,m}$  are the standard deviation and  $\bar{x}, \bar{y}$  are the mean values of the two time series. However, astronomical data are mostly unevenly sampled. For that reason, for a data series  $x_i, y_j$  utilizes the unbinned cross-correlation function (UCCF), described as

$$UDCF_{i,j} = \frac{(x_i - \bar{x})(y_j - \bar{y})}{\sigma_x \sigma_y} \quad (3.4)$$

where  $\sigma_x \sigma_y$  are the the standard deviation of the  $x_i, y_j$  data series. From this analysis, the obtained  $UDCF_{i,j}$  is calculated for each possible pair of time lag,  $\Delta t_{i,j} = t_{y,j} - t_{x,i}$ . Averaging the UCCF in time lag bins constrains the DCCF. Positive DCCF values exhibit correlated variability, whereas negative values correspond to anti-correlated, with an average time lag  $l$ . The final step of this analysis is the characterization of its significance. The significance of the estimated DCCF peak was calculated by following the method of [Emmanoulopoulos et al. \(2013\)](#) and [Connolly \(2015\)](#). Specifically, we simulated a total of 5000 light curves. The simulated data are then correlated with the observed radio data at 235 GHz and 15 GHz bands to calculate the 99% confidence levels. For the case of TXS 2013+370, a correlation is found between the  $\gamma$ -rays and the 235 GHz light curves, with the radio following the high energy activity by  $(45 \pm 30)$  days. A strong correlation is found also between 235 and 15 GHz showing a time lag of  $(15 \pm 15)$  days (see Fig. 3.11). The confidence level of this correlation exceeds 99%. The correlation between 15 GHz, and  $\gamma$ -rays exceeds the 95% significance level with a delay of  $(45 \pm 30)$  days, which is above the  $2\sigma$  statistical threshold.

### 3.3.5.2 Spearman's Rho Test

In order to confirm the degree of correlation, we perform a Spearman's correlation test ([Spearman 1904](#)) additionally. The Spearman's rho correlation coefficient ( $\rho$ ), is a statistical

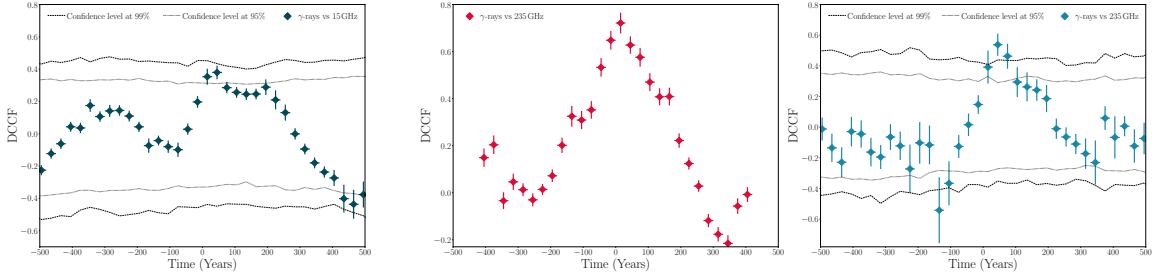


FIGURE 3.11: DCCF results between the  $\gamma$ -ray and 15 GHz light curve (left), 15-235 GHz (middle) and  $\gamma$ -rays-235 GHz (right). The dotted lines represent the  $2\sigma$  significance level of the correlations, whereas the dashed line the  $3\sigma$  level.

measure of the strength of a monotonic relationship between paired data, which in this case corresponds to the differences between the fluxes of the light-curves and is expressed as

$$\rho = 1 - \frac{6 \sum D_i^2}{n^3 - n} \quad (3.5)$$

where  $D_i = r_x - r_y$ , with  $r_x$ ,  $r_y$  to stand for ranks of corresponding variables (in our case the difference between the fluxes), and  $n$  is the number of observations. The value  $\rho = 1$  corresponds to a perfect positive correlation, whereas  $\rho = -1$  indicates an anti-correlation. For the case of TXS 2013+370, we used two light-curves at a time, assuming as a reference the delayed one, as established by the DCCF analysis. Hence, we shifted the other data set from 0 to 200 days with a step of 1 day and taking into account a coherence time of 2 days. For each iteration, we calculated the P-value to validate the significance of this statistical hypothesis. We performed this procedure in pairs, for  $\gamma$ -rays-235 GHz,  $\gamma$ -rays-15 GHz and 15 GHz-235 GHz. Uncertainties in the time-lag estimation have been set equal to the data sampling interval. The time lag between  $\gamma$ -rays-15 GHz was calculated based on the Spearman's Rho results of the other two data sets. The obtained time lag between  $\gamma$ -rays-15 GHz is  $(56 \pm 30)$  days with P-value= $1.5 \times 10^{-3}$ , for  $\gamma$ -rays-235 GHz  $(52 \pm 30)$  days with P-value= $2.1 \times 10^{-4}$  whereas the time lag between 235 and 15 GHz found to be  $(11 \pm 6)$  days with P-value= $9.5 \times 10^{-9}$ . As a sanity check, we searched for correlated activity between the 15 GHz data set and itself. The results was, as expected,  $\rho=0.997$  with P-value=0 at 0 days shift. Both methods, the DCCF and the Spearman's rho test, showed that the high energy emission leads the activity with respect to the radio band. This indicates that the high energy event occurred in a region that is opaque to radio waves (Fuhrmann et al. 2014; Pushkarev et al. 2010). The results of the DCCF analysis and the Spearman's Rho test are presented in Table 3.3 and in Fig. 3.11.

Overall, both methods, the DCCF and the Spearman's rho test, showed that the high energy emission leads the activity with respect to the radio band. In the following analysis, we use as the mean time lag that has been obtained by the two methods. Thus, we consider that the  $\gamma$ -rays variability is ahead of 235 GHz by  $(49 \pm 30)$  days. The 15 GHz data lag behind by another  $(13 \pm 11)$  days (relative to the 235 GHz data), while the lag between 15 GHz and  $\gamma$ -rays is  $(51 \pm 30)$  days (see column 4 in Table 3.3).



TABLE 3.3: DCCF, Spearmans rho test results and linear distance between  $\gamma$ -ray and VLBI core. Columns from left to right: (1) Data set pair, (2) Time lag estimation from DCCF, (3) Significance level of the DCCF results, (4) Time lag estimation from the Spearman's Rho test, (5) P-Value, (6) Mean time lag

. The uncertainty in the mean time lag was set equal with the data sampling.

Data set	DCCF Time lag (days)	Significance Level %	Spearman's Rho Time lag (days)	P-Value	Mean Time lag (days)
$\gamma - 15$	$45 \pm 30$	95	$56 \pm 30$	$1.5 \times 10^{-3}$	$51 \pm 30$
$\gamma - 235$	$45 \pm 30$	99	$52 \pm 30$	$2.1 \times 10^{-4}$	$49 \pm 30$
$235 - 15$	$15 \pm 15$	99	$11 \pm 6$	$9.5 \times 10^{-9}$	$13 \pm 11$

## 3.4 Discussion

### 3.4.1 Intrinsic Jet Parameters

The range of apparent speeds found in TXS 2013+370, with values ranging from moderate ( $\beta_{\text{app}} \sim 3$ ) to high ( $\beta_{\text{app}} \sim 14$ , see Table 3.2), is quite common among extragalactic jets (e.g., Fromm et al. 2013a; Rani et al. 2015; Karamanavis et al. 2016; Jorstad et al. 2017) and could result from several effects. The VLBI images show a jet bending from west to south at a distance of 0.1-0.2 mas from the core, and then again towards west on the scales probed at 15 GHz. Therefore a first hypothesis is that the apparent speed variations are geometry-dependent, with the apparent speed increasing when the jet points closer to the line of sight. By considering the position angles of the moving components in Tables A.2, A.4, A.5, there is indeed an indication that the slowest features are those moving towards south (A1, C3), while the highest speed is observed for C2, which follows a trajectory towards west and south-west. Another possibility is that the Lorentz factor is not constant along the jet, but increases as a function of distance. This hypothesis is supported by the observation of active jet collimation in the inner 0.5 mas of the jet (see Sect. 3.3.3), indicating that the terminal Lorentz factor is not yet reached on the scales probed by mm-VLBI, where the slowest apparent speeds are measured. Ultimately, it is likely that both geometrical effects and intrinsic variations of the bulk speed cause the observation of this wide range of apparent speeds in TXS 2013+370.

Based on this premise and the results of the kinematic analysis, in the following we estimate some of the intrinsic jet parameters. The observation of a maximum speed of  $\sim 13.9c$  for C2 implies that at a distance of  $\sim 1$ -2 mas from the core the flow has a minimum Lorentz factor  $\Gamma_{\text{min}} = 14.0 \pm 0.8$ , since  $\Gamma_{\text{min}}$  is expressed as

$$\Gamma_{\text{min}} = (\beta_{\text{app}}^2 + 1)^{1/2}. \quad (3.6)$$

The viewing angle that maximizes the apparent speed for a given Lorentz-factor is called the critical viewing angle  $\theta_c$

$$\theta_c = \sin^{-1}(1/\Gamma_{\text{min}}). \quad (3.7)$$

For C2 we obtain  $\theta_c = (4.1 \pm 0.2)^\circ$ . The critical viewing angle of the fastest moving component is often assumed in the literature to be equal to the characteristic jet viewing

angle (e.g., Vermeulen & Cohen 1994; Lister & Marscher 1997; Cohen et al. 2007). This angle could vary along the jet and be larger for those regions of the jet which are pointing towards south, and for which the slower speeds are measured (e.g.,  $\theta_c \simeq 16^\circ$  for components A1 & C3). However, for this paper we are mostly interested in the viewing angle of the inner jet and of the core region, where the plasma moves in a direction similar to C2. Therefore, we will adopt this viewing angle value in the following for the deprojection.

Concerning the bulk Lorentz factors, the high apparent speed measured for C2 indicates that the plasma is fast and highly boosted in the regions probed at 15 GHz ( $\Gamma > 14$ ). On the other hand, the low apparent speeds and the increase of the jet opening angle towards the jet apex suggests that the Lorentz factor is lower in the vicinity of the core than further downstream. For a jet orientation at  $\theta_c = (4.1 \pm 0.2)^\circ$  and the observed low apparent speed of A1 ( $\beta_{\text{app}} \sim 4.2$ ) we can estimate the jet Lorentz-factor to be of the order of 6 in the regions probed by millimeter VLBI. This also implies that the Doppler factor  $\delta = 1/(\gamma \cdot (1 - \beta \cos \theta))$  in the core region is not very large ( $\delta \leq 10$ ), which is in good agreement with the moderate variability of the source.

Having measured the opening angle and the Lorentz factor at different locations along the jet, we can also test how are these two quantities related to each other. Based on hydrodynamical (Blandford & Königl 1979) and magneto-hydrodynamical models (Komissarov et al. 2007) we expect the Lorentz factor  $\Gamma$  and the intrinsic jet opening angle  $\phi$  to be inversely proportional, with  $\Gamma\phi < 1$  for a causally connected jet. This is consistent with our results. In the outer jet, the constant apparent opening angle of  $\sim 23^\circ$  implies an intrinsic full opening angle  $\phi \sim 1.6^\circ$ , thus the product  $\Gamma\phi$  yields  $\sim 0.4$  rad for  $\Gamma = 14$ . In the inner jet, speeds should be lower, as discussed, and the opening angle is larger. Assuming as a reference an apparent opening angle of  $\sim 40^\circ$ , measured at distances of  $0.1 - 0.3$  mas from the core (Fig. 6, bottom panel), and  $\Gamma = 6$  as estimated above for the jet base, we obtain  $\Gamma\phi \sim 0.30$  rad. Both products in the two regions are in good agreement with the median value obtained for the MOJAVE sample,  $\Gamma\phi = 0.35$  rad (Pushkarev et al. 2017), as well as with the results of a statistical modeling considering the same population (Clausen-Brown et al. 2013)<sup>3</sup>.

### 3.4.2 Location of the Gamma-ray Emission

In Section 3.3, we investigated the existence of correlations between the variability observed in the radio band (15 GHz and 235 GHz) and the  $\gamma$ -ray band, and we derived time lags indicating that the high-energy activity leads the one in radio (see Table 3.3). Having identified the most likely intrinsic parameters of the innermost jet regions, we can now translate these time lags into de-projected physical scales. Following León-Tavares et al. (2011); Pushkarev et al. (2010), the distance between the dominant emission regions in two different bands  $\Delta r$  is related to the time lag  $\Delta t$  as

$$\Delta r = \frac{\beta_{\text{app}} c (\Delta t)}{\sin \theta (1 + z)}. \quad (3.8)$$

In our calculations, we adopt the mean time lags obtained in the DCCF analysis and through the Spearman's rho test analysis, the apparent speed of the innermost moving

<sup>3</sup>Note that Clausen-Brown et al. (2013) consider the half opening angle, obtaining  $\Gamma\theta = 0.2$ . Since we consider the full opening angle, there is a factor-of-2 difference in the product.

component, A1, as the best representative of the plasma speed in the region close to the core, and a viewing angle of  $4.1^\circ$ . The de-projected distances are in parsecs, for the three considered pairs of variability curves:

$$\Delta r_{\gamma-15} = (1.35 \pm 0.81) \text{ pc}$$

$$\Delta r_{\gamma-235} = (1.30 \pm 0.81) \text{ pc}$$

$$\Delta r_{235-15} = (0.34 \pm 0.29) \text{ pc}$$

Both the 2D cross-correlation between pairs of VLBI images and the results of the variability analysis indicate that the core shift in the frequency range between 15 GHz - 86 GHz is well below the resolution limit of our observations. In fact, a de-projected shift of 0.34 pc inferred between 235 and 15 GHz would translate into a projected angular separation of only  $\sim 0.003$  mas, which will be even smaller between, e.g., 43 GHz and 86 GHz. This result suggests that the observed VLBI cores may not be associated with the unit radio opacity surfaces ( $\tau = 1$ ), but that the core region may be a stationary shock. Negligible core shifts are derived for several blazars in the MOJAVE sample (Pushkarev et al. 2012) and, especially at higher frequencies, the characteristics of the VLBI core often resemble those of a stationary shock (see Jorstad et al. 2017, and references therein).

Based on the analysis of the jet expansion profile presented in Sect. 3.3.3, this possibly stationary core feature is located at a distance  $R \leq (0.019 \pm 0.009)$  mas from the jet apex, which translates to a de-projected separation of  $\leq (2.05 \pm 0.97)$  pc for a viewing angle of  $4.1^\circ$ . Following the results of the variability study for the most strongly correlated pair  $\gamma$ -1 mm ( $\Delta r = 1.30 \pm 0.81$  pc), we estimate the  $\gamma$ -ray emission location to be at a distance of  $\sim (0.75 \pm 1.26)$  pc downstream from the jet apex. By taking into account the estimated error bars, this result tells us that the high-energy event occurs on scales ranging from sub-parsec to about  $\sim 2$  pc distance from the jet apex.

On such scales, the most likely mechanism leading to high-energy production is highly dependent on the source type. In powerful blazars known as Flat-Spectrum Radio Quasars (FSRQs), intense external photon fields originating in the accretion disk, the Broad Line Region (BLR) or the dusty torus are likely to act as seeds for the inverse Compton radiation, while in BL Lac objects these fields are expected to be less prominent or even absent, and the high-energy emission is often well reproduced by synchrotron self-Compton models.

As mentioned in Sect. 3.1, the classification of TXS 2013+370 as a BL Lac object or an FSRQ is uncertain in blazar catalogs (e.g., Massaro et al. 2015); this is due to the significant Galactic extinction in the source direction, which prevents a solid determination of its optical properties to be obtained. However, the recently determined, relatively high redshift ( $z = 0.859$ , Shaw et al. 2013) is uncommon among BL Lacs (see, e.g., their redshift distribution in the latest *Fermi*-LAT catalog, Abdollahi et al. 2020). Moreover, Kara et al. (2012) have examined the spectral energy distribution (SED) of the source, showing it is characterized by a hard X-ray photon index and by the dominance of the inverse Compton component over the synchrotron one in power output, as usually observed in FSRQs. Indeed, reasonable fits of the SED were only obtained when including an external Compton (EC) contribution.

An estimate of the BLR size in this source can be obtained by considering the bolometric luminosity of the accretion disk  $L_d$ , as determined by Shaw et al. (2013), and then following the approach of Ghisellini & Tavecchio (2015), which assumes a spherical BLR with radius

$R_{\text{BLR}} = 10^{17} L_d^{1/2}$  cm. Through this method, we obtain a radius of the order of  $\sim 0.07$  pc. The analysis presented in this paper points towards distances larger than this for the location of the  $\gamma$ -ray emission. On scales of 1-2 parsecs from the central engine, the dusty torus is the best candidate for providing a rich seed photon field. Indeed, [Kara et al. \(2012\)](#) showed that the best fit in the SED modeling of TXS 2013+370 required equipartition conditions for the dominant emitting region and an external radiation field with a rather low temperature ( $T_{\text{ext}} \sim 10^2$  K), thus possibly originating from cold dust. Temperatures in this range are found in the outer regions of the torus. For instance, previous studies performed in 3C 454.3 and NGC 1068 ([Jaffe et al. 2004](#); [Shah et al. 2017](#)) have derived a temperature of the order 300-600 K at a distance of  $\sim 3.5$  pc from the SMBH. Therefore, the distance that we obtain from our analysis can also be considered as a lower limit for the outer radius of the dusty torus.

A physical scenario where the EC process is supplied by infrared photons (IR) from the dusty torus is supported by several studies of powerful blazars ([Sahayanathan & Godambe 2012](#); [Sikora et al. 2009](#)). [Costamante et al. \(2018\)](#) showed that in the vast majority of the *Fermi* FSRQs, the  $\gamma$ -ray emission appears to originate outside the BLR. Moreover, recent findings support a torus geometry that deviates significantly from the standard picture of a "donut"-like structure ([Carilli et al. 2019](#); [Asmus 2019](#); [Lyu & Rieke 2018](#); [Hönig & Beckert 2007](#)). The torus is likely to be rather clumpy, with polar molecular clouds providing an even richer photon field available for EC scattering.

### 3.4.3 Transition from parabolic to conical expansion

We observe a transition observed in the jet expansion profile, with the jet switching from a parabolic to a conical shape (Sect. 3.3.3). As the resolution of radio observations increases, this phenomenon is observed in more and more jets and supports the currently most favored physical models of magnetic jet launching. These predict the jet base to be actively collimated and accelerated along an extended region, up to parsec distances from the central engine (e.g., [Vlahakis & Konigl 2004](#); [Komissarov et al. 2007](#)).

In TXS 2013+370 the transition is observed at a separation of  $\sim 0.5$  mas from the jet apex, corresponding to a de-projected distance of  $\sim 54$  parsecs for  $\theta = 4.1^\circ$ . For a black hole mass of  $4 \times 10^8 M_\odot$  ([Ghisellini & Tavecchio 2015](#)), we estimate that the jet collimation stops at  $1.5 \times 10^6$  Schwarzschild radii from the black hole, which is of the same order as the transition distance found for M87 ([Asada & Nakamura 2012](#)) and other sources in the MOJAVE sample ([Kovalev et al. 2019](#)).

This result indicates that at millimeter wavelengths, we are probing jet regions where the magnetic field is still important and that the  $\gamma$ -ray emission in this source is produced in the magnetically-dominated part of the jet base.

### 3.4.4 Magnetic Field Strength Estimation

The knowledge of the TXS 2013+370 spectral shape enables us to investigate the strength of the magnetic field at the base of the jet. An estimate of the magnetic field strength for individual components can be obtained under the assumption that SSA is the dominant process in the jet. Following [Marscher \(1983\)](#) the strength of the magnetic field for a stationary feature can then be calculated as

$$B_{\text{SSA}} = 10^{-5} b(\alpha) \theta^4 \nu_{\text{m}}^5 S_{\text{m}}^{-2} \frac{\delta^{2+\alpha}}{1+z} \quad [G], \quad (3.9)$$

where  $b(\alpha)$  is a tabulated spectral index-dependent parameter (considering the measured optically thin spectral index of  $\alpha = -0.7$ ),  $b(\alpha) = 3.6$ , (see Table 1 in (Marscher 1983) and Appendix A in Pushkarev et al. 2019),  $\theta$  the component size in mas ( $1.8 \times \text{FWHM}$ ),  $\nu_{\text{m}}$  the spectral turnover frequency of the non flaring state in GHz, and  $S_{\text{m}}$  the spectral turnover flux density in Jy.

The most appropriate VLBI data frequency to estimate the B-field strength is the one closer to the jet turnover frequency (Marscher A. et al. 2020 in prep.). As the VLA data are taken in snapshot mode, the obtained flux density is core-dominated. For this reason, the core component of the space-VLBI source image at 22 GHz is the best to use for the B-field computation. By considering  $\delta = 4$  and the spectrum turnover parameters for the non-flaring state of the source we obtained that the 22 GHz core is characterized by a weak magnetic field strength of  $B_{\text{SSA}} = 0.36 \pm 0.16$  G.

### 3.5 Conclusions

In this thesis, we present a complete picture of the radio morphology and jet evolution of the blazar TXS 2013+370 during the last ten years, and we are able to constrain the location of gamma-ray emission site. To achieve this goal, we employed state-of-art VLBI observations from 15 GHz up to 86 GHz, along with space-VLBI data. Based on this unique data set we estimated the kinematic parameters of the source and the jet expansion profile, from which we derived the radial distance between the VLBI core and the jet apex. The quasi-simultaneous flux variability single-dish observations allowed us to investigate the possibility of correlated activity events between the radio and  $\gamma$ -ray bands. Specifically, the flux density distribution modeling of the source revealed the emergence of three new components, A1, N, and N1. Component A1 was ejected between 2005 and 2006, and since 2007, its trajectory was traceable at 43 and 86 GHz images. After 2011, A1 was also visible in the 15 GHz images. In early 2009, an ejection event took place, accompanied by a close in time  $\gamma$ -ray flare. A year after, high resolution, 86 GHz image revealed the appearance of the new knot N. Lastly, a space-VLBI *RadioAstron* image in 2012 shows the emergence of another knot, labeled as N1. Contemporaneous with the appearance of knot N1, we report increased emission in radio bands and  $\gamma$ -rays. The next step of the analysis was the estimation of the linear separation between the VLBI core and the jet apex. For this purpose, we studied the jet transverse expansion profile, which allowed us to quantify this distance as  $R = (2.04 \pm 0.97)$  pc. In parallel, we reveal that in TXS 2013+370 the jet undergoes a geometrical transition from parabolic to a conical shape, at a projected distance of  $\sim 0.5$  mas ( $\sim 3.85$  pc) of the jet apex. Based on simultaneous flux density observations from 4.8 to 43 GHz, we constrained the source spectrum. We report a spectral break at ( $\nu_{\text{m}} = 21 \pm 4$ ) GHz, with flux density of ( $S_{\text{m}} = 2.6 \pm 0.9$ ) Jy and optically thick and thin spectral indices  $\alpha = 0.71 \pm 0.14$ ,  $\alpha_{\text{t}} = 0.55 \pm 0.10$  respectively. By employing the results of the spectral analysis we found the synchrotron self-absorbed magnetic field strength  $B_{\text{SSA}}$  at the jet region of the 22 GHz core. The results showed a moderate magnetic field strength which ranges between 0.2 to 0.5 G. The correlated activity between  $\gamma$ -rays and radio bands, allowed us to translate the observed time lags to linear distances. The strongest correlation appeared to be between  $\gamma$ -rays and 1 mm activity, with the  $\gamma$ -rays leading by  $(49 \pm 30)$  days. The estimated delay, considering the close-to-apex plasma speed and the viewing angle of

the jet, leads us to estimate that the deprojected distance between  $\gamma$ -rays emission site and radio core to be  $\Delta r_{\gamma-235} = (1.30 \pm 0.81) \text{ pc}$ . The combination of the distance between jet apex and mm VLBI cores and  $\gamma$ -rays production region with the mm VLBI cores indicates that the origin of the  $\gamma$ -ray emission is  $(0.75 \pm 1.26) \text{ pc}$  downstream of the jet apex.

## Chapter 4

# Revealing the Jet Fine Structure in the Blazar OJ 287

### 4.1 Introduction

The bright BL Lacertae object OJ 287 (0851+202), is located at a redshift of  $z=0.306$  (Stickel et al. 1989) in the constellation of Cancer, and is a prominent and highly variable AGN in the mm-bands. There is a range of uncertainty about the mass of the SMBH harboured in its central region, with typical estimates ranging from  $\approx 10^8$  up to  $10^{10} M_\odot$ , where the latter comes from a theoretical model (Liu & Wu 2002; Valtonen et al. 2008). Since 1888, OJ 287 is well known for its flaring activity in the optical regime (Hudec et al. 2013). Besides the rapid short-time scale flux variability, Sillanpaa et al. (1988) reported a quasi-periodicity of about 11.6 years. Based on the assumption that perturbations in the accreting material are the cause of optical variations in this AGN, the authors proposed the existence of a binary black hole system triggering the observed periodicity. Numerous studies followed, suggesting the presence of a primary SMBH situated close to the gravitational center, and of a secondary one following an elliptical orbit around the primary (e.g. Lehto & Valtonen 1996; Sundelius et al. 1997, and references therein). In this model, the detected outbursts reflect the accretion variations via tidal forces, introduced by the secondary binary component while crossing the accretion disk of the primary. This scenario requires the production of two flaring events per period. A pictorial representation of the system is shown in Fig. 4.1.

Based on the hypothetical quasi-Keplerian motion of the secondary BH, its mass is estimated to be  $1.4 \times 10^8 M_\odot$  (Valtonen et al. 2008). A General Relativistic (GR) description of the system determines the major axis of the orbit to be 0.112 pc (corresponding to an angular scale of  $\sim 26 \mu\text{as}$ ), taking into account the GR precession and orbital shrinkage due to Gravitational Wave (GW) emission (Valtonen et al. 2008; Valtonen et al. 2010, 2011).

A big success of this model was the prediction of a prominent flare that took place in December 2015. According to Valtonen et al. (2016), the crossing in 2013 of the secondary BH through the disk of the primary BH led to the expected GR centenary optical outburst in 2015 December. This event should have also increased the accretion rate of the secondary, in a similar way as found in tidal disruption events (e.g. Zauderer et al. 2011). The observation of a prominent increase supports this prediction, as well as the softening in X-rays measured by Swift (Grupe et al. 2016; Verrecchia et al. 2016; Grupe et al. 2017) and



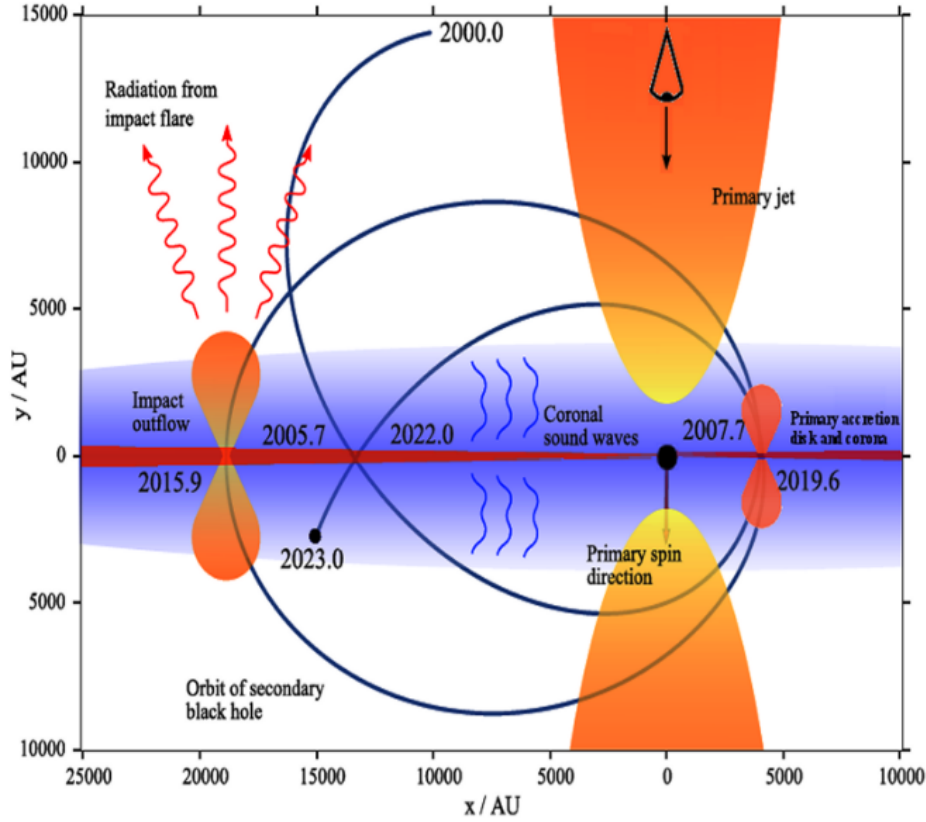


FIGURE 4.1: A conceptual illustration of the proposed binary BH model in the central region of OJ 287, and the predicted flaring events. Image credits: Ciprini et al. (2017).

the VHE emission ( $>100$  GeV) detection by VERITAS in 2017 February 1-4 (Mukherjee & VERITAS Collaboration 2017). In addition to the prominent optical variability, the source shows remarkable activity in the radio band too. For instance, the event mentioned above coincided with the strongest outburst at 1 mm during the last ten years, based on the SMA monitoring. The binary black hole model predicts enhanced radio variability to last over a time scale of few years (Valtonen et al. 2006). It is worth mentioning that, particularly after the first observation of gravitational waves (Abbott et al. 2016), OJ287 is a very interesting object given the proposed binary scenario. For instance, Valtonen & Lehto (1997) predicts a 10% loss of orbital energy of the secondary BH, resulting in the emission of GW from the system. Although the binary BH model is favored, alternative scenarios may explain these events as well. These are described in detail in the review paper by Villforth et al. (2010).

While the behavior of the source in optical seems to be well defined, the radio activity appears to exhibit a behavior that, in some cases, deviates from the expected. The monitoring of the source in the radio regime reveals a higher complexity of events related to the orientation and the morphology of the relativistic jet, not always connected to the optical flares. Whereas Tateyama & Kingham (2004), based on eight-year VLBI observations at 8.5 GHz, suggested a periodic wobbling of the jet base, in agreement with the binary BH model, Agudo et al. (2012) presented the results of a 16-year VLBI monitoring at 43 GHz supporting an erratic swing by  $>100^\circ$  (in the observer's frame). This dramatic change in the direction of the relativistic outflow occurred over a time range of  $\sim$  two years, ruling out the possibility that this event is connected to a binary BH system. Furthermore, the authors suggested the jet wobbling to be due to a non-steady plasma outflow, possibly connected with turbulence in the accretion disk, coupled with hydrodynamic instabilities.



This kind of instabilities can lead to a relativistic plasma outflow with non-ballistic trajectories that may explain the observed random changes in the direction of the inner jet. Similar studies (e.g., [Hodgson et al. 2017](#); [Britzen et al. 2018](#)) also report such extreme events. Other theoretical models indicate that the OJ 287 jet wobbling could be caused by Lense-Thirring precession around the disc of a single BH ([Britzen et al. 2018](#)). [Liska et al. \(2018\)](#), for instance, suggests that the innermost jet structure of OJ 287 may result from the precession of a tilted accretion disk. Relativistic magnetohydrodynamic simulations are consistent with a thin accretion disk tilted by  $60^\circ$  relative to the BH spin axis. Such a system can give rise to quasi-periodic disk-jet interactions that can potentially result in the repeating flaring events seen in OJ 287 light curves.

Finally, the jet behavior at mm and cm wavelengths could also be consistent with helical motion of the jet plasma. [Valtonen & Pihajoki \(2013\)](#), by assuming a helical jet emanating from the center and perpendicular to the accretion disk, could well simulate the projected jet path. Additionally, a binary BH system was also considered in the model. The results reproduced the observations nicely at optical and radio regimes, predicting that the jet geometry is a conical helix, and the plasma flow propagates outwards with a speed of  $\sim 0.85c$ . Helical jet patterns can reflect the existence of a large scale helical magnetic field or the development of plasma instabilities, such as Kelvin-Helmholtz instability ([Hardee 2000, 2011](#); [Mizuno et al. 2012](#)). Figure 4.2 displays the main results based in the work of [Myserlis et al. \(2018\)](#) and [Cohen \(2017\)](#), who suggest the existence of propagating helical plasma flow within a bent jet, under the assumption of a strong magnetic field.

In this chapter we present the results of multifrequency ground-based VLBI observations, as well as space-VLBI observation of OJ 287, focusing on the analysis of the intrinsic jet properties during a prominent flaring event. Moreover, the polarization properties on small spatial scales are investigated, enabling us to reveal the magnetic field topology and quantify the magnetic field strength in the proximity with the central engine. For all the calculations we adopt a  $\Lambda$ CDM cosmology with:  $\Omega_M = 0.27$ ,  $\Omega_\Lambda = 0.73$ ,  $H_0 = 71 \text{ km s}^{-1} \text{ Mpc}^{-1}$  ([Komatsu et al. 2009](#)), which result in a luminosity distance of  $D_L = 1.577 \text{ Gpc}$ . This implies a conversion factor of  $4.48 \text{ pc/mas}$  for the redshift  $z=0.306$ .

## 4.2 Observations, Data Calibration, and Imaging

### 4.2.1 Total Intensity Data Calibration

The VLBI data set comprises four quasi-simultaneous observations at 15, 22, 43, and 86 GHz, which were performed in the period April-May 2014. At 15 GHz we made use of the publicly available data from the MOJAVE program ([Lister et al. 2009b](#)), for which no a-priori calibration is needed.

The 22 GHz observations included the *RadioAstron* space-VLBI station (see Sec. 2.1.4.2), during the perigee of the spacecraft on April 4-5, 2014, with a ground array of 12 antennas (Table 4.1). The data were recorded in both left (LCP) and right (RCP) circular polarization, with a total bandwidth of 16 MHz per polarization, split into two intermediate frequency (IF) bands. Ground-space fringes during five close-in-time snapshot sessions were detected only at LCP. The data were correlated using the upgraded version of the DiFX correlator at the Max-Planck-Institut für Radioastronomie. The correlated data were reduced using the AIPS software package, following the standard procedure described in

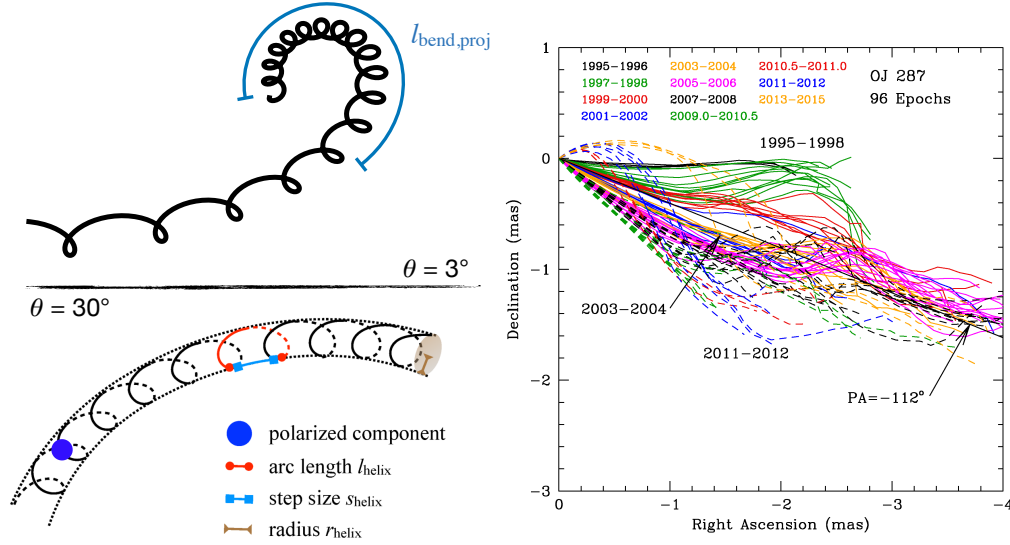


FIGURE 4.2: Rotating helical jet model for OJ 287. Left: The arc of the helical trajectory indicated by the VLBI images is estimated to have a length of 0.26 pc and radius to  $\geq 0.04$  pc. Right: Intensity ridge lines at 15 GHz over 10 years show a jet axis rotation.

Credits: Myserlis et al. (2018) and Cohen (2017) respectively.

Sec. 3.2.1. For the a priori amplitude calibration, we employed the measured system temperatures for the ground antennas and the Space Radio Telescope (SRT). The sensitivity parameters of the SRT are measured regularly during maintenance sessions. Ultimately, parallactic angle corrections were applied to the ground antennas in order to correct for the feed rotation.

The 43 GHz data were provided by the BU-BLAZAR monitoring program<sup>1</sup> (Jorstad et al. 2017). The radio observations were performed by almost all the VLBA stations and are available as a-priori calibrated visibilities.

The GMVA data-set comprises observations by all the VLBA stations that have 3 mm receivers, except the North Liberty station, and up to four European stations. The duration of each scan was eight minutes long. Data were recorded at 2 Gbps rate (512 MHz bandwidth) with 2 bit digitization, except for the Plateau de Bure observatory (PB), which recorded at 1 Gbps. A polyphase filter band (PFB) technology was used, and data were segmented into 16 IFs of 32 MHz bandwidth per polarisation. A summary of observations and the data is given in Table 4.1.

#### 4.2.2 Single-dish Observations

The single-dish observations used in this work were performed simultaneously to the VLBI observations by the ALMA telescope<sup>2</sup> at 103.5 GHz in total intensity, by the Effelsberg and IRAM telescopes within the F-GAMMA (FERMI-GST AGN Multi-frequency Monitoring Alliance) project at 2.64, 4.85, 8.35, 10.45 GHz in linear polarization and 43, 23 GHz in total intensity (Angelakis et al. 2019), and by OVRO at 15 GHz.

<sup>1</sup><https://www.bu.edu/blazars/VLBAProject.html>

<sup>2</sup><https://almascience.eso.org/alma-data/calibrator-catalogue>

TABLE 4.1: VLBI Observational Parameters. Columns from left to right: (1) Observing frequency, (2) Observing epoch, (3) Participating antennas, (4) Major axis of the convolving beam, (5) Minor axis of the convolving beam, (6) Position angle, (7) Image peak flux density, (8) Image total flux density, (9) Noise level, (10) Image polarized flux density, (11) Noise level. KVN: Korean VLBI Network array, ON: Onsala, SH: Sheshan, TR: Torun, NT: Noto, HH: Hartebeesthoek, EB: Effelsberg, YS: Yebes, GB: Green Bank, RA: *RadioAstron*, <sup>a</sup>, <sup>b</sup>: North Liberty not participate, <sup>c</sup>: the Hancock and Saint Croix telescopes do not have 3mm receivers.

Frequency (GHz)	Epoch (years)	Array Elements	$b_{maj}$ (mas)	$b_{min}$ (mas)	PA (deg)	$S_{peak}$ (Jy/beam)	Stotal (Jy)	rms (mJy/beam)	Ppeak (Jy/beam)	Ptotal (Jy)	$rms_P$ (mJy/beam)
15	2014.45	VLBA <sup>a</sup>	0.87	0.48	0.35	3.28	3.97	0.68	0.04	0.05	0.1
22	2014.26	KVN+ON+SH+TR+HH NT+EB+YS+GB+RA+KL	0.25	0.08	-88.6	1.18	2.38	1.81	0.02	0.03	9.32
43	2014.44	VLBA <sup>b</sup>	0.35	0.20	10.6	4.51	5.50	1.5	0.26	0.28	1.6
86	2014.50	VLBA <sup>c</sup> +PV+EB+ON+PB	0.21	0.04	-12.3	3.46	5.05	1.3	0.33	0.46	3.0

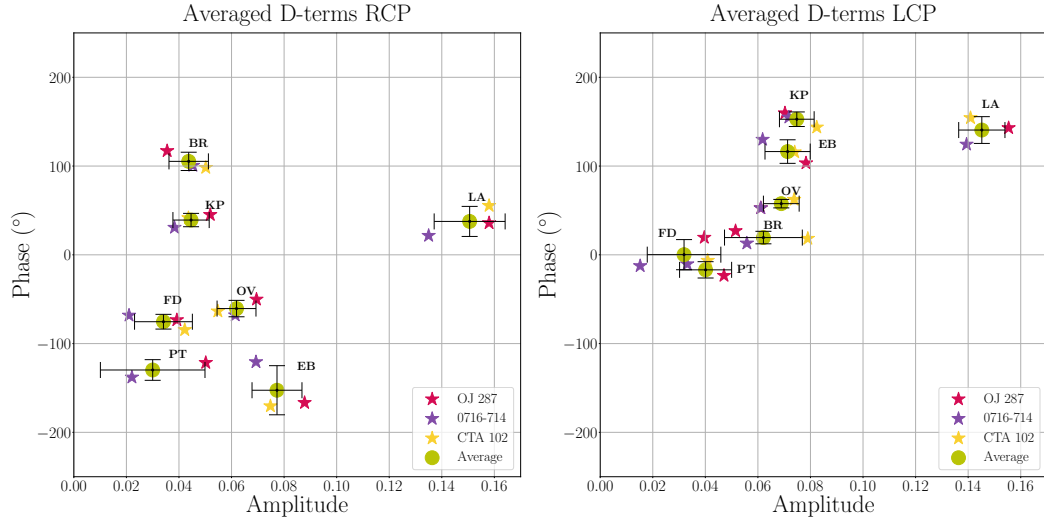


FIGURE 4.3: D-terms derived based on the data for OJ 287, 0716+714, and CTA 102, and their mean value, for the two polarizations. Labels mark the different radio telescopes.

### 4.2.3 Polarization Data Calibration

As described in Sec. 2.2.0.4, an essential step in the polarimetric data reduction is the estimation of the instrumental polarization. The signal contamination between the RCP and LCP orthogonal feeds depends exclusively on the telescope receivers and the corresponding waveguides, and is assumed to be stable during the observing session<sup>3</sup>. The impact of the “leakage” in the polarization image is significant, as the leakage factor is quite dominant in the cross-hand correlations (see Eq. 2.34). In this work, we used the task LPCAL in AIPS for the estimation of the polarization leakage.

A widely used method for this calibration is to estimate the instrumental polarization leakage based on the data of the target source itself. However, in many instances, this method fails, as either the source exhibits extended and complicated jet structure, or the parallactic angle coverage is poor. When one or both of the above conditions are valid, alternative methods should be followed. For instance, the estimation can be improved by considering the D-terms for a single, compact source with good parallactic angle coverage (Kim et al. 2019). Alternatively, an average D-term can be derived based on the analysis of several, bright calibrators observed in the same session (Casadio et al. 2017). In this work, we tested different methods.

First, we obtained the D-terms for the source itself for each IF and antenna, and then took the median of the solutions for each station. We found that the leakage-terms were consistent across all IFs, within a small range in amplitudes and phases of the order of  $\sim 2\%$  and  $13^\circ$  respectively. Next, by following the line of work of Casadio et al. (2019), we chose bright and compact sources with a large parallactic angle coverage ( $\geq 80^\circ$ ). The most suitable sources for this purpose during the May 2014 session were the blazar 0716+714 with a parallactic angle coverage of  $111^\circ$  and CTA 102 with a coverage of  $82^\circ$ .

As a first step, we estimated the leakage for each antenna and each source. We created linear polarization images of OJ 287, applying the D-terms from the source itself, those from 0716+714 and those from CTA 102. In the resulting images, the polarization morphology

<sup>3</sup><http://www.vlba.nrao.edu/memos/sci/sci30memo.ps>

was overall consistent for the core region. However, the position of the bright polarized feature at  $\sim 0.2$  mas appeared to vary. For determining if this feature was real or an artifact, and for confirming the overall polarized flux density level, we applied a third method. We determined the averaged D-terms for each station and we applied them to the OJ 287 data set. The uncertainties are estimated based on the standard deviation of the individual D-terms values. The results from all methods are presented in Fig. 4.3, and the corresponding polarization images in Fig. 4.4.

Among the four images, the one corrected with the D-terms from OJ 287 itself and the one corrected by the average are characterized by higher high dynamic range (dynamic range, or DR, is defined by the ratio of the peak image intensity to the image noise), with the highest DR obtained for the first one. Specifically, we obtained for all images:  $DR_{CTA\ 102} = 2515$ ,  $DR_{0716+714} = 2824$ ,  $DR_{Averaged} = 5524$  and  $DR_{OJ\ 287} = 7538$ . This result is in agreement with [Casadio et al. \(2017\)](#), who also analyzed the polarization structure of OJ287 at 86 GHz and the effect of the different methods. In the following we choose as the most reliable polarization image the one with the highest DR.

As a final remark, we report that the obtained range of D-terms (1% - 15%) for OJ 287 is in good agreement with the values that are estimated from similar studies ([Roberts et al. 1994](#); [Martí-Vidal et al. 2012](#); [Casadio et al. 2017](#); [Kim et al. 2019](#)).

#### 4.2.4 Uncertainties in Polarization Quantities

The error on the polarized flux density,  $\sigma_P$ , is estimated for all data sets by taking into account a calibration uncertainty of about 10% of the polarized flux density and a statistical error provided by the map thermal noise ([Lico et al. 2014](#))

$$\sigma_P = \sqrt{(0.1 \times P)^2 + rms_P^2}. \quad (4.1)$$

The error on the fractional polarization (determined as  $m = 100 (P/S)$ ) is given by

$$\Delta_m = \frac{1}{S} \sqrt{\sigma_P^2 + (m \times \sigma_S)^2 + \sigma_{D-term}^2}, \quad (4.2)$$

where  $S$  and  $\sigma_S$  is the measured total flux intensity and its error (see Table B.1). The term  $\sigma_{D-term}$ , represents the systematic polarization calibration error and is defined as ([Roberts et al. 1994](#); [Hovatta et al. 2012](#))

$$\sigma_{D-term} = \sigma_{amp} \frac{\sqrt{S_{total}^2 + (0.3 \times S_{peak})^2}}{\sqrt{N_{ant} N_{IF} N_{scan}}} \quad (4.3)$$

where  $\sigma_{amp}$  is the standard deviation of the D-term amplitudes,  $N_{ant}$  is the number of antennas,  $N_{IF}$  is the number of the IFs and  $N_{scan}$  is the number of independent scans with different parallactic angles. For the GMVA image we have  $\sigma_{amp} \sim 2\%$ ,  $N_{ant} = 7$ ,  $N_{scan} = 5$ ,  $N_{IF} = 16$ ,  $S_{peak} = 3.47$  Jy and  $S_{total} = 5.07$  Jy, which results in  $\sigma_{D-term} = 4.62$  mJy/beam. Similarly, for the *RadioAstron* data we have  $\sigma_{amp} \sim 1\%$ ,  $N_{ant} = 13$ ,  $N_{scan} = 6$ ,  $N_{IF} = 2$ ,  $S_{peak} = 1.18$  Jy and  $S_{total} = 2.38$  Jy, which results in  $\sigma_{D-term} = 1.92$  mJy/beam. For the

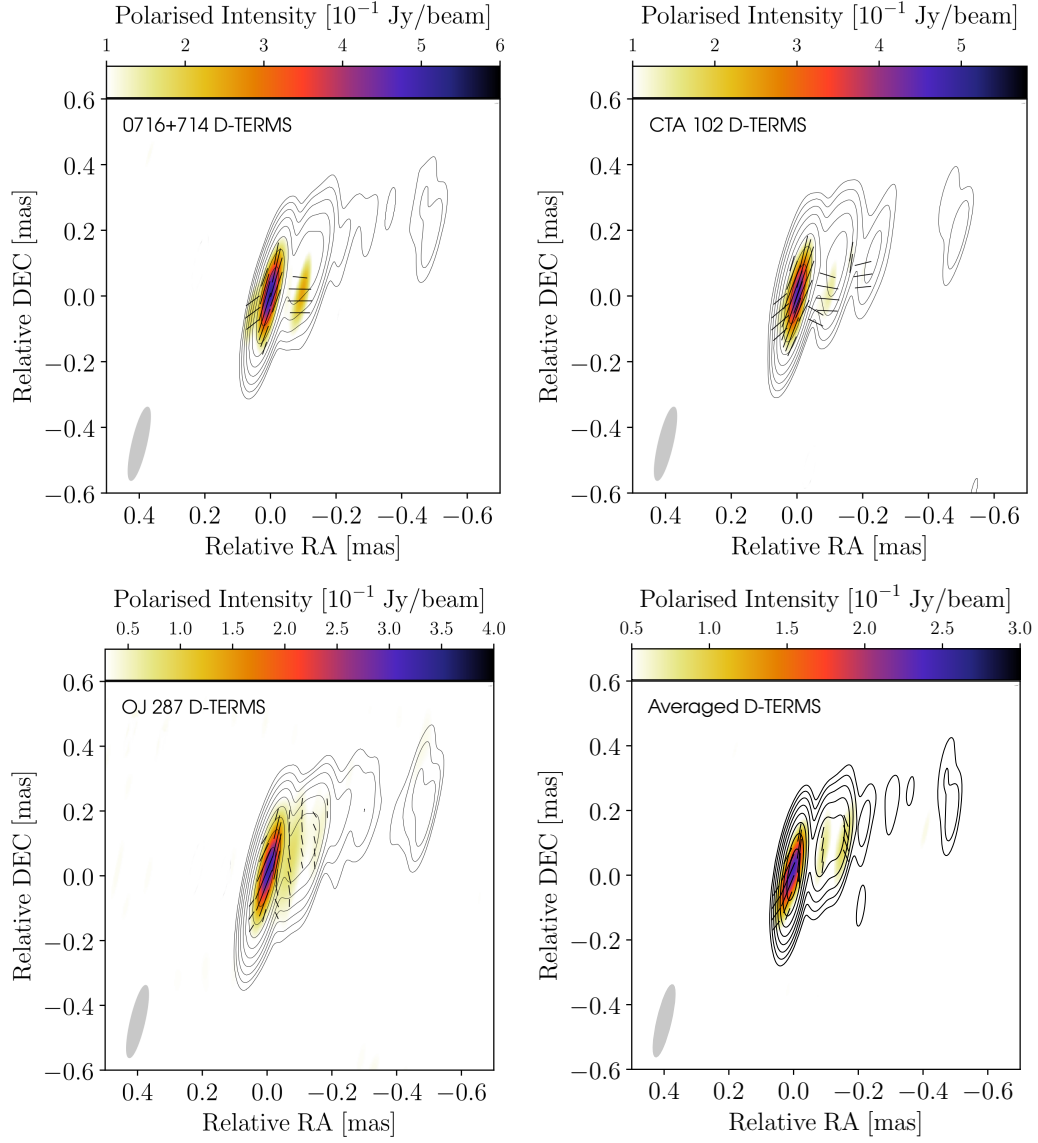


FIGURE 4.4: Polarization images of OJ 287, corrected through different methods. The contour level is set at 0.5%, 1.0%, 2.0%, 4.0%, 8.0%, 16.0%, 32.0%, 64.0% of the total intensity peak flux (see Table 4.1) and is the same for all plots. In the following analysis we consider the image in the bottom-left panel.

15 GHz data,  $\sigma_{D-term} \approx 2 \times rms_P$  (Hovatta et al. 2012), whereas for the 43 GHz data,  $\Delta m = 1\%$  (Jorstad et al. 2005).

The determination of the absolute electric vector position angle (EVPA) for the 86 GHz polarization image was obtained by considering polarimetric measurements from the IRAM 30 m telescope, as OJ 287 is part of the POLAMI monitoring program<sup>4</sup>. The uncertainties on this parameter for the POLAMI measurements  $\sigma_{POLAMI} \sim 5$  deg (Agudo et al. 2018a,b). The overall uncertainty on the EVPA  $\chi$  for the 86 GHz polarization images is determined as

$$\Delta\chi = \sqrt{\sigma_\chi^2 + \sigma_{POLAMI}^2 + \sigma_{phas}^2}, \quad (4.4)$$

<sup>4</sup><http://polami.iaa.es>

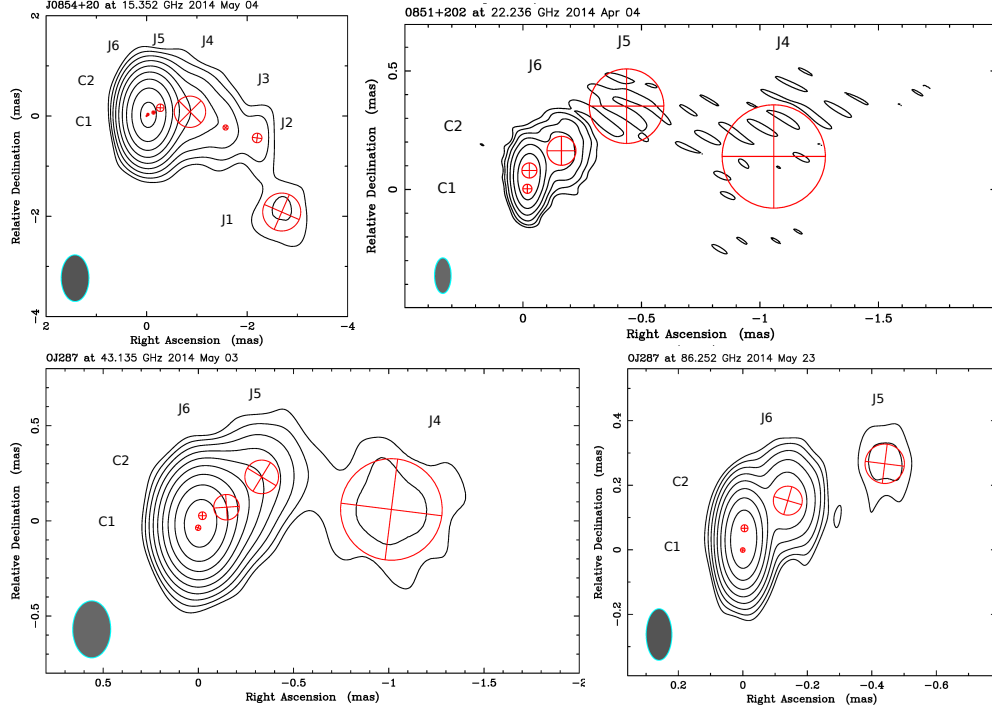


FIGURE 4.5: Model fit images of OJ 287 at 15, 22, 43 and 86 GHz. The data were imaged with a uniform weighting scheme. The convolving beam of each image is  $0.9 \times 0.5$ ,  $0.15 \times 0.7$ ,  $0.3 \times 0.2$  and  $0.16 \times 0.08$  mas respectively, oriented at PA  $0^\circ$ , whereas the contour levels are set to 10 times the rms level in each image (see Table 4.1).

where  $\sigma_\chi = 0.5/P\sqrt{Q^2\sigma_Q^2 + U^2\sigma_U^2}$  is the uncertainty due to thermal noise, based on the error propagation theory, and  $\sigma_{\text{phas}}$  is the standard deviation of the D-term phases. At 22 GHz, the error of the absolute EVPA calibration is also  $\sigma_{\text{POLAMI}} \sim 5^\circ$ . At 15 GHz data,  $\Delta_\chi = \sigma_P/2P$  (Hovatta et al. 2012), whereas at 43 GHz,  $\Delta_\chi \sim 5^\circ$  (Jorstad et al. 2005).

## 4.3 Data Analysis and Results

### 4.3.1 Jet Morphology and Modeling

OJ 287 is characterized by an one-sided jet, with a bright core region and a strong bending at a projected distance of  $\sim 1$  mas from the central region. The modeling of the flux density distribution along the jet was performed by fitting two-dimensional Gaussian components, using the DIFMAP package, and following the procedure described in Sec. 3.3.1. The imaging and modeling of the multifrequency VLBI data allowed us to resolve the central compact region of the jet. We cross-identified the individual components based on their radial position, flux density and size.

**15 GHz:** The source at 15 GHz shows a bright core region, and a strong bending by almost  $55^\circ$  at  $\sim 0.7$  mas to the south-west direction (Fig. 4.5). By super resolving the image with a 0.3 mas beam, the compact core can be described by two distinct and unevenly bright features, designated as C1 and C2. Further downstream, the curved plasma flow can be modeled by six more components, with parameters that are presented in Table B.1. We



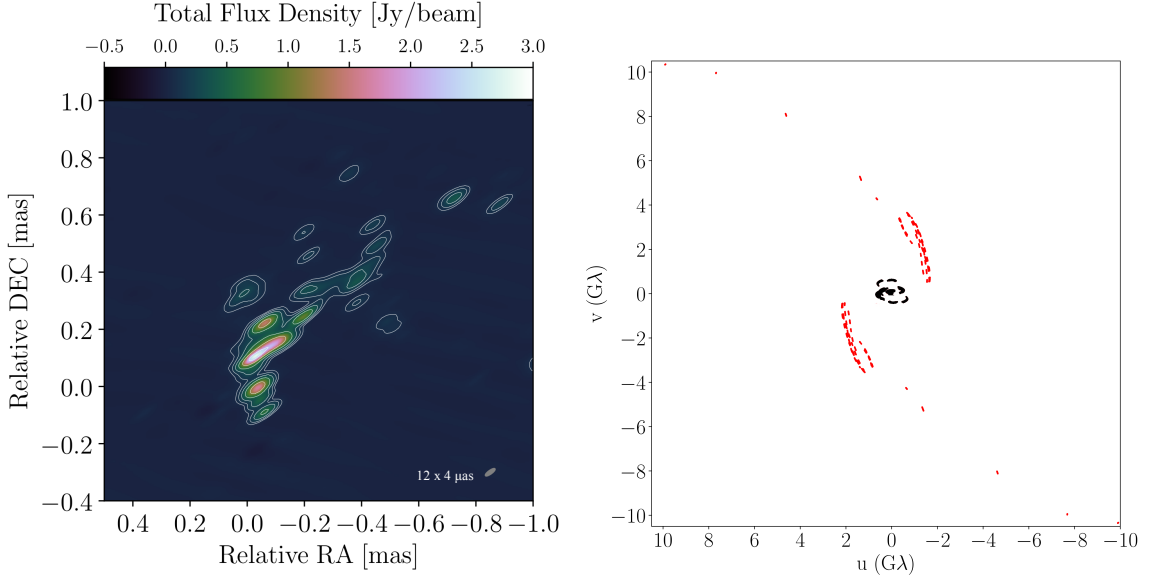


FIGURE 4.6: Left: Full-resolution, 22 GHz *RadioAstron* image of OJ287. Right: The uv coverage, taking into account baselines with  $\text{SNR} \geq 11.5$  (4 Earth diameters in projection length).

note that feature C1 is fainter than feature C2. In the following paragraphs, we will discuss further the nature of these components and the possible scenarios for such a structure.

**22 GHz:** The extreme high resolution that the  $\sim 350,000$  km *RadioAstron* baseline provide us with can be noticed in the 22 GHz image of the source Fig. 4.6. In this observation, not all the baselines showed the same SNR. If we set a low SNR limit ( $\text{SNR} \sim 11$ ), the angular resolution is increased down to  $10 \mu\text{as}$ . The two panels in Fig. 4.6 display the uv coverage and the image resulting in this assumption. However, in this work we set a hard limit by keeping only baselines with  $\text{SNR} \geq 50$  (which corresponds to  $30 \mu\text{as}$  resolution). On these scales, the jet shows a complicated structure, characterized by several sub-components. Among these, the brightest one does not correspond to the southern end of the jet component. In the upper right panel of Fig. 4.5, the modelfitted image of the source is presented. The flux density of the jet at 22 GHz is described by five features in total. We cross-identified all of the model components with the components in the 15 GHz image based on their radial distance from the core, their flux density and their position angle.

**43 and 86 GHz:** The OJ 287 image at 43 GHz is morphologically similar to the 22 GHz. The jet extends up to 1 mas from the core and then bends towards the south-west. The source structure can be modeled by two components, C1 and C2, and the jet components J6, J5. The core comprises two features, C1 and C2, and the brightest feature is again C2. Further downstream, components J6, J5, and J4 describe the jet radio emission. At 86 GHz, only the most compact regions in the inner jet are visible. Both the 43 and the 86 GHz modelfit images are presented in Fig. 4.5.

### 4.3.2 Linear Polarization Morphology

In Fig. 4.7 we present the results of the polarization imaging for the OJ 287 jet from 15 to 86 GHz, and in Table 4.2 the summary of the main characteristics of each polarized feature.



The source is polarized at all four frequencies. A strongly polarized core is continuously present, whereas polarized components of the outer jet are detectable at lower frequencies. In the core region, the EVPA orientation, surprisingly, is not significantly different at the different frequencies and different dates.

**15 GHz:** The polarization structure at 15 GHz consists of a polarized core and two semi-blended and highly polarized components, located at approximately one and 1.5 mas respectively. The secondary polarization components are labeled as P3 and P4. Both components can be considered as the polarization counterparts of the total intensity 2D Gaussian components J3 and J4, although they are slightly offset from the total intensity peak. This can be an indication that these features belong to an underlying, edge-brightened jet (Giovannini et al. 2018). The orientation of EVPAs appeared to be well aligned with the jet flow, suggesting that the dominant component of the magnetic field is perpendicular to the plasma flow.

**22 GHz:** The extremely high resolution of the RA image reveals a fine polarization sub-structure in the core region. In contrast, the polarized jet components P3 and P4 are not detectable anymore in the space-ground VLBI image. The nuclear region is resolved into the features P1 and P2, with P1 lying upstream of the latter. The positions of these two prominent features are in agreement with the position of total intensity components C1 and C2, respectively (see Fig. 4.5). Component C2 appears to exhibit higher fractional polarization than C1, and the orientation of EVPA is well ordered and parallel to the jet flow, indicating that it is related to a shocked compressed feature. Additionally, two small polarization features appear in the edges of the jet and close to the core region (see upper left panel of Fig. 4.7), supporting the scenario of the existence of an underlying, edge-brightened jet.

**43 GHz:** In this image, the core feature is well defined and polarized. At  $\sim 0.5$  mas, another polarized feature is present, labeled as P5. This component is characterized by a fractional polarization of  $m_{P5} = 3.4\%$ , whereas its position coincides with the total intensity component J5 (see Fig. 4.5). The EVPA orientation appears to be perpendicular to the jet axis, suggesting the dominance of the poloidal component of the local magnetic field.

**86 GHz:** The polarization structure of the 3 mm image consists of a core feature and a polarized sub-component, labeled as P6. The fractional polarization of the core component reaches the amount of  $m_{core} = 7.9\%$ , whereas P6 shows the highest fractional polarization of the source,  $m_{P6} = 16.7\%$ . The EVPA orientation of the core is similar to the other images, whereas the orientation of electric vectors of P6 is comparable with P5. The high fractional polarization indicates highly ordered magnetic fields compatible with those expected in a shocked compressed feature.

In summary, OJ 287 shows at all the observed frequencies a polarized feature in the core region, that becomes resolved into two distinct features P1 and P2 at a resolution of  $10\mu\text{as}$ . The overall fractional polarization shows an increasing trend as the frequency increases, with the 86 GHz image to exhibit the highest fractional polarization percentage of about  $\sim 8\%$ . Polarized sub-components are also detectable, namely P3, P4, P5 and P6. All the polarized components have a counterpart in the total intensity image. The EVPA orientation of all components indicates the existence of a helical magnetic field. Specifically, the B-field of the innermost region of the jet appears to be perpendicular to the flow axis up to  $\sim 0.16$  mas ( $0.72$  pc projected distance). Downstream and up to  $\sim 0.5$  mas the B-field orientation becomes parallel to the jet axes, showing a dramatic change of almost  $90^\circ$  further downstream. Lastly, we point out here that the VLBI data were obtained at the beginning

TABLE 4.2: Properties of the polarized components. The columns from left to right show (1) Component ID, (2) Observing frequency, (3) The degree of linear polarization, and (4) the EVPA.

ID	Freq. (GHz)	m %	$\chi$ °
Core	86	$7.9 \pm 0.9$	$-18.7 \pm 7.1$
	43	$5.3 \pm 0.1$	$-17.8 \pm 5.0$
	15	$1.3 \pm 0.2$	$-16.8 \pm 1.4$
P1	22	$1.9 \pm 1.2$	$-27.1 \pm 5.6$
P2	22	$2.5 \pm 1.1$	$-19.9 \pm 5.6$
P3	15	$12.5 \pm 11.7$	$-87.4 \pm 0.1$
P4	15	$3.8 \pm 1.6$	$-85.7 \pm 0.1$
P5	43	$3.4 \pm 0.1$	$6.4 \pm 5.0$
P6	86	$16.7 \pm 3.5$	$5.1 \pm 7.1$

and during the evolution of a very strong flare, in a time window of approximately two months. A more in-depth investigation of this topic is presented in the next section.

### 4.3.3 Spectral Index Analysis

The quasi-simultaneous observations in April-May 2014 give us the unique opportunity to study the spectral properties of the OJ 287 jet from parsec to sub-parsec scales. For this, we employed two different methods. For estimating the spectral parameters and search for spectral breaks, we assembled quasi-simultaneous spectra of individual superluminal knots, based on their flux density light curves. For the spectral evolution study, we constructed spectral index maps between VLBI images at different frequencies.

Quasi simultaneously with the 22 GHz space-ground VLBI observations, a multiwavelength outburst was observed. Single dish variability measurements at radio bands showed that, in early 2014, the flux density of the source was rising and peaked around the middle of June of the same year. Additionally, a polarization outburst has been reported at the optical V band on March 31st (Ganesh et al. 2014). As can be seen in Fig. 4.8, the flare is traceable at many frequencies, indicating a causally connected activity, but also reveals that the total flux density of the VLBI images is lower than the expected (as denoted by star symbols in Fig. 4.8). Flux density differences between single antenna and VLBI observations are a well-known problem. The interferometric data, while offering higher resolution, have the drawback of losing part of the source flux density that corresponds to the large scale structure. On the contrary, a single antenna observes with a larger beam, thus is obtaining the total flux density of the spatially unresolved source. Another significant problem that is related to flux density losses in high-resolution VLBI data is the accuracy of the absolute flux density calibration (Koyama et al. 2016). In the cases of GMVA images of the AGN 3C 84, 3C 454.3, CTA 102, BL Lac and OJ 287 in 2015, Kim et al. (2019) reported a flux density ratio  $S_{\text{VLBI}}/S_{\text{total}}$ , also known as compactness ratio, reaches the  $\sim 0.5$ , while the typical value in blazars is 0.8-0.9. Therefore in the following analysis, we will assume a compactness ratio of  $\sim 0.85$  at all frequencies.

Ultimately, since the VLBI observations have been performed over a time range of  $\sim$  two months, a period that coincides with the rapid evolution of a flaring event, we will use a

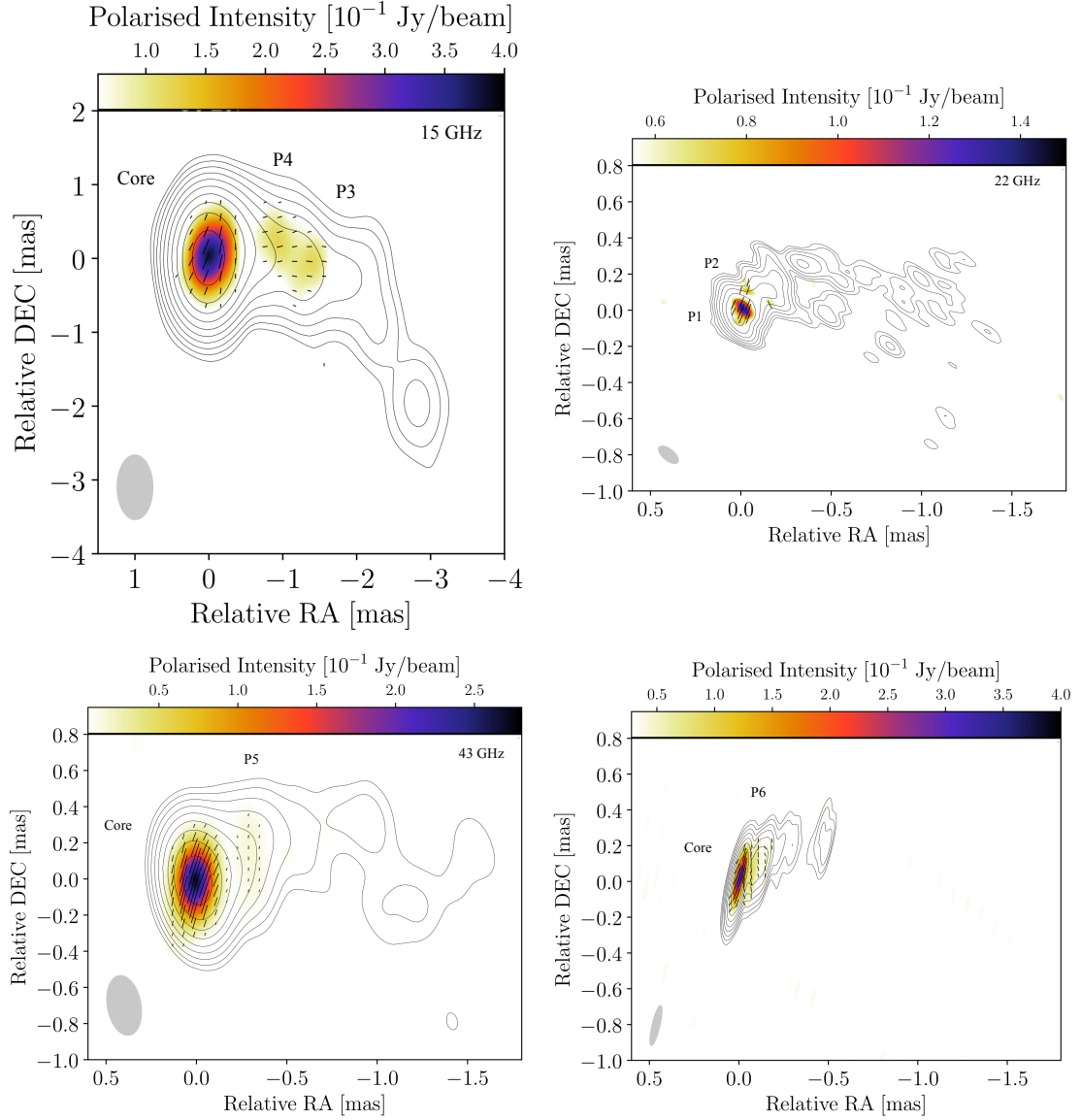


FIGURE 4.7: Polarimetric VLBI images of OJ 287 at 15, 22, 43 and 86 GHz. In all panels, the contours show the total intensity, starting from 10 times the rms level of each image (see Table 4.1). The convolving beam of each image is  $0.90 \times 0.55$ ,  $0.13 \times 0.06$ ,  $0.33 \times 0.18$  and  $0.23 \times 0.04$  mas respectively, oriented at  $PA_{15\text{ GHz}} = 0^\circ$ ,  $PA_{22\text{ GHz}} = 50.9^\circ$ ,  $PA_{43\text{ GHz}} = 10.3^\circ$  and  $PA_{86\text{ GHz}} = 0^\circ$ .

reference point date. As truly simultaneous observations are an important requirement in spectral index analysis of rapidly varying blazars, we will solve this problem by using the single-dish measurements as a reference. Hence, we will scale the VLBI image fluxes to the reference date of 2014.5, using linear interpolation from bracketing in time total flux measurements. The reference date was chosen to correspond to the best-sampled part of the lightcurve, both in total and VLBI observations. Therefore, the amplitudes of the 15 GHz VLBI data are upscaled by a factor  $g_{15} \sim 1.15$ , 22 GHz data by  $g_{22} \sim 2$ , 43 GHz  $g_{43} \sim 1.23$ , and the 86 GHz data by  $g_{86} \sim 1.33$ .

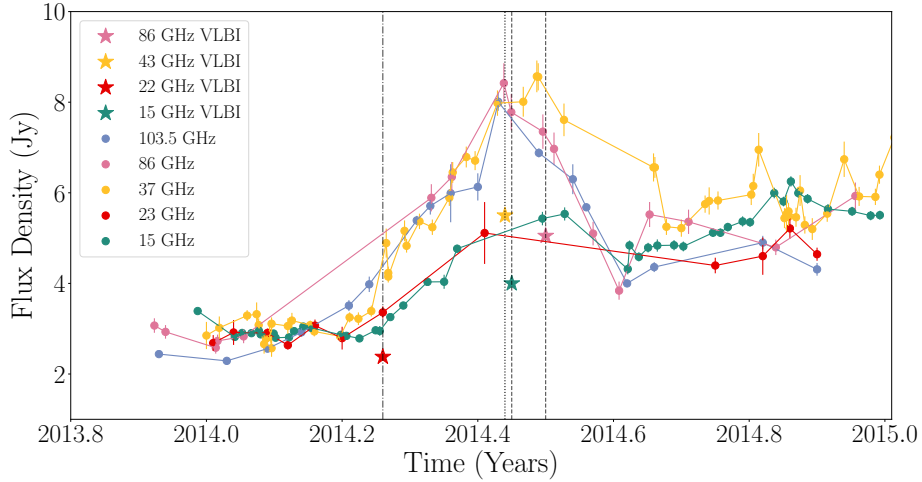


FIGURE 4.8: Single-dish variability (circles) and VLBI (stars) multifrequency measurements. During the observing interval, a prominent flaring event took place. In this plot, the vertical, dashed lines indicating the VLBI observing dates.

#### 4.3.3.1 Synchrotron Spectra from VLBI Knots

For calculating the synchrotron radio spectrum of the individual jet components we are going to employ Eq. 3.2. Thus, following the same procedure as in Sect. 3.3.4 and setting  $\alpha_{thick} = 5/2$  based on the theoretically expected spectrum of an optically thick, homogeneous synchrotron component (Pacholczyk 1970), we obtained the spectrum of knots C1, C2, J6, and J5. In this analysis we use  $S \approx \nu^\alpha$ . In general, the feature that corresponds to the VLBI core is expected to exhibit a flat or inverted spectrum, whereas for moving knots, one expects steeper spectra. In the right panel of Fig. 4.9, the SSA fitting for each component is displayed. The flattest spectrum in the core region is shown by component C1, characterized by  $\alpha_{thin} = -0.1$ . In this fitting, we exclude the 22 GHz data due to unexpected dimming of this feature. We assume that this behaviour is driven by structural changes introduced by the upcoming flare, since the data were obtained few days after the beginning of the flaring event (see the dashed line in Fig. 4.9). Component C2 also exhibits a flat spectrum with  $\alpha_{thin} = -0.2 \pm 0.3$  and turnover frequency almost identical to C1, at  $\sim 45$  GHz. Feature J6 also shows an almost flat spectrum, even if it is located  $\sim 0.1$  mas further downstream. Jorstad et al. (2005) reported the existence of quasi-stationary features at the locations  $\sim 0.1$ ,  $\sim 0.3$ , and  $\sim 1$  mas from the innermost jet feature. Also, the spectral index of shocks is expected to become flatter or even inverted (e.g., Marscher & Gear 1985; Mimica et al. 2009). Hence, we can assume that component J6 falls in this category. Knots J5 and J4 exhibit a steeper, optically thin spectral index of  $\sim -0.8$  and turnover frequency of  $\sim 9$  GHz, which is consistent with optically thin synchrotron emission and an older (cooled) electron population. A summary of the aforementioned results is presented in Table 4.3.

#### 4.3.3.2 Pixel-based Spectral Decomposition

The next step in this analysis is to reconstruct the spectral index distribution along the jet by using pairs of images at different frequencies. The spectral index,  $\alpha$ , is defined as

Knot	$S_m$ (Jy)	$\nu_m$ (GHz)	$\alpha_{thin}$
C1	$3.9 \pm 0.3$	$45.0 \pm 5.2$	$-0.1 \pm 0.3$
C2	$1.7 \pm 0.3$	$45.1 \pm 5.8$	$-0.2 \pm 0.3$
J6	$0.9 \pm 0.1$	$51.9 \pm 1.6$	$-0.1 \pm 0.01$
J5	$0.4 \pm 0.1$	$9.1 \pm 5.2$	$-0.8 \pm 0.2$
J4	$0.2 \pm 0.3$	$9.2 \pm 5.2$	$-0.9 \pm 0.3$

TABLE 4.3: Spectral index estimates based on Gaussian component fitting. Columns from left to right: (1) Component ID, (2) Turnover flux density, (3) Turnover frequency, (4) Optically thin spectral index. When errors could not be calculated, we adopted the highest value estimated among the rest of the components.

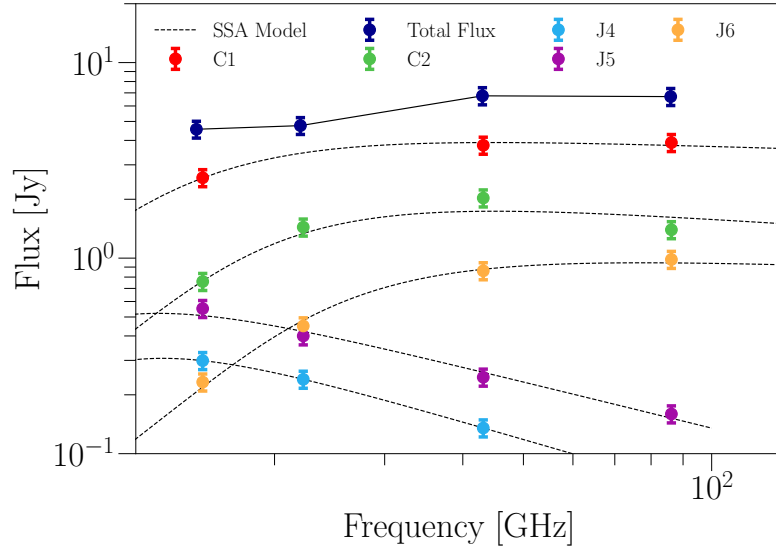


FIGURE 4.9: Synchrotron spectra of OJ 287 core and jet components from observations during April-May 2014.

$$\alpha = \frac{\ln(S_1/S_2)}{\ln(\nu_1/\nu_2)} \quad (4.5)$$

where  $S_{1,2}$  are the flux densities in each pixel, and  $\nu_1, \nu_2$  are the frequencies of each image. We choose the pairs 22-43 GHz and 43-86 GHz as the best representative frequency pairs for studying the spectral evolution close to the core (at 22 GHz we used the ground array data because of better matching resolution with the 43 GHz). An important step for the spectral index image production is the appropriate selection of the common beam and pixel size. For instance, a too-small beam size will introduce image artifacts, whereas a too-large pixel size will lead to the loss of sensitivity. In this work, we followed a widely accepted technique of using a circular beam, with an average radius between the beam sizes of the images and average pixel size. The final parameters for each pair are  $b_{22-43} = 0.3 \text{ mas}$  and  $0.005 \text{ mas}$  pixel size, while  $b_{43-86} = 0.2 \text{ mas}$  and  $0.004 \text{ mas}$  pixel for the two pairs respectively. No spectral index was calculated for pixels with flux density smaller than five times the RMS noise level. The uncertainties on the spectral index were calculated using error propagation.

Another significant correction one should take into account before creating a spectral index

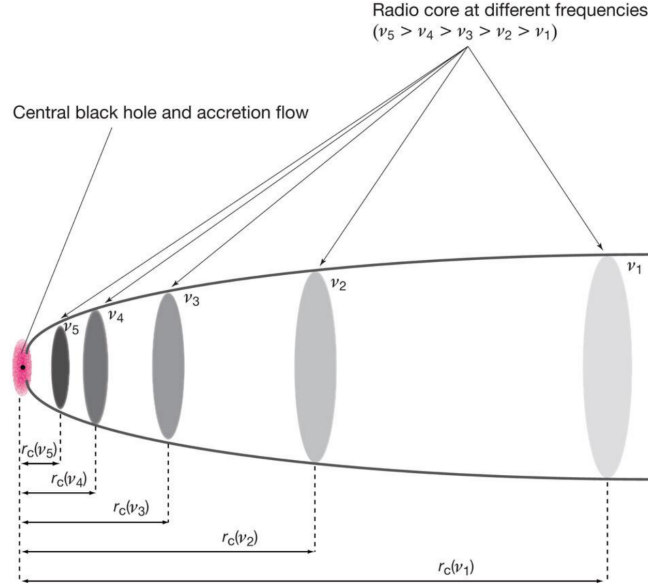


FIGURE 4.10: Conceptual illustration of the core-shift effect. Credits: (Hada et al. 2011).

map is the core-shift effect. The core-shift is the frequency-depended shift of the VLBI core position due to synchrotron opacity (Marcaide & Shapiro 1984; Zensus et al. 1995; Lobanov 1998). In Fig. 4.10, a conceptual illustration of the effect is displayed.

For the case of OJ 287 we obtained a shift of -0.02 mas for the 43-86 GHz image pair, and -0.05 mas for the 22-43 GHz image pair, by performing the image alignment employing a 2D cross-correlation analysis. The obtained (small) values are in agreement with Hodgson et al. (2017).

Lastly, a cut along the jet ridgeline is also done in order to highlight spectral index changes downstream of the core. The spectral index image and its cut at 22-43 GHz are presented in Fig. 4.11. The core region is optically thick and shows a highly inverted spectrum. Between 0.5 mas and 0.8 mas core separation, the spectral index profile shows a slightly increasing trend. Looking at other peaks in the plot, the local maximum observed around 0.8 mas can be related to a moving shock, as indicated by a kinematic analysis performed by the MOJAVE team at 15 GHz (see Lister et al. 2019). At the distance of 1 mas, we report a dip of the spectral index, indicative of the presence of an expansion region, possibly before the formation of a shock. Indeed, at 1.2 mas, we can see in the spectral index map an inverted spectral index region. The existence of standing shocks can cause such spectral behaviour. However, we note here that this spectral feature could also be not real, but an artifact due to the low flux of the jet in this region.

The spectral index image and the spectral index profile of the 43/86 GHz pair are presented in Fig. 4.12. In this case, we see a flat core, with the spectral index increasing slowly up to distances of 0.05 mas. Then the spectral index value decreases fast, to create a local minimum at 0.15 mas, and then shows a rapid increase, peaking at a distance of 0.25 mas. In this region, the spectral index becomes highly inverted, indicating that the component J6 is a standing shock, in agreement with Jorstad et al. (2005). The dip in the spectral index up to distances of 0.15 mas can be explained as an expansion region upstream of a standing shock. Further downstream, it flattens slightly and remains constant up to 0.35 mas.

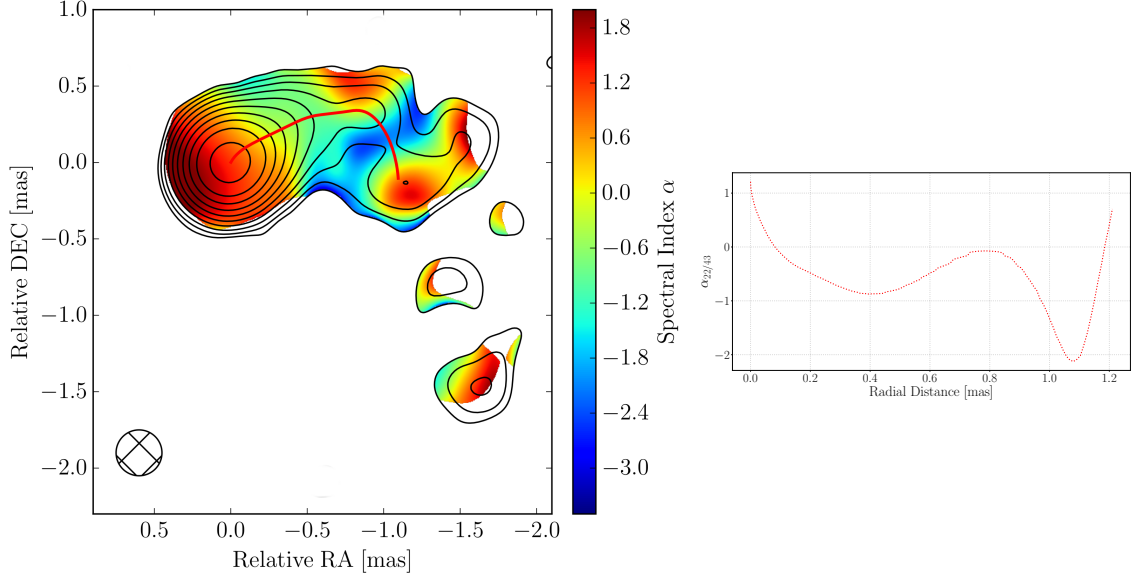


FIGURE 4.11: Left: Spectral index map between the 22 GHz and the 43 GHz. Right: The spectral index profile along the jet. The spectral index uncertainties, not displayed in this plot for illustration purposes, are based on a 10% error in flux density measurements propagated via error propagation theory.

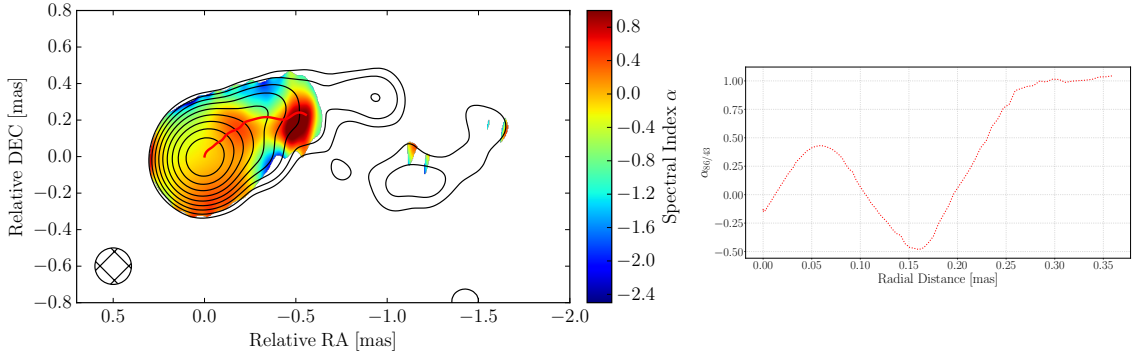


FIGURE 4.12: Left: Spectral index map between the 43 GHz and the 86 GHz. Right: The spectral index profile along the jet. The spectral index uncertainties, not displayed in this plot for illustration purposes, are based on a 10% error in flux density measurements propagated via error propagation theory.

## 4.4 Discussion

### 4.4.1 Magnetic Fields and Doppler Factor

Synchrotron emission in astrophysical sources indicates the co-existence of the magnetic field and relativistic electrons. The energy density of the particles can be expressed as

$$U_e = \int_{E_{min}}^{E_{max}} E N(E) dE = f(\alpha, \nu_1, \nu_2) L B^{-3/2}, \quad (4.6)$$

where  $L = 4\pi D_L^2 \int_{\nu_1}^{\nu_2} S d\nu$ ,  $f(\alpha, \nu_1, \nu_2)$  is a tabulated function defined as



$$f(\alpha, \nu_1, \nu_2) = 1.06 \times 10^{12} \left( \frac{2\alpha + 2}{2\alpha + 1} \right) \frac{\nu_1^{(1+2\alpha)/2} - \nu_2^{(1+2\alpha)/2}}{\nu_1^{1+\alpha} - \nu_2^{1+\alpha}} \quad (4.7)$$

where  $\nu_1$ ,  $\nu_2$  are the low and high-frequency cutoff frequencies, with typical values of  $10^7$ , and  $10^{11}$  Hz respectively and  $\alpha$  is the optically thin spectral index of the jet region (Pacholczyk 1970). Similarly, the magnetic field energy density, for a spherical region with radius  $R$ , is given by

$$U_B = B^2 / (8\pi) \frac{4}{3} \pi R^3 = B^2 \frac{R^3}{6}. \quad (4.8)$$

The total energy of a radio source can be expressed as a combination of Eq. 4.6 and 4.8 as

$$U_{tot} = (1 + \xi) U_e + U_B = (1 + \xi) f(\alpha, \nu_1, \nu_2) L B^{-3/2} + B^2 \frac{R^3}{6}, \quad (4.9)$$

where  $\xi$  is the ratio between electrons and heavy particles. The energy ratio that corresponds to electron-proton plasma is  $\xi \approx 2000$ , whereas the same ratio for an electron-positron plasma is  $\xi \approx 1$ . In this work, we will use a conservative value of  $\xi = 100$  (Pacholczyk 1970). The minimization of the total energy density, assuming equipartition between the magnetic field and the relativistic particles (Feng et al. 2006), can give us an estimation of the magnetic strength as

$$B_{eq} = (4.5 (1 + \xi) f(\alpha, \nu_1, \nu_2) L R^{-3})^{2/7} \approx 4 \times 10^{-4} \left( f(\alpha, 10^7, 10^{11}) (1 + z)^3 S_m \nu_m D_L^{-1} \theta^{-3} \right)^{2/7} (G), \quad (4.10)$$

considering that  $R = \frac{D_L \theta}{2(1+z)}$  and assuming that  $L = 4\pi D_L^2 \int_{\nu_1}^{\nu_2} S d\nu \approx S_m \nu_m$ . In this work, we considered the core to be unresolved if the size of the circular Gaussian component is smaller than the resolution limit (Lobanov 2005; Lee et al. 2008)

$$\theta_{min} = \frac{2^{1+\beta/2}}{\pi} \left( \pi \cdot \alpha \cdot b \cdot \ln 2 \cdot \ln \frac{SNR}{SNR - 1} \right)^{1/2} \quad (4.11)$$

where  $\alpha$  and  $b$  are the beam axes and  $\beta$  is a weighting function which is equal to 0 for natural weighting of the image and 2 for uniform weighting, and  $SNR$  is the component peak flux density to local rms ratio. For both components, C1 and C2, the estimated resolved size is  $\theta_{min} = 0.05$  mas. The spectral index values which we used for each component are the results of the spectral index decomposition in Table 4.3. By substituting  $D_L$  in Gpc,  $S_m$  in Jy,  $\nu_m$  in GHz and  $\theta = 1.8 \times \theta_{min}$  in mas, we obtain the equipartition magnetic field strength for each component.

On the other hand, the magnetic field of a homogeneous synchrotron self-absorbed region in the jet can be calculated as

$$B_{SSA} = 10^{-5} b(\alpha) \vartheta^4 \nu_m^5 S_m^{-2} \left( \frac{\delta^{2+\alpha}}{1+z} \right) (G). \quad (4.12)$$

TABLE 4.4: Columns from left to right: (1) Component ID, (2) magnetic field based on synchrotron self-absorption, (3) Equipartition magnetic field, (4) Equipartition Doppler factor.

Knot	$B_{SSA}(\delta)$ G	$B_{eq}(\delta)$ G	$\delta_{eq}$
C1	$0.010 \pm 0.004$	$1.39 \pm 0.11$	$2.9 \pm 0.2$
C2	$0.06 \pm 0.04$	$1.14 \pm 0.19$	$2.0 \pm 0.2$

Following the same approach as in Sec. 3.4.4, substituting the spectral parameters for each component and replacing the tabulated factor  $b(\alpha) = 1.8$  according to [Marscher \(1983\)](#), we compute the magnetic field from synchrotron self-absorption ( $B_{SSA}$ ) for the core region features.

The results obtained from the two methods for the features C1, C2 are presented in Table 4.4. This analysis showed a moderate magnetic field strength considering synchrotron self-absorption conditions in this jet region. In contrast, quite strong magnetic fields are needed to be present under the assumption of equipartition in the plasma.

The  $B_{eq}$  and the  $B_{ssa}$  magnetic field estimates show a different dependence on the Doppler factor. By combining Eq. 4.10 and Eq. 4.12 we can estimate the equipartition Doppler factor  $\delta_{eq}$ , which expresses the Doppler factor of the jet flow, based on the assumption that the source is at equipartition of energy between radiating particles and magnetic field. The equipartition Doppler factor can be computed by

$$\frac{B_{eq}}{B_{ssa}} \approx \left( \frac{\delta}{1+z} \right)^{6+\frac{16\alpha}{7}} \quad (4.13)$$

where  $\alpha$  is the optically thin spectral index, presented for each component in Table 4.3. All the above calculations are lying on various approximations. Hence, the results that we obtained can only be regarded as tentative. Nevertheless, the available evidence suggests that the Doppler factor values for each component are low considering a blazar jet. [Jorstad et al. \(2017\)](#), based on variability arguments, reports  $\delta = 8.6$  for a moving feature that is located  $\sim 0.3$  mas radial distance from the core. This diversity is an indication that in the core region the Doppler factor appears to be lower than further down in the jet. This could mean, similarly with the case of TXS 2013+370 in Chap. 3, either that the jet is bending away or that the Lorentz factor of the plasma flow is lower near the core. A third scenario, however, may be that the source is not in equipartition. For investigating the latter we are going to estimate the brightness temperature of each knot in Sec. 4.4.2. Lastly, if we combine our estimation of the  $B_{SSA}$  with a conservative Doppler factor value between 2-9, the resulting magnetic field strength of the same order of magnitude with the estimation of [Algaba et al. \(2012\)](#), who by using an indented method report  $B = 0.2$  G at 1 pc distance from the jet apex.

#### 4.4.2 Brightness Temperature Distribution

In this section, we calculate the brightness temperature for the core region, as well as along the jet, for all the VLBI knots. To determine this quantity, we employ the relation (e.g. [Pushkarev & Kovalev 2012](#))

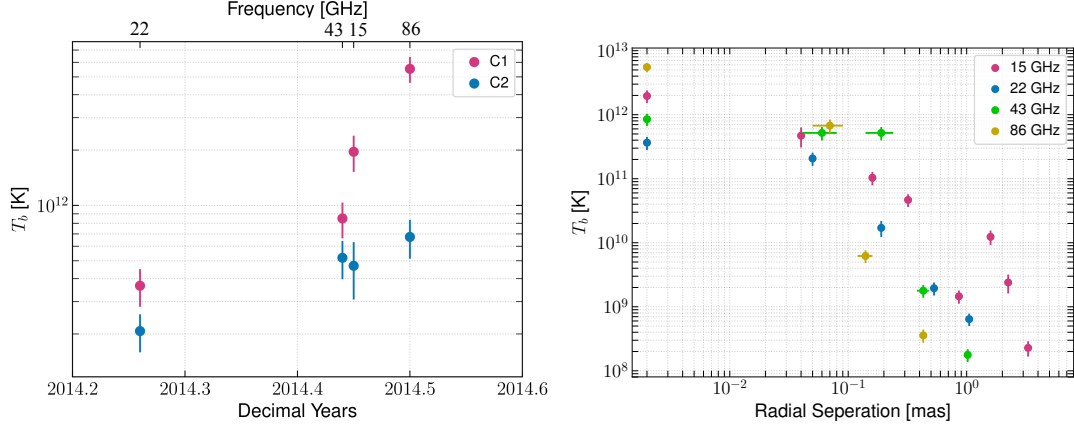


FIGURE 4.13: Brightness temperature distribution in OJ 287. Left: Core components C1 and C2 brightness temperature at all frequencies, during the April-May period. Right: Brightness temperature distribution with respect to radial separation from the core at all observing frequencies.

$$T_b = 1.22 \times 10^{12} (1 + z) \frac{S}{\theta_{\text{obs}}^2 \nu^2} \delta \text{ (K)}, \quad (4.14)$$

where  $S$  is the flux density of the component in Jy,  $\theta_{\text{obs}}$  is the size of the emitting region in mas,  $\nu$  is the observing frequency in GHz, and the factor  $(1 + z)$  corrects the cosmological effects on the observed brightness temperature. Owing to the high compactness of the cores, usually these features in VLBI images are unresolved. In the cases of unresolved components (where  $\theta \leq \theta_{\text{min}}$ ), the uncertainty on  $T_b$  is estimated considering  $\theta = \theta_{\text{min}}$  and the  $T_b$  value is considered as a lower limit. In the left panel of Fig. 4.13, the time evolution of  $T_b$  for the core region knots C1 and C2 is presented. Both features exhibit high  $T_b$ , ranging from  $10^{11}$  to  $10^{12}$  K. All the observations were performed during the evolution of a prominent radio flare. Figure 4.13 shows an increasing trend of the brightness temperature for components C1 and C2 with time. Typically,  $T_b$  for C1 is higher than C2; thus, we consider C1 to be the VLBI core. All the results are presented in Table B.1, Appendix B.

Assuming equipartition between the energy of the radiating jet particles and the energy of the magnetic field, the brightness temperature is characterized by the so-called equipartition limit of  $5 \times 10^{10}$  K (Readhead 1994). Nevertheless, often in extragalactic radio sources, brightness temperature values are measured to be close to  $10^{12}$  K. This value designates an upper limit, beyond which rapid inverse Compton cooling of the sources takes place by the upscattering of synchrotron photons. This process, known as inverse Compton catastrophe (Kellermann & Pauliny-Toth 1969), causes rapid electron energy losses. Readhead (1994) postulated a stricter upper limit of the order of  $10^{11.45}$ .

The intrinsic brightness temperature  $T_{\text{int}}$  is related observed one as  $T_{\text{int}} = T_b / \delta$ . Based on the lower limits obtained for C1 and C2, and assuming the Doppler factor from the analysis in Sec. 4.4.1,  $\delta_{\text{eq,C1}} = 2.9$  and  $\delta_{\text{eq,C2}} = 2$ , respectively, we obtain an intrinsic brightness temperatures ranging between  $10^{11} - 10^{12}$  K for C1 and  $10^{10} - 10^{11}$  K for C2. These results suggest that both components *are not in equipartition*, as it may be expected during a flaring event.

In the right panel of Fig. 4.13, the radial distribution of the observed brightness temperatures along the OJ 287 jet is displayed. The overall  $T_b$  distribution shows a steady

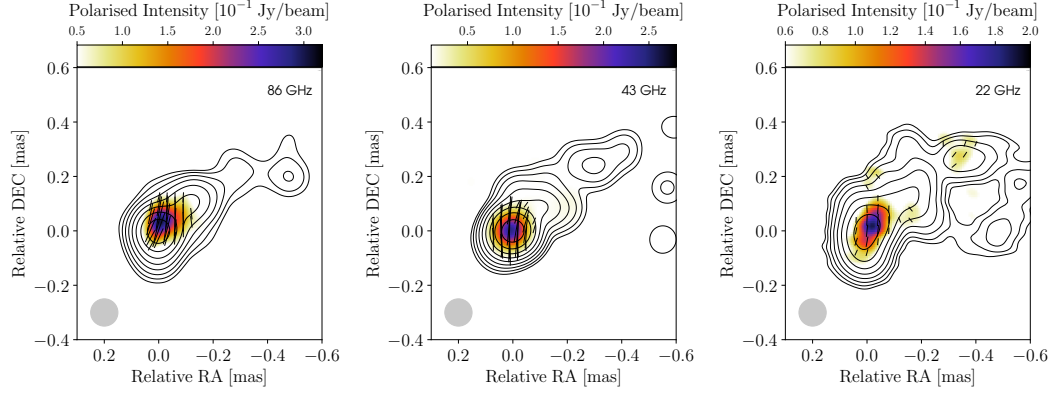


FIGURE 4.14: Comparison of the linearly polarized emission, total intensity and polarization angle  $\chi$  in the core region at 86, 43 and 22 GHz. All the images are super-resolved with a circular beam of 0.1 mas. The contour levels are 0.5, 1, 2, 4, 8, 16, 32, and 64% Jy/beam of the peak flux density (see Table 4.1).

decreasing trend. The core region is characterized by high  $T_b$  values, ranging between  $10^{11}$  K -  $10^{12}$  K. After the radial distance of 0.1 mas and down to 1.3 mas, the brightness temperature declines constantly from  $10^{10}$  to  $10^8$ . Typically, a blob of relativistic plasma, which is detected on a VLBI map as a bright jet component, loses a substantial amount of energy through synchrotron radiation and adiabatic expansion, as it propagates downstream of the jet. Those losses translate to a dimming of the knot and increasing size. These factors lead to a rapid decrease in brightness temperature along the jet.

### 4.4.3 Rotation Measure Analysis

#### 4.4.3.1 Magnetic Field Topology of the Core Region

In Fig. 4.14 the linear polarization distribution in the core region of OJ 287 at 22, 43 and 86 GHz is presented. All images are super-resolved in order to examine the fine polarization structure and the polarization angle  $\chi$ . Deliberately we omit to include 15 GHz data, as the convolving beam at this frequency is too large to reliably compare the super-resolved polarization image with the higher frequency images. The linearly polarized emission in the core region is significant at all images, with the 86 GHz image to exhibit the highest polarization level and the 22 GHz space VLBI image the lowest. The linearly polarized emission peaks coincide with the peak of the total intensity at all frequencies. The orientation of EVPAs reveals that  $\chi$  is not well aligned with the inner jet direction up to the distance of P1 (or C1 in total intensity models, see Sect. 4.3.2). The Faraday rotation analysis also indicates a RM gradient along the same direction of the jet swing.

At 22 GHz the core region consists of 2 polarized sub-components, namely P1 and P2. At higher frequencies (43 and 86 GHz), the core region appears only marginally resolved in polarized light. The dominant EVPA orientation is North-South, while the EVPA of the outer jet components is East-West. This change of orientation of the EVPAs with the observed jet flow suggests that the overall magnetic field topology (which is perpendicular to the EVPA) is toroidal, indicating the presence of a helical magnetic pinch.

We report the existence of polarized sub-components at the two opposite edges at the 22 GHz image. According to Gabuzda et al. (2014), this polarization structure could be

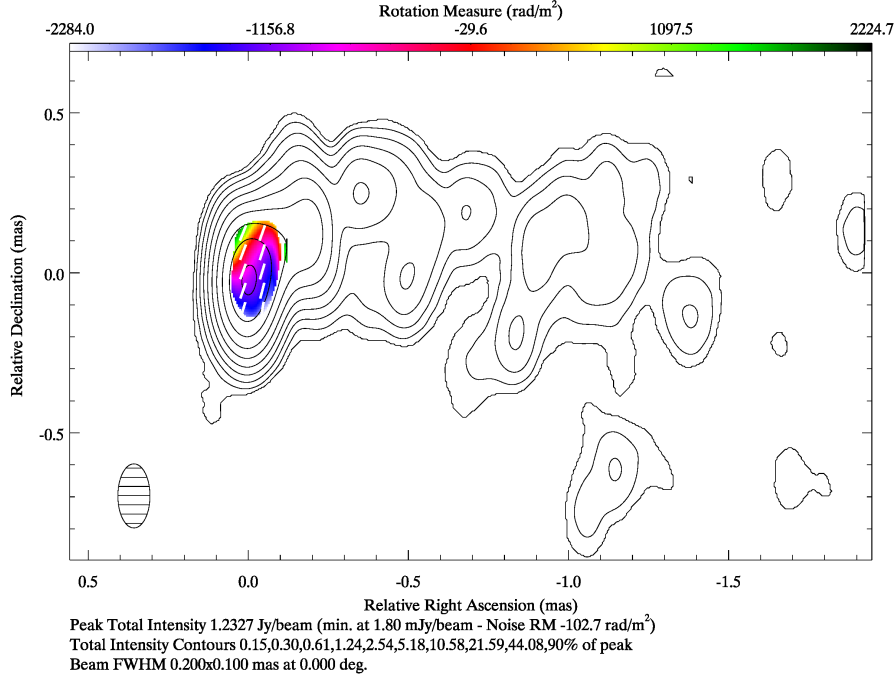


FIGURE 4.15: Rotation measure image, based on the combination of the 22, 43, and 86 GHz images.

resulted by a helical magnetic field. In such magnetic field configuration, the pitch angle of the helical magnetic field in combination with the viewing angle of the jet and the sky projection of the field, can appear transverse to the jet near the jet axis and longitudinal near the jet edges. This scenario is in agreement with the findings of Myserlis et al. (2018), which reports the existence of such a helical magnetic field along the OJ 287 jet.

Nowadays, more and more studies show that AGN relativistic outflows usually are not homogeneous, but it consists of multiple plasma layers with different physical characteristics. Several radio galaxies, like M 87 (Kim et al. 2018), Cygnus A (Boccardi et al. 2016) and 3C 84 (Giovannini et al. 2018; Kim et al. 2019) showed such a stratified structure, composed by a fast spine, surrounded by a slower and coaxial plasma sheath. Several cases of blazars have also reported showing limb brightening, an observational signature in total intensity images of such jet structure, like the blazar TXS 0506+056 (Ros et al. 2020), the blazar Mrk 501 (Koyama et al. 2016), the blazar PG 1553+113 (Lico et al. 2020) or the case of PKS 1510-089 (MacDonald et al. 2015). The polarized structure that OJ 287 shows at scales of 0.1 pc projected distance, can also be associated with a longitudinal magnetic field component of a sheath layer of a stratified jet.

#### 4.4.3.2 Rotation Measure from a Pixel-based Method

To study the intrinsic magnetic field orientation of OJ 287 we will first estimate the electric vector rotation introduced by the Faraday rotation effect (see 1.3.1.2). As introduced in Eq. 1.17 and 1.18, the intrinsic polarization vector,  $\chi_0$ , rotates when the polarized radiation is

passing through the magnetized plasma. Here, in order to estimate the RM gradient along the jet, we combine the VLBI images at 22, 43 and 86 GHz.

First, we aligned the three images by applying an image alignment method, based on a cross-correlation analysis of the total intensity images (Walker et al. 2000; Croke & Gabuzda 2008; Hovatta et al. 2012). From this analysis, we exclude the 15 GHz data, since the most prominent polarized features are located at a small radial distance from the core, in a region that the 15 GHz beam cannot resolve. All images were deconvolved with the same beam size of  $0.2 \times 0.1$  mas and with the same image dimensions and pixel size. The final RM image was obtained as described in Gómez et al. (2016), by performing a  $\lambda^2$  fit to the wavelength dependence of the EVPAs at each pixel, discarding the pixels with a poor fit based on the  $\chi^2$  criterion. An IDL routine performed the task, that estimated the minimum RM value for each pixel, taking into account the  $n\pi$  ambiguity problem. Specifically, a rotation measure value or image, is usually derived by fitting the quadratic wavelength dependence of the measured polarisation EVPAs. Since the EVPA is computed up to ambiguity of  $n\pi$ , where  $n$  stands for an integer number of vector rotations, there is a possibility of the appearance of misleading jumps, resulting from a false RM value. In Fig. 4.15, the pixel-based RM image of the source is presented.

By inspecting the RM distribution, we note that the RM could only be measured in the core region. A mild gradient in RM is observed in the longitudinal direction to the core centroid, ranging from  $-1100 \text{ rad/m}^2$  to  $-30 \text{ rad/m}^2$ . The largest RM values, of the order of  $-1100 \text{ rad/m}^2$ , are found in the area southeast of the core. In contrast, smaller values are obtained as the position angle increases towards the northwest direction, reaching values of  $\sim -30 \text{ rad/m}^2$ . Nevertheless, depolarization beam effects can severely complicate the interpretation of the RM gradients, as is shown by simulations (Broderick & McKinney 2010). It is commonly accepted that RM gradients within one beam width from the optically thick core are generally not significant. The variation of the EVPA as a function of frequency along the jet could be misinterpreted as a rotation measure, if the jet shows an opacity gradient (as suggested by Fig. 4.11 and 4.12). Also, we would like to mention that the core consists of sub-components, as can be seen in the high-resolution 22 GHz image (see Fig 4.6). Thus, blending effects could lead to an erroneous determination, and the real rotation may still be different. Therefore, we need higher resolution images of good fidelity to distinguish which scenario is valid.

Polarized light can exhibit Faraday rotation when it passes through the turbulent plasma flow inside the jet. However, significant RM can also be introduced by the intergalactic and Galactic medium, as they act as foreground Faraday screens. Thus, before we continue with the polarization analysis, their contribution must be removed. The intergalactic medium has embedded magnetic fields, strong enough for causing Faraday rotation (e.g. Akahori & Ryu 2011; Berné et al. 2012). The origin of these fields and their distribution is not yet well understood. Therefore, we cannot reliably estimate their contribution to polarization observations. Galactic magnetic field contribution, on the other hand, has been studied extensively to construct a complete picture of RM resulting from plasma in our Galaxy. In this work we will employ the external RM value for OJ 287, as estimated by Taylor et al. (2009), to be  $m_{ext} = (8.3 \pm 0.02) \%$  and  $RM_{ext} = 31.3 \pm 0.5 \text{ rad/m}^2$ .



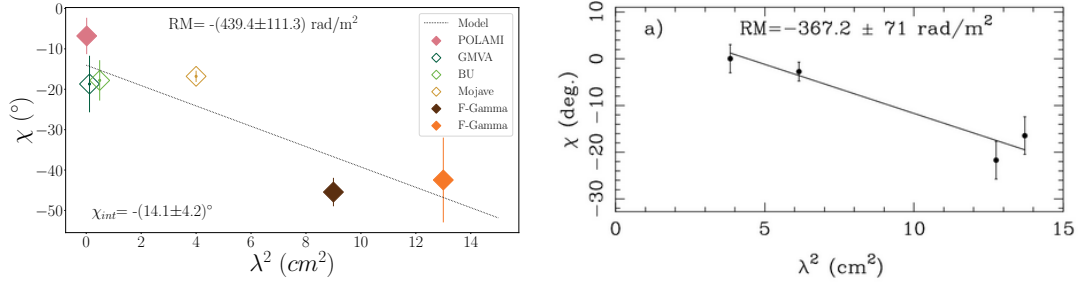


FIGURE 4.16: Electric vector position angle vs  $\lambda^2$ . The rotation measure corresponds to the gradient of the plotted lines. Left: Data from this work. Right: Rotation measure of the VLBI core between 4-15 GHz during 2006.32 (Hovatta et al. 2012).

#### 4.4.3.3 Rotation Measure Between 10.45-235 GHz

Besides the RM estimation based purely on VLBI images, an independent method for such estimation is to employ a large enough number of polarization-sensitive single-dish measurements at different frequencies. The RM is determined using a linear regression analysis via plotting the EVPA versus  $\lambda^2$  (see Fig. 4.16). For the case of OJ 287, we combined measurements at 235 GHz by POLAMI, 10.45, and 8.35 GHz from the F-Gamma project, combined with core measurements from the VLBI images, during the period March-May 2014. For this, we compute the spatially integrated EVPAs of the VLBI core region at 15, 43 and 86 GHz to be  $\chi_{15,core} = -17.3 \pm 2.4^\circ$ ,  $\chi_{43,core} = -19.0 \pm 1.1^\circ$ , and  $\chi_{86,core} = -20.0 \pm 1.2^\circ$ . We resolve the  $n\pi$  ambiguity following the work of Hovatta et al. (2012), which resulted in a rotation of  $-\pi$  for the 1 mm data. The obtained plot is shown in the left panel of Fig. 4.15. We report low RM value of  $-(439.4 \pm 111.3) \text{ rad/m}^2$ , which is comparable to the values found in the pixel-based analysis. By applying the correction for the external RM introduced by the intragalactic magnetic fields, the final rotation measure value is  $-(408.1 \pm 111.3) \text{ rad/m}^2$ . The results of this work are in good agreement with an independent core RM estimation based on simultaneous VLBI observations at 4-15 GHz, during 2006.32 (right panel of Fig. 4.15, Hovatta et al. 2012).

#### 4.4.3.4 Plasma Electron Density

The rotation measure can be expressed using the magnetic field and the electron density in

$$\frac{RM}{\text{rad/m}^2} = 8.1 \times 10^5 \int_{\text{source}}^{\text{telescope}} \left( \frac{n_e}{\text{cm}^{-3}} \right) \left( \frac{B_{||}}{G} \right) \left( \frac{dl}{pc} \right) \quad (4.15)$$

where  $n_e$  is the number density of the thermal electrons between the source of the synchrotron radiation and the telescope,  $B_{||}$  is the line-of-sight component of the magnetic field, and  $dl$  is the path length through the plasma from the source towards the observer. If we assume that the jet is uniform, the  $B$  is an average magnetic field strength, the RM is the same for all components and equal to  $408.1 \pm 11.3 \text{ rad/m}^2$ , and consider the mean angular size of each component  $\theta_m$  (see Table B.1), converted into path length of the synchrotron radiation through the jet, we can express Eq. 4.15 as



$$\frac{n_e}{\text{cm}^{-3}} \sim 1.2 \times 10^{-6} \left( \frac{RM}{\text{rad/m}^2} \right) \left( \frac{B}{G} \right)^{-1} \left( \frac{\theta_m}{\text{pc}} \right)^{-1}. \quad (4.16)$$

The results for components C1 and C2, considering  $B = 0.2 \text{ G}$  reveal a not very dense electron population in the innermost jet. Specifically, for the knot C1 is estimated that the electron density is  $0.03 \pm 0.01 \text{ particles/cm}^{-3}$ , and for component C2 drops to  $0.015 \pm 0.004 \text{ particles/cm}^{-3}$ .

#### 4.4.4 The Nature of the Core Features of OJ 287

The VLBI core is defined as the most compact and brightest feature located at the upstream end of the approaching flow (often showing the highest brightness temperature (Pushkarev et al. 2012)). Another characteristic of the VLBI core is that it exhibits a flat to inverted spectrum. It has been postulated that the radio core of a blazar often is associated with a standing recollimation shock (resulting from pressure imbalance between the jet and the surrounding) several parsecs downstream of the central supermassive black hole of the system or the unity opacity surface (e.g. Marscher et al. 2008; Cawthorne et al. 2013). In this thesis, we showed that knots C1 and C2 exhibit similar properties, with the characteristics of C1 to indicate that this is the core feature (that could be the  $\tau = 1$  surface or just another recollimation shock). We also note that C1 is more variable than C2 and has higher brightness temperature. The space-VLBI image of OJ 287 at the extreme resolution of  $10 \mu\text{as}$  (see Fig. 4.6) reveals that the inner region exhibits a higher complexity in the jet structure.

The nature of C2 is a matter of debate, as this feature is detected for the first time in this work, so we cannot eliminate the possibility that it is a shock, propagating along the jet, which was ejected in near past. However, the flat radio spectrum, the high brightness temperature and the similar magnetic field strength with knot C1, suggest that this feature can be a recollimation shock. In this case, one possible scenario of the origin of C2, is that it could be related to a change in the jet direction. For instance, Hodgson et al. (2017) and Agudo et al. (2010, 2012) report for the feature J6 (designated it as C1 and S respectively) to exhibit higher flux density than the core feature since the present study. The appearance of knot J6 is reported in 2004 by Agudo et al. (2012), accompanied by a change in the projected direction of the innermost jet by almost  $90^\circ$ .

## 4.5 Conclusions

In this thesis, we present a complete picture of the radio morphology of the blazar OJ 287 during April-May 2014. We were able to constrain the spectral index evolution and the magnetic field strength and topology along the jet. To achieve this goal, we employed state-of-art VLBI observations from 15 GHz up to 86 GHz, along with space-VLBI data. The results of this analysis can be summarized as follows:

- The VLBI imaging at 15, 43 and 86 GHz in combination with space-VLBI image at 22 GHz revealed that OJ 287 jet structure is characterized by a relativistic jet, which bends from North-South to East-West direction. In this thesis, we present for the

first time the source morphology at an extreme angular resolution of  $10\ \mu\text{as}$  ( $0.04\text{ pc}$  projected distance).

- From the 2D Gaussian modeling of the flux density distribution of OJ 287, we report the detection of a new feature, labeled as C2.
- The spectral decomposition from quasi-simultaneous VLBI observations allowed us to estimate the magnetic field strength of the core components to be of the order of  $\sim 0.2\text{ G}$ .
- The linear polarization analysis of the source showed that the jet is polarized, with the most of polarized components located near its origin.
- The polarization structure of the jet at  $22\text{ GHz}$  showed beside the main core polarization structure, sub-components at the opposite edges of the jet. This polarization structure could result from a helical magnetic field in the jet, which is in agreement with the findings of Myserlis et al. (2018). Thus, from our analysis we confirm the existence of a helical magnetic field in the inner jet region on scales of  $0.1\text{ pc}$  projected distance.
- A rotation measure analysis was also performed and revealed a marginal value of the order of  $\text{RM} \sim -400\text{ rad/m}^2$ . Moreover, we report that the magnetic field orientation in the core region is perpendicular to the jet, an indication of a poloidal magnetic field geometry.
- We suggest that the nature of the secondary core feature, C2, based on its spectrum, magnetic field strength, and brightness temperature, can be interpreted as a recollimation shock.

## Chapter 5

# Probing the Peculiar Jet Kinematics in the Blazar 3C 454.3

### 5.1 Introduction

The compact radio source 3C 454.3 is a well-known FSRQ (Lynds 1967), located at  $z=0.859$  (Jackson & Browne 1991) in the Pegasus constellation. The mass of the SMBH that resides in its center is estimated to be within a the range of  $0.5 - 1.5 \times 10^9 M_{\odot}$  (Woo & Urry 2002; Liu et al. 2006; Sbarrato et al. 2012), whereas it shows extreme variability across the electromagnetic spectrum. For this, it is also known as “crazy diamond” (Vercellone et al. 2009).

In late 2009, and during 2010, a series of bright  $\gamma$ -ray flares were recorded (Ackermann et al. 2010; Vercellone et al. 2011; Coogan et al. 2016), with the last one being the brightest  $\gamma$  ray flare ever observed in the sky ( $F=8.5 \pm 0.5 \times 10^{-5}$  photons  $\text{cm}^{-2} \text{s}^{-1}$ , Abdo et al. 2011). Time series analysis of high energy and broadband radio observations revealed that the  $\gamma$ -ray variability was also echoed in radio frequencies, and in other bands as well (e.g., Jorstad et al. 2010). In Fig. 5.1 we illustrate the flaring activity of the source from  $\gamma$  to radio regime. Based on monthly VLBI monitoring of the source at 43 GHz, Jorstad et al. (2013) reported that these outbursts are associated with the appearance and the propagation of two superluminal knots, labeled as K09 and K10. The viewing angle of those features is measured to be very well aligned to our line of sight, with  $1.35^{\circ}$  and  $0.4^{\circ}$ , respectively. The authors suggest that the

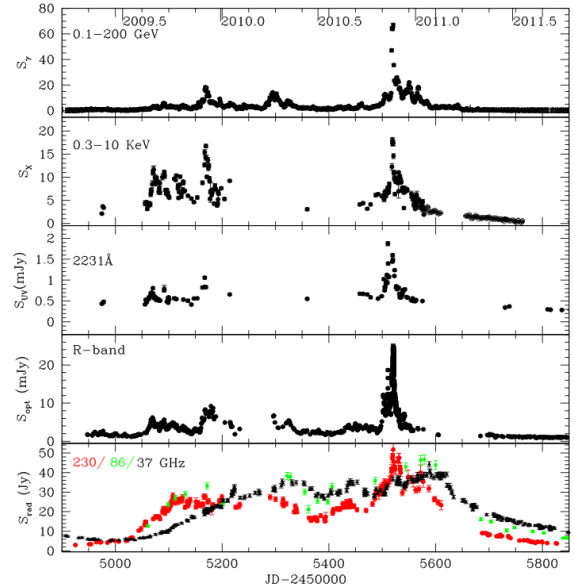


FIGURE 5.1: The remarkable, multi wavelength activity of 3C 454.3 during the period 2009-2011.

Plot credits: Jorstad et al. (2013).

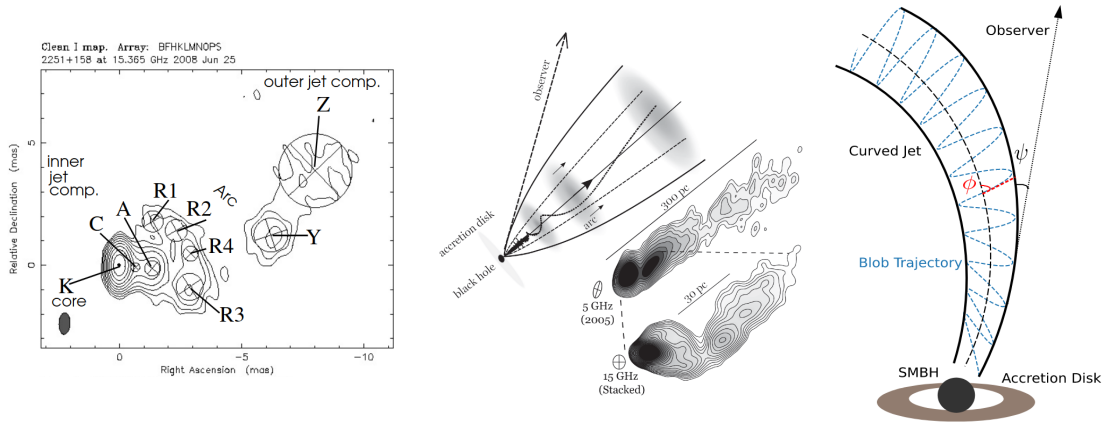


FIGURE 5.2: Left: The arc-like structure, detected in the jet of 3C 454.3. Middle: A cartoon of a physical model that explains such arc-like structures. Right: Conceptual illustration of a possible jet geometry that can cause the observed quasi-periodic oscillating activity in 3C 454.3. Image credits: [Britzen et al. \(2013\)](#), [Zamaninasab et al. \(2013\)](#), and [Sarkar et al. \(2020\)](#) respectively.

knots were ejected along different position angles with respect to the average jet axis, implying the possibility of a precessing jet nozzle.

[Britzen et al. \(2013\)](#) reported another remarkable behaviour of 3C 454.3. The kinematic analysis during the period 1995.57 to 2005.76, at 15 and 43 GHz, revealed the formation of an arc-like structure at a radial distance of  $\sim 2$  mas, which can be seen in the left panel of Fig. 5.2. This peculiar arc of VLBI components appeared to move with an apparent speed of  $\sim 9c$  for more than 14 years. A possible physical interpretation for the formation of this structure is suggested to be the ejection of an arc-shaped feature, which propagates along the jet. An alternative interpretation of this structure is jet precession, in which the jet axis points in different directions with time. In this model, the arc is the result of projection effects and relativistic amplification. A third possible scenario is the existence of a helical jet/magnetic field that is illuminated by a propagating shock, revealing extended and faint regions of the jet. [Zamaninasab et al. \(2013\)](#), based on multifrequency polarimetric VLBI imaging of the outflow postulated that an ordered helical magnetic field dominates the parsec-scale jet of 3C 454.3. Magnetohydrodynamic simulations showed that the observed jet structure could result from large-scale poloidal magnetic fields at the jet base that evolve into a helical magnetic field further downstream. Based on these results, the authors suggest that the arc-like structure started as “a sudden injection of energy” at the jet apex. This disturbance moved downstream on the jet, illuminating the faint outer regions (middle panel of Fig. 5.2). Other alternative scenarios, such as jet nozzle precession with a period of  $\sim 14.5$  yr was suggested by [Qian et al. \(2014\)](#). The driving force in such a system, according to the authors, is a spinning SMBH in the center of the AGN, surrounded an accretion disk. The jet precession in this model is caused by frame-dragging (Lense-Thirring effect). Many studies also examined the scenario of a binary black hole system, which its orbital motion causes the jet precession ([Gu et al. 2001](#); [Vol’Vach et al. 2008](#); [Li et al. 2015](#)). These scenarios, however, are affected by severe limitations, as they described by many parameters and lying on many assumptions ([Zamaninasab et al. 2013](#); [Qian et al. 2014](#)). Recently, [Sarkar et al. \(2020\)](#) reported the detection of quasi-periodic oscillation in the  $\gamma$ -ray and optical flux variability of 3C 454.3. Among the different physical models that they tested, the most plausible interpretation of this quasi-periodicity is to be caused by

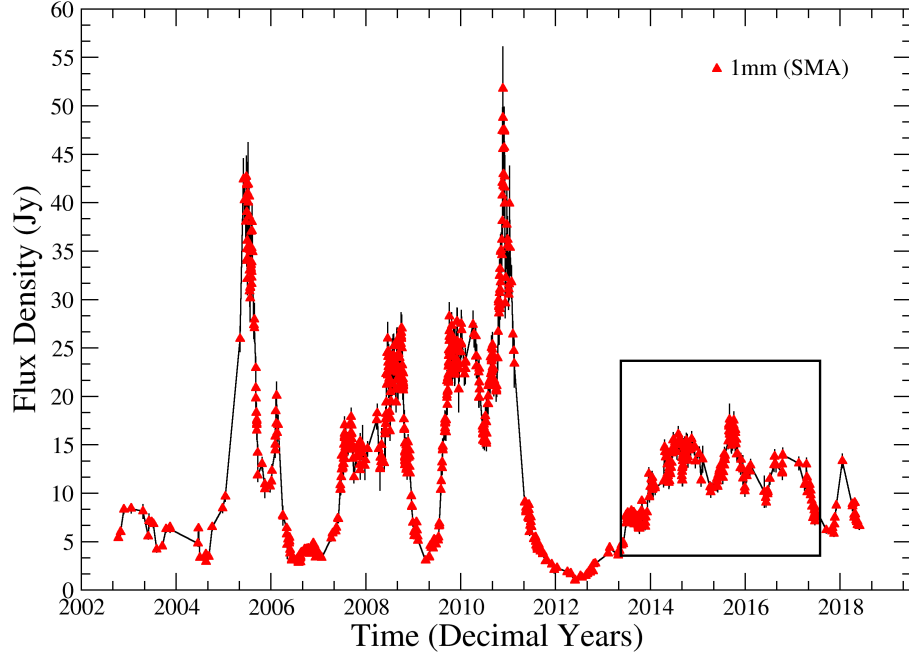


FIGURE 5.3: Flux density variability of the source at 235 GHz, as observed by the SMA during the period 2002-2018. The box indicates the time range that we are going to study in this chapter.

the motion of a jet component along a helical path in a curved jet (see the right panel of Fig. 5.2).

Next to the large scale morphology and the extreme flux variability, one of the most interesting features of this jet is a quasi-stationary component at  $\sim 0.6$  mas radial separation from the core. The first report of the existence of this knot came by [Pauliny-Toth et al. \(1987\)](#), who presented results of an extensive monitoring program of 3C 454.3, covering about five years of observations at 10.7 GHz. In addition to moving features, the authors report the presence of a pair of quasi-stationary components, one situated at 0.6 mas core separation, and a second one at 1 mas. [Gómez et al. \(1999\)](#) few years later, attempted to investigate the nature of this component by suggesting that it is either the result of a jet bending towards our line-of-sight or a recollimation shock. Later studies confirmed this feature and described its interaction with moving disturbances in the jet (e.g., [Jorstad et al. 2001, 2005](#)). To date, the real physical nature of this knot is still an active area of research.

In this work, we present a five-year structural and kinematic analysis of the source at 86 GHz, during the observing interval 2013-2017. Supplementary to the high-resolution images, high cadence 43 GHz VLBI images were also studied. The combination of this data enabled us to construct a detailed description of the morphological evolution, variability properties, and intrinsic parameters of the radio jet, during a stage of lower activity (see Fig. 5.3). For our calculations, we adopt the following cosmological parameters:  $\Omega_M = 0.27$ ,  $\Omega_\Lambda = 0.73$ ,  $H_0 = 71 \text{ km s}^{-1} \text{ Mpc}^{-1}$  (similar to those used by [Lister et al. 2016](#), and references therein), which result in a luminosity distance  $D_L = 5.489 \text{ Gpc}$  and a linear-to-angular size conversion of  $7.7 \text{ pc/mas}$  for a redshift of  $z=0.859$ .

## 5.2 Observations and Data Reduction

### 5.2.1 VLBI Observations

The VLBI data set we used for this work is comprised of observations at 43, and 86 GHz. In total, 44 images were made to study the jet kinematics of 3C 454.3 during the period 2013-2017. The 86 GHz observations were obtained with the GMVA (see Sec. 2.1.4.1), as a complementary part of the “Millimeter-wave Imaging of the Gamma-Ray Emitting Regions of Blazar Jets” monitoring program at 43 GHz <sup>1</sup>. The VLBA 43 GHz data are publicly available from the archive of the VLBA-BU-Blazar program, which includes regular monthly observations of 24 radio bright AGN. We re-analyzed 36 epochs that cover a period from 2013 to 2017, and which were observed during the time range covered by the 86 GHz data. A summary of the individual VLBI observations is presented in Table 5.1.

#### 5.2.1.1 VLBI Data Calibration and Imaging

The data reduction (total intensity and polarization calibration), the imaging and the model fitting was performed in the same manner as described in Sec. 2.2, 3.2, 4.2 and 4.2.3. The *a-priori* calibration of the 43 GHz data was carried out by the BU team (Jorstad et al. 2005), whereas the imaging and the Gaussian modeling of the source was performed by me. The resulting images are shown in Fig. 5.4 and Fig. 5.5, while the parameters of the Gaussian components are reported in Tables C.1 and C.2 in Appendix C.

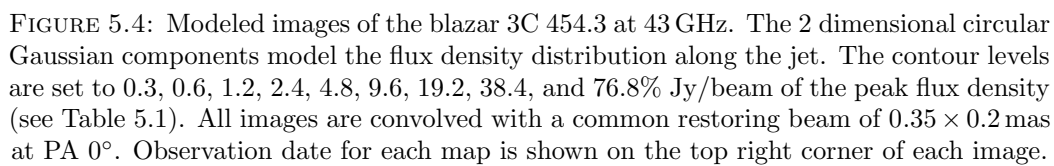
## 5.3 Data Analysis and Results

### 5.3.1 Source Structure and Jet Kinematics

Our imaging at 43, and 86 GHz shows that 3C 454.3 exhibits a very complex structure. In all images, the compact regions in the inner jet, as well as faint structures of the jet are visible (see Fig. 5.4 and Fig. 5.5). The most prominent features of the jet are the core and a group of knots, located at 0.6 mas radial distance, along the eastern-western direction. During the observing interval 2013-2017, the knots sometimes appear brighter than the core feature. We determined the kinematics of the individual jet knots in a similar manner, described in Chapters 3 and 4, by using the parameters of the Gaussian components derived from the model fits of each data set. The component cross-identification between the observing epochs (and frequencies) was done by comparing their positions, flux densities, and sizes. The identified features are labeled in order of decreasing distance from the core. The angular proper motion  $\mu$  of the components was computed through linear fits of their radial core separation as a function of time. Lastly, the apparent speed,  $\beta_{\text{app}}$ , was computed by following Eq. 3.1.

**43 GHz:** Figure 5.4 presents the 43 GHz contour images with super-imposed circular Gaussian model-fit components. At this frequency, the source is well modeled by a core component (labeled as Core), which is present in all images, and a number of moving and stationary features. In Fig. 5.6 we plot the core separation of the jet features. In the

<sup>1</sup><https://www.bu.edu/blazars/vlbi3mm/index.html>





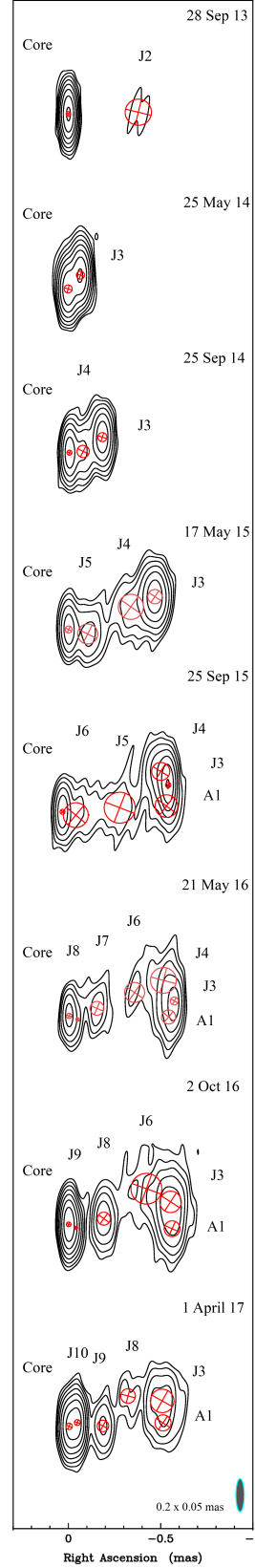


FIGURE 5.5: Modeled images of the blazar 3C 454.3 at 86 GHz. The two-dimensional circular Gaussian components model the flux density distribution along the jet. The contour levels are set to 0.5, 1, 2, 4, 8, 16, 32, and 64% Jy/beam of the image peak flux density (see Table 5.1). All the images are convolved with a common beam of  $0.2 \times 0.05$  mas at PA  $0^\circ$ .

TABLE 5.1: VLBI Observational Parameters. Columns from left to right: (1) Observing frequency, (2) Observing year, (3) Participating antennas, (4) Major axis of the convolving beam, (5) Minor axis of the convolving beam, (6) Position angle, (7) Image peak flux density, (8) Noise level, (9) Image total flux density. The sub-script to the VLBA indicates the number of antennas that participated. <sup>a</sup> : Fort Davis not participate. <sup>b</sup> : North Liberty not participate. <sup>c</sup> : Ovro not participate. <sup>d</sup> : Hancock not participate. <sup>e</sup> : Los Alamos not participate. <sup>f</sup> : Mauna Kea not participate. <sup>g</sup> : Hancock and Saint Croix have not 3mm receivers.

Frequency (GHz)	Epoch (yyyy-mm-dd)	Array Elements	$b_{\text{maj}}$ (mas)	$b_{\text{min}}$ (mas)	PA (deg)	$S_{\text{peak}}$ (Jy)	rms (mJy/beam)	$S_{\text{total}}$ (Jy/beam)
43	2013.56	VLBA <sub>9</sub> <sup>a</sup>	0.32	0.15	-4.2	4.84	0.58	6.36
43	2013.65	VLBA <sub>9</sub> <sup>a</sup>	0.36	0.14	-9.2	5.31	0.73	6.47
43	2013.87	VLBA <sub>9</sub> <sup>a</sup>	0.36	0.14	-4.42	8.33	0.73	9.90
43	2014.15	VLBA <sub>9</sub> <sup>a</sup>	0.35	0.14	-6.07	9.95	0.84	12.07
43	2014.37	VLBA <sub>9</sub> <sup>b</sup>	0.32	0.13	-6.07	12.71	0.76	18.03
43	2014.47	VLBA <sub>10</sub>	0.32	0.14	-1.51	21.1	0.69	32.04
43	2014.57	VLBA <sub>10</sub>	0.32	0.13	-4.08	8.30	0.96	15.01
43	2014.72	VLBA <sub>9</sub> <sup>d</sup>	0.37	0.13	-4.12	7.84	0.78	15.90
43	2014.99	VLBA <sub>10</sub>	0.35	0.13	-6.95	4.64	0.23	13.54
43	2015.12	VLBA <sub>10</sub>	0.57	0.18	24.6	6.76	0.59	14.11
43	2015.28	VLBA <sub>10</sub>	0.41	0.18	13.1	7.46	0.99	16.18
43	2015.36	VLBA <sub>10</sub>	0.37	0.17	10.3	7.89	1.12	15.81
43	2015.44	VLBA <sub>10</sub>	0.33	0.14	-6.81	8.32	0.61	17.45
43	2015.58	VLBA <sub>10</sub>	0.36	0.14	-11.5	8.36	0.35	17.08
43	2015.73	VLBA <sub>10</sub>	0.34	0.14	-8.67	8.07	0.70	16.57
43	2015.92	VLBA <sub>10</sub>	0.39	0.15	-11.7	6.56	0.61	14.70
43	2016.08	VLBA <sub>10</sub>	0.32	0.13	-6.26	5.71	0.42	14.24
43	2016.31	VLBA <sub>10</sub>	0.31	0.13	-4.12	5.68	0.86	15.46
43	2016.44	VLBA <sub>10</sub>	0.35	0.14	-3.87	5.11	0.69	14.05
43	2016.51	VLBA <sub>10</sub>	0.35	0.14	-7.77	5.65	0.48	14.52
43	2016.68	VLBA <sub>10</sub>	0.46	0.15	-19.6	6.87	0.86	18.54
43	2016.80	VLBA <sub>10</sub>	0.35	0.15	-4.33	4.05	0.89	13.90
43	2016.90	VLBA <sub>10</sub>	0.33	0.14	-5.02	4.62	0.73	12.47
43	2016.97	VLBA <sub>10</sub>	0.37	0.13	-9.31	5.72	0.86	16.13
43	2017.09	VLBA <sub>10</sub>	0.38	0.14	-7.41	10.71	0.70	19.67
43	2017.29	VLBA <sub>10</sub>	0.34	0.14	-6.39	7.02	0.41	13.17
43	2017.37	VLBA <sub>10</sub>	0.32	0.13	-5.25	10.91	0.95	21.32
43	2017.60	VLBA <sub>10</sub>	0.32	0.12	-9.48	6.98	0.45	15.57
86	2013.74	VLBA <sub>7</sub> <sup>eg</sup> +YS+PV+EB+ON	0.28	0.05	-11.8	4.36	0.64	5.50
86	2014.40	VLBA <sub>7</sub> <sup>bg</sup> +EB+ON+PB	0.27	0.04	-4.55	4.28	0.79	11.72
86	2014.73	VLBA <sub>8</sub> <sup>g</sup> +PV+EB+PB+GB	0.28	0.05	-9.65	4.72	0.98	14.81
86	2015.38	VLBA <sub>7</sub> <sup>bg</sup> +EB+ON+PB	0.28	0.05	-9.65	1.86	0.58	7.17
86	2015.73	VLBA <sub>7</sub> <sup>bg</sup> +EB+ON+GB+KVN	0.28	0.07	-11.7	5.75	0.95	15.2
86	2016.39	VLBA <sub>8</sub> <sup>g</sup> +EB	0.23	0.06	-10.9	2.70	0.70	9.70
86	2016.74	VLBA <sub>7</sub> <sup>fg</sup> +EB+ON+KVN+GB	0.21	0.05	-7.7	3.67	0.97	8.38
86	2017.25	VLBA <sub>8</sub> <sup>g</sup> +EB+ON+PV+GB	0.28	0.05	-7.95	3.67	0.17	8.86

following, we describe the source kinematics in detail. At the beginning of the observed sample time range, the source was characterized at 43 GHz by the core feature and the knots J1 and J2, moving with an apparent speed of  $\beta_{\text{appJ1}} = 12.6 \pm 3.7$  and  $\beta_{\text{appJ2}} = 6.1 \pm 0.9$  respectively.

In early 2014, a new component emerged from the VLBI core, labeled as J3. This new feature shows a remarkable brightness enhancement during its propagation downstream of the jet. During the same period, the core feature appears to flare (see lower right panel of Fig. 5.6). The motion of J3 is characterized by an apparent speed of  $\beta_{\text{appJ3}} = 21.5 \pm 0.5$ . Gradually, in September 2014, the feature J3 becomes brighter than the core, and besides an intermediate flux-density drop early 2015, it continues to be the brightest feature until late 2016. In December 2014, another new component appeared, designated as J4. This feature

seems to follow a similar path as knot J3, with an apparent speed of  $\beta_{\text{appJ4}} = 24.6 \pm 4.7$ . The knot J4 appears to be considerably fainter than J3. The trajectory of J3 and J4 appears to deviate significantly from the path of knots J1 and J2, with the latter propagating along a position angle of  $\sim -100^\circ$ , whereas the newer knots at  $\sim -65^\circ$ . The position angles of the components paths are shown in Fig. 5.7.

A few months later, in May 2015, we report the ejection of yet another feature from the VLBI core. The speed of J5 is measured to be  $\beta_{\text{appJ5}} = 19.2 \pm 1.4$ . The position angle to its trajectory is  $\sim -87^\circ$ , different than the two previously detected trajectories. Prior to the appearance of J5, the core component showed a moderate flux-density enhancement. During the period June-August 2015, the knot J4 appears to exhibit a dramatic altering of its position, by moving upwards of J3. Feature J3 on the other hand, appears to reach the 0.6 mas radial distance from the core (labeled as Region S) since April 2015, and stops there until the ending of our observing interval. Furthermore, a new feature becomes visible in this region, which is labeled as A1. The nature of this knot differs from the propagating disturbances that we discussed until now, as it appears further downstream of the core and shows negligible motion. In December 2015 we detected for the first time feature J6. This jet disturbance appears to propagate with an apparent speed of  $\beta_{\text{appJ6}} = 26.1 \pm 42$ . The observation of J6 in only two epochs limits the accuracy of its speed determination.

Until April 2016, J6 has been blended with J4 and could not be detected afterward. In the same epoch, J7 has emerged from the core. Its ejection position angle is similar to the knots J3 and J4. In July 2016, the new feature J8 can be modeled at a distance of 0.15 mas from the core and afterward is propagating downstream of the jet with a speed of  $\beta_{\text{appJ8}} = 15.4 \pm 5.1$ . Before its appearance, the core feature increased its flux density, which dropped at the time of our 43 GHz observation. Knot J7 in this image is blended with component J4. In November 2016 we detected knot J9. Similarly, with components J5 and J8, the core exhibits again an increased flux density stage, which declines at the time of the detection of the knot. The apparent speed of J9 is  $\beta_{\text{appJ9}} = 14.5 \pm 5.1$ , whereas its trajectory follows a similar orientation as the trajectory of J5.

Since February 2017, knot J4 cannot be modeled anymore. From our 43 GHz kinematic analysis, we infer that J6 is the fastest component of the jet, moving with an apparent speed of  $\beta_{\text{appJ6}} = 26.1 \pm 42$ , whereas J3 is the second reliably fastest knot with an apparent speed of  $\beta_{\text{appJ3}} = 21.6 \pm 0.5$ . We note that for all components, we perform a linear fit to describe the motion of the knots.

**86 GHz:** Figure 5.5 shows the model-fit images of the source at the high resolution that 86 GHz VLBI observations can offer. The jet structure can be modeled by a compact core that is continuously present. Besides this feature, we report the detection of one new feature in every GMVA image. This suggests that the time sampling of the GMVA observations is not sufficient to trace the rapid structural variability seen in 3C 454.3. The overall morphology of the relativistic outflow is described by a straight jet up to  $\sim 0.25$  mas and afterward shows a gentle bending to the northwest direction until the region S.

In September 2013, the source appeared very compact and only the brightest parts of the jet can be seen. Besides the core, knot J2 is visible too. The component J3 dominates the source during the May 2014 GMVA epoch, with its flux density exceeding the core flux density by 117%. Its trajectory follows a northwest direction in the jet. Half a year later, knot J4 is resolved, whereas J3 propagates downstream of the jet. We point out that along all the GMVA images, the flux density of the core, J3 and J4 show a very similar variability pattern (see lower left panel of Fig. 5.6). In May 2015, J5 appeared to emerge

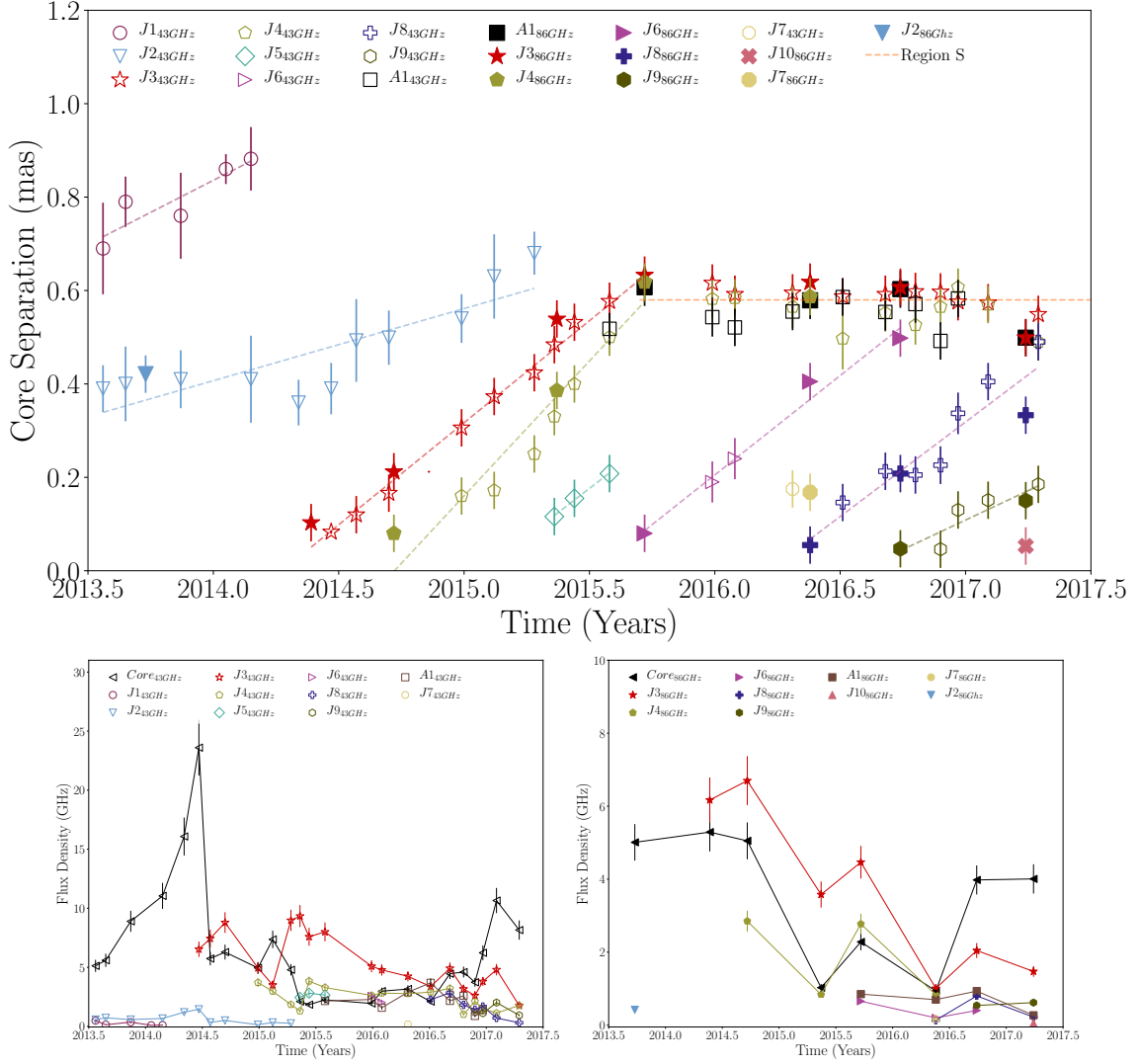


FIGURE 5.6: Upper panel: Plot of the radial core separation of the identified jet components in 3C 454.3. Lower panels: Flux density evolution of the VLBI components at 43 GHz (left) and 86 GHz (right).

from the core, to a northwestern direction, significantly different than the direction of J3 and J4. Six months later, in September 2014, the bright region S can be decomposed into a blend of 3 individual components, namely J3, J4, and A1. Also, we witness knot J6 to be just detached from the core and moving with an apparent speed of  $\beta_{\text{appJ6}} = 19.6 \pm 2.8$ . In the next two epochs, knots J7, J8 and J9 appeared, whereas in April 2017, a new feature, designated as J10, is ejected in the same direction as J3.

In summary, the source 3C 454.3 shows a complex jet and remarkable structural variability during the period 2013-2017. We report the detection of 7 new jet components. The most prominent component among them is J3, which appears to be often brighter than the core, both at 43 GHz and 86 GHz. The moving knots J3 and J4 seem to become stationary, when they reach region S. The ejection times for several jet components could be estimated and is reported in Table 5.2. The component separation and flux density variability as a function of time are presented in Fig. 5.6. The physical interpretation of the wide range of apparent speeds and on the implications for the intrinsic jet parameters (e.g., Doppler factor and viewing angle) will be discussed in Sect. 5.4.1.

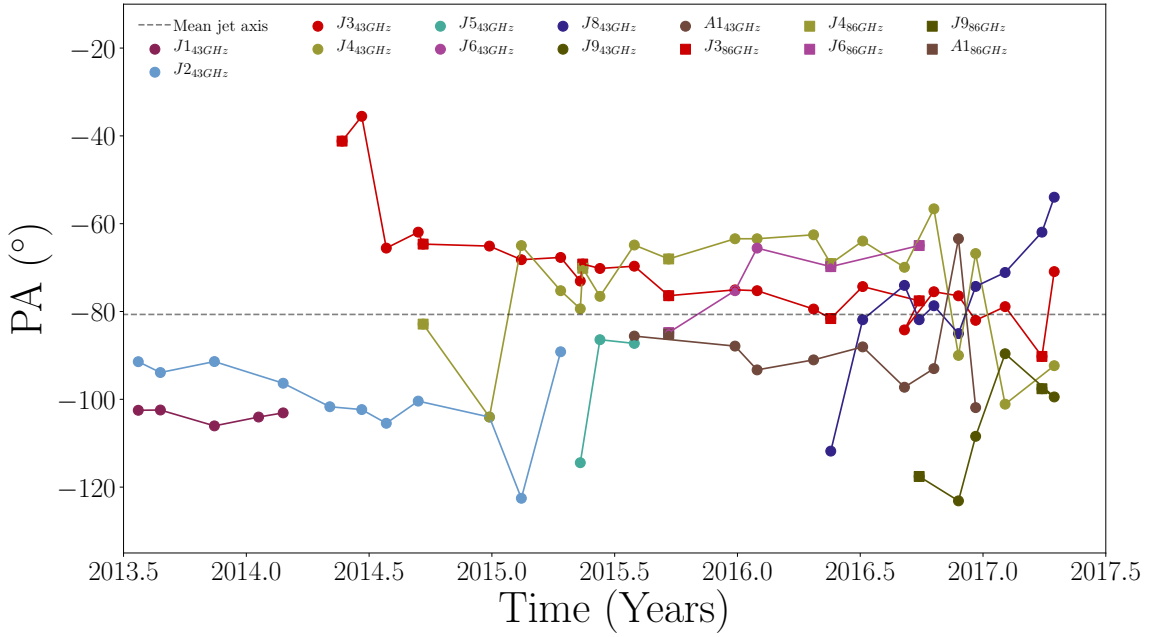


FIGURE 5.7: Position angle evolution of all model-fit components versus time. The new knots were ejected along different position angles, with respect to the average jet axis (dashed line).

## 5.4 Discussion

### 5.4.1 Intrinsic Jet Parameters

The observed apparent speeds in 3C 454.3, as we discussed in Sec. 5.3.1, range from 8–26 c. These measurements are in agreement between 43 & 86 GHz. In some cases, however, sparse data at 86 GHz leads to a less accurate determination of  $\beta_{\text{app}}$ . The physical cause of such speed diversity is uncertain.

A first hypothesis that can explain such variations of the apparent speed is to be geometry-dependent. In such a case,  $\beta_{\text{app}}$  can appear to vary as a function of the line-of-sight orientation. Indeed, Fig. 5.4 indicates that the lower speed values correspond to components J1 and J2, where the highest apparent speed values are registered for knots that are propagated upstream of this region. This observable indicates that the jet until region S exhibits a smaller viewing angle. After this region, the jet alters its direction to point slightly away from the line of sight. We also note that in blazar-type objects, owing to the small viewing angle of the overall jet funnel, even small directional changes of the plasma flow are significantly amplified in the observer’s frame (see Sec. 1.6). [Jorstad et al. \(2005\)](#) reported beyond region S, trajectories of moving components separate into two different groups. One in the northwestern part of the jet and the other towards the southwestern jet direction. The position angle difference between those two projected trajectories was estimated to be  $\sim 70^\circ$ . The suggested interpretation of this diversity by the authors is that the direction of the jet near the location of 0.5–0.6 mas lying very close to the line of sight, thereby producing substantial differences in projected trajectories of moving components beyond this region, even if the intrinsic trajectories are similar (see Sec. 5.4.3).

TABLE 5.3: Cross-identification of jet features between this work and previous studies.

This work	Knot			
	A1	J8	J2	J1
<a href="#">Jorstad et al. (2017)</a>	C	K16	B10	B11
<a href="#">Gomez et al. (1999)</a>	St	-	-	-
<a href="#">Cawthorne &amp; Gabuzda (1996)</a>	K7	-	-	-
<a href="#">Pauliny-Toth et al. (1987)</a>	2	-	-	-

Another explanation is that the Lorentz factor is not constant along the jet, but varies as a function of core separation. In this case, the terminal Lorentz factor is reached on the scales probed by cm-VLBI, where the faster apparent speeds are measured.

Ultimately, it is likely that both geometrical effects and intrinsic variations of the bulk speed cause the observation of this wide range of apparent speeds in 3C 454.3. Based on this premise and the results of the kinematic analysis, we estimate in the following some of the intrinsic jet parameters, in a similar manner as in Chapter 3. We also note that speed values are comparable between 43 and 86 GHz, which argues against frequency-dependent jet stratification. Our findings are presented in Table 5.2.

As a final remark, we report that the newly detected features are ejected along different position angles (see Fig. 5.7). This finding points towards more complicated ejection scenarios, for instance, jet precession (nozzle and/or accretion disk), or rotating jet instabilities (e.g., [Agudo 2009](#)).

TABLE 5.2: Kinematic parameters of the identified jet components at 43, and 86 GHz. Columns from left to right: (1) Component ID, (2) Observing frequency, (3) Number of data points, (4) Proper motion, (5) Apparent speed, (6) Doppler factor, (7) Viewing angle, (8) Ejection time. For components J9 at 86 GHz and J6 at 43 GHz the estimation of the ejection time was obtained based on their appearance time in the VLBI images.

Knot	Freq. (GHz)	N	$\mu$ (mas/year)	$\beta_{\text{app}}$ (c)	$\delta$	$\theta$ ( $^{\circ}$ )	Ejection time (Years)
J9	43	4	$0.31 \pm 0.11$	$14.5 \pm 5.1$	$14.5 \pm 5.1$	$3.9 \pm 1.4$	$2016.55 \pm 0.13$
	86	2	$0.21 \pm 0.21$	$9.8 \pm 9.3$	$9.9 \pm 9.3$	$5.8 \pm 5.8$	$\geq 2016$
J8	43	7	$0.46 \pm 0.07$	$21.4 \pm 5.1$	$21.4 \pm 5.1$	$2.7 \pm 1.2$	$2016.26 \pm 0.1$
	86	3	$0.31 \pm 0.05$	$14.5 \pm 2.3$	$14.5 \pm 2.3$	$3.9 \pm 0.6$	$2016.01 \pm 0.13$
J6	43	2	$0.56 \pm 0.91$	$26.1 \pm 42.0$	$26.2 \pm 41.9$	$2.2 \pm 3.5$	$\geq 2015$
	86	3	$0.42 \pm 0.06$	$19.6 \pm 2.8$	$19.6 \pm 2.8$	$2.9 \pm 0.4$	$2015.49 \pm 0.09$
J5	43	3	$0.41 \pm 0.03$	$19.1 \pm 1.4$	$19.2 \pm 1.4$	$3.0 \pm 0.1$	$2015.13 \pm 0.15$
J4	43	14	$0.52 \pm 0.11$	$24.7 \pm 4.7$	$24.7 \pm 4.7$	$2.36 \pm 0.45$	$2014.72 \pm 0.07$
	86	4	$0.52 \pm 0.05$	$24.3 \pm 2.3$	$24.3 \pm 2.3$	$2.4 \pm 0.2$	$2014.73 \pm 0.08$
J3	43	19	$0.46 \pm 0.01$	$21.5 \pm 0.5$	$21.5 \pm 0.5$	$2.7 \pm 0.1$	$2014.48 \pm 0.09$
	86	7	$0.41 \pm 0.03$	$19.1 \pm 1.4$	$19.2 \pm 1.4$	$3.0 \pm 0.2$	$2013.93 \pm 0.09$
J2	43	11	$0.17 \pm 0.02$	$8.1 \pm 0.9$	$8.1 \pm 0.9$	$8.1 \pm 1.1$	$2009.95 \pm 0.46$
J1	43	5	$0.25 \pm 0.08$	$11.6 \pm 3.7$	$11.6 \pm 3.7$	$4.5 \pm 1.3$	$2010.92 \pm 0.29$

### 5.4.2 Comparison with Previous Studies

The quasar 3C 454.3 is an archetypal object, well known for its remarkable activity. Since 1987, the source structure is studied by [Pauliny-Toth et al. \(1987\)](#), who performed an extensive monitoring program at 2.8 cm. These observations revealed the existence of superluminal components, with apparent speeds ranging between 10 and 16 c. Quasi-stationary components were also detected, to be situated at 0.6 (labeled as 2) and 1 mas radial distance from the core, respectively. A few years later, [Cawthorne & Gabuzda \(1996\)](#) conducted polarimetric imaging of the source at 6 cm, which confirms the existence of a stationary feature at about 0.6 mas, and they designated it as component K7. In the same year, [Kemball et al. \(1996\)](#) presented the first polarimetric VLBI image of the source at 43 GHz. In the image, three prominent components could be distinguished. The core, the stationary component previously found by [Pauliny-Toth et al. \(1987\)](#) and [Cawthorne & Gabuzda \(1996\)](#), and a new component located between them.

A few years later, [Marscher \(1998\)](#), based on eleven images at 43 GHz, reported the existence of another stationary feature at about 0.2 mas from the core. The extensive kinematic study of 3C 454.3 by [Pauliny-Toth \(1998\)](#) reveals apparent knot speeds of the order of 32 c in the outer jet region, whereas from 2 up to 4 mas in the core region. [Gomez et al. \(1999\)](#) present three-epoch polarimetric images at 22 and 43 GHz, in which the source is described by a core component and another prominent feature, labeled as St. The latter is situated at 0.6 mas core separation. Knot St can be cross-identified with components 2 and K7 from [Pauliny-Toth et al. \(1987\)](#) and [Cawthorne & Gabuzda \(1996\)](#), respectively. Worth mentioning that [Gomez et al. \(1999\)](#) reports that St is located at a different position angle than previously reported, which can be an indication of an inner jet swing towards the north. Another study that reported the existence of this feature came by [Jorstad et al. \(2001\)](#). The authors report that besides the core component, are detected 3 additional moving features, designated as B1, B2, and B3, and a stationary component at 0.6 mas radial distance, labeled as C. The apparent motion range of the moving components until they reach the 0.6 mas radial distance seems to vary from 6.5 to 25 c, although they follow similar trajectories. [Jorstad et al. \(2017\)](#), [Jorstad et al. \(2010\)](#) and [Jorstad et al. \(2013\)](#) report also the existence of component C at approximately the same location.

In this study, we suggest that component A1 can be identified with the stationary component C. The two components are similar in flux, position and size among the studies mentioned above. The fact that A1 could not be modeled until J3 and J4 were well positioned in the region, can be explained by the fact that A1 during that period was faint and below the detection threshold in our images. Moreover, [Jorstad et al. \(2017\)](#) reports the existence of components B10 and B11. Here, we suggest that those features could be identified with J1 and J2. Additionally, the new knot K16, which is reported by both at [Jorstad et al. \(2017\)](#) and [Weaver et al. \(2019\)](#), can be identified with knot J8. We would like to mention also the study by [Coogan et al. \(2016\)](#). The authors, based on correlation analysis between  $\gamma$ -ray and radio flux variability during the period May-June 2014 (after the appearance of knot J3 in our VLBI image), put constraints on the location of the emission region to be  $1.3 \times R_{\text{BLR}}^{\text{out}}$ . This location is well outside of the broad-line region. The combination of our findings with [Coogan et al. \(2016\)](#), point towards a scenario in which shock-in-jet interactions of component J3 triggered the flaring activity of 3C 454.3 during that period.

In Table 5.3 we summarize the component identifications from the aforementioned studies.



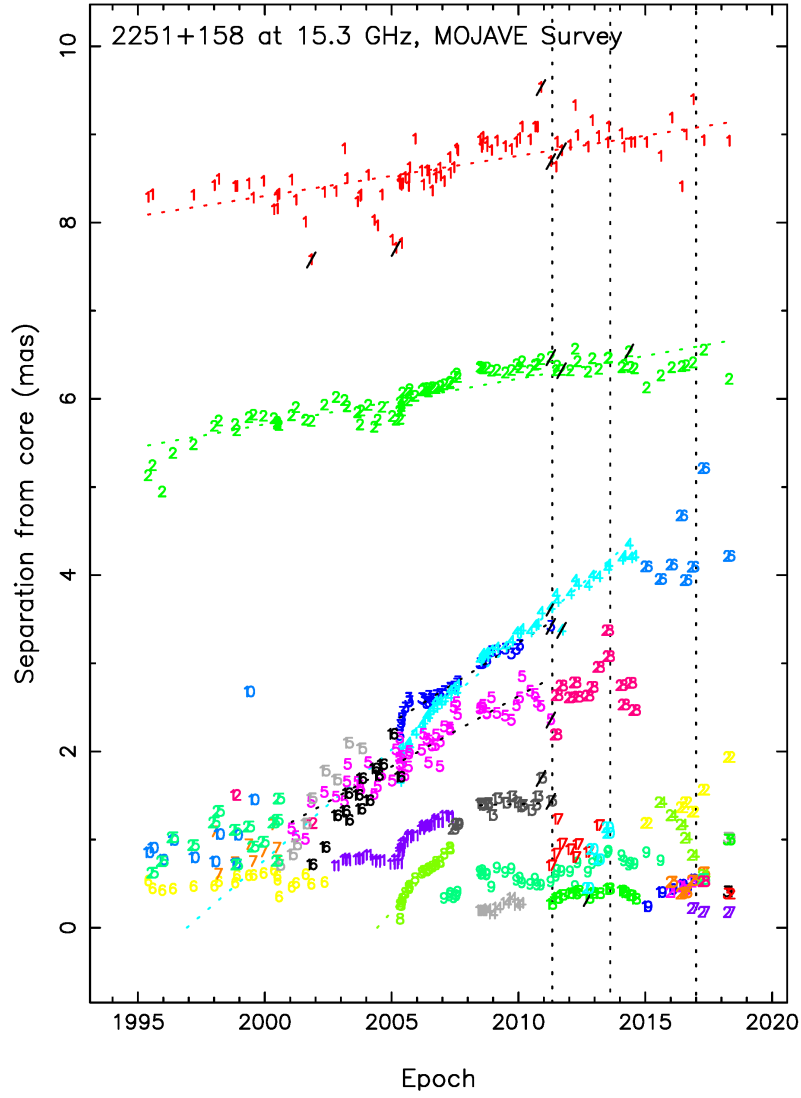


FIGURE 5.8: Parsec-scale jet kinematics of 3C 454.3 at 15 GHz over a period of 25 years.  
Credits: [Lister et al. \(2018\)](#) and Lister et al. 2020 in preparation.

### 5.4.3 The Nature of Region S

The behavior and the properties of this jet region remain elusive, since the first VLBI image of 3C 454.3. In this work, the region S shows peculiar kinematics, ranging from being too-faint-to-be-modeled at the end of 2013, to consist of 3 stationary features during 2015-2016. The apparent stationarity of components in this region could be caused due to jet geometry or due to intrinsic jet physics.

A first hypothesis that can explain this unusual behaviour in region S is a local jet bend toward the line of sight. Indeed, the jet of 3C 454.3 is already observed to bend toward the northwest direction, further downstream, at about 4-5 mas from the core (e.g., [Lister et al. 2009a](#)). [Jorstad et al. \(2005\)](#), base on VLBI polarimetric observation at 43 GHz presents evidence that feature C is lying very close to our line of sight. The remarkable polarization levels of C that are reported in the aforementioned work also supports this scenario. Remarkable is also the kinematics of the region, as moving knots that are detected beyond

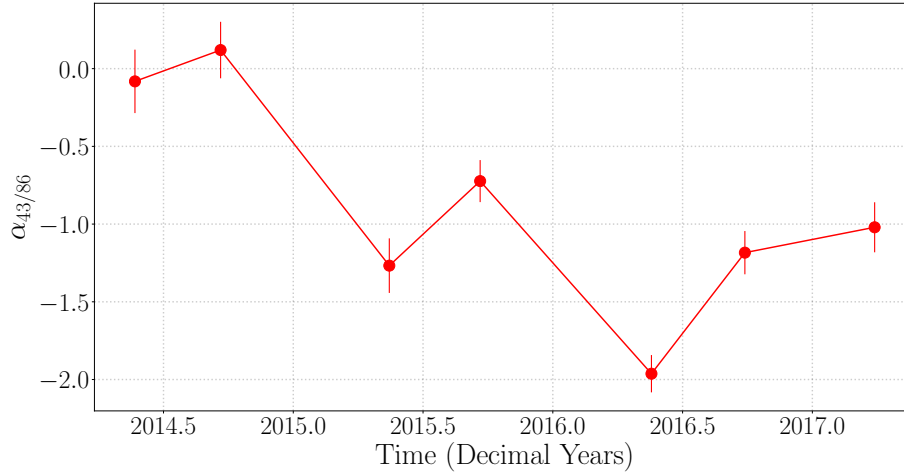


FIGURE 5.9: The two-component spectrum of region S.

C, appear to follow trajectories that correspond to two different groups, a northwestern and southwestern. The projected difference between those trajectories is measured to be  $70^\circ$ . This particular result, is consistent with the scenario in which the direction of the jet near C is lying very close to our line of sight. Such geometry can introduce substantial differences in projected trajectories of moving components indeed, even if the intrinsic trajectories differ only slightly. If this hypothesis is valid, a systematic change in the apparent motion of all components that are passing this region would be expected to be seen in this work too. Indeed, beyond region S the components become invisible. VLBI observations of the large scale structure during the period 1995-2020 (see Fig. 5.8) show that during this time-range, the outer jet faded already at 15 GHz, preventing detection of jet motion. However, the hypothesis that the stationarity in region S is caused by geometry appears unlikely, because we observe the components to reach region S with very high speed. Additionally, the knots that reach this region, although appear to stop, get fainter. If the viewing angle was coming close to zero, the Doppler factor would rise too. However, J3 and J4 light curves appeared to decline as they reach S, by a similar amount of -30%. This contradiction leads us to conclude that a small viewing angle cannot characterize region S.

An alternative scenario that may explain the nature of region S, is that components merge, and region S may be a recollimation shock. [Gomez et al. \(1999\)](#) supported this scenario by postulating that the stationarity of component St (region S in this work), corresponds to a recollimation shock. Based on the kinematic and flux density characteristics both of the moving knot and the stationary one, the authors report that the apparent speed, and the flux density of both correspond to a blending event of a moving feature that is passing through a standing shock. This is consistent with the stationarity which we find in our data. The second argument in favor of a recollimation shock is that the spectral index of the region is relatively flat. A standing shock can be described as a high plasma compression, where second-order Fermi acceleration is taking place. From such an emitting region, we expect a flat spectrum of the order of -0.25 [Kirk et al. \(2000\)](#). To test this, we sum up the fluxes of the existing components (in order to avoid possible problems in the component identification due to blending). We present the spectrum of these two components in Fig. 5.9. In our observational interval, the spectral index of the region appears to be extremely variable, covering a range between 0 to -2, which is not consistent with the simple hypothesis of a standing shock. Another observational signature of a recollimation shock would be the existence of an ordered and parallel to the jet magnetic

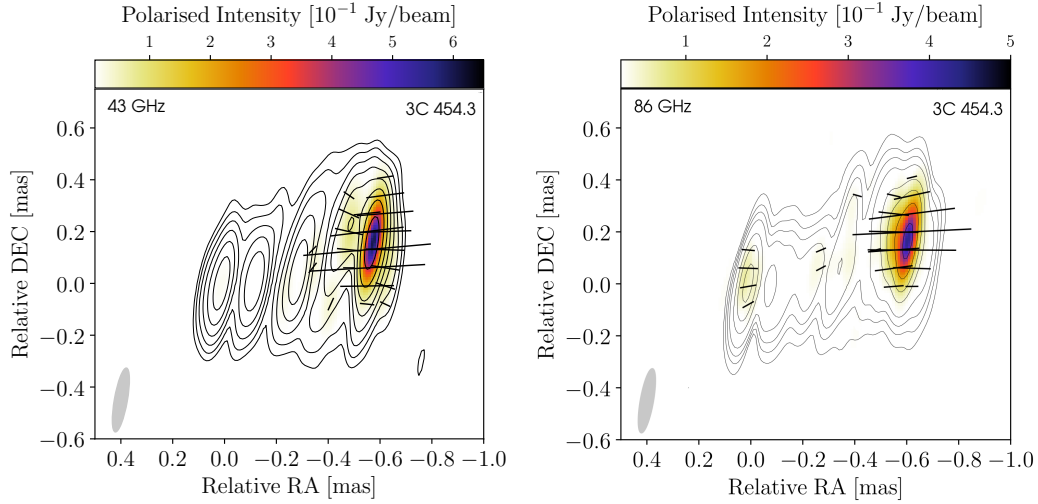


FIGURE 5.10: Polarization images of 3C 454.3 in September 2015. The contour level is set at 0.5%, 1.0%, 2.0%, 4.0%, 8.0%, 16.0%, 32.0%, 64.0% of the total intensity peak flux (see Table 5.1) and is the same for both plots. The restoring beam is common and equal to  $0.25 \times 0.05$  mas/beam at  $PA = -10^\circ$ .

field. Polarization images of the source at 43 GHz and 86 GHz during September 2015 (see Fig. 5.10), reveal that the EVPAs are ordered and parallel to the jet, indicating a strong perpendicular magnetic field component, which support the recollimation shock scenario.

Alternative scenarios, however, can also explain the observables of region S. For instance, local density enhancements can be triggered or caused by Kelvin Helmholtz of some MHD instabilities. Such local density enhancements can have similar behaviour with what we detect in this study. Nevertheless, plasma instabilities are mainly produce moving patterns, which is in contrast with the observed stationarity that we observe.

Overall, we report that the nature of S cannot be determined throughout this analysis. A more detailed understanding is needed of the complex jet kinematics. This can be obtained with higher cadence 86 GHz data (e.g., a dense polarimetric GMVA monitoring) in combination with sophisticated hydrodynamic or MHD jet modeling, which is in our plans.

#### 5.4.4 Trailing Components?

Agudo et al. (2001) and Aloy et al. (2003), based on relativistic hydrodynamic simulations, reported the appearance of trailing features that are formed behind a major flow disturbance that is propagating along the jet. The plasma simulations show that strong jet perturbations interact with the underlying jet and the external medium as they propagate. This can lead to the formation of shocks and rarefactions regions that follow the main perturbation and are triggered by plasma instabilities. Observationally, such a type of knot appears to split from the primary component and will not necessarily emerge from the core (see Fig. 5.11).

This scenario is in good agreement with the nature of component J4, and probably also J7, as their kinematic properties match expectations for the above phenomenon. Indeed, the J4 trajectory can be explained better as a result of splitting from component J3, whereas

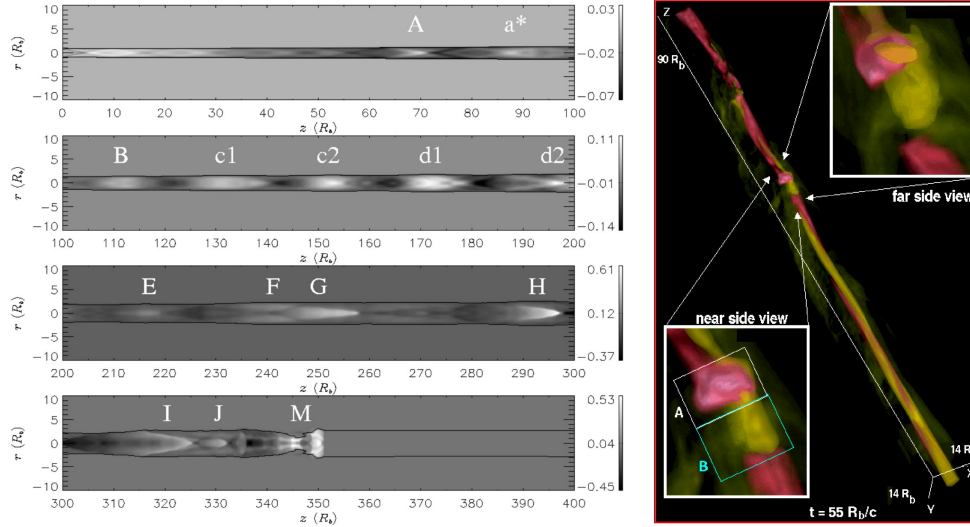


FIGURE 5.11: Numerical 2D and 3D hydrodynamic simulations of propagating disturbances in a jet. Left: Multiple conical shocks appear to form behind a strong shock-wave which is propagating downstream of the jet. Right: A prominent disturbance was ejected into a precessing relativistic jet, with a result the formation of trailing components in the wake of the primary superluminal component. Credits: [Agudo et al. \(2001\)](#) and [Aloy et al. \(2003\)](#) respectively.

J7 could be of the same nature, by following knot J6. However, for the latter component, the lack of additional VLBI observations does not allow us to draw a conclusion.

The primary motivation for postulating that J4 and possibly also J7, are trailing components results from two findings: i) their trajectories being very similar to the “leading” components (J3 and J6 respectively), and ii) ejection at periods without preceding core flare (see lower right panel of Fig. 5.6).

Trailing components behind dominant radio knots have been observed in the past for several objects ([Gómez et al. 2001](#); [Jorstad et al. 2005](#)). Nonetheless, the expected velocities of the trailing shocks are often smaller than the velocity of the main perturbation. Radio knot J4 does not appear to follow this apparent speed pattern. Additionally, the detailed trajectory of J4 in Fig. 5.6 and Fig. 5.7, indicates a different slope between J3 and J4. This behaviour can be an indication that J3 and J4 are two independent components, which are ejected close in time. If there is no systematic error in our kinematics, this is a strong point against the trailing component scenario of J4 and J7. In the case that J3 and J4 are two different ejected components, the slightly different speeds and trajectories that could be an indication that J4 is a component that is moving on the other side of a stratified jet.

An additional criterion that a trailing knot should meet is that it should exhibit different polarization properties from those of the primary blob, as it is related to a conical shock. The future continuation of this project will study in-depth the polarization properties of each knot and will help to answer the question of the presence of trailing shocks.

## 5.5 Conclusions

In this study, we presented a detailed description of the radio morphology and jet evolution of the blazar 3C 454.3 during a 5-year period, which is a period of reduced activity after a prominent flare of  $\sim 50$  Jy. For this purpose, we employed state-of-art VLBI observations at 7 mm, as well as, monitoring of the structural variations at 3 mm (8 GMVA maps that presented in this work for the first time). This unique data set allowed us to investigate the kinematic properties of the jet structural evolution on sub-mas scales. Based on our analysis we could draw conclusions about the jet orientation and witness new component ejections. The results can be summarized as follows:

- In this work we present an image sequence of the innermost jet region of 3C 454.3 at the extreme resolution of 86 GHz ( $50 \mu\text{as} = 0.22 \text{ pc}$  projected distance). The jet morphology consists of a complex structure, with jet components that move on slightly different trajectories in East-West direction.
- We report the appearance of 7 new VLBI components during the period 2013-2017, which move with apparent speeds in the range of  $8 - 26 c$ .
- Components J4 and J7 seen to follow the paths of their precursors J3 and J6, respectively. This is consistent with the expectation for trailing jet features, which corresponds to rarefaction regions behind a strong shock.
- We report the presence of a region (labeled as S) where moving features appear to become stationary and merge. Better resolution and time sampling are needed in order to follow the merging process in more detail. Until then, the physical interpretation of the stationary region S remains ambiguous, with possible interpretations involving local jet bending, standing shock or plasma instabilities, with the most probable scenario, region S to be characterized by a superposition of more than one phenomena.

## Chapter 6

# Concluding Remarks and Future Perspectives

The existence of highly relativistic jets in AGN are an excellent example of the most powerful and extreme physical phenomena in the Universe. Accreting SMBHs, strong magnetic fields and plasma accelerated to relativistic speeds are some of the fundamental cosmic ingredients to create jets. However, several crucial processes are not yet fully understood. As we describe in Sec. 1.3.1, the only chance that astronomers have to study these spectacular objects is through the light that they emit. This emitted radiation carries information about the processes, as well as the location where these events happened. In this thesis, we focus on our analysis on three mm-bright targets, namely TXS 2013+370, OJ 287 and 3C 454.3. All three objects are members of a particular class of AGN, called blazars. The main characteristic of a blazar is its high variability across the electromagnetic spectrum, which is enhanced by an orientation almost “face-on” to Earth. This geometrical coincidence gives us the unique opportunity to probe very small variations in the jet outflow, which are magnified, due to relativistic amplification and aberration. Data obtained via very-long baseline interferometry at cm- and mm- wavelengths were employed. Notably, the GMVA data at 86 GHz enabled us to make images with an ultra-high angular resolution of  $\sim 50 \mu\text{as}$ . In addition, data from space-VLBI with the *RadioAstron* satellite, provided us with jet images characterized by a world recorded angular resolution of up to  $\sim 10 \mu\text{as}$  at 22 GHz.

The science goal of this work is to shed some light on a number of open questions related to AGN and blazar physics. Specifically, in this thesis, we provide information for the following key physical aspects:

- The location of the blazar zone of gamma-ray production and the origin of the seed photons reservoir.
- The nature of the mm-radio core.
- The topology of the magnetic field and its strength close to the jet apex, in the region where jets are launched.
- The nature of moving and standing features, which are observed on sub-pc scales in these AGN jets.

The study of the blazar TXS 2013+370 aims towards a better understanding of the first question. A combination of broadband radio variability data, together with  $\gamma$ -ray variability and a 10-year, multifrequency VLBI monitoring of the source, allowed us to put constraints on the location of the high-energy emission. The primary mechanism of  $\gamma$ -ray production in blazars is via inverse Compton scattering, where photons are up-scattered by relativistic electrons. Current scenarios which address the location of the blazar zone discuss whether the IC photon field is externally or internally to the jet. The first case is based on the framework of external Compton processes (EC), which suggest that the  $\gamma$  rays are produced using up-scattered photons from the accretion disk, photons of the BLR, or IR photons from the molecular torus (e.g., Donea & Protheroe 2003; Costamante et al. 2018). In these scenarios, the high-energy production region is located below the outer radius of the molecular torus ( $\sim 100$  pc for a clumpy torus, Alloin (2006)). The alternative scenarios, which use jet-internal effects, postulate that  $\gamma$  rays can be produced several parsecs downstream from the SMBH, e.g. when a moving knot interacts with the underlying plasma flow inside the jet. In this case, the seed photons for the  $\gamma$ -ray production are the synchrotron photons from the jet itself. *In this work, we found, based on a 10-year data sample, that in TXS 2013+370, the blazar zone is located  $\leq 2$  pc downstream of the jet apex. This location indicates as  $\gamma$ -ray mechanism the EC process, with a possible photon reservoir from the BLR or the photon field from the torus. On top of this, we report a geometrical transition of the jet width from parabolic to conical shape at about 4 pc projected distance downstream from the jet apex.* Worth mentioning that Beskin & Nokhrina (2006) predict that such a transition should take place at the location where the kinetic energy flux of the jet plasma becomes equal to the Poynting energy flux. The cross-correlation analysis of the broad band variability of the flux density, as well as quasi-simultaneous VLBI images of the source at different frequencies, revealed no strong core-shift. The core of a jet could be either the  $\tau=1$  surface of the jet at a given frequency, or a standing, conical recollimation shock, which is situated downstream of the jet (Marscher 2008). Our data suggest the latter, though we cannot rule out higher order combinations of the aforementioned effects. In any case, the VLBI core in most blazars is usually the brightest and the most compact feature, which is present in the jet (Pushkarev et al. 2012). In some sources, however, this is not always true. One of these exceptional cases is the blazar OJ 287, which we summarize in the following section.

With the study of one of the best candidates of a super-massive binary black hole (SMBBH), OJ287, we were able to address the second and third blazar research topic in the aforementioned list. Utilizing the extreme angular resolution from space-VLBI at 22 GHz, in combination with the high resolution and opacity penetration depths from mm-VLBI (both at 86 GHz and 43 GHz), we imaged the inner core region and detect a secondary core feature, that dominates the image. By super-resolving the 15 GHz and 43 GHz images a bit, we were able to model this feature also at lower frequencies. We investigated the nature of this knot, as well as the nature of the fainter, innermost core component. Luckily, during our observing interval, a prominent flare took place. This event allowed us to study the brightness temperature evolution of each component. This showed that the southern most jet feature exhibits the highest value of all other jet components. The spectral decomposition of both features, as well as their polarization signature and the magnetic field strength, suggests that both are probably recollimation shocks. Additionally, the  $10 \mu$ s-resolution image showed that the core region of OJ 287 is characterized by a more complex fine structure, comprising several sub-components. *Thus, the core region of OJ 287 is characterized by a number of sub-components, in which the brightest of them*



*does not correspond to the innermost one. The nature of these features is probably related to recollimation shocks that are located in front of the unity opacity surface.* Another significant outcome of this analysis is the polarization structure of the jet at 22 GHz. The linear polarization image of the source showed beside the main core polarization structure, sub-components at the opposite edges of the jet. Based on similar observational studies in other blazars (e.g., Gabuzda et al. 2014), this polarization structure could result from a helical magnetic field in the jet. In such a magnetic field configuration, the pitch angle of the helix, in combination with the viewing angle of the jet and the sky projection of the field, can appear transverse near the jet axis and longitudinal near the jet edges. This scenario is in agreement with the findings of Myserlis et al. (2018), who also suggested the presence of helical fields from polarization variability data of this source. Thus, from our analysis *we confirm the existence of a helical magnetic field in the inner jet region on scales of 0.1 pc projected distance.*

The third part of this project focuses on the structural evolution on sub-parsec scales of the blazar 3C 454.3. This source, which recently was named “crazy diamond” (Vercellone et al. 2009), is an archetypal blazar that was always at the center of the astronomers’ attention due to its very prominent flux variability across the whole electromagnetic spectrum. Here we studied the source during a relatively quiescent stage, which, however, still revealed a rich kinematics. During the observing period 2013-2017, we report the appearance of 7 new jet features. However, the trajectories of the new knots appear to be unusual, in the sense that their motion appears to stop when they reach a region at  $\sim 0.6$  mas separation from the VLBI core. This specific region, is known as quasi-stationary since 1987 (Pauliny-Toth et al. 1987) and has been in the focus of earlier studies. During our observing interval, we report that the new, superluminal jet components decelerate and blend when they reach this jet region and vanish beyond. From the study of the spectral index evolution, the kinematics and the flux density evolution, we finally conclude that this region is unlikely to be a simple stationary recollimation shock. Although the polarization properties suggest a magnetic field orthogonal to the jet, which in principle could be due to shock compression, the flux density variability and spectral properties point more towards a plasma instability. Hence, we suggest that *the nature of the 0.6 mas region is a superposition of more than one effect (local jet bending, recollimation shock, MHD instability).* Another important finding in the study of the source kinematics is the detection of trailing components. These are features, which are formed in the wake of the leading superluminal plasma disturbance. In this study, *we found indications that two of the newly detected components are trailing components, or that they are ejected contemporaneously/simultaneously, with a more prominent leading jet feature.*

A future continuation of all the projects mentioned above it is necessary. Nevertheless, it is also mandatory to improve the quality of the research’s milestone, the data set. The first step towards this direction is to enrich our sample with higher cadence mm-VLBI images. For instance, a monthly basis VLBI observations at 86 GHz with the GMVA will lead us to achieve a more accurate tracing of the jet kinematics. In the same vein, observations with higher sensitivity are highly desired too. A better array sensitivity can lead us to obtain higher fidelity VLBI images and ultimately to a more accurate determination of the physical phenomena that are taking place in jet regions close to the launching point and to the central engine. One way that higher sensitivity can be achieved is to add more and more sensitive VLBI antennas. For example, the addition of the ALMA produces a factor  $\sim 2$  improvement in the north-south resolution and a factor  $>3$  improvement in sensitivity. These improvements are essential for resolving the transverse structure of the innermost

jet region, in particular for sources, which are close to the celestial equator or at southern declination. Also, nowadays, an upgrade of the IF chains and VLBI recording equipment at the GMVA telescopes is performed, which aims at a further increase of the observing bandwidth (for GMVA currently 500 MHz). This equipment upgrade will be a key factor in future mm-VLBI observations. Another significant step that should be taken in order to take the projects one step further is to observe the sources at higher frequencies. VLBI observations at 230 GHz with the EHT (or in the near future also at 345 GHz) can enable us to resolve fine structures and spatial scales near the BH that have never be seen before. Of course, a combination of VLBI observations at multiple frequencies is highly recommended, to facilitate a better determination of the spectral index of the VLBI components, the RM and the magnetic field strength and topology. For this, one needs coordinated and close in time VLBI campaigns, in order to overcome limitations set by the source variability. To date, steps in this direction are taken by East-Asia researchers, where new radio-telescope receivers are being developed, which operate multiple frequencies simultaneously (e.g. Vera: 22/43 GHz; KVN: 22/43/86/128 GHz). In the more distant future also space VLBI may become available at mm-wavelength (e.g., Millimetron; [Kardashev et al. 2014](#)), which will further increase the angular resolution. For VLBI observations in the sub-mm regime (at 345 GHz and above), even missions are now discussed, which operate without ground-arrays (e.g. [Roelofs et al. 2019](#)).

# Appendix A

## A.1 Relevance of Interstellar scattering

As mentioned in Sec. 3.1, TXS 2013+370 location close to the Galactic plane raises concerns that observations of this source may be effected by interstellar scattering. The interstellar scattering can introduce a wide variety of observational effects. Hence, we attempt to ascertain the effect, if any, the intervening dust has on our VLBI observations. The broadening of the apparent angular size of an object is one of the scattering effects, can be approximated by a  $\nu^{-2}$  size dependence. For examining the existence of such a size-frequency dependence, we created a common data set, combining the VLBI data with size measurements from the publicly available *RadioAstron* database (Pushkarev & Kovalev 2015). The uncertainties of the component angular sizes are set to 10% of the FWHM.

Following Lazio et al. (2008)(and references therein) , we fit the data using the relation:

$$\theta_{obs}^2 = (\theta_s \nu^{-2.2})^2 + (\theta_i \nu^k)^2, \quad (\text{A.1})$$

where  $\theta_s$  is the scattered and  $\theta_i$  is the intrinsic source size. The values of  $\theta_s$  and  $\theta_i$  are obtained using a minimum  $\chi^2$  fitting approach. The results of the fit are presented in Table A.1 For the shake of completeness, we considered two cases for the power-law index of the intrinsic angular size. The value of  $k = 0$  corresponds to a frequency-independent intrinsic size of an FSRQ (Blandford & Königl 1979), whereas  $k = -1$  is adopted as a typical frequency scaling for an inhomogenous synchrotron source Kellermann & Pauliny-Toth (1981). Again, we choose as the most accurate value, the one that is characterized by the lowest  $\chi^2$ . The fitting results are presented in Table A.1 and in Fig. A.1. The results show that the data below 10 GHz, are most affected from angular broadening. This outcome is in a good agreement with the earlier findings of Spangler et al. (1986) and Fey et al. (1989). However, for frequencies higher than 10 GHz, the intrinsic source size begins to dominate, showing the expected slope for an SSA jet.

Another phenomenon that might be induced by interstellar scattering is the so-called ‘intra-day’ variability (IDV, Heeschen 1984; Witzel et al. 1986), which is present in 30 – 50 % of all flat-spectrum quasars and BL Lac objects in cm-wavelengths (Quirrenbach et al. 1992; Lovell 2008). We note that TXS 2013+370 was observed in several IDV monitoring campaigns with the 100 m telescope at Effelsberg at 5 GHz, as part of the coordinated ground support for the *RadioAstron* space-VLBI experiments (Liu et al. 2018). According to  $\chi^2$ -tests, the source did not show significant fast variability over  $\sim 3$  days. This can be explained by quenched refractive interstellar scintillation (Narayan 1992), with a source size

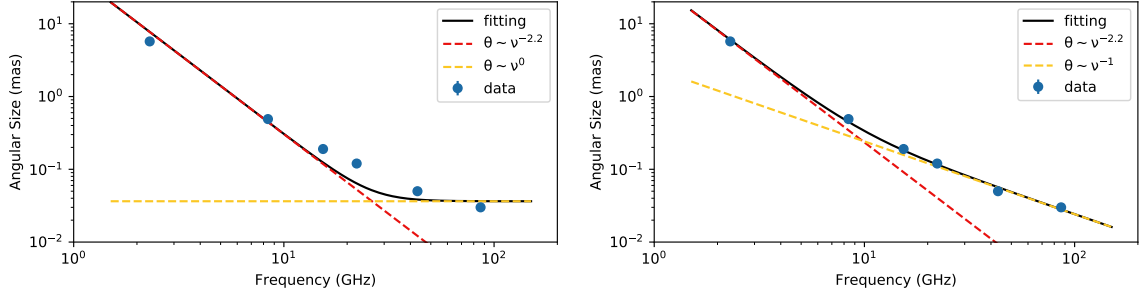


FIGURE A.1: Display of size versus frequency relation for the blazar TXS 2013+370. Left: Considering a power-law index  $k = 0$ . Right: Considering a power-law index  $k = -1$ . In both plots, blue circles represent the FWHM angular size of the core component, whereas the solid dashed line represents the best fit to the data. The red color corresponds to the inferred scattering size, and the green for the inferred intrinsic size.

TABLE A.1: Fitted scattering and intrinsic sizes and  $\chi^2$ . Columns from left to right: (1) Power-law index, (2) Observed angular size, (3) Intrinsic angular size, (4) Chi-square value.

$k$	$\theta_s$ (mas)	$\theta_i$ (mas)	$\chi^2$
0	$48.2 \pm 10.3$	$(3.6 \pm 1.0) \times 10^{-2}$	56.9
-1	$37.1 \pm 3.0$	$2.4 \pm 0.1$	3.5

larger than the scattering size at 5 GHz. The Scattering Measure (SM) in the Cygnus region varies by a factor of 2 – 5 on angular scales of only a few degrees. Although TXS 2013+370 is scatter broadened, it shows a much lower SM than some other prominent AGN in the same region, like e.g., 2005+403, which is separated by only  $\sim 4^\circ$  (c.f. Fig. 6 in Fey et al. 1989). We, therefore, conclude that for TXS 2013+370, interstellar scattering is not very strong and is dominant only at the longer cm-wavelengths. Thus it should not affect the mm-flux density and imaging significantly.

## A.2 Image and model-fitting parameters of TXS 2013+370

TABLE A.2: Model-fitting parameters at 15 GHz. Columns from left to right: (1) Component ID, (2) Observed epoch, (3) Observing frequency, (4) Flux density, (5) Radial distance from the core, (6) Position angle, (7) Component size

ID	Epoch (years)	Freq. (GHz)	S (Jy)	r (mas)	PA ( $^{\circ}$ )	FWHM (mas)
Core	2002.51	15	$2.630 \pm 0.263$	-	-	$0.12 \pm 0.01$
	2003.04	15	$1.71 \pm 0.17$	-	-	$0.11 \pm 0.01$
	2003.24	15	$2.10 \pm 0.21$	-	-	$0.11 \pm 0.01$
	2005.35	15	$2.31 \pm 0.23$	-	-	$0.19 \pm 0.02$
	2005.39	15	$2.13 \pm 0.21$	-	-	$0.18 \pm 0.02$
	2005.44	15	$2.09 \pm 0.21$	-	-	$0.20 \pm 0.02$
	2005.99	15	$1.95 \pm 0.20$	-	-	$0.24 \pm 0.02$
	2006.00	15	$1.91 \pm 0.19$	-	-	$0.19 \pm 0.02$
	2006.36	15	$0.95 \pm 0.01$	-	-	$0.25 \pm 0.03$
	2008.41	15	$3.32 \pm 0.33$	-	-	$0.22 \pm 0.02$
	2008.75	15	$2.79 \pm 0.28$	-	-	$0.19 \pm 0.02$
	2009.15	15	$3.81 \pm 0.38$	-	-	$0.23 \pm 0.02$
	2010.46	15	$1.91 \pm 0.19$	-	-	$0.17 \pm 0.02$
	2011.53	15	$1.43 \pm 0.14$	-	-	$0.16 \pm 0.02$
	2012.48	15	$3.41 \pm 0.34$	-	-	$0.20 \pm 0.02$
C3	2002.51	15	$2.21 \pm 0.22$	$0.153 \pm 0.118$	$-156.8 \pm 0.7$	$0.22 \pm 0.02$
	2003.04	15	$1.78 \pm 0.18$	$0.27 \pm 0.12$	$-147.5 \pm 0.4$	$0.22 \pm 0.02$
	2003.24	15	$1.41 \pm 0.14$	$0.24 \pm 0.11$	$-147.0 \pm 1.2$	$0.18 \pm 0.02$
	2005.35	15	$0.015 \pm 0.002$	$0.43 \pm 0.10$	$-156.5 \pm 0.3$	$0.20 \pm 0.02$
	2005.39	15	$0.12 \pm 0.01$	$0.26 \pm 0.23$	$-169.1 \pm 0.7$	$0.32 \pm 0.03$
	2005.44	15	$0.18 \pm 0.02$	$0.26 \pm 0.12$	$-169.1 \pm 0.4$	$0.30 \pm 0.03$
	2005.99	15	$0.05 \pm 0.01$	$0.43 \pm 0.12$	$-161.2 \pm 0.3$	$0.20 \pm 0.02$
	2006.00	15	$0.024 \pm 0.002$	$0.52 \pm 0.14$	$-157.4 \pm 0.3$	$0.17 \pm 0.02$
	2006.36	15	$0.21 \pm 0.02$	$0.21 \pm 0.12$	$-158.2 \pm 0.5$	$0.30 \pm 0.03$
	2008.41	15	$0.11 \pm 0.01$	$0.26 \pm 0.12$	$-160.2 \pm 0.4$	$0.15 \pm 0.02$
	2008.75	15	$0.040 \pm 0.004$	$0.27 \pm 0.12$	$-151.1 \pm 0.3$	$0.19 \pm 0.02$
	2009.15	15	$0.28 \pm 0.03$	$0.31 \pm 0.11$	$-161.0 \pm 0.3$	$0.11 \pm 0.01$
	2010.46	15	$0.77 \pm 0.08$	$0.31 \pm 0.12$	$-155.1 \pm 0.4$	$0.23 \pm 0.02$
	2011.53	15	$0.82 \pm 0.08$	$0.21 \pm 0.12$	$-151.0 \pm 0.5$	$0.17 \pm 0.02$
	2012.48	15	$0.47 \pm 0.05$	$0.22 \pm 0.12$	$-131.4 \pm 0.5$	$0.16 \pm 0.02$

TABLE A.2: Model-fitting parameters at 15 GHz. Columns from left to right: (1) Component ID, (2) Observed epoch, (3) Observing frequency, (4) Flux density, (5) Radial distance from the core, (6) Position angle, (7) Component size

ID	Epoch (years)	Freq. (GHz)	S (Jy)	r (mas)	PA ( $^{\circ}$ )	FWHM (mas)
C2	2002.51	15	$0.19 \pm 0.02$	$0.76 \pm 0.12$	$-143.0 \pm 0.2$	$0.42 \pm 0.04$
	2003.04	15	$0.13 \pm 0.01$	$0.99 \pm 0.12$	$-146.2 \pm 0.1$	$0.61 \pm 0.06$
	2003.24	15	$0.25 \pm 0.03$	$0.63 \pm 0.11$	$-142.8 \pm 0.7$	$0.35 \pm 0.04$
	2005.35	15	$0.24 \pm 0.02$	$1.17 \pm 0.12$	$-147.3 \pm 0.1$	$0.52 \pm 0.05$
	2005.39	15	$0.24 \pm 0.02$	$1.15 \pm 0.23$	$-147.1 \pm 0.2$	$0.50 \pm 0.05$
	2005.44	15	$0.24 \pm 0.02$	$1.16 \pm 0.12$	$-148.1 \pm 0.1$	$0.55 \pm 0.06$
	2005.99	15	$0.19 \pm 0.02$	$1.23 \pm 0.19$	$-148.6 \pm 0.1$	$0.98 \pm 0.10$
	2006.00	15	$0.14 \pm 0.01$	$1.29 \pm 0.14$	$-151.2 \pm 0.1$	$0.64 \pm 0.06$
	2006.36	15	$0.13 \pm 0.01$	$1.39 \pm 0.17$	$-149.7 \pm 0.1$	$0.83 \pm 0.08$
	2008.41	15	$0.022 \pm 0.002$	$2.00 \pm 0.12$	$-143.1 \pm 0.1$	$0.58 \pm 0.06$
	2008.75	15	$0.05 \pm 0.01$	$2.21 \pm 0.17$	$-146.2 \pm 0.1$	$0.83 \pm 0.08$
	2009.15	15	$0.026 \pm 0.003$	$2.19 \pm 0.14$	$-145.8 \pm 0.1$	$0.70 \pm 0.07$
	2010.46	15	$0.044 \pm 0.004$	$2.89 \pm 0.23$	$-147.4 \pm 0.1$	$1.17 \pm 0.12$
	2011.53	15	$0.041 \pm 0.004$	$3.40 \pm 0.22$	$-148.10 \pm 0.03$	$1.11 \pm 0.11$
	2012.48	15	$0.031 \pm 0.003$	$3.57 \pm 0.20$	$-147.91 \pm 0.03$	$0.98 \pm 0.10$
C1	2002.51	15	$0.11 \pm 0.01$	$2.77 \pm 0.25$	$-157.24 \pm 0.04$	$1.27 \pm 0.13$
	2003.04	15	$0.07 \pm 0.01$	$3.02 \pm 0.16$	$-156.00 \pm 0.04$	$0.82 \pm 0.08$
	2003.24	15	$0.09 \pm 0.01$	$3.08 \pm 0.28$	$-155.2 \pm 0.2$	$1.40 \pm 0.14$
	2005.35	15	$0.06 \pm 0.01$	$3.31 \pm 0.20$	$-156.30 \pm 0.03$	$1.01 \pm 0.10$
	2005.39	15	$0.06 \pm 0.01$	$3.38 \pm 0.25$	$-154.8 \pm 0.1$	$1.25 \pm 0.13$
	2005.44	15	$0.06 \pm 0.01$	$3.34 \pm 0.25$	$-154.28 \pm 0.04$	$1.23 \pm 0.12$
	2005.99	15	$0.004 \pm 0.004$	$3.89 \pm 0.16$	$-155.21 \pm 0.03$	$0.82 \pm 0.08$
	2006.00	15	$0.06 \pm 0.01$	$3.54 \pm 0.19$	$-154.23 \pm 0.04$	$0.94 \pm 0.09$
	2006.36	15	$0.06 \pm 0.01$	$3.40 \pm 0.28$	$-154.41 \pm 0.04$	$1.41 \pm 0.14$
	2008.41	15	$0.09 \pm 0.01$	$3.55 \pm 0.27$	$-155.74 \pm 0.03$	$1.34 \pm 0.13$
	2008.75	15	$0.07 \pm 0.01$	$3.72 \pm 0.23$	$-156.74 \pm 0.03$	$1.14 \pm 0.11$
	2009.15	15	$0.08 \pm 0.01$	$3.55 \pm 0.26$	$-156.04 \pm 0.03$	$1.28 \pm 0.13$
	2010.46	15	$0.06 \pm 0.01$	$4.15 \pm 0.25$	$-158.20 \pm 0.03$	$1.24 \pm 0.12$
	2011.53	15	$0.041 \pm 0.004$	$4.41 \pm 0.25$	$-158.85 \pm 0.03$	$1.24 \pm 0.12$
	2012.48	15	$0.06 \pm 0.01$	$4.48 \pm 0.26$	$-158.65 \pm 0.03$	$1.30 \pm 0.13$
A1	2011.53	15	$0.18 \pm 0.02$	$0.57 \pm 0.12$	$-57.5 \pm 0.2$	$0.38 \pm 0.04$
	2012.48	15	$0.13 \pm 0.01$	$0.64 \pm 0.12$	$-159.9 \pm 0.2$	$0.60 \pm 0.06$

TABLE A.3: Model-fitting parameters at 22 GHz. Columns from left to right: (1) Component ID, (2) Observed epoch, (3) Observing frequency, (4) Flux density, (5) Radial distance from the core, (6) Position angle, (7) Component size

ID	Epoch (years)	Freq. (GHz)	S (Jy)	r (mas)	PA ( $^{\circ}$ )	FWHM (mas)
Core	2012.82	22	$1.63 \pm 0.16$	-	-	$0.12 \pm 0.01$
N1	2012.82	22	$0.90 \pm 0.09$	$0.11 \pm 0.03$	$-81.9 \pm 0.3$	$0.09 \pm 0.01$
C3	2012.82	22	$0.410 \pm 0.004$	$0.26 \pm 0.03$	$-121.9 \pm 0.1$	$0.07 \pm 0.01$
A1	2012.82	22	$0.19 \pm 0.02$	$0.57 \pm 0.06$	$-133.7 \pm 0.1$	$0.29 \pm 0.03$
N	2012.82	22	$0.11 \pm 0.01$	$0.71 \pm 0.03$	$-153.4 \pm 0.04$	$0.17 \pm 0.02$

TABLE A.4: Model-fitting parameters at 43 GHz. Columns from left to right: (1) Component ID, (2) Observed epoch, (3) Observing frequency, (4) Flux density, (5) Radial distance from the core, (6) Position angle, (7) Component size

ID	Epoch (years)	Freq. (GHz)	S (Jy)	r (mas)	PA ( $^{\circ}$ )	FWHM (mas)
Core	2007.81	43	$3.05 \pm 0.31$	-	-	$0.05 \pm 0.01$
	2008.79	43	$2.46 \pm 0.25$	-	-	$0.05 \pm 0.01$
	2009.21	43	$5.00 \pm 0.50$	-	-	$0.05 \pm 0.01$
	2009.86	43	$1.38 \pm 0.13$	-	-	$0.05 \pm 0.01$
A2	2007.81	43	$0.023 \pm 0.002$	$0.11 \pm 0.08$	$-103.0 \pm 0.3$	$0.023 \pm 0.002$
	2008.79	43	$0.015 \pm 0.002$	$0.12 \pm 0.08$	$-104.0 \pm 0.3$	$0.06 \pm 0.01$
	2009.21	43	$0.25 \pm 0.03$	$0.12 \pm 0.08$	$-119.0 \pm 0.3$	$0.06 \pm 0.01$
	2009.86	43	$0.95 \pm 0.09$	$0.14 \pm 0.03$	$-123.9 \pm 0.2$	$0.10 \pm 0.01$
A1	2007.81	43	$0.23 \pm 0.02$	$0.17 \pm 0.08$	$-172.6 \pm 0.2$	$0.09 \pm 0.01$
	2008.79	43	$1.19 \pm 0.12$	$0.21 \pm 0.08$	$-152.9 \pm 0.1$	$0.13 \pm 0.01$
	2009.21	43	$1.51 \pm 0.15$	$0.24 \pm 0.08$	$-157.1 \pm 0.1$	$0.13 \pm 0.01$
	2009.86	43	$0.42 \pm 0.04$	$0.30 \pm 0.05$	$-154.6 \pm 0.11$	$0.20 \pm 0.02$
C3	2007.81	43	$0.10 \pm 0.01$	$0.32 \pm 0.08$	$-160.5 \pm 0.1$	$0.22 \pm 0.02$
	2008.79	43	$0.033 \pm 0.003$	$0.37 \pm 0.03$	$-166.4 \pm 0.1$	$0.038 \pm 0.004$
	2009.21	43	$0.020 \pm 0.002$	$0.37 \pm 0.03$	$-164.2 \pm 0.1$	$0.027 \pm 0.003$
	2009.86	43	$0.07 \pm 0.01$	$0.46 \pm 0.05$	$-163.4 \pm 0.1$	$0.14 \pm 0.01$



TABLE A.5: Model-fitting parameters at 86 GHz. Columns from left to right: (1) Component ID, (2) Observed epoch, (3) Observing frequency, (4) Flux density, (5) Radial distance from the core, (6) Position angle, (7) Component size

ID	Epoch (years)	Freq. (GHz)	S (Jy)	r (mas)	PA ( $^{\circ}$ )	FWHM (mas)
Core	2009.35	86	$2.04 \pm 0.20$	-	-	$0.037 \pm 0.004$
	2009.77	86	$1.58 \pm 0.16$	-	-	$0.013 \pm 0.001$
	2010.34	86	$2.07 \pm 0.21$	-	-	$0.030 \pm 0.003$
A2	2009.35	86	$0.31 \pm 0.03$	$0.08 \pm 0.04$	$-117.9 \pm 0.2$	$0.05 \pm 0.01$
	2009.77	86	$1.72 \pm 0.17$	$0.09 \pm 0.04$	$-125.9 \pm 0.2$	$0.012 \pm 0.001$
	2010.34	86	$0.072 \pm 0.002$	$0.06 \pm 0.06$	$-119.9 \pm 0.1$	$0.037 \pm 0.002$
A1	2009.35	86	$0.83 \pm 0.08$	$0.25 \pm 0.09$	$-159.8 \pm 0.1$	$0.18 \pm 0.02$
	2009.77	86	$0.25 \pm 0.03$	$0.30 \pm 0.05$	$-171.6 \pm 0.1$	$0.10 \pm 0.01$
A1+C3	2010.34	86	$0.29 \pm 0.03$	$0.40 \pm 0.09$	$-155.7 \pm 0.1$	$0.17 \pm 0.02$
N	2010.34	86	$0.71 \pm 0.07$	$0.16 \pm 0.08$	$-134.5 \pm 0.1$	$0.16 \pm 0.02$

# Appendix B

## B.1 Image and model-fitting parameters of OJ 287

TABLE B.1: Model-fitting parameters of OJ 287 during April-May 2014. Columns from left to right: (1) Component ID, (2) Observing frequency, (3) Flux density, (4) Radial distance from the core, (5) Position angle, (6) Component size, (7) Brightness Temperature.

Knot	Freq. GHz	S Jy	r mas	PA (deg)	FWHM mas	$T_b$ $10^{10}$ K
C1	15	$2.24 \pm 0.22$	-	-	$0.022 \pm 0.002$	$195.83 \pm 0.43$
	22	$0.52 \pm 0.05$	-	-	$0.038 \pm 0.004$	$36.59 \pm 8.46$
	43	$3.07 \pm 0.31$	-	-	$0.031 \pm 0.003$	$84.96 \pm 18.67$
	86	$2.93 \pm 0.21$	-	-	$0.021 \pm 0.002$	$553.21 \pm 88.92$
C2	15	$0.65 \pm 0.07$	$0.04 \pm 0.14$	$-44.1 \pm 1.3$	$0.047 \pm 0.005$	$49.61 \pm 16$
	22	$0.81 \pm 0.10$	$0.05 \pm 0.01$	$-11.3 \pm 1.2$	$0.063 \pm 0.006$	$20.73 \pm 4.85$
	43	$1.53 \pm 0.15$	$0.06 \pm 0.05$	$-18.4 \pm 1.2$	$0.028 \pm 0.003$	$51.90 \pm 12.23$
	86	$1.05 \pm 0.11$	$0.07 \pm 0.02$	$-8.5 \pm 1.1$	$0.017 \pm 0.002$	$67.41 \pm 16$
J6	15	$0.20 \pm 0.02$	$0.16 \pm 0.14$	$-63.4 \pm 0.4$	$0.065 \pm 0.007$	$10.34 \pm 2.45$
	22	$0.25 \pm 0.02$	$0.19 \pm 0.01$	$-46.5 \pm 0.6$	$0.122 \pm 0.012$	$1.70 \pm 0.47$
	43	$0.68 \pm 0.07$	$0.19 \pm 0.05$	$-53.9 \pm 0.7$	$0.134 \pm 0.013$	$1.01 \pm 0.22$
	86	$0.74 \pm 0.07$	$0.14 \pm 0.02$	$-52.3 \pm 0.8$	$0.089 \pm 0.009$	$0.62 \pm 0.13$
J5	15	$0.48 \pm 0.05$	$0.32 \pm 0.14$	$-58.7 \pm 0.4$	$0.150 \pm 0.015$	$4.66 \pm 1.05$
	22	$0.19 \pm 0.02$	$0.53 \pm 0.01$	$-52.2 \pm 0.3$	$0.315 \pm 0.032$	$0.19 \pm 0.04$
	43	$0.21 \pm 0.02$	$0.43 \pm 0.05$	$-51.1 \pm 0.3$	$0.177 \pm 0.018$	$0.17 \pm 0.04$
	86	$0.08 \pm 0.01$	$0.43 \pm 0.02$	$-62.4 \pm 0.3$	$0.122 \pm 0.012$	$0.035 \pm 0.008$
J4	15	$0.26 \pm 0.03$	$0.86 \pm 0.14$	$-84.4 \pm 0.2$	$0.625 \pm 0.063$	$0.14 \pm 0.03$
	22	$0.12 \pm 0.01$	$1.05 \pm 0.01$	$-84.1 \pm 0.1$	$0.436 \pm 0.044$	$0.06 \pm 0.01$
	43	$0.19 \pm 0.02$	$1.02 \pm 0.05$	$-84.5 \pm 0.3$	$0.534 \pm 0.053$	$0.02 \pm 0.003$
J3	15	$0.06 \pm 0.01$	$1.59 \pm 0.14$	$-98.3 \pm 0.1$	$0.103 \pm 0.01$	$1.23 \pm 0.31$
J2	15	$0.04 \pm 0.01$	$2.24 \pm 0.14$	$-101.3 \pm 0.1$	$0.191 \pm 0.019$	$0.23 \pm 0.08$
J1	15	$0.06 \pm 0.01$	$3.30 \pm 0.14$	$-125.5 \pm 0.1$	$0.758 \pm 0.076$	$0.022 \pm 0.006$

# Appendix C

## C.1 Image and model-fitting parameters of 3C 454.3

TABLE C.1: Model-fitting parameters at 43 GHz. Columns from left to right: (1) Component ID, (2) Observed epoch, (3) Observing frequency, (4) Flux density, (5) Radial distance from the core, (6) Position angle, (7) Component size

ID	Epoch (years)	Freq. (GHz)	S (Jy)	r (mas)	PA ( $^{\circ}$ )	FWHM (mas)
Core	2013.56	43	$5.13 \pm 0.51$	-	-	$0.05 \pm 0.04$
	2013.65	43	$5.59 \pm 0.56$	-	-	$0.05 \pm 0.04$
	2013.87	43	$8.90 \pm 0.89$	-	-	$0.05 \pm 0.04$
	2014.15	43	$11.05 \pm 1.11$	-	-	$0.05 \pm 0.01$
	2014.34	43	$16.08 \pm 1.61$	-	-	$0.08 \pm 0.01$
	2014.47	43	$23.60 \pm 2.36$	-	-	$0.11 \pm 0.01$
	2014.57	43	$5.74 \pm 0.57$	-	-	$0.10 \pm 0.01$
	2014.70	43	$6.29 \pm 0.63$	-	-	$0.10 \pm 0.01$
	2014.99	43	$4.95 \pm 0.50$	-	-	$0.10 \pm 0.01$
	2015.12	43	$7.36 \pm 0.74$	-	-	$0.10 \pm 0.01$
	2015.28	43	$4.79 \pm 0.48$	-	-	$0.14 \pm 0.01$
	2015.36	43	$2.11 \pm 0.21$	-	-	$0.11 \pm 0.01$
	2015.44	43	$1.84 \pm 0.18$	-	-	$0.06 \pm 0.01$
	2015.58	43	$2.25 \pm 0.23$	-	-	$0.06 \pm 0.01$
	2015.99	43	$1.94 \pm 0.19$	-	-	$0.07 \pm 0.01$
	2016.08	43	$2.98 \pm 0.30$	-	-	$0.07 \pm 0.01$
	2016.31	43	$3.16 \pm 0.32$	-	-	$0.06 \pm 0.01$
	2016.51	43	$2.10 \pm 0.21$	-	-	$0.05 \pm 0.01$
	2016.68	43	$4.46 \pm 0.45$	-	-	$0.06 \pm 0.01$
	2016.80	43	$4.60 \pm 0.46$	-	-	$0.07 \pm 0.01$
	2016.90	43	$3.74 \pm 0.37$	-	-	$0.04 \pm 0.003$
	2016.97	43	$6.23 \pm 0.62$	-	-	$0.06 \pm 0.01$
	2017.09	43	$10.66 \pm 1.07$	-	-	$0.04 \pm 0.006$
	2017.29	43	$8.15 \pm 0.82$	-	-	$0.08 \pm 0.01$

TABLE C.1: Model-fitting parameters at 43 GHz. Columns from left to right: (1) Component ID, (2) Observed epoch, (3) Observing frequency, (4) Flux density, (5) Radial distance from the core, (6) Position angle, (7) Component size

ID	Epoch (years)	Freq. (GHz)	S (Jy)	r (mas)	PA ( $^{\circ}$ )	FWHM (mas)
J9	2016.90	43	$1.17 \pm 0.12$	$0.05 \pm 0.04$	$-143.13 \pm 0.76$	$0.07 \pm 0.01$
	2016.97	43	$1.11 \pm 0.11$	$0.13 \pm 0.04$	$-108.43 \pm 0.34$	$0.11 \pm 0.01$
	2017.09	43	$2.01 \pm 0.20$	$0.15 \pm 0.04$	$-89.62 \pm 0.28$	$0.17 \pm 0.02$
	2017.29	43	$0.94 \pm 0.09$	$0.19 \pm 0.04$	$-99.46 \pm 0.21$	$0.15 \pm 0.02$
J8	2016.51	43	$2.26 \pm 0.23$	$0.15 \pm 0.04$	$-81.87 \pm 0.29$	$0.07 \pm 0.01$
	2016.68	43	$2.84 \pm 0.28$	$0.21 \pm 0.04$	$-74.05 \pm 0.21$	$0.09 \pm 0.01$
	2016.80	43	$1.82 \pm 0.18$	$0.21 \pm 0.04$	$-78.69 \pm 0.20$	$0.15 \pm 0.02$
	2016.90	43	$1.41 \pm 0.14$	$0.23 \pm 0.04$	$-85.03 \pm 0.19$	$0.20 \pm 0.02$
	2016.97	43	$1.68 \pm 0.17$	$0.34 \pm 0.04$	$-74.29 \pm 0.14$	$0.22 \pm 0.02$
	2017.09	43	$1.13 \pm 0.11$	$0.40 \pm 0.04$	$-101.11 \pm 0.08$	$0.15 \pm 0.01$
	2017.29	43	$1.77 \pm 0.18$	$0.49 \pm 0.04$	$-92.34 \pm 0.08$	$0.19 \pm 0.02$
J7	2016.31	43	$2.10 \pm 0.21$	$0.18 \pm 0.04$	$-66.37 \pm 0.24$	$0.19 \pm 0.02$
J6	2015.99	43	$2.58 \pm 0.26$	$0.19 \pm 0.04$	$-75.26 \pm 0.20$	$0.22 \pm 0.02$
	2016.08	43	$2.02 \pm 0.20$	$0.24 \pm 0.04$	$-65.56 \pm 0.16$	$0.22 \pm 0.02$
J5	2015.36	43	$2.45 \pm 0.25$	$0.12 \pm 0.04$	$-114.44 \pm 0.35$	$0.11 \pm 0.01$
	2015.44	43	$2.81 \pm 0.28$	$0.16 \pm 0.04$	$-86.42 \pm 0.28$	$0.09 \pm 0.01$
	2015.58	43	$2.65 \pm 0.27$	$0.21 \pm 0.04$	$-87.27 \pm 0.21$	$0.11 \pm 0.01$
J4	2014.99	43	$3.71 \pm 0.37$	$0.16 \pm 0.04$	$-104.04 \pm 0.37$	$0.08 \pm 0.01$
	2015.12	43	$2.97 \pm 0.30$	$0.17 \pm 0.04$	$-64.98 \pm 0.31$	$0.14 \pm 0.01$
	2015.28	43	$1.85 \pm 0.19$	$0.25 \pm 0.04$	$-75.26 \pm 0.25$	$0.18 \pm 0.02$
	2015.36	43	$1.30 \pm 0.13$	$0.33 \pm 0.04$	$-79.38 \pm 0.13$	$0.21 \pm 0.02$
	2015.44	43	$3.83 \pm 0.38$	$0.40 \pm 0.04$	$-76.55 \pm 0.09$	$0.20 \pm 0.02$
	2015.58	43	$3.29 \pm 0.33$	$0.53 \pm 0.04$	$-64.86 \pm 0.08$	$0.12 \pm 0.01$
	2015.99	43	$2.62 \pm 0.26$	$0.58 \pm 0.04$	$-63.43 \pm 0.07$	$0.15 \pm 0.02$
	2016.08	43	$2.82 \pm 0.28$	$0.58 \pm 0.04$	$-63.43 \pm 0.07$	$0.17 \pm 0.02$
	2016.31	43	$2.77 \pm 0.28$	$0.57 \pm 0.04$	$-62.53 \pm 0.08$	$0.22 \pm 0.02$
	2016.51	43	$2.90 \pm 0.29$	$0.5 \pm 0.07$	$-63.95 \pm 0.09$	$0.33 \pm 0.03$
	2016.68	43	$3.21 \pm 0.32$	$0.55 \pm 0.04$	$-69.93 \pm 0.08$	$0.20 \pm 0.02$
	2016.80	43	$1.01 \pm 0.10$	$0.53 \pm 0.04$	$-56.61 \pm 0.08$	$0.21 \pm 0.02$
	2016.90	43	$2.12 \pm 0.21$	$0.57 \pm 0.04$	$85.91 \pm 0.08$	$0.14 \pm 0.01$
	2016.97	43	$1.51 \pm 0.15$	$0.61 \pm 0.04$	$-66.8 \pm 0.08$	$0.22 \pm 0.02$

TABLE C.1: Model-fitting parameters at 43 GHz. Columns from left to right: (1) Component ID, (2) Observed epoch, (3) Observing frequency, (4) Flux density, (5) Radial distance from the core, (6) Position angle, (7) Component size

ID	Epoch (years)	Freq. (GHz)	S (Jy)	r (mas)	PA ( $^{\circ}$ )	FWHM (mas)
J3	2014.47	43	$6.53 \pm 0.65$	$0.08 \pm 0.004$	$-35.54 \pm 0.45$	$0.02 \pm 0.002$
	2014.57	43	$7.44 \pm 0.74$	$0.12 \pm 0.04$	$-65.56 \pm 0.35$	$0.06 \pm 0.01$
	2014.70	43	$8.79 \pm 0.88$	$0.17 \pm 0.04$	$-61.93 \pm 0.26$	$0.07 \pm 0.01$
	2014.99	43	$4.95 \pm 0.50$	$0.31 \pm 0.04$	$-65.10 \pm 0.21$	$0.11 \pm 0.01$
	2015.12	43	$3.50 \pm 0.35$	$0.37 \pm 0.04$	$-68.20 \pm 0.14$	$0.06 \pm 0.01$
	2015.28	43	$8.98 \pm 0.90$	$0.42 \pm 0.04$	$-67.69 \pm 0.12$	$0.12 \pm 0.01$
	2015.36	43	$9.34 \pm 0.93$	$0.48 \pm 0.04$	$-73.07 \pm 0.09$	$0.10 \pm 0.01$
	2015.44	43	$7.59 \pm 0.76$	$0.53 \pm 0.04$	$-70.20 \pm 0.08$	$0.08 \pm 0.01$
	2015.58	43	$8.01 \pm 0.80$	$0.58 \pm 0.04$	$-69.68 \pm 0.08$	$0.10 \pm 0.01$
	2015.99	43	$5.09 \pm 0.51$	$0.62 \pm 0.04$	$-75.07 \pm 0.06$	$0.06 \pm 0.01$
	2016.08	43	$4.78 \pm 0.48$	$0.59 \pm 0.04$	$-75.26 \pm 0.07$	$0.04 \pm 0.004$
	2016.31	43	$4.24 \pm 0.42$	$0.60 \pm 0.04$	$-79.44 \pm 0.07$	$0.06 \pm 0.01$
	2016.51	43	$3.37 \pm 0.34$	$0.59 \pm 0.04$	$-74.32 \pm 0.07$	$0.08 \pm 0.01$
	2016.68	43	$4.92 \pm 0.49$	$0.59 \pm 0.04$	$-84.19 \pm 0.08$	$0.08 \pm 0.01$
	2016.80	43	$3.17 \pm 0.32$	$0.60 \pm 0.04$	$-75.50 \pm 0.07$	$0.11 \pm 0.01$
	2016.90	43	$2.61 \pm 0.26$	$0.60 \pm 0.04$	$-76.43 \pm 0.07$	$0.10 \pm 0.01$
	2016.97	43	$3.81 \pm 0.38$	$0.58 \pm 0.04$	$-82.01 \pm 0.08$	$0.10 \pm 0.01$
	2017.09	43	$4.80 \pm 0.48$	$0.57 \pm 0.04$	$-78.89 \pm 0.08$	$0.16 \pm 0.02$
	2017.29	43	$1.76 \pm 0.18$	$0.55 \pm 0.04$	$-70.91 \pm 0.07$	$0.16 \pm 0.02$
J2	2013.56	43	$0.58 \pm 0.06$	$0.39 \pm 0.05$	$-91.43 \pm 0.11$	$0.25 \pm 0.03$
	2013.65	43	$0.72 \pm 0.07$	$0.40 \pm 0.08$	$-93.90 \pm 0.09$	$0.40 \pm 0.04$
	2013.87	43	$0.58 \pm 0.06$	$0.41 \pm 0.06$	$-91.40 \pm 0.11$	$0.31 \pm 0.03$
	2014.15	43	$0.67 \pm 0.07$	$0.41 \pm 0.09$	$-96.34 \pm 0.09$	$0.47 \pm 0.05$
	2014.34	43	$1.20 \pm 0.12$	$0.36 \pm 0.05$	$-101.69 \pm 0.14$	$0.24 \pm 0.02$
	2014.47	43	$1.45 \pm 0.15$	$0.39 \pm 0.06$	$-102.34 \pm 0.12$	$0.28 \pm 0.03$
	2014.57	43	$0.34 \pm 0.03$	$0.49 \pm 0.09$	$-105.46 \pm 0.09$	$0.44 \pm 0.04$
	2014.70	43	$0.50 \pm 0.05$	$0.50 \pm 0.06$	$-100.41 \pm 0.09$	$0.29 \pm 0.03$
	2014.99	43	$0.14 \pm 0.01$	$0.54 \pm 0.05$	$-104.04 \pm 0.12$	$0.26 \pm 0.03$
	2015.12	43	$0.33 \pm 0.03$	$0.63 \pm 0.09$	$-122.54 \pm 0.08$	$0.45 \pm 0.05$
J1	2015.28	43	$0.26 \pm 0.03$	$0.68 \pm 0.05$	$-89.17 \pm 0.07$	$0.23 \pm 0.02$
	2013.56	43	$0.49 \pm 0.05$	$0.69 \pm 0.10$	$-102.5 \pm 0.06$	$0.49 \pm 0.05$
	2013.65	43	$0.14 \pm 0.01$	$0.79 \pm 0.05$	$-102.44 \pm 0.06$	$0.27 \pm 0.03$
	2013.87	43	$0.36 \pm 0.04$	$0.76 \pm 0.09$	$-106.05 \pm 0.06$	$0.46 \pm 0.05$
	2014.05	43	$0.09 \pm 0.01$	$0.86 \pm 0.03$	$-104.04 \pm 0.05$	$0.16 \pm 0.02$
A1	2014.15	43	$0.11 \pm 0.01$	$0.88 \pm 0.07$	$-103.09 \pm 0.05$	$0.34 \pm 0.03$
	2015.58	43	$2.15 \pm 0.22$	$0.52 \pm 0.03$	$-85.60 \pm 0.08$	$0.17 \pm 0.02$
	2015.99	43	$2.28 \pm 0.23$	$0.54 \pm 0.04$	$-87.88 \pm 0.07$	$0.21 \pm 0.02$
	2016.08	43	$1.58 \pm 0.16$	$0.52 \pm 0.04$	$-93.30 \pm 0.08$	$0.18 \pm 0.02$
	2016.31	43	$2.89 \pm 0.29$	$0.56 \pm 0.04$	$-91.02 \pm 0.08$	$0.15 \pm 0.02$
	2016.51	43	$3.69 \pm 0.37$	$0.59 \pm 0.04$	$-88.06 \pm 0.07$	$0.08 \pm 0.01$
	2016.68	43	$2.16 \pm 0.22$	$0.55 \pm 0.04$	$-97.25 \pm 0.08$	$0.11 \pm 0.01$
	2016.80	43	$2.59 \pm 0.26$	$0.57 \pm 0.04$	$-93.01 \pm 0.07$	$0.15 \pm 0.02$
	2016.90	43	$0.89 \pm 0.09$	$0.49 \pm 0.04$	$-63.43 \pm 0.09$	$0.18 \pm 0.02$
	2016.97	43	$1.39 \pm 0.14$	$0.58 \pm 0.04$	$-101.89 \pm 0.08$	$0.19 \pm 0.02$
	2017.09	43	$0.71 \pm 0.07$	$0.59 \pm 0.04$	$-71.11 \pm 0.10$	$0.13 \pm 0.01$
	2017.29	43	$0.31 \pm 0.03$	$0.41 \pm 0.04$	$-53.97 \pm 0.11$	$0.16 \pm 0.02$

TABLE C.2: Model-fitting parameters at 86 GHz. Columns from left to right: (1) Component ID, (2) Observed epoch, (3) Observing frequency, (4) Flux density, (5) Radial distance from the core, (6) Position angle, (7) Component size

ID	Epoch (years)	Freq. (GHz)	S (Jy)	r (mas)	PA ( $^{\circ}$ )	FWHM (mas)
Core	2013.73	86	$5.01 \pm 0.50$	-	-	$0.03 \pm 0.003$
	2014.39	86	$5.29 \pm 0.53$	-	-	$0.04 \pm 0.004$
	2014.72	86	$5.05 \pm 0.51$	-	-	$0.03 \pm 0.003$
	2015.37	86	$1.03 \pm 0.10$	-	-	$0.04 \pm 0.004$
	2015.72	86	$2.28 \pm 0.23$	-	-	$0.04 \pm 0.004$
	2016.38	86	$0.94 \pm 0.09$	-	-	$0.03 \pm 0.003$
	2016.74	86	$3.98 \pm 0.40$	-	-	$0.03 \pm 0.003$
	2017.24	86	$4.01 \pm 0.40$	-	-	$0.03 \pm 0.004$
J10	2017.24	86	$3.39 \pm 0.34$	$0.05 \pm 0.04$	$-68.20 \pm 0.43$	$0.04 \pm 0.002$
J9	2016.74	86	$0.54 \pm 0.05$	$0.05 \pm 0.04$	$-117.57 \pm 0.40$	$0.02 \pm 0.007$
	2017.24	86	$0.62 \pm 0.06$	$0.15 \pm 0.04$	$-97.59 \pm 0.16$	$0.07 \pm 0.01$
J8	2016.38	86	$0.14 \pm 0.01$	$0.06 \pm 0.04$	$-111.8 \pm 0.38$	$0.02 \pm 0.002$
	2016.74	86	$0.80 \pm 0.08$	$0.21 \pm 0.04$	$-81.87 \pm 0.10$	$0.08 \pm 0.01$
	2017.24	86	$0.22 \pm 0.02$	$0.33 \pm 0.04$	$-61.93 \pm 0.07$	$0.09 \pm 0.01$
J7	2016.38	86	$0.50 \pm 0.05$	$0.17 \pm 0.04$	$-75.96 \pm 0.13$	$0.08 \pm 0.01$
J6	2015.72	86	$0.66 \pm 0.07$	$0.08 \pm 0.04$	$-84.81 \pm 0.07$	$0.08 \pm 0.01$
	2016.38	86	$0.20 \pm 0.02$	$0.41 \pm 0.04$	$-69.78 \pm 0.05$	$0.12 \pm 0.01$
	2016.74	86	$0.40 \pm 0.04$	$0.50 \pm 0.04$	$-64.98 \pm 0.04$	$0.18 \pm 0.02$
J5	2015.37	86	$0.95 \pm 0.09$	$0.11 \pm 0.04$	$-105.26 \pm 0.21$	$0.11 \pm 0.01$
J4	2014.72	86	$2.85 \pm 0.29$	$0.08 \pm 0.04$	$-82.87 \pm 0.29$	$0.07 \pm 0.01$
	2015.37	86	$0.84 \pm 0.08$	$0.39 \pm 0.04$	$-70.14 \pm 0.06$	$0.15 \pm 0.01$
	2015.72	86	$2.77 \pm 0.28$	$0.62 \pm 0.04$	$-68.03 \pm 0.04$	$0.11 \pm 0.01$
	2016.38	86	$0.83 \pm 0.08$	$0.59 \pm 0.04$	$-69.10 \pm 0.04$	$0.15 \pm 0.02$
J3	2014.39	86	$6.17 \pm 0.62$	$0.10 \pm 0.04$	$-41.19 \pm 0.21$	$0.04 \pm 0.004$
	2014.72	86	$6.70 \pm 0.67$	$0.21 \pm 0.04$	$-64.65 \pm 0.11$	$0.05 \pm 0.01$
	2015.37	86	$3.58 \pm 0.36$	$0.54 \pm 0.04$	$-69.19 \pm 0.04$	$0.08 \pm 0.01$
	2015.72	86	$4.47 \pm 0.45$	$0.63 \pm 0.04$	$-76.40 \pm 0.04$	$0.03 \pm 0.003$
	2016.38	86	$1.01 \pm 0.10$	$0.62 \pm 0.04$	$-81.61 \pm 0.04$	$0.05 \pm 0.005$
	2016.74	86	$2.05 \pm 0.20$	$0.61 \pm 0.04$	$-77.57 \pm 0.03$	$0.13 \pm 0.01$
	2017.24	86	$1.47 \pm 0.15$	$0.50 \pm 0.04$	$-90.23 \pm 0.05$	$0.14 \pm 0.01$
J2	2013.73	86	$0.22 \pm 0.02$	$0.42 \pm 0.04$	$-88.64 \pm -88.64$	$0.16 \pm 0.02$

# Bibliography

- Abbott, B. P., Abbott, R., Abbott, T. D., et al. 2016, *Phys. Rev. Lett.*, 116, 061102
- Abdo, A. A., Ackermann, M., Agudo, I., et al. 2010, *ApJ*, 716, 30
- Abdo, A. A., Ackermann, M., Ajello, M., et al. 2011, *ApJ*, 733, L26
- Abdollahi, S., Acero, F., Ackermann, M., et al. 2020, *ApJS*, 247, 33
- Abeysekara, A. U., Archer, A., Aune, T., et al. 2018, *ApJ*, 861, 134
- Acero, F., Ackermann, M., Ajello, M., et al. 2015, *ApJ*, 218, 23
- Ackermann, M., Ajello, M., Allafort, A., et al. 2011, *Science*, 334, 1103
- Ackermann, M., Ajello, M., Baldini, L., et al. 2010, *ApJ*, 721, 1383
- Agudo, I. 2009, *ASP Conf. Ser.*, 402, 330
- Agudo, I. 2013, in *European Physical Journal Web of Conferences*, Vol. 61, *European Physical Journal Web of Conferences*, 04002
- Agudo, I., Gómez, J.-L., Martí, J.-M., et al. 2001, *ApJ*, 549, L183
- Agudo, I., Jorstad, S. G., Marscher, A. P., et al. 2012, *Journal of Physics: Conference Series*, 355, 012032
- Agudo, I., Jorstad, S. G., Marscher, A. P., et al. 2010, *ApJ*, 726, L13
- Agudo, I., Marscher, A. P., Jorstad, S. G., et al. 2011, *ApJ*, 735, L10
- Agudo, I., Thum, C., Molina, S. N., et al. 2018a, *MNRAS*, 474, 1427
- Agudo, I., Thum, C., Ramakrishnan, V., et al. 2018b, *MNRAS*, 473, 1850
- Aharonian, F. A. 2000, *New A*, 5, 377
- Akahori, T. & Ryu, D. 2011, *ApJ*, 738, 134
- Aleksić, J., Ansoldi, S., Antonelli, L. A., et al. 2014, *A&A*, 569, A46
- Aleksić, J., Antonelli, L. A., Antoranz, P., et al. 2011, *ApJ*, 730, L8
- Algaba, J. C., Gabuzda, D. C., & Smith, P. S. 2012, *MNRAS*, 420, 542
- Alloin, D. 2006, *Physics of Active Galactic Nuclei at all Scales*, Vol. 693 (Springer, Berlin, Heidelberg)
- Aloy, M.-Á., Martí, J.-M., Gómez, J.-L., et al. 2003, *ApJ*, 585, L109



- Angelakis, E., Fuhrmann, L., Myserlis, I., et al. 2019, *A&A*, 626, A60
- Antonucci, R. R. J. & Miller, J. S. 1985, *ApJ*, 297, 621
- Appl, S., Lery, T., & Baty, H. 2000, *A&A*, 355, 818
- Asada, K. & Nakamura, M. 2012, *ApJ*, 745, L28
- Asmus, D. 2019, *MNRAS*, 2220
- Atwood, W. B., Abdo, A. A., Ackermann, M., et al. 2009, *ApJ*, 697, 1071
- Bassani, L., Landi, R., Malizia, A., et al. 2014, *A&A*, 561, A108
- Beckwith, S. V. W., Stiavelli, M., Koekemoer, A. M., et al. 2006, *The Astronomical Journal*, 132, 1729
- Begelman, M. C. 1998, *ApJ*, 493, 291
- Bennett, C. L., Larson, D., Weiland, J. L., et al. 2013, *ApJS*, 208, 20
- Bernet, M. L., Miniati, F., & Lilly, S. J. 2012, *ApJ*, 761, 144
- Beskin, V. S. & Nokhrina, E. E. 2006, *MNRAS*, 367, 375
- Birkinshaw, M. 1991, *The stability of jets* (Cambridge University Press), 278
- Blandford, R. D. & Königl, A. 1979, *ApJ*, 232, 34
- Blandford, R. D. & Levinson, A. 1995, *ApJ*, 441, 79
- Blandford, R. D. & McKee, C. F. 1982, *ApJ*, 255, 419
- Blandford, R. D. & Payne, D. G. 1982, *MNRAS*, 199, 883
- Blandford, R. D. & Znajek, R. L. 1977, *MNRAS*, 179, 433
- Blanton, E. L., Randall, S. W., Clarke, T. E., et al. 2011, *ApJ*, 737, 99
- Błażejowski, M., Sikora, M., Moderski, R., & Madejski, G. M. 2000, *ApJ*, 545, 107
- Blumenthal, G. R. & Gould, R. J. 1970, *Rev. Mod. Phys.*, 42, 237
- Boccardi, B., Krichbaum, T. P., Bach, U., et al. 2016, *A&A*, 585, A33
- Boettcher, M. 2012, arXiv e-prints, arXiv:1205.0539
- Boettcher, M. & Schlickeiser, R. 1995, *A&A*, 302, L17
- Bosch-Ramon, V. 2018, *A&A*, 617, L3
- Böttcher, M., Reimer, A., Sweeney, K., & Prakash, A. 2013, *ApJ*, 768, 54
- Bridle, A. H. 1996, in *Astronomical Society of the Pacific Conference Series*, Vol. 100, *Energy Transport in Radio Galaxies and Quasars*, ed. P. E. Hardee, A. H. Bridle, & J. A. Zensus, 383
- Britzen, S., Fendt, C., Witzel, G., et al. 2018, *MNRAS*, 478, 3199
- Britzen, S., Qian, S.-J., Witzel, A., et al. 2013, *A&A*, 557, A37

- Broderick, A. E. & McKinney, J. C. 2010, *ApJ*, 725, 750
- Bruni, G., Anderson, J., Alef, W., et al. 2016, *Galaxies*, 4, 55
- Bruni, G., Gómez, J. L., Casadio, C., et al. 2017, *A&A*, 604, A111
- Burn, B. J. 1966, *MNRAS*, 133, 67
- Carilli, C. L., Perley, R. A., Dhawan, V., & Perley, D. A. 2019, *ApJ*, 874, L32
- Carroll, B. W. & Ostlie, D. A. 2006, *An introduction to modern astrophysics and cosmology* (Pearson, Addison-Wesley)
- Casadio, C., Krichbaum, T., Marscher, A., et al. 2017, *Galaxies*, 5, 67
- Casadio, C., Marscher, A. P., Jorstad, S. G., et al. 2019, *A&A*, 622, A158
- Cawthorne, T. V. & Gabuzda, D. C. 1996, *MNRAS*, 278, 861
- Cawthorne, T. V., Jorstad, S. G., & Marscher, A. P. 2013, *ApJ*, 772, 14
- Celotti, A. & Ghisellini, G. 2008, *MNRAS*, 385, 283
- Ciprini, S., Valtonen, M. J., Zola, S., Goyal, A., & Pihajoki, P. 2017, in *Proceedings of the 7th International Fermi Symposium*, 41
- Clausen-Brown, E., Savolainen, T., Pushkarev, A. B., Kovalev, Y. Y., & Zensus, J. A. 2013, *A&A*, 558, A144
- Cohen, M. 2017, *Galaxies*, 5, 12
- Cohen, M. H., Cannon, W., Purcell, G. H., et al. 1971, *ApJ*, 170, 207
- Cohen, M. H., Lister, M. L., Homan, D. C., et al. 2007, *ApJ*, 658, 232
- Collinson, J. S., Ward, M. J., Landt, H., et al. 2017, *MNRAS*, 465, 358
- Comeron, F., Torra, J., & Gomez, A. E. 1998, *A&A*, 330, 975
- Connolly, S. 2015, *arXiv e-prints*, arXiv:1503.06676
- Coogan, R. T., Brown, A. M., & Chadwick, P. M. 2016, *MNRAS*, 458, 354
- Cornwell, T. & Fomalont, E. B. 1999, *Astronomical Society of the Pacific Conference Series*, Vol. 180, *Self-Calibration* (The name of the publisher), 187
- Costamante, L., Cutini, S., Tosti, G., Antolini, E., & Tramacere, A. 2018, *MNRAS*, 477, 4749
- Cotton, W. D. 1995, *Astronomical Society of the Pacific Conference Series*, Vol. 82, *Fringe Fitting*, 189
- Cotton, W. D. 1999, *Astronomical Society of the Pacific Conference Series*, Vol. 180, *Polarization in Interferometry*, 111
- Croke, S. M. & Gabuzda, D. C. 2008, *MNRAS*, 386, 619
- Curtis, H. D. 1918, *Publications of Lick Observatory*, 13, 9
- Daly, R. A. & Marscher, A. P. 1988, *ApJ*, 334, 539

- Davelaar, J., Bronzwaer, T., Kok, D., et al. 2018, *Computational Astrophysics and Cosmology*, 5, 1
- Dermer, C. D., Finke, J. D., Krug, H., & Böttcher, M. 2009, *ApJ*, 692, 32
- Dermer, C. D. & Giebels, B. 2016, *Comptes Rendus Physique*, 17, 594
- Dermer, C. D., Murase, K., & Takami, H. 2012, *ApJ*, 755, 147
- Dermer, C. D. & Schlickeiser, R. 1993, *ApJ*, 416, 458
- Dermer, C. D., Schlickeiser, R., & Mastichiadis, A. 1992, *A&A*, 256, L27
- Diltz, C. & Böttcher, M. 2016, *ApJ*, 826, 54
- Donato, D., Ghisellini, G., Tagliaferri, G., & Fossati, G. 2001, *A&A*, 375, 739
- Donea, A.-C. & Protheroe, R. J. 2003, *Astroparticle Physics*, 18, 377
- Dotson, A., Georganopoulos, M., Kazanas, D., & Perlman, E. S. 2012, *ApJ*, 758, L15
- Edelson, R. A. & Krolik, J. H. 1988, *ApJ*, 333, 646
- Emmanoulopoulos, D., McHardy, I. M., & Papadakis, I. E. 2013, *MNRAS*, 433, 907
- Ertley, C. 2014, in *American Astronomical Society Meeting Abstracts*, Vol. 223, American Astronomical Society Meeting Abstracts #223, 118.03
- Event Horizon Telescope Collaboration, Akiyama, K., Alberdi, A., et al. 2019, *ApJ*, 875, L1
- Fabian, A. C., Zoghbi, A., Ross, R. R., et al. 2009, *Nature*, 459, 540
- Fanaroff, B. L. & Riley, J. M. 1974, *MNRAS*, 167, 31P
- Fath, E. A. 1909, PhD thesis, UNIVERSITY OF CALIFORNIA, BERKELEY.
- Feng, S. W., Shen, Z. Q., Cai, H. B., et al. 2006, *A&A*, 456, 97
- Feretti, L., Fanti, R., Parma, P., et al. 1995, *A&A*, 298, 699
- Ferrarese, L. & Merritt, D. 2000, *ApJ*, 539, L9
- Fey, A. L., Spangler, S. R., & Mutel, R. L. 1989, *ApJ*, 337, 730
- Finke, J. D. 2013, *ApJ*, 763, 134
- Forman, W., Nulsen, P., Heinz, S., et al. 2005, *ApJ*, 635, 894
- Fossati, G., Maraschi, L., Celotti, A., Comastri, A., & Ghisellini, G. 1998, *MNRAS*, 299, 433
- Frieden, R. R. & Wells, D. C. 1978, *Journal of the Optical Society of America (1917-1983)*, 68, 93
- Fromm, C. M., Ros, E., Perucho, M., et al. 2013a, *A&A*, 551, A32
- Fromm, C. M., Ros, E., Perucho, M., et al. 2013b, *A&A*, 557, A105
- Fuhrmann, L., Larsson, S., Chiang, J., et al. 2014, *MNRAS*, 441, 1899

- Gabuzda, D. 2015, in *Astrophysics and Space Science Library*, Vol. 414, *The Formation and Disruption of Black Hole Jets*, ed. I. Contopoulos, D. Gabuzda, & N. Kylafis, 45
- Gabuzda, D. C., Reichstein, A. R., & O'Neill, E. L. 2014, *MNRAS*, 444, 172
- Galeev, A. A., Rosner, R., & Vaiana, G. S. 1979, *ApJ*, 229, 318
- Ganesh, S., Mishra, A., Chandra, S., & Baliyan, K. S. 2014, *The Astronomer's Telegram*, 6054, 1
- Garmany, C. D. & Stencel, R. E. 1992, *A&AS*, 94, 211
- Gaskell, C. M. 2009, *New A Rev.*, 53, 140
- Geldzahler, B. J., Shaffer, D. B., & Kuhr, H. 1984, *ApJ*, 286, 284
- Ghisellini, G., ed. 2013, *Lecture Notes in Physics*, Berlin Springer Verlag, Vol. 873, *Radiative Processes in High Energy Astrophysics*
- Ghisellini, G. 2015, *Journal of High Energy Astrophysics*, 7, 163
- Ghisellini, G., Celotti, A., Fossati, G., Maraschi, L., & Comastri, A. 1998, *MNRAS*, 301, 451
- Ghisellini, G. & Madau, P. 1996, *MNRAS*, 280, 67
- Ghisellini, G. & Tavecchio, F. 2008a, *MNRAS*, 386, L28
- Ghisellini, G. & Tavecchio, F. 2008b, *MNRAS*, 387, 1669
- Ghisellini, G. & Tavecchio, F. 2009, *MNRAS*, 397, 985
- Ghisellini, G. & Tavecchio, F. 2015, *MNRAS*, 448, 1060
- Ghisellini, G., Villata, M., Raiteri, C. M., et al. 1997, *A&A*, 327, 61
- Giovannini, G., Savolainen, T., Orienti, M., et al. 2018, *Nature Astronomy*, 2, 472
- Giovannini, G., Savolainen, T., Orienti, M., et al. 2018, *Nature Astronomy*, 2
- Goddi, C., Martí-Vidal, I., Messias, H., et al. 2019, *Publications of the Astronomical Society of the Pacific*, 131, 075003
- Gokus, A. 2017, Master's thesis, Friedrich-Alexander-Universität Erlangen-Nürnberg, Schloßplatz 4, 91054 Erlangen
- Gómez, J. L., Lobanov, A. P., Bruni, G., et al. 2016, *ApJ*, 817, 96
- Gómez, J. L., Lobanov, A. P., Bruni, G., et al. 2016, *ApJ*, 817, 96
- Gómez, J.-L., Marscher, A. P., & Alberdi, A. 1999, *ApJ*, 522, 74
- Gomez, J.-L., Marscher, A. P., & Alberdi, A. 1999, *ApJ*, 522, 74
- Gómez, J.-L., Marscher, A. P., Alberdi, A., Jorstad, S. G., & Agudo, I. 2001, *ApJ*, 561, L161
- Gómez, J. L., Martí, J. M., Marscher, A. P., Ibáñez, J. M., & Alberdi, A. 1997, *ApJ*, 482, L33

- Green, D. A. 2014, *Bulletin of the Astronomical Society of India*, 42, 47
- Greisen, E. W. 1990, in *Acquisition, Processing and Archiving of Astronomical Images*, ed. G. Longo & G. Sedmak, 125–142
- Groves, B. 2007, in *Astronomical Society of the Pacific Conference Series*, Vol. 373, *The Central Engine of Active Galactic Nuclei*, ed. L. C. Ho & J.-W. Wang, 511
- Grupe, D., Komossa, S., amp, & Falcone, A. 2017, *The Astronomer’s Telegram*, 10043, 1
- Grupe, D., Komossa, S., & Gomez, J. L. 2016, *The Astronomer’s Telegram*, 9629, 1
- Gu, M., Cao, X., & Jiang, D. R. 2001, *MNRAS*, 327, 1111
- Gubbay, J., Legg, A. J., Robertson, D. S., et al. 1969, *Nature*, 224, 1094
- Gurwell, M. A., Peck, A. B., Hostler, S. R., Darrah, M. R., & Katz, C. A. 2007, in *Astronomical Society of the Pacific Conference Series*, Vol. 375, *From Z-Machines to ALMA: (Sub)Millimeter Spectroscopy of Galaxies*, ed. A. J. Baker, J. Glenn, A. I. Harris, J. G. Mangum, & M. S. Yun, 234
- Haardt, F. & Maraschi, L. 1991, *ApJ*, 380, L51
- Haardt, F., Maraschi, L., & Ghisellini, G. 1997, *ApJ*, 476, 620
- Hada, K., Doi, A., Kino, M., et al. 2011, *Nature*, 477, 185
- Halpern, J. P., Eracleous, M., Mukherjee, R., & Gotthelf, E. V. 2001, *ApJ*, 551, 1016
- Hamaker, J. P., Bregman, J. D., & Sault, R. J. 1996, *A&AS*, 117, 137
- Hardee, P. E. 2000, *ApJ*, 533, 176
- Hardee, P. E. 2011, in *IAU Symposium*, Vol. 275, *Jets at All Scales*, ed. G. E. Romero, R. A. Sunyaev, & T. Belloni, 41–49
- Hayashi, T. J., Doi, A., & Nagai, H. 2013, *The Astrophysical Journal*, 772, 4
- Hazard, C., Mackey, M. B., & Shimmins, A. J. 1963, *Nature*, 197, 1037
- Heeschen, D. S. 1984, *AJ*, 89, 1111
- Hewitt, A. & Burbidge, G. 1993, *ApJS*, 87, 451
- Hodgson, J. A., Krichbaum, T. P., Marscher, A. P., et al. 2017, *A&A*, 597, A80
- Högbom, J. A. 1974, *A&AS*, 15, 417
- Homan, D. C. 2005, in *Astronomical Society of the Pacific Conference Series*, Vol. 340, *Future Directions in High Resolution Astronomy*, ed. J. Romney & M. Reid, 133
- Homan, D. C., Lister, M. L., Aller, H. D., Aller, M. F., & Wardle, J. F. C. 2009, *ApJ*, 696, 328
- Homan, D. C. & Wardle, J. F. C. 2003, *Ap&SS*, 288, 29
- Hönig, S. F. & Beckert, T. 2007, *MNRAS*, 380, 1172
- Hoskin, M. A. 1976, *Journal for the History of Astronomy*, 7, 169

- Hovatta, T., Lister, M. L., Aller, M. F., et al. 2012, *AJ*, 144, 105
- Hubble, E. P. 1929, *ApJ*, 69
- Hudec, R., Bašta, M., Pihajoki, P., & Valtonen, M. 2013, *A&A*, 559, A20
- Jackson, N. & Browne, I. W. A. 1991, *MNRAS*, 250, 414
- Jaffe, W., Meisenheimer, K., Röttgering, H. J. A., et al. 2004, *Nature*, 429, 47
- Jansky, K. G. 1933, *Nature*, 132, 66
- Jaynes, E. T. 1957, *Phys. Rev.*, 106, 620
- Jennison, R. C. 1958, *MNRAS*, 118, 276
- Jorstad, S. G., Marscher, A. P., Larionov, V. M., et al. 2010, *ApJ*, 715, 362
- Jorstad, S. G., Marscher, A. P., Lister, M. L., et al. 2005, *AJ*, 130, 1418
- Jorstad, S. G., Marscher, A. P., Mattox, J. R., et al. 2001, *ApJS*, 134, 181
- Jorstad, S. G., Marscher, A. P., Morozova, D. A., et al. 2017, *ApJ*, 846, 98
- Jorstad, S. G., Marscher, A. P., Morozova, D. A., et al. 2017, *ApJ*, 846, 98
- Jorstad, S. G., Marscher, A. P., Smith, P. S., et al. 2013, *ApJ*, 773, 147
- Kara, E., Errando, M., Max-Moerbeck, W., et al. 2012, *ApJ*, 746, 159
- Karamanavis, V., Fuhrmann, L., Krichbaum, T. P., et al. 2016, *A&A*, 586, A60
- Karamanavis, V. V. 2015, PhD thesis, Universität zu Köln, Albertus-Magnus-Platz, 50923 Köln
- Kardashev, N. S., Alakoz, A. V., Kovalev, Y. Y., et al. 2015, *Solar System Research*, 49, 573
- Kardashev, N. S., Khartov, V. V., Abramov, V. V., et al. 2013, *Astronomy Reports*, 57, 153
- Kardashev, N. S., Novikov, I. D., Lukash, V. N., et al. 2014, *Physics Uspekhi*, 57, 1199
- Kataoka, J., Mattox, J. R., Quinn, J., et al. 1999, *ApJ*, 514, 138
- Kellermann, K. I. & Pauliny-Toth, I. I. K. 1969, *ApJ*, 155, L71
- Kellermann, K. I. & Pauliny-Toth, I. I. K. 1981, *ARA&A*, 19, 373
- Kemball, A. J., Diamond, P. J., & Pauliny-Toth, I. I. K. 1996, *ApJ*, 464, L55
- Kettenis, M., van Langevelde, H. J., Reynolds, C., & Cotton, B. 2006, *Astronomical Society of the Pacific Conference Series*, Vol. 351, *ParselTongue: AIPS Talking Python*, 497
- Kim, J. Y., Krichbaum, T. P., Lu, R. S., et al. 2018, *A&A*, 616, A188
- Kim, J. Y., Krichbaum, T. P., Marscher, A. P., et al. 2019, *A&A*, 622, A196
- Kirk, J. G., Guthmann, A. W., Gallant, Y. A., & Achterberg, A. 2000, *ApJ*, 542, 235

- Komatsu, E., Dunkley, J., Nolte, M. R., et al. 2009, *ApJS*, 180, 330
- Komissarov, S. S., Barkov, M. V., Vlahakis, N., & Königl, A. 2007, *MNRAS*, 380, 51
- Komissarov, S. S. & Falle, S. A. E. G. 1997, *MNRAS*, 288, 833
- Königl, A. 1980, *Physics of Fluids*, 23, 1083
- Kovalev, Y. Y., Pushkarev, A. B., Nokhrina, E. E., et al. 2019, arXiv e-prints, arXiv:1907.01485
- Koyama, S., Kino, M., Giroletti, M., et al. 2016, *A&A*, 586, A113
- Kraus, J. D. 1966, *Radio astronomy*
- Krolik, J. H. 1998, *Active Galactic Nuclei: From the Central Black Hole to the Galactic Environment*
- Krolik, J. H. 1999, *Active galactic nuclei : from the central black hole to the galactic environment*
- Lasota, J. P., Gourgoulhon, E., Abramowicz, M., Tchekhovskoy, A., & Narayan, R. 2014, *Phys. Rev. D*, 89, 024041
- Lazio, T. J. W., Ojha, R., Fey, A. L., et al. 2008, *ApJ*, 672, 115
- Lee, S.-S., Lobanov, A. P., Krichbaum, T. P., et al. 2008, *AJ*, 136, 159
- Lehto, H. J. & Valtonen, M. J. 1996, *ApJ*, 460, 207
- León-Tavares, J., Valtaoja, E., Tornikoski, M., Lähteenmäki, A., & Nieppola, E. 2011, *A&A*, 532, A146
- Leppänen, K. J., Zensus, J. A., & Diamond, P. D. 1994, in *Compact Extragalactic Radio Sources*, ed. J. A. Zensus & K. I. Kellermann, 207
- Leppanen, K. J., Zensus, J. A., & Diamond, P. J. 1995, *AJ*, 110, 2479
- Li, H. Z., Chen, L. E., Yi, T. F., et al. 2015, *PASP*, 127, 1
- Lico, R., Giroletti, M., Orienti, M., et al. 2014, *A&A*, 571, A54
- Lico, R., Liu, J., Giroletti, M., et al. 2020, *A&A*, 634, A87
- Lind, K. R. & Blandford, R. D. 1985, *ApJ*, 295, 358
- Liska, M., Hesp, C., Tchekhovskoy, A., et al. 2018, *MNRAS*, 474, L81
- Lister, M. L., Aller, H. D., Aller, M. F., et al. 2009a, *AJ*, 137, 3718
- Lister, M. L., Aller, M., Aller, H., et al. 2011, *ApJ*, 742, 27
- Lister, M. L., Aller, M. F., Aller, H. D., et al. 2018, *ApJS*, 234, 12
- Lister, M. L., Aller, M. F., Aller, H. D., et al. 2013, *AJ*, 146, 120
- Lister, M. L., Aller, M. F., Aller, H. D., et al. 2016, *AJ*, 152, 12
- Lister, M. L., Cohen, M. H., Homan, D. C., et al. 2009b, *AJ*, 138, 1874



- Lister, M. L., Homan, D. C., Hovatta, T., et al. 2019, *ApJ*, 874, 43
- Lister, M. L., Homan, D. C., Kadler, M., et al. 2009, *ApJ*, 696, L22
- Lister, M. L. & Marscher, A. P. 1997, *ApJ*, 476, 572
- Liu, F. K. & Wu, X. B. 2002, *A&A*, 388, L48
- Liu, J., Bignall, H., Krichbaum, T., et al. 2018, *Galaxies*, 6, 49
- Liu, Y., Jiang, D. R., & Gu, M. F. 2006, *ApJ*, 637, 669
- Livio, M. 1997, in *Astronomical Society of the Pacific Conference Series*, Vol. 121, IAU Colloq. 163: Accretion Phenomena and Related Outflows, ed. D. T. Wickramasinghe, G. V. Bicknell, & L. Ferrario, 845
- Lobanov, A. P. 1998, *A&A*, 330, 79
- Lobanov, A. P. 2005, arXiv e-prints, arXiv:astro-ph/0503225
- Lovell, J. 2008, *ApJ*, 689, 108
- Lynds, C. R. 1967, *ApJ*, 147, 837
- Lyu, J. & Rieke, G. H. 2018, *ApJ*, 866, 92
- Lyutikov, M., Pariev, V. I., & Gabuzda, D. C. 2005, *MNRAS*, 360, 869
- MacDonald, N. R., Marscher, A. P., Jorstad, S. G., & Joshi, M. 2015, *ApJ*, 804, 111
- Mannheim, K. & Biermann, P. L. 1992, *A&A*, 253, L21
- Maraschi, L., Ghisellini, G., & Celotti, A. 1992, *ApJ*, 397, L5
- Marcaide, J. M. & Shapiro, I. I. 1984, *ApJ*, 276, 56
- Marr, J., Snell, R., & Kurtz, S. 2019, *Fundamentals of Radio Astronomy, Astronomy and Astrophysics* (Taylor & Francis Incorporated)
- Marscher, A. P. 1983, *ApJ*, 264, 296
- Marscher, A. P. 1998, *Astronomical Society of the Pacific Conference Series*, Vol. 144, *The Blazar Paradigm: Synchro-Compton Emission from Relativistic Jets*, 25
- Marscher, A. P. 2006, in *American Institute of Physics Conference Series*, Vol. 856, *Relativistic Jets: The Common Physics of AGN, Microquasars, and Gamma-Ray Bursts*, ed. P. A. Hughes & J. N. Bregman, 1–22
- Marscher, A. P. 2008, *Astronomical Society of the Pacific Conference Series*, Vol. 386, *The Core of a Blazar Jet*, 437
- Marscher, A. P. 2013, *ApJ*, 780, 87
- Marscher, A. P. & Gear, W. K. 1985, *ApJ*, 298, 114
- Marscher, A. P., Jorstad, S. G., D’Arcangelo, F. D., et al. 2008, *Nature*, 452, 966
- Martí-Vidal, I., Krichbaum, T. P., Marscher, A., et al. 2012, *A&A*, 542, A107

- Martí-Vidal, I., Muller, S., Vlemmings, W., Horellou, C., & Aalto, S. 2015, *Science*, 348, 311
- Massaro, E., Maselli, A., Leto, C., et al. 2015, *Ap&SS*, 357, 75
- Matheson, H., Safi-Harb, S., & Kothes, R. 2013, *ApJ*, 774, 33
- Mattox, J. R., Bertsch, D. L., Chiang, J., et al. 1996, *ApJ*, 461, 396
- McNamara, B. R. & Nulsen, P. E. J. 2007, *ARA&A*, 45, 117
- Meier, D. L. 2003, *New A Rev.*, 47, 667
- Meier, D. L., Koide, S., & Uchida, Y. 2001, *Science*, 291, 84
- Michelson, A. A. & Morley, E. W. 1887, *Sidereal Messenger*, 6, 306
- Middelberg, E. & Bach, U. 2008, *Reports on Progress in Physics*, 71, 066901
- Mimica, P., Aloy, M.-A., Agudo, I., et al. 2009, *ApJ*, 696, 1142
- Mizuno, Y., Lyubarsky, Y., Nishikawa, K.-I., & Hardee, P. E. 2012, *ApJ*, 757, 16
- Mo, H., van den Bosch, F. C., & White, S. 2010, *Galaxy Formation and Evolution*
- Moran, J. M. 1998, *Astronomical Society of the Pacific Conference Series*, Vol. 144, *Thirty Years of VLBI: Early Days, Successes, and Future*, 1
- Mukherjee, R. & VERITAS Collaboration. 2017, *The Astronomer's Telegram*, 10051, 1
- Myserlis, I., Komossa, S., Angelakis, E., et al. 2018, *A&A*, 619, A88
- Nair, D. G., Lobanov, A. P., Krichbaum, T. P., et al. 2019, *A&A*, 622, A92
- Nair G., D. 2019, PhD thesis, Universität zu Köln, Albertus-Magnus-Platz, 50923 Köln
- Napier, P. J. 1994, in *IAU Symposium*, Vol. 158, *Very High Angular Resolution Imaging*, ed. J. G. Robertson & W. J. Tango, 117
- Narayan, R. 1992, *Philosophical Transactions of the Royal Society of London Series A*, 341, 151
- Narayan, R., Kumar, P., & Tchekhovskoy, A. 2011, *MNRAS*, 416, 2193
- Netzer, H. 2013, *The Physics and Evolution of Active Galactic Nuclei*
- Osterbrock, D. E. 1981, *ApJ*, 249, 462
- Pacholczyk, A. G. 1970, *Radio astrophysics. Nonthermal processes in galactic and extra-galactic sources*
- Padovani, P. 2007, *Ap&SS*, 309, 63
- Padovani, P. & Giommi, P. 1995, *MNRAS*, 277, 1477
- Pardo, J. R., Cernicharo, J., & Serabyn, E. 2001, *IEEE Transactions on Antennas and Propagation*, 49, 1683
- Pauliny-Toth, I., Porcas, R., Zensus, J. A., et al. 1987, *Nature*, 328

- Pauliny-Toth, I. I. K. 1998, *Astronomical Society of the Pacific Conference Series*, Vol. 144, Structural Variations in the Quasar 3C 454.3, 75
- Pelletier, G. & Pudritz, R. E. 1992, *ApJ*, 394, 117
- Penrose, R. & Floyd, R. M. 1971, *Nature Physical Science*, 229, 177
- Perucho, M. & Martí, J. M. 2007, *MNRAS*, 382, 526
- Peterson, B. M. & Horne, K. 2006, Reverberation mapping of active galactic nuclei, 89
- Petrov, L., Kovalev, Y. Y., Fomalont, E. B., & Gordon, D. 2011, *AJ*, 142, 35
- Poutanen, J. & Stern, B. 2010, *ApJ*, 717, L118
- Poutanen, J. & Svensson, R. 1996, *ApJ*, 470, 249
- Pushkarev, A. B., Butuzova, M. S., Kovalev, Y. Y., & Hovatta, T. 2019, *MNRAS*, 482, 2336
- Pushkarev, A. B., Hovatta, T., Kovalev, Y. Y., et al. 2012, *A&A*, 545, A113
- Pushkarev, A. B. & Kovalev, Y. Y. 2012, *A&A*, 544, A34
- Pushkarev, A. B. & Kovalev, Y. Y. 2015, *MNRAS*, 452, 4274
- Pushkarev, A. B., Kovalev, Y. Y., & Lister, M. L. 2010, *ApJ*, 722, L7
- Pushkarev, A. B., Kovalev, Y. Y., Lister, M. L., & Savolainen, T. 2017, *MNRAS*, 468, 4992
- Qian, S.-J., Britzen, S., Witzel, A., et al. 2014, *Research in Astronomy and Astrophysics*, 14, 249
- Quirrenbach, A., Witzel, A., Kirchbaum, T. P., et al. 1992, *A&A*, 258, 279
- Randall, S. W., Forman, W. R., Giacintucci, S., et al. 2011, *ApJ*, 726, 86
- Rani, B., Krichbaum, T. P., Marscher, A. P., et al. 2015, *A&A*, 578, A123
- Readhead, A. C. S. 1994, *ApJ*, 426, 51
- Rees, M. J. 1966, *Nature*, 211, 468
- Reynolds, C., Cawthorne, T. V., & Gabuzda, D. C. 2001, *MNRAS*, 327, 1071
- Richards, J. L., Max-Moerbeck, W., Pavlidou, V., et al. 2011, *ApJS*, 194, 29
- Roberts, D. H., Wardle, J. F. C., & Brown, L. F. 1994, *ApJ*, 427, 718
- Rodrigues, X., Gao, S., Fedynitch, A., Palladino, A., & Winter, W. 2019, *ApJ*, 874, L29
- Roelofs, F., Falcke, H., Brinkerink, C., et al. 2019, *A&A*, 625, A124
- Ros, E., Kadler, M., Perucho, M., et al. 2020, *A&A*, 633, L1
- Rybicki, G. B. & Lightman, A. P. 1979, *Radiative processes in astrophysics*
- Ryle, M. 1962, *Nature*, 194, 517
- Sahayanathan, S. & Godambe, S. 2012, *MNRAS*, 419, 1660

- Salpeter, E. E. 1964, *ApJ*, 140, 796
- Sambruna, R. M., Maraschi, L., & Urry, C. M. 1996, *ApJ*, 463, 444
- Sarkar, A., Gupta, A. C., Chitnis, V. R., & Wiita, P. J. 2020, arXiv e-prints, arXiv:2003.01911
- Sbarrato, T., Ghisellini, G., Maraschi, L., & Colpi, M. 2012, *MNRAS*, 421, 1764
- Schmidt, M. 1963, *Nature*, 197, 1040
- Seyfert, C. K. 1943, *ApJ*, 97, 28
- Shah, Z., Sahayanathan, S., Mankuzhiyil, N., et al. 2017, *MNRAS*, 470, 3283
- Shakura, N. I. & Sunyaev, R. A. 1973, *A&A*, 24, 337
- Shang, X., Klasmann, P., & Lancaster, M. J. 2016, 2016 46th European Microwave Conference (EuMC), 365
- Shaw, M. S., Romani, R. W., Cotter, G., et al. 2013, *ApJ*, 764, 135
- Shepherd, M. C., Pearson, T. J., & Taylor, G. B. 1994, in *BAAS*, Vol. 26, Bulletin of the American Astronomical Society, 987–989
- Sikora, M., Begelman, M. C., & Rees, M. J. 1994, *ApJ*, 421, 153
- Sikora, M., Stawarz, L., Moderski, R., Nalewajko, K., & Madejski, G. M. 2009, *ApJ*, 704, 38
- Sillanpaa, A., Haarala, S., Valtonen, M. J., Sundelius, B., & Byrd, G. G. 1988, *ApJ*, 325, 628
- Singal, A. K. 2016, *ApJ*, 827, 66
- Śniegowska, M. & Czerny, B. 2019, arXiv e-prints, arXiv:1904.06767
- Sokolovsky, K. 2014, in *COSPAR Meeting*, Vol. 40, 40th COSPAR Scientific Assembly, E1.10–8–14
- Sol, H., Pelletier, G., & Asseo, E. 1989, *MNRAS*, 237, 411
- Spangler, S. R. & Cordes, J. M. 1998, *ApJ*, 505, 766
- Spangler, S. R., Mutel, R. L., Benson, J. M., & Cordes, J. M. 1986, *ApJ*, 301, 312
- Spearman, C. 1904, *The American Journal of Psychology*, 15, 72
- Spruit, H. C., Foglizzo, T., & Stehle, R. 1997, *Monthly Notices of the Royal Astronomical Society*, 288, 333
- Stecker, F. W. 2010, in *American Institute of Physics Conference Series*, Vol. 1223, American Institute of Physics Conference Series, ed. C. Cecchi, S. Ciprini, P. Lubrano, & G. Tosti, 192–206
- Stickel, M., Fried, J. W., & Kuehr, H. 1989, *A&AS*, 80, 103
- Stokes, G. G. 1851, *Transactions of the Cambridge Philosophical Society*, 9, 399

- Sulentic, J. W., Zamfir, S., Marziani, P., et al. 2003, *ApJ*, 597, L17
- Sundelius, B., Wahde, M., Lehto, H. J., & Valtonen, M. J. 1997, *ApJ*, 484, 180
- Tateyama, C. E. & Kingham, K. A. 2004, *ApJ*, 608, 149
- Taylor, A. R., Stil, J. M., & Sunstrum, C. 2009, *ApJ*, 702, 1230
- Thompson, A. R., Moran, J. M., & Swenson, G. W. 2017, *Geometrical Relationships, Polarimetry, and the Interferometer Measurement Equation* (Cham: Springer International Publishing), 109–151
- Thompson, D., Digel, S., & Racusin, J. 2012, *Physics Today*, 65, 39
- Thum, C., Agudo, I., Molina, S. N., et al. 2017, *Monthly Notices of the Royal Astronomical Society*, 473, 2506
- Toma, K. & Takahara, F. 2014, *MNRAS*, 442, 2855
- Trippe, S., Neri, R., Krips, M., et al. 2012, *A&A*, 540, A74
- Türler, M. 2011, *Mem. Soc. Astron. Italiana*, 82, 104
- Türler, M., Courvoisier, T. J.-L., & Paltani, S. 2000, *A&A*, 361, 850
- Unwin, S. C., Shao, M., Tanner, A. M., et al. 2008, *Publications of the Astronomical Society of the Pacific*, 120, 38
- Urry, C. M. & Padovani, P. 1995, *PASP*, 107, 803
- Uyaniker, B., Fürst, E., Reich, W., Aschenbach, B., & Wielebinski, R. 2001, *A&A*, 371, 675
- Valtonen, M. & Pihajoki, P. 2013, *A&A*, 557, A28
- Valtonen, M. J. & Lehto, H. J. 1997, *ApJ*, 481, L5
- Valtonen, M. J., Lehto, H. J., Nilsson, K., et al. 2008, *Nature*, 452, 851
- Valtonen, M. J., Lehto, H. J., Sillanpää, A., et al. 2006, *ApJ*, 646, 36
- Valtonen, M. J., Lehto, H. J., Takalo, L. O., & Sillanp, A. 2011, *ApJ*, 729, 33
- Valtonen, M. J., Mikkola, S., Merritt, D., et al. 2010, *ApJ*, 709, 725
- Valtonen, M. J., Zola, S., Ciprini, S., et al. 2016, *ApJ*, 819, L37
- van der Laan, H. 1966, *Nature*, 211, 1131
- Vercellone, S., Donnarumma, I., Bulgarelli, A., et al. 2009, in *American Institute of Physics Conference Series*, Vol. 1112, *American Institute of Physics Conference Series*, ed. D. Bastieri & R. Rando, 121–128
- Vercellone, S., Striani, E., Vittorini, V., et al. 2011, *ApJ*, 736, L38
- Vermeulen, R. C. & Cohen, M. H. 1994, *ApJ*, 430, 467
- Verrecchia, F., Ciprini, S., Valtonen, M., & Zola, S. 2016, *The Astronomer’s Telegram*, 9709, 1

- Verschuur, G. L. & Kellermann, K. I. 1988, Galactic and extra-galactic radio astronomy
- Villforth, C., Nilsson, K., Heidt, J., et al. 2010, MNRAS, 402, 2087
- Vlahakis, N. & Konigl, A. 2004, ApJ, 605, 656
- Volonteri, M. 2012, Science, 337, 544
- Vol’Vach, A. E., Vol’Vach, L. N., Larionov, M. G., et al. 2008, Astronomy Reports, 52, 867
- Wagner, S. J. & Witzel, A. 1995, ARA&A, 33, 163
- Walker, R. C. 1995, Astronomical Society of the Pacific Conference Series, Vol. 82, Practical VLBI Imaging, ed. J. A. Zensus, P. J. Diamond, & P. J. Napier, 247
- Walker, R. C., Dhawan, V., Romney, J. D., Kellermann, K. I., & Vermeulen, R. C. 2000, ApJ, 530, 233
- Wardle, J. F. C. 2013, in European Physical Journal Web of Conferences, Vol. 61, European Physical Journal Web of Conferences, 06001
- Wardle, J. F. C., Homan, D. C., Ojha, R., & Roberts, D. H. 1998, Nature, 395, 457
- Weaver, Z. R., Balonek, T. J., Jorstad, S. G., et al. 2019, ApJ, 875, 15
- Wernecke, S. J. & D’Addario, L. R. 1977, IEEE Transactions on Communications, 26, 351
- Whitney, A. R., Shapiro, I. I., Rogers, A. E. E., et al. 1971, Science, 173, 225
- Witzel, A., Heeschen, D. S., Schalinski, C., & Krichbaum, T. 1986, Mitteilungen der Astronomischen Gesellschaft Hamburg, 65, 239
- Woo, J.-H. & Urry, C. M. 2002, ApJ, 581, L5
- Wucknitz, O. 2010, in ISKAF2010 Science Meeting, 58
- Yuan, F. & Narayan, R. 2014, ARA&A, 52, 529
- Zamaninasab, M., Savolainen, T., Clausen-Brown, E., et al. 2013, MNRAS, 436, 3341
- Zauderer, B. A., Berger, E., Soderberg, A. M., et al. 2011, Nature, 476, 425
- Zel’dovich, Y. B. 1964, Soviet Physics Doklady, 9, 195
- Zensus, J. A., Cohen, M. H., & Unwin, S. C. 1995, ApJ, 443, 35

# Personal Acknowledgements

At this terminal point of my Ph.D. I would like to thank all the people that helped me to conduct this project. First, I deeply thank Prof. Dr. J. Anton Zensus for allowing me to work and facilitate this study in the VLBI group at the MPIfR. Also, I thank my second supervisor, Prof. Dr. Andreas Eckart, for giving me the chance to perform a Ph.D. under his guidance. Next, I would like to express my gratitude to my thesis advisor Dr. Thomas Krichbaum. He was always there for me, ready to share his deep and wide knowledge in science, to discuss, help, guide, and teach me how to defend my scientific beliefs. Without him, it would be impossible to facilitate this study. I would also like to sincerely thank Dr. Bia Boccardi. Since the first days of my Ph.D. until today, she was there to support, encourage, and inspire me. It was a pleasure working with her. My deepest gratitude goes to Prof. Dr. Eduardo Ros. He was always ready to listen and provide me with his endless knowledge about everything. Special thanks I owe to Dr. Emmanouil Angelakis. His valuable scientific input to my projects and our long stimulating discussions were precious. I deeply thank Dr. Carolina Casadio. The discussions with her about polarization helped me to become familiar with the topic and come up with several scientific ideas. I also express my sincere appreciation to Dr. Alan Roy, Dr. Andrei Lobanov, Dr. Ioannis Myserlis and Dr. Vassilis Karamanavis, as well as each and every member of the VLBI group. Working with such amazing people was a life-time experience. I especially thank Dr. Rocco Lico for the long and fruitful conversations about everything. I would like to say a big and warm thanks from the bottom of my heart to all my to my fellow Ph.D. students and office-mates; Jae-Young, Anne, Dhanya, Laura, Roberto, Celine, Felix, Dongjin, Georgios and Telemachos. Without them, my life in Bonn would not have been the same. Additional thanks go to Felix for his great job in translating the abstract into German and to Dr. Nicholas R. MacDonald for reviewing my thesis. As a member of the International Max Planck Research School (IMPRS) for Astronomy and Astrophysics and a student at the University of Cologne, I would like to express my gratitude for providing me their support and facilities. Administrative support from Priv.-Doz. Dr. Rainer Mauersberger, Dr. Simone Pott, Ms. Beate Naunheim, Ms. Tuyet-Le Tran, Ms. Barbara Menten, and Ms. Sylvia Mertens were an important part of my Ph.D. life. Besides, I also would like to acknowledge the contribution of external collaborators and researchers. Prof. Alan P. Marscher and Dr. Svetlana Jorstad for giving me the chance to work for the GMVA monitoring project and for their helpful comments. Prof. Dr. Ivan Agudo for including me to the POLAMI project and providing me the IRAM 30m Telescope data. I also thank the staff of the observatories participating in the GMVA, the MPIfR Effelsberg 100 m telescope, the IRAM Plateau de Bure Interferometer, the IRAM Pico Veleta 30 m telescope, the Yebes Radio Observatory, the Metsähovi Radio Observatory, the Onsala Space Observatory, and the VLBA. Ultimately, I want to sincerely thank my family for everything.



# Funding, Data, and Software

## Acknowledgements

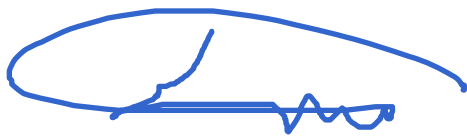
E. Traianou is supported for this research by the International Max-Planck Research School (IMPRS) for Astronomy and Astrophysics at the University of Bonn and Cologne. This research has made use of data obtained with the Global Millimeter VLBI Array (GMVA), which consists of telescopes operated by the MPIfR, IRAM, Onsala, Metsahovi, Yebes, the Korean VLBI Network, the Green Bank Observatory and the Long Baseline Observatory (LBO). The VLBA is an instrument of the NRAO, which is a facility of the National Science Foundation operated by Associated Universities, Inc. The data were correlated at the correlator of the MPIfR in Bonn, Germany. This work made use of the Swinburne University of Technology software correlator, developed as part of the Australian Major National Research Facilities Programme and operated under licence. This study makes use of 43 GHz VLBA data from the VLBA-BU Blazar Monitoring Program (VLBA-BU-BLAZAR; <http://www.bu.edu/blazars/VLBaproject.html>), funded by NASA through the Fermi Guest Investigator Program. This research has made use of data from the MOJAVE database that is maintained by the MOJAVE team (Lister et al., 2009). This thesis makes use of ALMA data. ALMA is a partnership of ESO (representing its member states), NSF (USA) and NINS (Japan), together with NRC (Canada), MOST and ASIAA (Taiwan), and KASI (Republic of Korea), in cooperation with the Republic of Chile. The Joint ALMA Observatory is operated by ESO, AUI/NRAO and NAOJ. This research has made use of data from the OVRO 40-m monitoring program (Richards, J. L. et al. 2011, ApJS, 194, 29), which is supported in part by NASA grants NNX08AW31G, NNX11A043G, and NNX14AQ89G and NSF grants AST-0808050 and AST-1109911. This research has made use of data from the Submillimeter Array, which is a joint project between the Smithsonian Astrophysical Observatory and the Academia Sinica Institute of Astronomy and Astrophysics and is funded by the Smithsonian Institution and the Academia Sinica. This research has made use of NASA's Astrophysics Data System. This work has made use of data from the *RadioAstron* project, which is led by the Astro Space Center of the Lebedev Physical Institute of the Russian Academy of Sciences and the Lavochkin Scientific and Production Association under a contract with the State Space Corporation ROSCOSMOS, in collaboration with partner organizations in Russia and other countries. The *Fermi*-LAT Collaboration acknowledges the generous ongoing support from a number of agencies and institutes that have supported both the development and the operation of the LAT, as well as scientific data analysis. These include the National Aeronautics and Space Administration and the Department of Energy in the United States; the Commissariat à l'Energie Atomique and the Centre National de la Recherche Scientifique/Institut National de Physique Nucléaire et de Physique des Particules in France; the Agenzia Spaziale Italiana and the Istituto Nazionale di Fisica Nucleare in Italy; the Ministry of Education, Culture, Sports, Science and Technology (MEXT), High Energy Accelerator Research Organization

(KEK), and Japan Aerospace Exploration Agency (JAXA) in Japan; and the K. A. Wallenberg Foundation, the Swedish Research Council, and the Swedish National Space Board in Sweden. Additional support for science analysis during the operations phase is gratefully acknowledged from the Istituto Nazionale di Astrofisica in Italy and the Centre National d'Etudes Spatiales in France.

# Erklärung

Ich versichere, dass ich die von mir vorgelegte Dissertation selbständig angefertigt, die benutzten Quellen und Hilfsmittel vollständig angegeben und die Stellen der Arbeit – einschließlich Tabellen, Karten und Abbildungen –, die anderen Werken im Wortlaut oder dem Sinn nachentnommen sind, in jedem Einzelfall als Entlehnung kenntlich gemacht habe; dass diese Dissertation noch keiner anderen Fakultät oder Universität zur Prüfung vorgelegen hat; dass sie –abgesehen von unten angegebenen Teilpublikationen– noch nicht veröffentlicht worden ist, sowie, dass ich eine solche Veröffentlichung vor Abschluss des Promotionsverfahrens nicht vornehmen werde. Die Bestimmungen der Promotionsordnung sind mir bekannt. Die von mir vorgelegte Dissertation ist von Prof. Dr. Andreas Eckart und Prof. Dr. J. Anton Zensus betreut worden.

Köln, den 25.03.2020

A handwritten signature in blue ink, consisting of a large, sweeping loop followed by a series of smaller, more intricate strokes.

---

Efthalia Traianou

## Astronomy and Astrophysics

Editor in Chief: T. Forveille

### T. Forveille

Astronomy & Astrophysics  
Observatoire de Paris  
61, avenue de l'Observatoire  
75014 Paris, France

Tel.: 33 0(1) 43 29 05 41  
Fax: 33 0(1) 43 29 05 57  
e-mail: [aanda.paris@obspm.fr](mailto:aanda.paris@obspm.fr)  
Web: <http://www.aanda.org>

merging  
Annales d'Astrophysique  
Arkiv for Astronomi  
Bulletin of the Astronomical Institutes  
of the Netherlands  
Bulletin Astronomique  
Journal des Observateurs  
Zeitschrift für Astrophysik  
Bulletin of the Astronomical Institutes  
of Czechoslovakia

Paris, December 20, 2019

## Reprint Permission

### Material:

Article by Traianou et al. 2020, A&A, in press, DOI 10.1051/0004-6361/201935756

### To be used in:

PhD thesis entitled "High Resolution Millimeter VLBI Studies of the Blazars TXS 2013+370, OJ 287, and 3C 454.3", Universität zu Köln (University of Cologne)

### Permission granted to:

Efthalia Traianou  
[etraianou@mpifr-bonn.mpg.de](mailto:etraianou@mpifr-bonn.mpg.de)

I hold copyright on the material referred to above, and hereby grant permission for its use as requested herewith.

The article should be reproduced as a whole in a coherent fashion fully consistent with the version published in A&A.

Credit should be given as follows:

Credit: Author, A&A, vol, page, year, reproduced with permission © ESO.



Thierry Forveille  
A&A Editor-in-Chief

Sponsored by Argentina, Armenia, Austria, Belgium, Bulgaria, Chile, Croatia, Czech Republic, Denmark, Estonia, Finland, France, Germany, Greece, Hungary, Italy, Lithuania, Netherlands, Norway, Poland, Portugal, Slovak Republic, Spain, Sweden, and Switzerland.

Produced and distributed by EDP Sciences for ESO.